Exploring Star Formation in high-z Galaxies using Atomic and Molecular Emission Lines

Bitten Gullberg

Munich 2016

Exploring Star Formation in high-z Galaxies using Atomic and Molecular Emission Lines

Bitten Gullberg

Dissertation
at the Faculty of Physics
the Ludwig–Maximilians–University
Munich

submitted by
Bitten Gullberg
from Solrød strand, Denmark

Munich, First submission: October 28, 2015
Munich, Second submission: March 18, 2016

First referee: Prof Ralf Bender
Second referee: Prof Andreas Burkert
Date of oral exam: 14th March 2016

To my parents
My sturdy rocks in a turbulent world

Det er svært at spå - især om fremtiden.
Prediction is very difficult, especially about the future.
(Unknow author)

Contents

List of Figures

List of Tables

Abstract

The conditions under which stars are formed and the reasons for triggering and quenching of starburst events in high-z galaxies, are still not well understood. Studying the interstellar medium (ISM) and the morphology of high-z galaxies are therefore key points in order to understand galaxy evolution. The cosmic star formation rate density peaks between $1 < z < 3$. This period in the history of the Universe is therefore crucial to investigate in order to know more about the star-formation triggering and quenching mechanisms. Phenomena such as major mergers and galactic nuclear activity are believed to be mechanisms dominating the star formation activity at this period of time. It is therefore necessary to study galaxy populations which show signs of major merger events and active galactic nuclei (AGN). This thesis presents three studies of the ISM conditions in high-z galaxies and their morphologies by:

Exploring the physical conditions of the ISM in a sample of dusty star-forming galaxies (DSFGs) using the relative observed line strength of ionised carbon ([CII]) and carbon monoxide (CO). We find that the line ratios can best be described by a medium of [CII] and CO emitting gas with a higher excitation temperature of [CII] than of CO, high CO optical depth $\tau_{\mathrm{CO(1–0)}} \gg 1$, and low to moderate [CII] optical depth $\tau_{\mathrm{[CII]}} \lesssim 1$.

Combining millimetre/sub-millimetre and optical data cubes for the high-z radio galaxy (HzRG) MRC0943-242, has revealed a much more complicated morphology than seen in the individual data sets. The millimetre/sub-millimetre observations data have allowed us to spatially separate the AGN and starburst dominated components, which are $\sim 65\,\mathrm{kpc}$ apart. The optical data reveal structures of emitting and absorbing gas at multiple wavelengths.

A deep high resolution millimetre/sub-millimetre study of the HzRG MRC1138-262, shows emission from water (H_2O) and an unusually large amount of neutral atomic carbon ([CI]) relative to highly excited CO compared to lensed DSFGs. The detection of water (H_2O) emission, which is not associated with the 235 GHz continuum emission, suggests excitation by shocks. The uncommon line ratio between [CI]2-1 and CO(7–6) might be due special conditions of the ISM in MRC1138-262 dominated by cosmic rays or differential lensing in other DSFGs thereby not representing the intrinsic ratio.

These three studies of the physical conditions of the ISM and morphology of high-z galaxies at $z > 2$, pave the road for future investigations of the star-forming ISM in high-z galaxies, by illustrating the importance of multi-wavelength, fine structure- and molecular line studies.

Zusammenfassung

Die Bedingungen für Sternentstehung und die Gründe für das Auslösen und Dämpfen von Starburst-Ereignissen in hoch-rotverschobenen Galaxien sind bisher nicht gut verstanden. Untersuchungen des interstellaren Mediums (ISM) und der Morphologie hoch-rotverschobener Galaxien sind daher Kernpunkte um die Entwicklung von Galaxien zu verstehen. Das Maximum der kosmischen Sternentstehungsratendichte liegt zwischen $1 < z < 3$. Diese Periode des Universums zu studieren ist daher von entscheidender Bedeutung um mehr über die Auslösungs- und Dämpfungsmechanismen der Sternentstehung zu erfahren. Man glaubt, dass Phänomene wie Fusionen von Galaxien und galaktische Kernaktivität die Sternentstehungsaktivität zu dieser Zeit dominieren. Daher ist es nötig Galaxienpopulationen, die Zeichen von Fusionsereignissen oder Aktiver Galaktischer Kerne (AGNs) zeigen, zu untersuchen. Diese Doktorarbeit stellt drei Studien des ISMs in hoch-rotverschobenen Galaxien und deren Morphologien vor:

Zuerst wurden die physikalischen Bedingungen des ISMs in einer Reihe von staubigen Sternentstehungsgalaxien (DSFGs) mit Hilfe der relativen beobachteten Linienstärke von ionisiertem Kohlenstoff ([CII]) und Kohlenmonoxid (CO) untersucht. Wir fanden heraus, dass die Linienverhältnisse am besten durch ein [CII] und CO emittierendes Gas beschrieben werden können, welches eine höhere Anregungstemperatur für [CII] als CO sowie eine hohe CO optische Dichte $\tau_{\mathrm{CO(1–0)}} \gg 1$ und eine niedrige bis mäßige [CII] optische Dichte $\tau_{\mathrm{[CII]}} \lesssim 1$ zeigt.

Die Kombination von Millimeter/Submillimeter- und optischen Datenkuben für die hoch-rotverschobene Radiogalaxie (HzRG) MRC0943-242 brachte eine viel komplizierte Morphologie zum Vorschein als in den einzelnen Datensätzen. Die Millimeter/Submillimeter-Daten ermöglichten die räumliche Trennung der AGN- und der Starburst-dominierten Komponenten, welche $\sim 65\,\mathrm{kpc}$ voneinander entfernt sind. Die optischen Daten zeigen Strukturen emittierenden und absorbierenden Gases bei mehreren Wellenlängen.

Eine tiefe, hochauflösende Millimeter/Submillimeter-Studie der HzRG MRC1138-262 offenbarte H_2OEmission und eine ungewöhnlich hohe Menge neutralen atomaren Kohlenstoffs ([CI]) relativ zu hoch-angeregtem CO im Vergleich zu Linsen-DSFGs. Die Entdeckung der Wasser-Emission (H_2O), die nicht mit der 235 GHz Kontinuumemission zusammenhängt, deutet auf die Anregung durch Schocks hin. Das ungewöhnliche Verhältnis zwischen [CI]2-1 and CO(7–6) ist möglicherweise auf den Differentiallinseneffekt in anderen DSFGs zurückzuführen, welches somit nicht das intrinsische Verhältnis repräsentiert, oder auf besondere Bedingungen des ISM in MRC1138-262, welche durch kosmische Strahlung

dominiert werden.

Diese drei Studien der physikalischen Bedingungen des ISM und der Morphologie der hoch-rotverschobenen Galaxien ($z > 2$) ebnen den Weg für zukünftige Untersuchungen des sternbildenden ISMs in hoch-rotverschobenen Galaxien durch die Verdeutlichung der Bedeutung von Feinstruktur- und Molekülllinien-Beobachtungen bei mehreren Wellenlängen.

Chapter 1

Introduction

1.1 Galaxy Evolution

Understanding galaxy evolution is one of Cosmology's most pressing issues. Piecing together the puzzle to establish how the galaxies we observe in the local Universe came to be, is a challenge. The most common type of galaxies in the local Universe are 'normal' star-forming galaxies such as the Milky Way and more extreme galaxy populations such as local (ultra) luminous infrared galaxies ((U)LIRGs) and active galactic nuclei (AGN) dominated galaxies are much less common. Identifying the role of (U)LIRGs in galaxy evolution, their high redshift counterparts and role of AGN are difficult tasks.

Local LIRGs and ULIRGs are defined by having infrared (IR) luminosities of $10^{11} < L_{\rm IR} < 10^{12}\,{\rm L}_{\odot}$ and $10^{12} < L_{\rm IR} < 10^{13}\,{\rm L}_{\odot}$ respectively, and studies of their structures and morphologies in the optical, near-IR via their molecular gas and dust suggest that these galaxies are major mergers of two roughly equally sized galaxies. The majority of these (U)LIRGs have IR luminosities $> 10^{11.5}\,{\rm L}_{\odot}$ and star formation rates (SFR) above $50\,{\rm M}_{\odot}\,{\rm yr}^{-1}$. The correlation between high IR luminosity, and high SFR in conjunction with major mergers resulted in the widely accepted evolutionary picture first presented by Sanders et al. (1988). In this scenario, the (U)LIRG and AGN 'populations' are phases in the galaxy evolution sequence, which starts with the collision of two gas-rich disk galaxies. This collision ignites intense star-formation as the gas rapidly compresses and cools. This intense star-formation results in the production of large amounts of dust particles, which absorb the optical and ultra-violet (UV) light emitted by young blue O and B stars and re-radiate at IR/sub-millimetre wavelengths during the (U)LIRG phase. When the supermassive black holes in the cores of the galaxies merge, the merging galaxies enter a phase dominated by AGN activity. The AGN is fed by the surrounding disk of gas and dust, which is fuelled by in-falling material from the outer parts of the merging system. The (U)LIRG phase is believed to be short due to the intense formation of stars which depletes the gas reservoir and possible winds from the AGN blowing the gas outwards. The system might shine brightly after the ULIRG phase as an obscured (or un-obscured) AGN, but eventually the system will lack gas to form new stars and ends up as an elliptical galaxy,

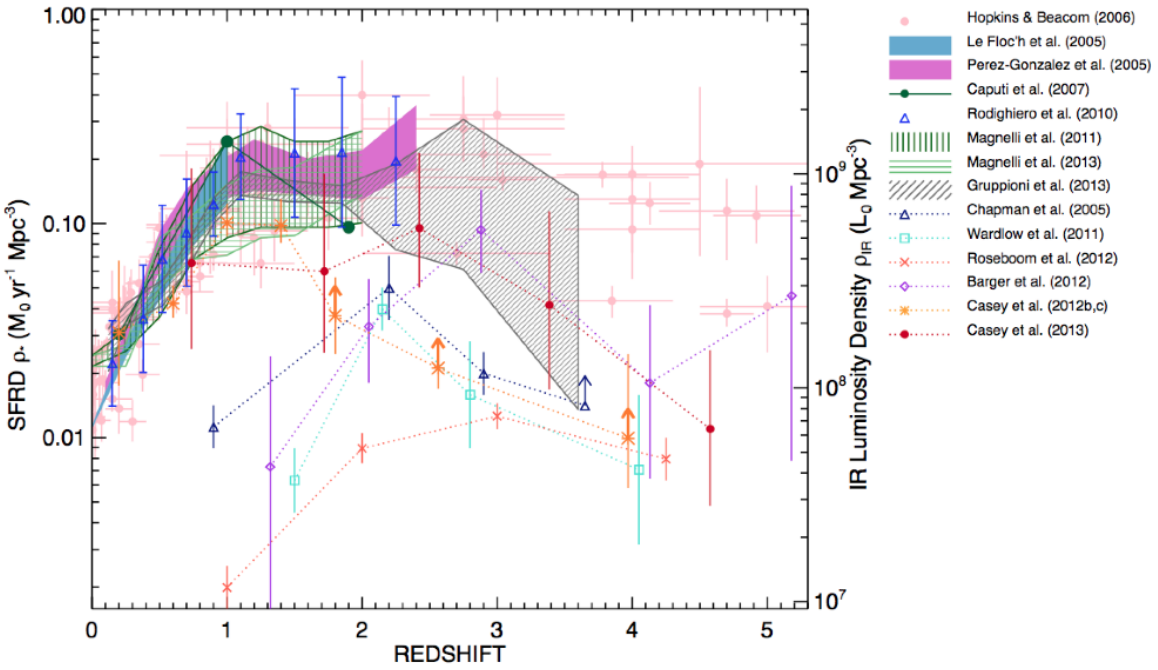

Figure 1.1: The star formation rate density (SFRD) plotted against the redshift, known as the Lilly-Madau plot and here reproduced from Casey et al. (2014). The plot shows an increase in SFRD between $0 < z < 1$ of about an order of magnitude. The evolution peaks between $1 < z < 3$ and flattens out at $z > 3$.

characterised by an old stellar population.

This evolutionary picture is very clean and simple and explains the formation of massive elliptical galaxies in the Universe. However, local (U)LIRGs are rare compared to 'normal' star-forming galaxies like the Milky Way. (U)LIRGs do therefore not contribute significantly to the cosmic SFR density (SFRD) at $z = 0$. The SFRD represents the total SFR occurring per unit time and volume at a given epoch. Determining the contribution to the SFRD of the Universe from low and high-z (U)LIRGs has been an important focus in understanding the role of dust obscured galaxies at high redshifts. The SFRD is often split into redshift bins and plotted against the redshift, which gives more detailed information on the evolution of the sample. This is known as the Lilly-Madau plot as it was first discussed by Lilly et al. (1995) and Madau et al. (1996) (see Fig. 1.1). The Lilly-Madau plot presents the evolution of the SFRD from $z = 0$ to $z \sim 5$, and clearly shows that the SFRD increases steeply by more than an order of magnitude between $0 < z < 1$, and peaks between $1 < z < 3$. Early versions of the plot showed a decrease after the peak out to $z \sim 6$, but as the high-z tail of the distribution is filled out, the SFRD for some samples seems to form a plateau. To determine the SFRD of a survey requires a good understanding of its depth and sky area coverage. The Lilly-Madau plot shown in Fig. 1.1 includes galaxy samples known to suffer from incompleteness and biases. However, it has proven to be a useful tool to illustrate the contribution from the given samples. Though ULIRGs play an insignificant role in the cosmic SFRD in the local Universe, they contribute with

$\sim 10\%$ at $z \sim 1$ and $\sim 50\%$ at $z \sim 2$. The questions are then: Were the high-z equivalent of (U)LIRGs more common in the early Universe? Are these major mergers dominating the cosmic SFRD at these times? Is another evolutionary sequence causing the presence of local (U)LIRGs?

The two galaxy populations, dusty star-forming galaxies (DSFGs) and high-z radio galaxies (HzRGs) are both galaxy populations (or phases in galaxy evolution) which can reveal more about intense star formation in the early Universe and the influence of an AGN on the star-forming medium. These two 'galaxy populations' will be the focus of this thesis.

1.2 Dusty Star-Forming Galaxies

The discovery of the first DSFG[1], SMMJ 02399−0136 with the Submillimeter Common-User Bolometer Array (SCUBA) in 1997 (Smail et al., 1997; Ivison et al., 1998) provided a new window in the study of galaxy formation and evolution. SMMJ 02399−0136 gave the first glimpse of an extreme galaxy population. DSFGs are found at high redshifts ($z > 1$), have high stellar masses ($M_* \sim 10^{11}\,\mathrm{M}_\odot$, e.g. Hainline et al. 2011), are considerably more gas-rich and turbulent than galaxies in the present day Universe ($M_{\rm gas} \sim 3 - 5 \times 10^{10}\,\mathrm{M}_\odot$, Tacconi et al. e.g. 2010; Bothwell et al. e.g. 2013b) and have SFRs of $\approx 10^3\,\mathrm{M}_\odot\,\mathrm{yr}^{-1}$, (e.g. Swinbank et al., 2014). They have proven to be a major challenge for conventional galaxy-formation models (e.g. Hayward et al., 2013; Lacey et al., 2015) which have had mixed success in modelling DSFGs (Narayanan et al., 2015). They are the perfect laboratories to study the conditions under which stars are formed in the progenitors of massive galaxies seen locally, in order to learn more about star formation in extreme environments.

1.2.1 Properties of DSFGs

DSFGs contain large amounts of dust, often obscuring the stellar light and star-formation, which emit at UV and optical wavelengths. DSFGs are therefore very problematic to identify at these wavelengths, making it difficult to determine the precise redshifts of individual sources. The dust obscuration hence makes it more insightful to study DSFGs in the far-IR (FIR), since the rest-frame UV photons are re-processed by being absorbed by dust grains, which heat the grains, and re-emit thermal emission as FIR and sub-millimetre continuum photons.

The K-correction (Blain & Longair, 1993) corrects for the bandpass shifting by redshifts. If the flux density of an object *decreases* with increasing, redshift then the K-corrections is called 'positive', and if the flux density of an object *increases* with redshift, then the K-correction is said to be 'negative' [2]. Galaxies emitting at sub-millimetre wavelengths

[1]The term DSFG covers all sources selected at both millimetre and sub-millimetre wavelengths, and will be the term used through-out this thesis

[2]The terminology of decreasing flux referred to as 'positive' and vice versa, originates from the optical magnitude scheme, where smaller numbers refer to brighter objects.

have a negative K-correction, as the dust emission resembles a modified blackbody peaking at rest-frame wavelengths $\sim 100\,\mu$m, and the long-wavelength regime is the Rayleigh-Jeans regime. The negative K-correction for high-z sub-millimetre sources is so significant that these sources have roughly constant brightness at sub-millimetre wavelengths at $z = 1 - 8$ (Blain et al., 2002). This means that across a wide redshift range, for which the Rayleigh-Jeans approximation applies, the observed flux density is roughly constant and might even increase slightly, making high-z DSFGs more easy to detect.

At the time of the first deep field SCUBA maps (Smail et al., 1997; Hughes et al., 1998; Barger et al., 1998), it was suspected that sub-millimetre sources would be predominantly located at high redshifts, as these sources benefit from having a negative K-correction.

1.2.2 Discovering DSFGs

The discovery of DSFGs has been limited by the opacity of the Earth's atmosphere or by the size of instruments we are able to send to space. The search for high-z DSFGs was focused on the 230 GHz (1.4 mm) and 345 GHz (850 μm) atmospheric windows. However, the search has been expanded to other frequencies with the improvement of instruments. Since the early 1980s and until now about 20 single dish facilities with detectors sensitive to 12 μm-1.4 mm emission have been used in the search for DSFGs (Casey et al., 2014). Some of the most ground breaking surveys were done using the SCUBA (1997-2005, and taking over by SCUBA-2 which is still running), *Herschel* (2009-2013), the Large Apex BOlometer CAmera (LABOCA, 2006-present), and the South Pole Telescope (SPT, 2008-present).

SCUBA was commissioned on the James Clerk Maxwell Telescope (JCMT) in 1997 and observed simultaneously at 450 μm (670 GHz) and 850 μm (345 GHz). The high sensitivity of SCUBA made it the front runner. The sensitivity of the 850 μm arrays could reach down to 2 mJy sensitivity with six hours integration time, therewith capable of detecting $10^{12.5}\,L_\odot$ galaxies out to $z \sim 5$. This meant that in the first deep-field observations several galaxies were detected within several arcmin. The detection of these sources confirmed that there had to be a strong evolution of the cosmic SFRD out to high redshift.

With the launch of the *Herschel Space Telescope* in May 2009, two instruments (the Spectral and Photometric Imaging Receiver (SPIRE), and the Photodetector Array Camera & Spectrometer (PACS)) became available to the community. SPIRE consisted of both a spectrometer and an imaging photometer which operated in three wavelength bands simultaneously: 250 μm, 350 μm and 500 μm. SPIRE was (among others) successful in discovering rare isolated FIR bright sources, some of which have been found to be lensed sub-millimetre galaxies. PACS consisted of an integral field spectrometer and an imaging photometer operating at 70 μm, 100 μm and 160 μm. Due to the wavelengths of PACS detecting emission on the Wien side of the SED, it could not take advantage of the negative K-correction, and was therefore not as efficient at mapping large areas of the sky. It was therefore not used as much for high redshift studies as SPIRE.

LABOCA was developed by the Max-Planck-Institute für Radioastronomie and is a multi-channel bolometer array for 870 μm continuum mapping. It has been installed at the Atacama Pathfinder EXperiment (APEX) telescope in Chile and was at full science

operation in 2008. DSFGs discovered with LABOCA in the LESS survey were some of the first sources to be follow-up in continuum observations with the Atacama Large Millimeter/submillimeter Array (ALMA) (Karim et al., 2013; Hodge et al., 2013)

The South Pole Telescope (SPT) commissioned in 2008 and located at the geographic South Pole in Antarctica, is a 10 m diameter dish operating at millimetre wavelengths. It is designed to detect anisotropies in the cosmic microwave background (Carlstrom et al., 2011), and galaxy clusters via the Sunyaev-Zel'dovish effect (Staniszewski et al., 2009). When the full 2500 $\deg^2$ survey area was completed in 2011, about 100 bright DSFGs had been detected in the survey (Vieira et al., 2010). Follow-up studies of these DSFGs showed that they were gravitationally lensed (Hezaveh et al., 2013).

Surveys such as those with SCUBA, *Herschel* and SPT are compared based on luminosity limits, as they are all performed at different wavelengths. However, the conversion from flux to luminosity introduces an uncertainty, which depends on the often ill determined shape of the SED of a given source. Additionally, the depth of the survey is dependent on the redshift, meaning that selections at shorter wavelengths will be most sensitive to low luminosity sources at low redshifts, while selections at longer wavelengths will be sensitive to higher redshifts due to the negative K-corrections (Béthermin et al., 2015). The characteristic of the SED for individual DSFGs and the success in detecting counterparts at different wavelengths, create biases in the DSFGs selection methods. These selection biases have to be taken into account when comparing sources selected from different surveys.

Gravitational lensing

The surveys performed using *Herschel* (H-ATLAS; Eales et al. 2010 and HerMES; Oliver et al. 2012) and SPT (Weiß et al., 2013; Vieira et al., 2013) have resulted in large samples of rare and bright DSFGs. Multi-wavelength follow-up observations are required to establish if a source is gravitationally lensed or intrinsically very bright. In the case of gravitational lensing, another galaxy lies on the line of sight to the DSFG. The foreground galaxy (or galaxy cluster) acts as a lens, where the gravitational potential of the mass bends the path of the light from the DSFG behind it, and therewith amplifies the brightness of the DSFG (see Fig 1.2). The amplification is dependent on the relative position along the line of sight of the foreground galaxy (or galaxy cluster) and the DSFG. If they are (close to) aligned, then the image of the DSFG will be a ring around the foreground galaxy, this is known as an Einstein ring. If there is a small mis-alignment between the two galaxies, then the background galaxy will show up as arcs around the foreground galaxy (see Fig. 1.3).

Multi-wavelength observations of 13 DSFGs from the *Herschel* selected sample revealed that 93% of these sources are gravitationally lensed and only 7% are intrinsically bright (Wardlow et al., 2013). About 250 DSFGs with a flux density of $S_{500\mathrm{GHz}} > 100$ mJy have been detected in the SPIRE imaging data covering 1200 $\deg^2$. However, it required large amounts of observing time at multiple wavelengths to confirm if these sources were lensed. High-resolution interferometric imaging, or a combination of a confirmed redshift of the background DSFG and an optical image of the foreground galaxy, can determine if a lensing event is taking place or not. The determined magnification factors of the *Herschel* selected

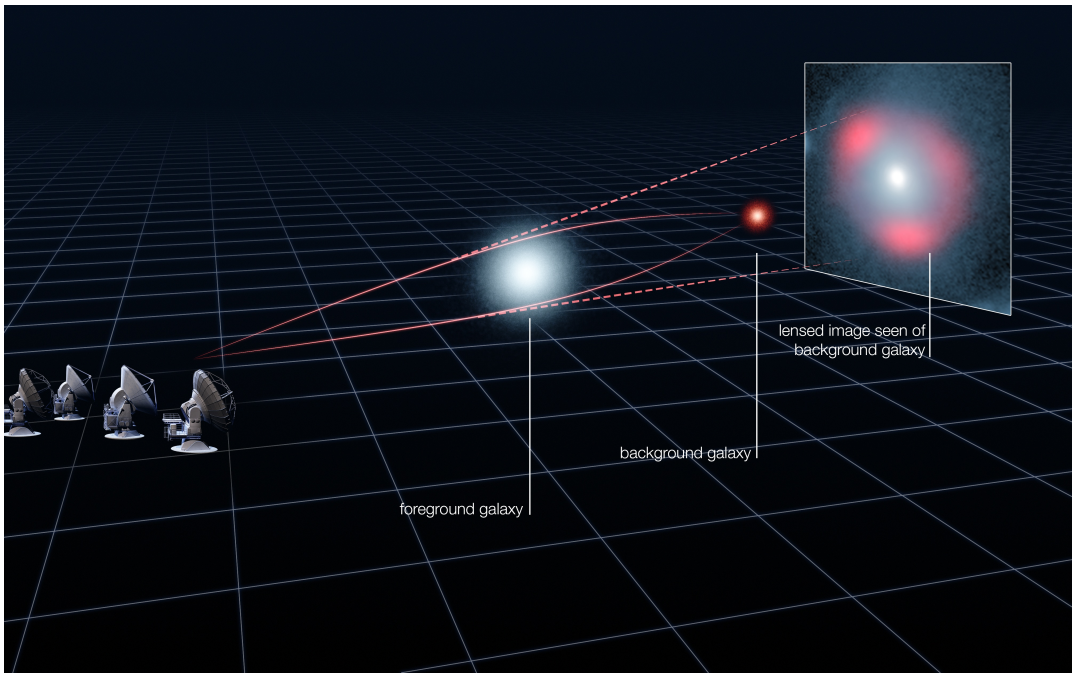

Figure 1.2: A reproduction of an artist impression of how light from a background source is amplified by the gravitational potential of the foreground galaxy or galaxy cluster (reproduced from ESO PR1313). The resulting image observed is shown as the red clumpy ring around the lensing source.

DSFGs has a mean of 6^{+5}_{-3} (Bussmann et al., 2013) implying that not only are these DSFGs lensed, but they are also intrinsically bright and have intrinsic luminosities corresponding to ULIRGs-like luminosities.

A complementary ALMA and *HST* imaging program showed that sources selected from the SPT survey were all amplified by gravitational lensing (see Fig 1.3, Hezaveh et al., 2013; Ma et al., 2015). Point sources in the 2500 deg^2 sky area with $S_{1.4\mathrm{mm}} > 20$ mJy was followed up with ALMA (Cycle 0) in a blind CO redshift survey (Vieira et al., 2013; Weiß et al., 2013). This blind survey resulted in 44 detected atomic and molecular emission lines from CO, carbon and H_2O, confirming the redshifts for 12 out of 23 DSFGs with double line detections. Single lines were detected for 11 sources, of which almost all have been confirmed later with molecular and atomic line observed with APEX. No lines were detected in three sources (see Fig 1.4). About half of these spectroscopically confirmed sources are at $z > 4$, which doubled the number of sources at these redshifts and at least two sources are at $z \sim 5.7$. The magnification factors determined for the SPT selected DSFGs showed a range of 5-22 and an average magnification of ~ 10 (Hezaveh et al., 2013). These values are based on only a handful of galaxies, meaning that this is small number statistics, but is comparable to the lensing magnifications derived for the *Herschel* selected DSFGs. Though the lensing magnifications are comparable the *Herschel* and SPT selected sources still have selection effect biases. *Herschel* selected sources are at lower redshifts due to the longer selection wavelengths compared to the SPT selected sources.

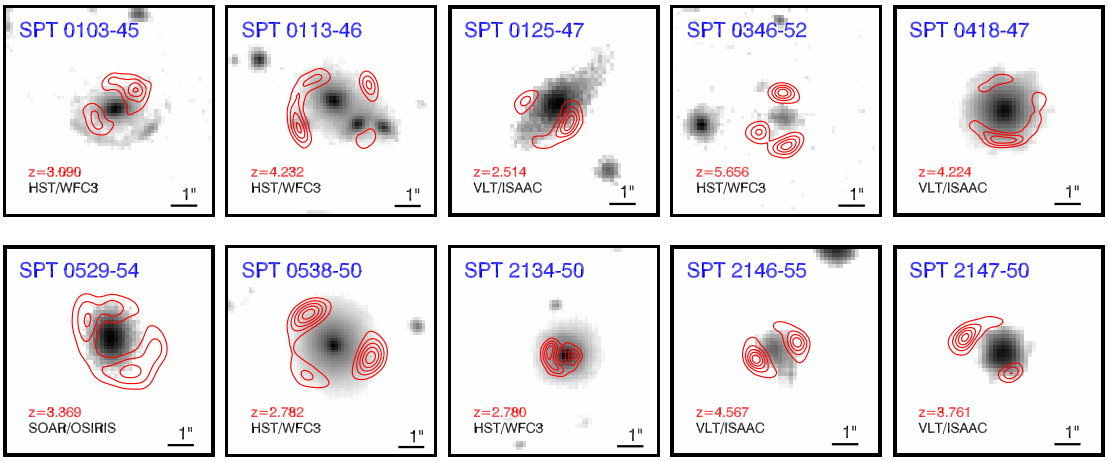

Figure 1.3: Ten lensed dusty star-forming galaxies from the SPT survey (reproduced from Vieira et al. 2013). The background shows the *HST* image in grey and overlaid in red contours is the ALMA dust continuum emission, showing the lensed background source.

Gravitational lensing gives us the opportunity and possibility to detect and study DSFGs at high redshift. However, it does also introduce the disadvantageous of differential lensing. Due to differential lensing the interstellar medium (ISM) components get magnified differently depending on the density and position of the medium. A dense medium close to the lensing caustic is more likely to have a higher magnification factor than the diffuse extended gas. One therefore has to be aware of the possibility of differential lensing, which makes it difficult to characterise the dense and diffuse gas components of the ISM in lensed DSFGs.

Redshift determination and distribution

One of the challenging aspects of discovering DFSGs is to determine their redshifts. The two main ways of determining the redshift are via photometry and spectroscopy. The millimetric photometric redshift (i.e. photo-z or $z_{\rm photo}$) is determined using the shape of the spectral energy distribution (SED) at FIR or sub-millimetre wavelengths. This method assumes a shape of the FIR SED of DSFGs (e.g. the one of Arp 220) and thereby fits the redshifts. The photometric redshift method is not very precise and the accuracy of the determined redshift is dependent on the intrinsic variations of the SED of DSFGs. The dust temperature manifests itself as the peak of the SED and it correlates with the IR luminosity which both are degenerate with redshift (Casey et al., 2014). This means that if the SED of a source which peaks at 400 μm in the observed-frame, is fitted with an assumed temperature of 30 K, the photometric redshift would be $z_{\rm photo} \sim 2.2$. While if the same source is fitted with an assumed temperature of 50 K, then the estimated photometric

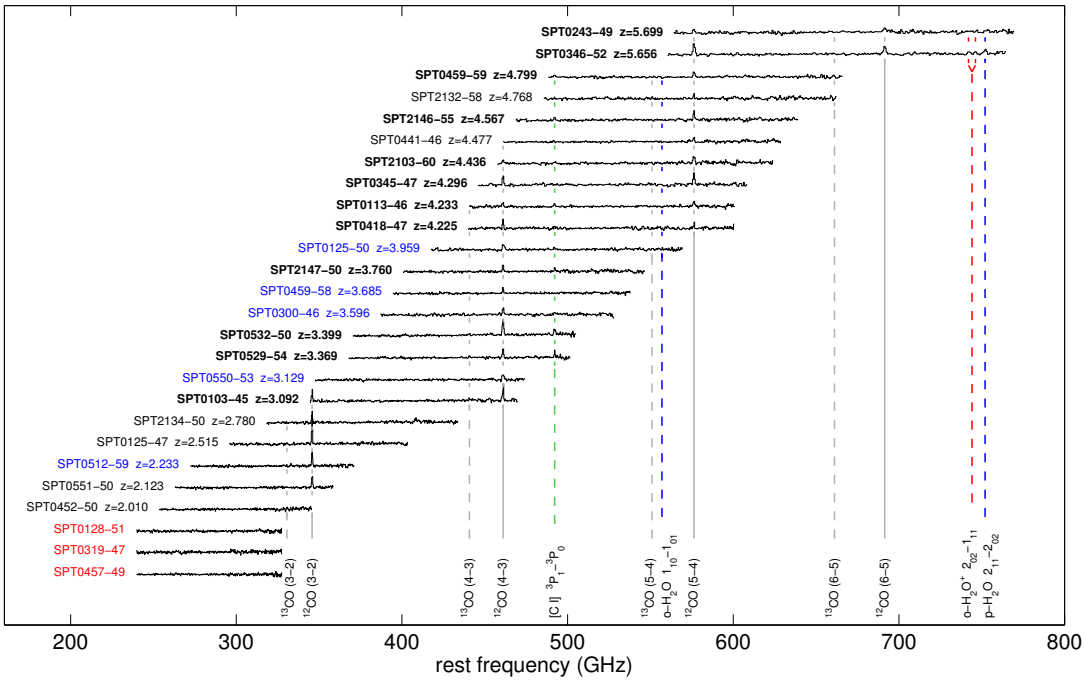

Figure 1.4: Spectra of the 26 SPT selected DSFGs observed with ALMA (Cycle 0) in a blind CO survey (reproduced from Vieira et al. 2013). Forty-four molecular and atomic emission lines were observed for 23 sources, while no lines were observed for three sources.

redshift would be $z_{\rm photo} \sim 4.6$. Though this method is not very accurate, it can still be used to give a rough estimate of the redshift of sources, which are impossible to probe via other methods.

The most accurate method to establish the redshift of a source is spectroscopic redshift determination, by detecting at least two emission lines. The optimal way to determine redshifts of DSFGs is by using their millimetre emission lines as these are directly related to their dust continuum emission. This redshift determination technique benefits from the knowledge that the observed sources are already detected at millimetre wavelengths, and are therefore expected to have luminous millimetre-emission lines. Despite the knowledge of luminous millimetre-emission lines millimetre-spectroscopic redshifts determinations were limited by the bandwidth of the receivers up through the 2000s. The bandwidths were simply too narrow to serve as an efficient way to search for lines. The first instrument to really open up for redshift determinations via millimetre emission lines was WIDEX at the Plateau de Bure Interferometer (PdBI) with a bandwidth of 3.6GHz. Afterwards, more facilities followed such as the EMIR receiver at the IRAM 30 m (Weiß et al., 2009), Z-spec and ZEUS at Caltech Submillimeter Observatory (CSO, Bradford et al. 2009; Nikola et al. 2003), and the Redshift Search Receiver at the Large Millimetre Telescopes (Zavala et al., 2015). Since its commissioning in the 2011, ALMA has been the preferred facility to perform millimetre-spectroscopic redshift determinations via emission lines from for example CO, [CI] and [CII]. A complication of the spectroscopic redshift determination

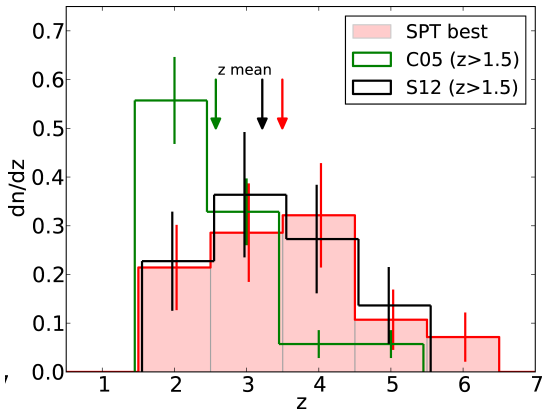

Figure 1.5: The number of DSFGs as a function of redshift (reproduced from Weiß et al. (2013)). The red histogram shows the distribution of the SPT selected DSFGs, the green histogram the distribution of the DSFGs from Chapman et al. (2005) and the black histogram the distribution of the sources from Smolcic et al. (2012). A comparison between the three distributions shows that the SPT DSFGs and sources from Smolcic et al. (2012) peak at higher redshifts than the sample from Chapman et al. (2005).

method is the so called redshift deserts. A redshift desert is a redshift range for which an instrument would not be able to detect any strong emission or absorption lines, as the lines are shifted out of the observed band. The span of the redshift desert is dependent on the wavelength range of the instrument and therefore varies from instrument to instrument, and can create a bias in samples using only one instrument for spectroscopic redshift determinations.

The different redshift distributions of DSFGs samples show significant variations. The different distributions reflect the selection techniques and biases within the samples. The 850 μm selected DSFG population is the to date best studied, and one of the most comprehensive studies of this population was by Chapman et al. (2005), who presented a sample of 73 850 μm selected DSFGs with radio counterparts, which had been spectroscopically observed with the Low-Resolution Imaging Spectrometer (LRIS) instrument at Keck Observatory (Oke et al., 1995). This sample showed a median redshift of $z = 2.2$ (see green histogram in Fig 1.5). A similar median redshift of $z \sim 2.5$ was found for a sample of 126 870 μm selected DSFGs by Wardlow et al. (2011) who presented an optical/near-IR study of LABOCA selected sources. The median of the redshift distribution of 28 1.1 mm selected DSFGs detected with AzTEC was determined by Chapin et al. (2009) to $z = 2.7$, which they claim to be statistically different from $z = 2.2$ found by Chapman et al. (2005). A study of 17 1.1 mm selected DSFGs by Smolcic et al. (2012) yield an even higher median redshift of $z = 3.1$ (see black histogram in Fig. 1.5). Smolcic et al. (2012) used another strategy for determining the photometric redshift by considering multiple minima in the χ^2 photometric redshift fitting. The discrepancy could be due to cosmic variances, as the sources are selected from the COSMOS field, which is known for having several very distant DSFGs at $z > 4.5$. The sample of 26 1.4 mm selected DSFGs from the SPT survey presented by Weiß et al. (2013), has a median redshift for $z = 3.5$ (see red histogram in

Fig. 1.5). This sample has spectroscopic redshifts determined by CO, [CI] and [CII] line observations from ALMA, ATCA and APEX. All sources in this sample are lensed. The SPT survey is too shallow to detect distant non-gravitationally lensed DSFGs, which introduces a bias in the redshift distribution, as lower redshift sources ($z < 2$) are less likely to be gravitationally lensed by a foreground galaxy. This effect is strong for $z < 2$ sources and even stronger for $z < 1$, but has little effect on the higher redshift sources. Another phenomenon that could have an influence on the redshift distribution of the SPT selected sources is an evolution of the source sizes (Weiß et al., 2013). If the sizes of DSFGs evolve with redshift, then it can effect the lensing of the source: the more compact - the higher redshift and the more likely it is to be detected in the 1.4 mm SPT survey as a lensed DSFG.

Only future studies and redshift determinations of more sources will make the true redshift distribution clearer. Using phenomenological models, Béthermin et al. (2015) showed that the dominating effect driving the different redshift distributions is the selection wavelength.

1.2.3 Stars in DSFGs

Determining the stellar masses for DSFGs has been proven to be highly uncertain. A good example of this is Hainline et al. (2011) and Michałowski et al. (2012) who determined the stellar masses of *the same* sample of 850 μm selected DSFGs and found an order of magnitude different stellar masses.

One of the sources of uncertainty is the assumed star formation history (SFH), which can be: exponentially declining, constant, single starburst or a multi-component SFH. A multi-component SFH can lead to a higher inferred stellar mass than a single starburst component (Dunlop, 2011). On the other hand, a single component SFH typically results in an underestimation of the stellar mass.

The assumed stellar population synthesis model, i.e. the assumed evolution model of the stars, along with the choice of initial mass function (IMF) can cause differences in the calculated stellar masses. Even minor difference in the IMF (e.g. using the Chabrier (2003) or Salpeter (1955) IMF) can result in a $\sim$ 80% difference in the stellar masses. Observations and theories are trying to pin down an IMF for high-z DSFGs, but this has resulted in a wide range of potential options. The IMFs at high redshifts tend to have more massive stars and less low mass stars compared to local IMFs.

Hainline et al. (2011) found that 10% of a sample of $\sim$ 70 DSFGs had substantial contributions to the SED from AGN. Using the H-band luminosity (1.6 μm), which probes the peak of stellar emission more directly than the K-band luminosity (2.2 μm) which can be contaminated by AGN emission, they found a more accurate measure of the stellar mass. They hereby estimate lower stellar masses than for other DSFG samples and measure a median of $\langle M_* \rangle \sim 7 \times 10^{10}\,\mathrm{M}_\odot$. The same sample was examined by Michałowski et al. (2010), who found a median of $\langle M_* \rangle \sim 3.5 \times 10^{11}\,\mathrm{M}_\odot$. Correcting for the IMF effects, the result of Hainline et al. (2011) comes within a factor ~ 3 of the result of Michałowski et al. (2010). A follow-up study by Michałowski et al. (2012), investigating the discrepancy

between the estimated stellar masses, concluded that the discrepancy is dominated by the choice of IMF, population synthesis model and SFH.

In order to constrain the stellar mass of DSFGs better, more accurate measurements of e.g. the dynamical mass using CO or [CII] spatially resolved observations, disentanglement of the AGN and stellar emission and in lensed objects the foreground galaxy and the DSFGs (e.g. Ma et al., 2015) are necessary. Accurately constraining the stellar masses in DSFGs will be a crucial step forward in the understanding of their relation to other high-z galaxies and how they lie on the galaxy-main sequence.

1.3 High-z Radio Galaxies

Among the rare galaxy species are the radio loud active galactic nuclei (AGN). The discovery of quasi-stellar objects, QSOs or quasars, in the 1960s revealed galaxies at even higher redshifts than normal galaxies, indeed for several decades the most distant galaxies were radio loud objects. At this time, the discovery of the first QSO, demonstrated that the space density of radio sources varies with cosmic epoch - a discovery in disagreement with the Steady State Cosmology. Up until the end 1970s, the highest redshift radio galaxies observed was at $z \sim 1$, whose discovery was made possible only thanks to a large investment of time at the Lick telescope (Spinrad, 1976; Spinrad et al., 1977; Smith & Spinrad, 1980). The radio sources discovered during these observations were not considered important in the scheme of galaxy evolution, but were merely regarded as useful for pinpointing distant galaxies. With the technical revolution in the 1980s and 1990s photographic plates were replaced by CCDs in optical astronomy, allowing for the discovery of a large number of radio galaxies out to $z \sim 5$. These radio sources are known as high-z radio galaxies (HzRGs).

Along with the technical revolution came the discovery of the alignment of the host galaxy observed in optical wavelength and the radio sources, indicating an interaction between the host galaxy and the radio source. The additional discovery of the relation between the masses of elliptical galaxies and the inferred masses of the central super massive black holes led to the conclusion that all galaxies go through a stage dominated by nuclear activity at some point in their history. The invention of new techniques to hunt high-z galaxies such as the drop-out techniques (Illingworth, 1999) made radio galaxies less important for cosmological use, but they are still crucial for exploring galaxy evolution and the start of nuclear activity all galaxies are believed to go through (Merloni & Heinz, 2013).

1.3.1 Active galactic nuclei

The unification model

The paradigm that a super massive black hole in the centre of the galaxy accreting matter is the driver of the radio source, was developed in the 1980s and was the seed for the 'Orientation unification' model (see Fig. 1.6). The model describes the active nucleus as

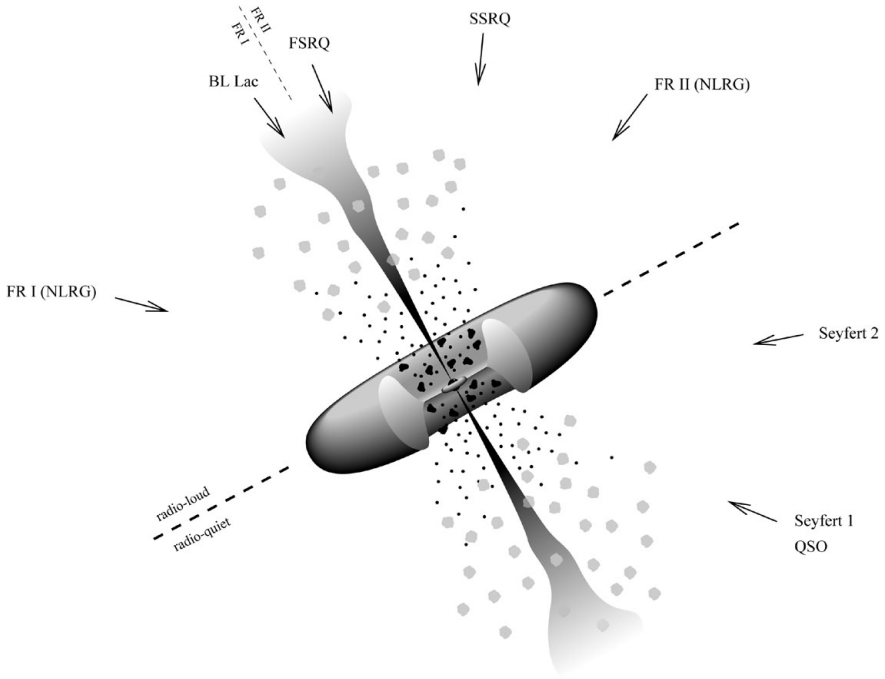

Figure 1.6: A sketch of the unification model, showing that the observed properties are highly dependent on the viewing angle (reproduced from Torres 2003).

an axial structure where the central black hole is accreting material from a surrounding disk of gas and dust extending $\sim 100\,\mathrm{AU}$ from the centre. The gravitational potential of the material is transferred into radiation via viscous dissipation and results in a source radiating across the full electromagnetic spectrum. The inner part of the accretion disk, a few AUs, is believed to be responsible for the observed X-ray emission.

Just surrounding the X-ray emitting region, is the broad line region (BLR). The broad emission lines emitted from this region of the accretion disk, play an important role in our understanding of AGN. The lines portray the bulk motions in the BLR, which are almost certainly controlled by the central source. Additionally, the BLR reprocesses ionising UV continuum photons, which provide indirect information about this part of the continuum. This means that brightness variations in the emitted BLR lines, reflect the changes in the underlying continuum. The line emitted from the BLR is Doppler-broadened and even a single spectrum can show emission lines of different widths. The broadening of the lines, however, can become a disadvantage as the lines can blend together and make a complete de-blending impossible.

At a distance of $\sim 10^4\,\mathrm{AU}$ from the centre the emission from the accretion disk is believed to be dominated by IR radiation. At these distances we also find the narrow line region (NLR). This is low density gas, whose motions are dominated by gravity. The NLR is the largest spatial scale region, where the ionising radiation from the central source dominates. It is the only AGN component, which can be spatially resolved in the optical. This gives important information about how the NLR is illuminated by the central source

Radio properties	Orientation	
	Face-on	Edge-on
Radio quiet	Seyfert I	Seyfert II
	QSO	
Radio loud	BL Lac	FR I
	BLRG	NLRG
	Quasar/OVV	FR II

Table 1.1: Overview of the different AGN types, classified by their orientation and if they are radio quite or loud.

in a non-isotropic way, and can tell us how the central source is fuelled. The spatial extent of the region means that the physical and kinematic distribution of the gas, to some extent, can be mapped directly. The low density of the gas in the NLR allow forbidden transitions to not be collisionally suppressed. The intensity ratios of certain pairs of forbidden lines, allow us to measure the electron density and temperature of the NLR gas (Peterson, 1997). In contrast to the broad lines from the BLR, the forbidden lines are isotropic since self-absorption in the narrow lines is negligible, and they therefore do not reflect variations in the underlying continuum.

Evidence of gas-jet interaction in the form of shock-heating and outflows has been found at the NLR location in the disk. The unresolved AGN-environment is further surrounded by an optically thick obscuring torus, limiting the radiation from the AGN to escape only along the torus axis. In radio loud sources the radio axis are aligned with the torus axis, but these do not show a preferred orientation with the rotation axis of the host galaxies (Drouart et al., 2012).

The unification model assumes that the intrinsic diversity of AGN is less than what is observed. The wide variety of observed AGN is a combination of actual variations in the physical parameters, and apparent variations, depending on the viewing angle. The dominant factor in the classification of an AGN in this scheme is the orientation of the system. The classification therefore becomes a function (mostly) of the viewing angle. If the AGN is observed face-on (i.e. the line of sight is parallel to the axis of the torus), then the central accretion disk and the BLR are un-obscured and the broad lines can be detected, this is known as a Seyfert I or QSO for the radio quiet galaxies, and a BL Lac or OVV for the radio loud galaxies. If the system is viewed more edge-on, then the central part is not visible and the broad lines are not detected, this is know as a Seyfert II galaxies for the radio quiet, and a FR I or FR II for the radio loud galaxies (see Fig. 1.6 and Table 1.1).

There are two main differences between Seyfert I and II:

1) broad emission lines are observed for Seyfert I but not for Seyfert II and

2) the AGN continuum to the stellar continuum ratio of Seyfert IIs are about a magnitude weaker than of Seyfert Is.

The most obvious candidate causing these differences is dust obscuration. However, this hypothesis does have problems:

i) The featureless continua observed for Seyfert IIs look like power laws, although a reddened power law should no longer look like a power law (Peterson, 1997).

ii) The continua of Seyfert IIs are only about one magnitude weaker than for Seyfert Is, which is surprising as the broad lines are completely extinguished.

To explain the still visible continua for Seyfert IIs, Osterbrock (1978) introduced an additional component, the 'scattering medium'. This medium lies above the hole in the torus and scatters the continuum emission, such that it is visible to the observer viewing the system edge-on. The suggestion of an additional scattering medium, is supported by the very weak and broad emission lines in the linear polarisation spectrum observed for the nearby Seyfert II galaxy NCG1068 (e.g. Antonucci & Miller, 1985). Scattering or reflection of the AGN continuum emission by either dust or electrons can result in a polarised spectrum. The continuum for NCG1068 is polarised by 16% and the polarised spectrum is wavelength independent far into the UV ($\sim$ 1500Å) (Code et al., 1993), which suggests that electrons are the scattering particles. The narrow emission lines are only polarised by 1%, indicating that they are observed directly and not after scattering (Vernet et al., 2001).

The simplicity of the unification model appeals to our belief that any description of nature should be as simple as possible, if there is no evidence for the contrary, also known as Occam's razor. However, it is still unclear what the fundamental parameters of the unification model are. Intrinsic luminosity and orientation provide good starting points for describing the systems, but there might be other important factors such as the morphology and gas to dust content, which influence the appearance of the system. Other model such as an unification model by evolution has been suggested. Nevertheless, the unification model has become a popular interpretation scheme of the different types of AGN.

1.3.2 Properties of HzRGs

The properties of radio galaxies differ between high and low redshift sources and change with luminosity. HzRGs are often defined by being at $z > 2$ and having a radio luminosity at rest frame frequency 500 MHz of $L_{500\mathrm{GHz}} > 10^{27}\,\mathrm{W\,Hz^{-1}}$. The spectrum of H$z$RGs consist of two components; an extended steep-spectrum component and a compact flat-spectrum component. The extended component is a double-lobed structure centred at the compact component, and emission from the core arises in a beamed jet-like structure. The flux ratio between the emission from the core and the lobe is used as a measure of orientation i.e. the angle between the jet direction and the line of sight (e.g. Orr & Browne, 1982). Sources with a high core-to-lobe flux ratio (R), where the beamed component dominates by being close to the line of sight, are known as core-dominated radio sources. Sources with a low R are known as lobe-dominated sources, in these cases the beamed component is far from the line of sight. The spectra of these two types of radio sources are very different, with the core-dominated sources having a flat-spectrum and lobe-dominated sources having a steep-spectrum. The extended structure of a HzRG is double-lobed, and the jet-structure is more often only one sided and co-aligned with the axis of the extended radio lobes. The relativistic beaming and therewith large Lorentz factor of the jet-structure explains why

the approaching jet is often detected, while the receding jet is not. The spectra of such sources are typically steep, non-thermal, collimated and extended over tens of kpc.

Radio-loud quasars have evoked three main concerns when comparing observations and expectations;

i) If the two-component-model describing the radio-loudness is close to correct, and the jet-axis is randomly oriented, then the observed galaxies would often have a jet oriented close to the plane of the sky. In such a case the two sides of the jet should have about the same surface brightness, which is not in agreement with observations.

ii) If the sources are randomly oriented in the sky, then it is expected that steep-spectrum sources should outnumber the flat-spectrum sources, which contradicts observations (Phinney, 1985).

iii) If the extended and compact components share a common axis (which they most certainly do, based on comparison with edge-on systems), then the extended emission in sources where the line of sight and jet are close to each other can de-project to a linear size on the sky of $\sim 1\,\mathrm{Mpc}$.

It has been argued by Barthel (1989) that these three concerns can be explained using the unification model: quasars with an axis close to the plane of the sky are not detected as radio-loud quasars but as radio galaxies. Barthel (1989) showed that this is consistent with the distribution of quasars and radio galaxies. However, using the unification model as an explanation, causes a problem with the observed [OIII] emission line luminosities observed for quasars and radio galaxies, as the quasars are observed to have 4-10 times higher [OIII] line luminosities than the radio galaxies. If quasars and radio galaxies are from the same parent galaxy population, and if the [OIII] luminosity is isotropic, such a luminosity difference should not be observed. This means that if the unification model is retained as an explanation, then the [OIII] emission must be anisotropic, preferentially along the radio axis (Jackson & Browne, 1991).

Spectral properties

The SED of HzRG (and AGN in general) cannot be described by blackbody emission of a single temperature or a composite of a small range of temperatures. Non-thermal, primary incoherent synchrotron radiation, is required to explain the shape of AGN spectra. The SED of an AGN is broad and often approximated with a power law, which in some cases is too crude an approximation. The slope of the power law (i.e. the spectral index) is denoted α and can vary for different wavelength ranges. The spectral index is usually in the range $-1 > \alpha > 0$.

$z - \alpha$ correlation

The steepness of the spectra (i.e. spectral index) of radio galaxies show a correlation with the redshift of the associated galaxies (Tielens et al., 1979; Blumenthal & Miley, 1979). It has been shown that radio sources with very steep spectra at low frequencies of $\nu \lesssim 1\,\mathrm{GHz}$, are often associated with high redshifts. This correlation has proven very efficient in finding

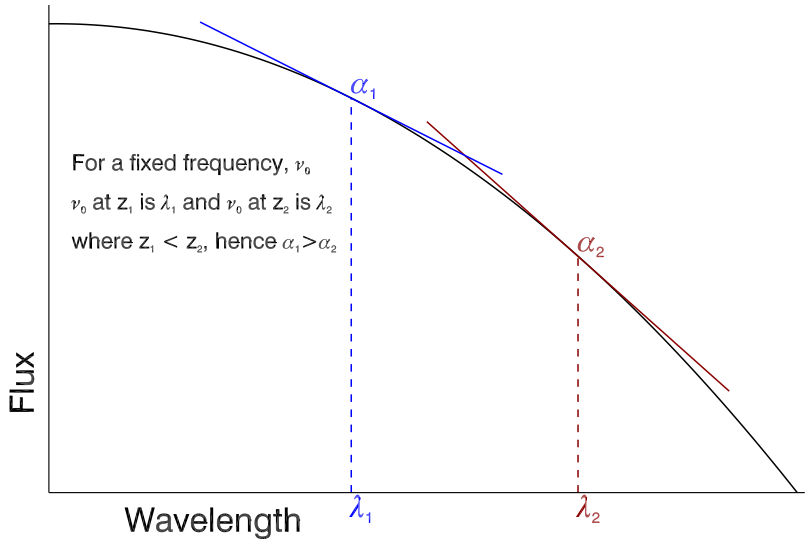

Figure 1.7: Illustration of the change in the spectral index, depending on the observed wavelength. On the x-axis is wavelength and on the y-axis is flux. For a fixed observed frequency, different redshifts yield different observed wavelength and therewith different spectral indices.

HzRG, where most have been found by followup observation of the ten percentile of radio sources with the steepest spectral index i.e. $\alpha \lesssim -1$. The conventional explanation for the $z - \alpha$ correlation is a coupling between the concave shape of the radio spectrum and the radio K-correction. Observing high-z sources at a *fixed* observed frequency will probe emission at *higher* rest-frame frequencies where the spectrum is steeper. Consider the fixed observed frequency ν_0. For redshift z_1, ν_0 is equivalent to λ_1, and for a redshift z_2 where $z_1 < z_2$, ν_0 is equivalent to λ_2 i.e. $\lambda_1 < \lambda_2$, hence $\alpha_1 > \alpha_2$ (see Fig. 1.7).

The concave shape of HzRG spectra is due to synchrotron and inverse Compton energy loss at high frequencies (Klamer et al., 2006) and synchrotron self-absorption at low frequencies. Radio colour-colour plots show evidence of systematic concave curvatures of HzRG spectra (Bornancini et al., 2007). However, this is not sufficient to explain the observed $z - \alpha$ correlation, as many luminous HzRGs show no concave curvature of the spectrum at the relevant frequencies. The HzRG 4C 41.17 is an example of a source with an extremely straight spectrum in the relevant frequency range of 40 MHz to 5 GHz (Chambers et al., 1990). The spectrum of 4C 41.17 starts to steepen at frequencies above 5 GHz, but these are too high frequencies to contribute to the $z - \alpha$ correlation. 4C 41.17 is not the only HzRG with a non concave spectrum; Klamer et al. (2006) showed that $\sim 90\%$ of sources in their sample have straight spectra between 0.8 GHz and 18 GHz.

One explanation for the observed $z - \alpha$ correlation is an indirect manifestation of a luminosity-spectral index ($L - \alpha$) effect (Chambers et al., 1990; Blundell & Rawlings, 1999). Synchrotron theory predicts that a continuous injection of particles will result in a spectrum with a low-frequency cut-off (ν_l), which is dependent on the luminosity (L) by $\nu_l \sim L^{-6/7}$. This means that for a flux limited sample the Malmquist bias (Malmquist,

1924) will cause the high redshift sources to have a higher radio luminosity. This effect will manifest itself in an observed $z \sim \alpha$ relation. However, studies of samples with a restricted luminosity range show the same $z \sim \alpha$ correlation (Athreya & Kapahi, 1998), implying that the $L - \alpha$ effect cannot be the full explanation of the $z \sim \alpha$ correlation.

Another explanation to the $z - \alpha$ correlation is that the ambient density of the radio source increases with redshift, and that this increased density can cause a steepening of the spectral index (Athreya & Kapahi, 1998; Klamer et al., 2006). The steepening is due to the denser environment causing the upstream fluid velocity of the relativistic particles to decrease, leading an acceleration process to produce a steeper synchrotron spectrum. The explanation would result in both a $z \sim \alpha$ and $L \sim \alpha$ correlation, and provide a natural physical link between the HzRGs and the low-z cluster halos. This interpretation has, like the other one, problems as the clumpy morphologies seen in UV and optical indicate non-uniform densities around the HzRGs, where the densities are higher closer to the nucleus than the outer regions. The observed spatial variations of the spectral indices within the individual sources, are smaller than the source-to-source variations. The internal spectral index variation then raises the question, how a non-uniform density medium on one side of the radio source can know about the ultra steep spectral index on the other side of the radio source. The ultra-steep spectra are therefore more likely produced by mechanisms in the galactic nucleus, rather than the environment at the location of the radio lobes.

Both explanations have difficulties to fully re-produce the observed $z - \alpha$ correlation, meaning that the cause of this effect is still unclear, and that more detailed information of the radio spectra dependence on the redshift is necessary.

1.3.3 Survey selections

Finding and cataloging distant radio galaxies involves multiple steps, which can be summarised in four main tasks:

1) The HzRGs are filtered from the large number of radio sources (Röttgering et al., 1994; Blundell et al., 1998; De Breuck et al., 2000b, 2004) using criteria based on the i) radio colour (i.e. the steepness of the spectra) and ii) the small angular size.

2) The nearby relatively bright sources are filtered out by comparing the radio positions with wide-field shallow surveys at optical and near-IR (NIR) wavelengths.

3) The positions are refined to arc-second accuracy to be able to identify their faint counterparts in the optical and NIR. These identifications were done using optical CCDs up until the 1990s (e.g. Röttgering et al., 1995; McCarthy et al., 1996), but as sensitive NIR detectors became available the NIR K-band was found more efficient for the identification of distant galaxies. More than 94% of bright radio galaxies are identified down to $K = 22$ (De Breuck et al., 2004).

4) Spectroscopic follow-up observations with large optical and NIR telescopes of the remaining HzRG candidates, to determine the redshifts using emission lines.

Especially the fourth step is expensive in telescope time, as the HzRG candidates are located far apart in the sky, and therefore do not allow for multi-object spectroscopy. This

means that the individual fields have to be observed in order to determine the redshifts of the candidates. The spectroscopic determination of the redshift introduces a bias in the source selection, as only the redshift governs if the emission lines are within the observed wavelength range. There is additionally a redshift desert at $1.2 < z < 1.8$ (e.g. Cruz et al., 2006), where the lines usually used for the redshift determination (e.g. Lyα, HeII, Hα) are either too red or too blue to be easily observed from ground based facilities. This means that sources in the redshift desert are under-represented in the HzRG samples.

Another bias is the incompleteness of the redshift distribution. A small fraction ($\sim 4\%$) of radio sources is not identified down to $K \sim 22$, and a third of the sample, does not show any emission or absorption lines, even after long exposures on 8-10 m class optical and IR telescopes. These sources are either so dusty that the emission lines are hidden by obscuration (e.g. De Breuck et al., 2001; Reuland et al., 2003a), or located at such high redshift that the bright emission lines are shifted out of the easily observed wavelength ranges, or they are so peculiar that they emit no strong emission lines.

Redshift distribution

The redshift distribution of the sources with un-ambiguous redshift shows a number density of typical sources with $L_{1.2\mathrm{GHz}} > 10^{33}\,\mathrm{erg\,s^{-1}\,Hz^{-1}\,ster^{-1}}$ and in the redshift range $2 < z < 5$ of a few times $10^{-8}\,\mathrm{Mpc^{-3}}$ (Dunlop & Peacock, 1990; Willott et al., 2001; Venemans et al., 2007). This means that HzRGs are extremely rare. While HzRGs are sparsely distributed at high redshift, they are almost non-existent at low redshifts. Similar to the shape of the Lilly-Madau plot (see Fig. 1.1), the co-moving space density of luminous steep spectrum radio sources increases by a factor of 100-1000 between $0 < z < 2.5$ and then flattens out at $z > 2.5$ (Willott et al., 2001; Jarvis et al., 2001). Though there is a large uncertainty on the determined high-z luminosity function, no significant cut-off in this density has yet been seen. The point at which the space density flattens out, is a crucial time in the history of the Universe, it is not only the time at which the SFRD increases by more than an order of magnitude, but it is also the time at which the most luminous quasars appear to have their maximum space density (Pei, 1995; Fan et al., 2001), and the time at which galaxy clusters start to form as not yet gravitational bound structures. Why the most luminous radio sources then became extinct in the local Universe is still not understood.

1.3.4 Stars in HzRGs

Stars are a major part of HzRGs, and their presence is reflected in *i*) the shape of the SED, as it has a plateau between 1 μm and 2 μm (Simpson & Eisenhardt, 1999; Seymour et al., 2007), *ii*) rest-frame UV stellar absorption lines (Dey et al., 1997) and *iii*) the morphologies of several HzRGs follow the surface brightness profile of elliptical galaxies (e.g. van Breugel et al., 1998; Pentericci et al., 2001; Zirm et al., 2005). The young stars (< 0.5 Gyr) dominate the SED in the UV and the older stellar population (~ 1 Gyr) dominates at wavelengths < 4000 Å. However, disentangling the stellar and non-stellar contribution to the SED is

complicated, as the rest-frame UV wavelengths have contributions from scattered quasar light and nebular continuum emission.

One of the remarkable and surprising characteristics of the stellar distribution in HzRGs is the alignment between the radio and optical continuum emission (e.g. Chambers et al., 1987; McCarthy et al., 1987). *HST* images have revealed that HzRG hosts generally have clumpy optical morphologies (Pentericci et al., 1998, 1999). By an examination of the close relationship between the radio, rest-frame UV and optical morphologies, Pentericci et al. (1999, 2001) found that the alignment effect extends into the rest-frame optical and that the sources at $z > 2.5$ have more clumpy morphologies than the lower redshift sources. The same redshift dependence of the clumpy structures was seen by van Breugel et al. (1998). However, this dependence is difficult to interpret as the observed wavelength changes with redshift.

The proposed models for this alignment are induced scattering of light from a hidden quasar by dust (Tadhunter et al., 1998) or triggering of star formation by the radio jet as it propagates outwards (De Young, 1989; Rees, 1989; Begelman & Cioffi, 1989; Bicknell et al., 2000). Scattering of AGN light is evident in some HzRGs in the form of polarised light. However scattering of light is not enough to explain the detailed optical morphologies and the alignment of the continuum emission red-wards of the rest-frame 4000 Å break.

An additional source for the alignment is jet induced star formation. The interaction between the high-powered ($\sim 10^{46}\,\mathrm{erg\,s^{-1}}$) jet and the dense gas has been observed to induce star formation and shock excited emission lines in multiple objects such as 4C 41.17 (Bicknell et al., 2000), 3C40 (van Breugel et al., 1985; Croft et al., 2006), 3C 285 (van Breugel & Dey, 1993) and Centaurus A (Graham, 1998) and to be more prevalent at $z > 2$. This increased importance of the jet-induced star formation with redshift was suggested by van Breugel et al. (1998) to be causing the clumpy structures of HzRGs at $z > 3$.

Old stars

The old stellar population ($> 1\,\mathrm{Gyr}$) peaks in the NIR, and the bright observed K-band luminosities have long been used as an argument that HzRGs are very massive with masses of up to $10^{12}\,\mathrm{M_\odot}$ (Rocca-Volmerange et al., 2004). This makes HzRGs some of the most massive galaxies in the early Universe and places them in the upper end of the stellar mass function of the redshift range $0 < z < 4$ (e.g. Rocca-Volmerange et al., 2004). HzRGs form a remarkably narrow correlation in the K-z diagram introduced by Lilly & Longair (1984) out to $z \sim 3$. This correlation is even tighter than seen for NIR selected field galaxies (e.g. De Breuck et al., 2002), and the small scatter has been found to correlate weakly with the radio luminosity (e.g. Best et al., 1998). The radio power is dominated by the Eddington limited luminosity from the nuclear supermassive black hole (Rawlings & Saunders, 1991), which is then a measure of the mass of the black hole. The well-established relation between the mass of the black hole and the bulge mass (e.g. Magorrian et al., 1998) then implies that the radio power is correlated with the mass of the host galaxy, which appears to be the case for low-z less-luminous radio galaxies (Best et al., 2005).

However, caution has to be exercised when interpreting the details of the K-z diagram in terms of galaxy masses. The disentanglement of *i)* the stellar component, *ii)* the contribution to the K-band flux from warm dust, and *iii)* (at high redshift) also bright emission lines is difficult. This means that the estimated masses derived from the uncorrected colours are often overestimated (Eales & Rawlings, 1996; Rocca-Volmerange et al., 2004). Additionally, stellar population models, whereon the masses are based, are subject to uncertainties. For example, incorporating thermal pulsations from asymptotic giant branch stars reduces the derived masses significantly (Bruzual, 2007).

The *Spitzer Space Telescope* made it possible for Seymour et al. (2007) to investigate 69 HzRGs in the redshift range $1 < z < 5.2$, and decompose the rest-frame optical to IR SED into stellar, AGN and dust components. They hereby determined the stellar contribution to the rest-frame H-band, and by deriving the stellar luminosity at the rest-frame wavelength peak of the stellar emission (near $\lambda_{\rm rest} = 1.6\,\mu$m), minimised the contamination from the AGN and line emission, and eliminated the effect in the K-z diagram, originating from observing sources of different redshifts with the same bands. The stellar masses derived by Seymour et al. (2007) of $10^{11} - 10^{12}\,{\rm M}_{\odot}$ confirming what had previously been found by Rocca-Volmerange et al. (2004).

Young stars

HzRGs undergo vigorous star formation, which is visible both as emission lines and in the SED. The young stars have rest-frame UV photospheric stellar absorption lines and P-Cygni features driven by stellar winds. Detecting these absorption lines requires large amounts of observing time on 10 m class telescopes and has therefore only been detected for a handful of galaxies e.g. the SVλ1502 for 4C41.17 (Dey et al., 1997), CIIIλ1428 for TNJ2007-1316 (De Breuck & Reuland, 2005) and MRC1138-242 (Miley et al., 2006; Nesvadba et al., 2006; Hatch et al., 2007).

The vigorous star formation is also visible in the SED at sub-millimetre wavelengths, as the UV photons from the young stars heat the gas, which are re-emitted in the IR and observed in the sub-millimetre regime. The amount of energy required to heat the dust corresponds to SFRs of $\gtrsim 1000\,{\rm M}_{\odot}\,{\rm yr}^{-1}$, similar to DSFGs (Archibald et al., 2001; Reuland et al., 2003b).

1.4 Gas in high-z galaxies

The empirical description of the relation between SFR and gas density introduced by Schmidt (1959) and Kennicutt (1989) is known as the Star Formation Law, the Kennicutt-Schmidt law or the KS-relation. This relation is expressed in terms of the observed surface density terms:

$$\Sigma_{\rm SFR} = \epsilon' \Sigma_{\rm gas}^{\beta}, \tag{1.1}$$

where $\Sigma_{\rm SFR}$ is the SFR surface density, $\Sigma_{\rm gas}$ is the gas surface density, ϵ' is the normalisation and β is the slope of the relation.

The normalisation, ϵ', reflects the inverse of the depletion timescale and therewith how easily stars are formed out of a parcel of gas. The gas depletion times is dependent on feedback processes, and turbulence, which all drive the density distribution function. This factor has been shown to be $\sim$ 10 times higher for ULIRGs and DSFGs than for disk galaxies, meaning that a ULIRG may form stars 10 times faster than a disk galaxy, which has the same gas surface density. The slope of the KS-relation, β, can give insight into the underlying small scale physics and can be used to distinguish different theoretical models.

Kennicutt (1998b) studied 36 nearby IR-selected galaxies and by comparing their SFR he determined an index of $\beta = 1.4$. Studies in the following decade (e.g. Wong & Blitz, 2002) showed that the SFR is correlated with the molecular hydrogen (H_2) gas and not the atomic hydrogen (HI) gas. When the KS-relation is referenced in the literature, it is therefore most often the molecular gas density that is referred to, discarding any contribution from the atomic gas. This has been confirmed many times hereafter (e.g. Walter et al., 2005; Leroy et al., 2009; Helfer et al., 2003; Bigiel et al., 2008).

The slope of the KS-relation appears to steepen at the transition from normal galaxies to starburst (see Fig. 1.8). This transition could be due to the conversion factor from CO-to-H_2 (see § 1.4.1), but may also reflect the change in physical conditions in the ISM, which results in a decrease in the star formation efficiency.

Although there has been great progress in the understanding of the KS-relation, there is still open questions. Precisely determining the observed slope and the dispersion in the slope is an extremely difficult task, but crucial for constraining the theory of star formation.

1.4.1 Molecular gas

The relation between the SFR surface density and gas surface density expressed by the KS-relation establishes the relation between the gas content and physical conditions of the gas with the efficiency in forming stars from this gas. Stars are believed to be formed in giant molecular clouds with $n > 100\,{\rm cm}^{-3}$ in which the main component is H_2rather than HI. H_2 is mainly produced on the surface of dust grains acting as a catalyst for converting H into H_2 in areas with a minimum density of $> 50\,{\rm cm}^{-3}$. The H_2 molecules are dissociated by UV photons of energy 11.2 eV or higher, which is why H_2 must be shielded against the interstellar radiation field (ISRF) by dust grains or self-shielding to exist. H_2 in the outer layers of the molecular clouds is destroyed via photo-dissociation, however, at a column

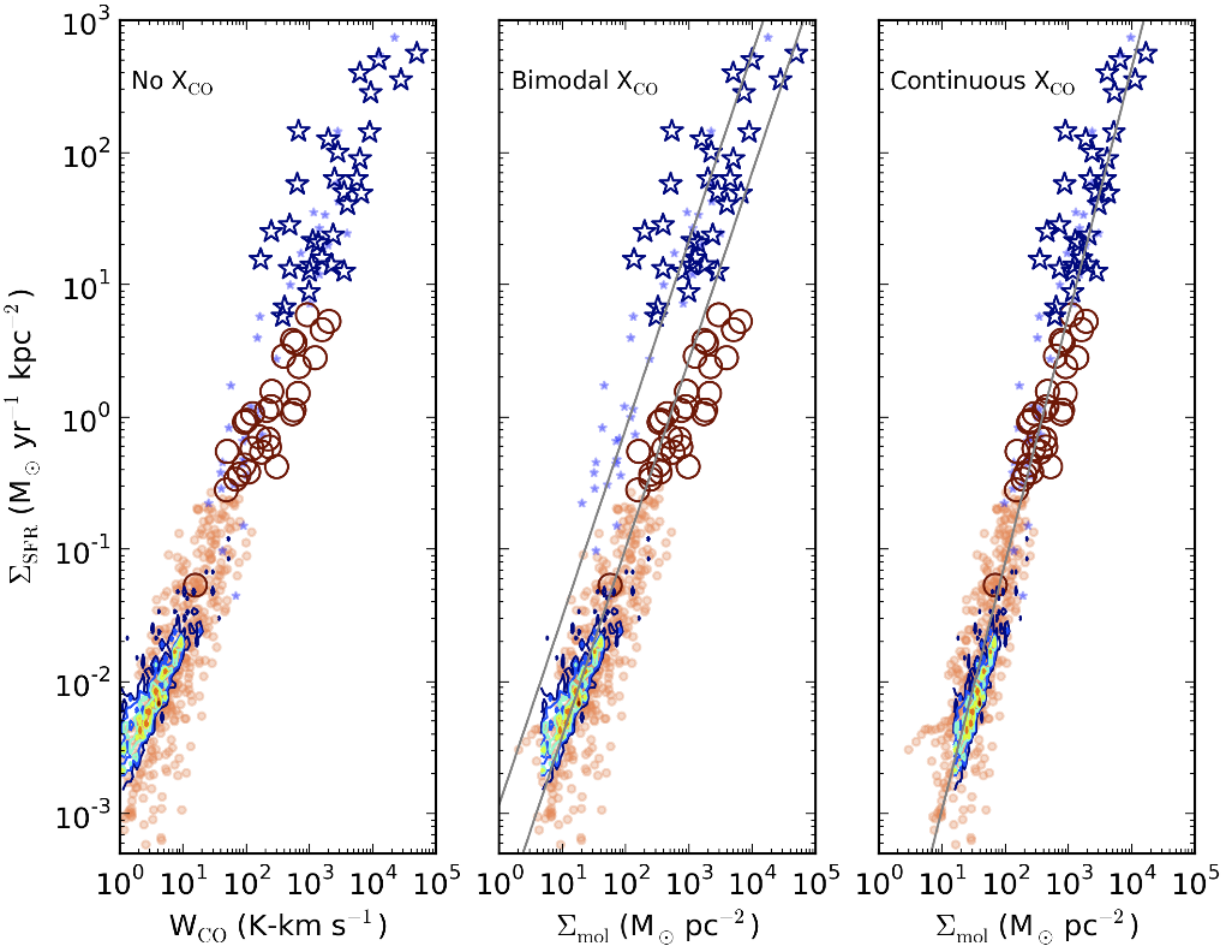

Figure 1.8: The KS-relation for local and high-z galaxies (reproduced from Casey et al. 2014). On the x- and y-axes, the molecular gas surface density and the SFR surface density are plotted, respectively. For all three panels, circles and stars represent quiescently star-forming galaxies and starburst galaxies, respectively. These two populations are further divided into small orange circles and small blue stars representing local galaxies and large red circles and large blue stars representing galaxies at high redshifts. The contours show resolved data from Bigiel et al. (2008). *Left:* The KS-relation where the conversion from CO-to-H_2 has not been applied. *Middle:* The KS-relation assuming a bimodal CO-to-H_2 conversion factor. The grey curves indicate the best fit sequences to the quiescent galaxies and ULIRGs. *Right:* The KS-relation for a smoothly varying CO-to-H_2 conversion factor.

density of $\sim 10^{20}\,\mathrm{cm}^{-2}$ H_2 starts to become self-shielded. Self-shielding and dust extinction prevents the dissociating radiation from penetrating deep into the cloud.

H_2 is a mono-atomic molecule. It therefore does not have a permanent electric dipole momentum and the rotational transitions from H_2 are unfortunately very difficult to detect due to limited atmospheric transition (Stahler & Palla, 2005). Instead, carbon monoxide (CO), the simplest most abundant molecule after H_2, is used as a tracer of molecular gas. CO has a permanent electric dipole momentum and emits strongly at radio frequencies. The CO molecules form only through gas-phase reactions by oxidation of the product of a hydrogenate reaction:

$$\mathrm{H_3^+ + C \rightarrow CH^+ + H_2}$$
$$\mathrm{CH + O \rightarrow CO + H}$$

CO has a strong binding energy of 11.1 eV, preserving the molecules from being destroyed by further reactions. CO is (like H_2) self-shielding against the surrounding ISRF leading to CO building up in a similar manner as H_2 in the outer regions of molecular clouds, though CO remains dissociated to greater depths. The most abundant isotope of CO is $^{12}C^{16}O$ which is easily detected, but has a high optical depth. Other CO isotopes such as $^{13}C^{16}O$, $^{12}C^{18}O$, $^{12}C^{17}O$ and $^{13}C^{18}O$ are mostly optically thin and are therefore better at probing the centres of molecular clouds. They are, however, not as easy to detect as $^{12}C^{16}O$, due to lower abundances.

The relative population of the rotational levels (J) in the CO molecule, described by the spectral line energy distribution (CO SLED), provide a window into the bulk physical properties of the molecular gas in a given system. The relative population of the CO molecules and therewith the shape of the SLED is dependent on the physical parameters of the gas i.e. the temperature and density: the warmer and denser the gas is, the more heavily are the upper levels populated compared to the lower. The higher rotational levels have higher excitation energies, and it therefore becomes increasingly more difficult to excite high-J lines, high enough to maintain local thermal equilibrium (LTE) with lower-J lines. For a system in LTE, the level populations can be described by the Maxwell-Boltzmann distribution and the intensity of the lines are given by the Planck function. Systems in LTE are referred to as thermal or thermalised, and if the level population falls below what is expected from LTE, it is called 'sub-thermal' or 'sub-thermalised'. The fact that higher energies are required to keep the high-J CO lines in LTE with low-J CO lines is expressed as a higher critical density and excitation temperature (Stahler & Palla, 2005). The lowest-J CO lines therefore trace the diffuse and extended molecular gas, while the high-J CO lines trace the denser, more compact and star-forming molecular gas. This implies that the lowest CO(1–0) transition in general is a better tracer of the total amount of molecular gas in galaxies as it is less sensitive to the gas excitation conditions than higher-J CO transition.

CO-to-H_2 conversion factor

CO has been the primary tracer of H_2 in the Milky Way since its first detection in the Orion molecular cloud in the 1970s (Wilson et al., 1970), and in extragalactic sources since 1975 (Rickard et al., 1975). One of the primary uncertainties of deriving the molecular properties of galaxies at all redshifts is converting the observed CO flux densities to the H_2 molecular gas mass. This conversion from CO-to-H_2 is known as the $X_{\rm CO}$ (X-factor) or $\alpha_{\rm CO}$. Formally, $X_{\rm CO}$ is related to the velocity integrated CO intensity and is given in units of $\mathrm{K\,km\,s^{-1}}$, and $\alpha_{\rm CO}$ has the unit $\mathrm{M_\odot\,pc^{-2}\,(K\,km\,s^{-1})^{-1}}$, and converts the CO line luminosity to the total gas mass by:

$$M_{\rm H_2} = \alpha_{\rm CO} L'_{\rm CO}. \tag{1.2}$$

The two conversion factors are linearly related. $\alpha_{\rm CO}$ has been a subject of many Galactic and extra galactic studies, and has been determined for the Milky Way and the Local group (aside from the Small Magallenic Cloud) to be in the narrow range between $3 - 6\,\mathrm{M_\odot\,pc^{-2}\,(K\,km\,s^{-1})^{-1}}$. The $\alpha_{\rm CO}$ factor has been shown to vary depending on the metallicity of the molecular gas and the SFRD. In low metallicity dwarf galaxies, the conversion factor appears to rise (e.g. Tacconi & Young, 1987), while a high SFRD appears to decrease the conversion factor (e.g. Strong et al., 2004; Sandstrom et al., 2013). The latter effect of the conversion factor is the most important when dealing with high-z star-forming galaxies, as applying a Milky Way conversion factor on a high-z starburst galaxy, will result in a molecular gas mass higher than the estimated dynamical mass (Solomon & Sage, 1988). A bimodal CO-to-H_2 conversion factor has been custom in extragalactic literature, despite an observed dispersion in local ULIRGs. A value of $\alpha_{\rm CO} \sim 4$ is typically assumed for 'normal' star-forming (Milky Way type) galaxies, while a value of 0.8 is typically assumed for starburst galaxies and mergers. Though the bimodal conversion factor is custom, it has been shown by many studies of both high and low-z galaxies that no clear bimodal or single value is applicable to all galaxies of a given luminosity or merger status (e.g. Tacconi et al., 2008).

Applying bimodal conversion factors to low and high-z galaxies results in a bimodal KS-relation reflecting two modes of star formation in galaxies: a quiescent and starburst mode (e.g Daddi et al., 2010; Genzel et al., 2010). Some argue that the bimodality is real and that galaxies go through short periods of extreme star formation efficiency (Teyssier et al., 2010), while other propose that the bimodal KS-relation is an artefact introduced by the bimodal X-factor, and that the KS-relation can be reduced to a single relation by using an either constant or smoothly varying X-factor (Ostriker & Shetty, 2011; Narayanan et al., 2012).

This boils down to assuming that either all starburst galaxies have the same physical conditions (the same is the case for 'normal' star-forming galaxies) or that the physical conditions vary from galaxy to galaxy. This has a significant influence on the analysis of a given system, but is difficult to correct for.

Dense molecular gas tracers

A consensus from dense gas observations is that high-z galaxies have a higher dense gas fraction than low-z galaxies. This is evident in the CO SLEDs which peak at higher-J CO transitions than for low-z systems. Dense molecular gas can be traced by the high-J CO lines, but is better traced by molecules with a higher critical density such as CS, HCO^+, HCN or H_2O.

Studies of high density gas using HCN have shown that there is a correlation between the FIR luminosity of the galaxy and the HCN luminosity (e.g. Solomon et al., 1992; Gao & Solomon, 2004a,b; Gao et al., 2007). While there is a correlation between the two luminosities, the high-z studies of DSFGs and AGN show an offset correlation compared to the low-z correlation. It is unclear what causes this offset, it could be due to a higher gas density probability distribution function (Krumholz & Thompson, 2007; Narayanan et al., 2008) or a contribution to the IR luminosity from an AGN. However, evidence of a non-linear FIR-HCN trend has also been observed by Greve et al. (2006) and Riechers et al. (2007) for high-z systems.

Another dense gas tracer that has become more popular is rotational transitions in H_2O. H_2O has a critical density of $\sim 10^8\,\mathrm{cm}^{-3}$ and therefore traces the extremely dense parts of the star-forming clouds. Most dense gas studies have been conducted at low redshifts (e.g. Yang et al., 2013), but lately the observations have been pushed to high redshifts (e.g. Omont et al., 2013). Seven rotational H_2O lines were detected for HFLS3 at $z = 6.34$ by Riechers et al. (2013). A clear result of the H_2O studies is a correlation between the IR and the H_2O luminosities in the IR luminosity range $L_{\mathrm{IR}} \sim 10^{12} - 10^{14}\,\mathrm{L}_\odot$. Future studies of HCN and H_2O in high-z systems in comparison with low-z systems will prove crucial for understanding the physical conditions that govern star formation (e.g. Krumholz & McKee, 2005; Andrews & Thompson, 2011; Hopkins et al., 2013).

Molecular gas in DSFGs

The morphology and dynamics reflected by molecular and atomic lines can provide information about the physical origin of the galaxy, i.e. if it is dynamically hot (as in the case of a merger) or dynamically cold. CO observations can reveal the spatial extent of the H_2 gas and therewith where a given galaxy lies on the KS-relation. Multiple CO observations can additionally provide a map of the thermal and density distribution across a galaxy. However, as different CO transitions trace different density components, they trace molecular gas of different spatial extent. Therefore care must be taken when interpreting dynamics determined from high-J CO lines, as they trace the denser, more compact gas in the ISM. Only few high-z DSFGs have been detected in the CO ground transition (e.g. Ivison et al., 2011; Riechers et al., 2011c). These observations show molecular gas reservoirs of $\sim 3-16\,\mathrm{kpc}$ size, which is significantly different from the sizes of $\sim 1-3\,\mathrm{kpc}$ found using high-J CO lines for the sample of sources (Tacconi et al., 2008; Engel et al., 2010) The widths of the molecular lines reflect the mass enclosed in the emitting region and the spatial extent of the gas, but it is not a direct measure of the size of the source.

CO mapping can also reveal the dynamics of the gas. Studying the dynamics of DSFGs is driven by the motivation for understanding what governs the high luminosity and SFR of these high-z galaxies: Is it mergers or secular processes within disk galaxies? The results of these studies differ: Some find evidence for rotating molecular disks in DFSGs and QSOs (e.g. Tacconi et al., 2008; Bothwell et al., 2010; Carilli et al., 2010; Hodge et al., 2012; Deane et al., 2013), or disrupted systems (e.g. Tacconi et al., 2008; Engel et al., 2010; Bothwell et al., 2013b; Riechers et al., 2011a, 2013), while others find evidence of ongoing mergers (e.g. Engel et al., 2010; Yan et al., 2010; Riechers et al., 2011b; Ivison et al., 2013; Fu et al., 2013). However, multiple counter-arguments have been found for each case, and numerical simulations (Springel & Hernquist, 2005; Hopkins et al., 2009) have shown that gas rich mergers can quickly re-form gaseous disks soon after a merger scenario, due to the dissipational nature of gas.

Molecular gas in HzRGs

In a few HzRGs, the CO emission appears to be spatially resolved (Papadopoulos et al., 2000; Greve et al., 2004; De Breuck et al., 2005), and extends over 10-20 kpc, providing information about the kinematics of the gas. Studies have shown alignments between the molecular gas and the radio morphology (Klamer et al., 2004), however recent studies claim that this is not always the case (e.g. Emonts et al., 2014, 2015b; Gullberg et al., 2015). The biases involved with the current CO observations which are induced by:

i) selection based on the 850 μm dust emission: Sources detected in CO are not always detected in 850 μm emission (e.g. 53W002 and TNJ0924-2201, Scoville et al. 1997; Alloin et al. 2000), suggesting a systematic underestimation of the gas-to-dust ratio in high-z CO samples, due to a bias in favour of the dusty galaxies.

ii) detections are more likely to be published than non-detections: The non-detections are often reported with large redshift uncertainties. These uncertain redshifts are often due to the presence of an offset between the CO and optical redshift, the unknown width of the CO line, and the limited bandwidth of the spectrographs.

iii) The high redshift sources need to be detected in high-J CO lines: the observational constraint set by the atmospheric transmission limits the CO transitions observable to the high-J CO lines. This means that only observing high-J CO lines, which mainly probe the dense molecular gas, results in the spatial extent of the diffuse molecular gas to be unclear. For sources at high enough redshift (i.e. $z > 3.6$) the low-J CO lines can be observed with the Very Large Array (VLA) and Australian Telescope Compact Array (ATCA). However, this can still result in an incomplete CO SLED, which can complicate constraining the density and temperature of the molecular gas.

1.4.2 Atomic gas

The dominant cooling lines of the diffuse ISM are emission lines from neutral and ionised carbon, nitrogen and oxygen. These emission lines can provide information about both the cold neutral medium, HII regions and photodissociation regions (PDRs) in galaxies.

The [CII] fine structure emission line at 158 μm is the most dominant when it comes to studies of the atomic gas in galaxies, due to it being relatively bright compared to the other fine structure lines and CO emission lines, and can contribute up to 1% of the IR luminosity of a galaxy (Nikola et al., 1998). It can be excited by both collisions with atomic or molecular hydrogen in which case [CII] will have a critical density of $\sim 1 - 8 \times 10^3\,\mathrm{cm}^{-3}$ or with free electrons and protons at high enough electron densities, in which case the critical density of [CII] will be $\sim 5 - 50\,\mathrm{cm}^{-3}$ (Goldsmith et al., 2012). Because of the relatively low ionisation potential of 11.3 eV (which is lower than the 13.6 eV characteristic for HI), [CII] emission can arise from both neutral and ionised regions. This means that the origin of the [CII] emission line can be diverse and the power of the [CII] line as a diagnostic probe for the physical conditions of the ISM is therefore still debated.

Combining detections of [CII] with detections of [NII] can serve as a diagnostic for the amount of the [CII] arising from the ionised medium. The [NII] fine structure line at 205 μm with an ionisation potential of 14.5 eV has a critical density and second ionisation potential similar to [CII] (Decarli et al., 2014).

Emission lines from neutral carbon ([CI]) have gained traction during the past decade. The three level system of [CI] emits the two fine structure lines [CI]1-0 and [CI]2-1, which are both optically thin and are relatively good tracers of diffuse, low extinction molecular gas. Observations of both [CI] lines allow to constrain the excitation temperature and column density of carbon. The critical densities of the [CI]1-0 and [CI]2-1 lines are $\sim 500\,\mathrm{cm}^{-3}$ and $\sim 10^3\,\mathrm{cm}^3$, similar to that of CO(1–0) and CO(2–1), which are usually used as tracers of the diffuse molecular gas reservoir. The lower optical depth of [CI] compared to CO means that [CI] is a better tracer of the diffuse/low density molecular gas as it can trace large column-densities. Though the H_2 tracing capability of [CI] decreases for low metallicities, it is still a better probe of H_2 gas than ^{12}CO (Papadopoulos et al., 2004; Glover et al., 2015). The ground-state transition, [CI]1-0, is the better tracer of the H_2 gas mass of the two [CI] lines, because it is less sensitive to the excitation conditions of the gas.

Atomic gas in DSFGs

Tracing morphologies and dynamics using CO in high-z DSFGs can introduce uncertainties, as low metallicity sources can suffer from decreased CO abundances and low SFR surface densities will often have lower CO excitations. This has been the motivation for using [CII] as an alternative gas dynamics tracer in high-z galaxies. Using ALMA, Walter et al. (2012) and De Breuck et al. (2014) have shown the power of this facility to examine the dynamics of the [CII]-emitting gas in high-z galaxies, and even showed that some galaxies potentially show signs of rotating disks.

As the [CII] is brighter than the other fine structure and molecular lines, it can be easier detected in high-z galaxies, and does not suffer from heavy extinction as many of the other traditional shorter-wavelength SFR tracers.

There are two of the reasons why [CII] is sometimes used as a SFR tracer, though the reliability of [CII] as a SFR tracer is under debate. If a reasonable calibration between

the [CII] and SFR is found, it can be a powerful tool for studying star-formation in high-z galaxies. A number of studies (Leech et al., 1999; De Looze et al., 2011; Sargsyan et al., 2012; Farrah et al., 2013) find a positive correlation between the [CII] emission and SFRs from UV and sub-millimetre observations of galaxies. However, the [CII] 'deficit' seen for high IR luminosity galaxies (see § 2.4.2) suggests that [CII] might not be a good SFR tracer for IR luminous sources. The scatter seen in the correlation may arise from the fact that [CII] traces multiple phases of the ISM, i.e. also the non-star-forming gas. Additionally, a number of [CII]-non-detections have questioned the reliability of [CII] emission as a SFR tracer in high-z galaxies. These [CII]-non-detections, of among others the luminous galaxy Himiko at $z \sim 6.5$, known to have a SFR of $\sim 100\,\mathrm{M_\odot\,yr^{-1}}$ (Ouchi et al., 2013), suggest that [CII] emission might not be everywhere in the early Universe. The origin, dynamical and SFR tracing capability and reliability of [CII] require more investigation.

Atomic gas in HzRGs

The molecular gas phase is often detected for both DSFGs and HzRGs, unlike the hot and warm ionised phase which is rarely observed for DSFGs. These observations, however, can open a window to the understanding of the processes taking place in HzRGs.

Warm ionised gas
The warm ($\sim 10^{4.5}\,\mathrm{K}$) ionised gas emits both permitted recombination lines and forbidden collisional excited lines. These lines make it possible to determine the redshift of the emitting radio galaxy, which was an important reason for HzRGs being crucial cosmological probes. At the same time, these lines are powerful tools for studying the physical conditions of the gas in HzRGs.

Recombination lines are emitted when a free electron is captured by an atom, and the electron cascades down to the ground state of the atom. A series of recombination lines are emitted as it cascades down. The most prominent of the recombination lines observed in HzRG spectra, are from hydrogen and helium - the two most abundant elements in the Universe. The brightest hydrogen lines are from the Lyman and Balmer series. The lines of the Lyman series occurs when the electron cascades down to the ground state, while the Balmer series occur when the electron cascades down to the state just above the ground state.

The forbidden (and half-forbidden) lines have a tiny probability of occurring compared to the permitted transitions. They occur because the energy levels lie within a few kT of the ground state levels, and are therefore easily populated by collisions. Most of the elements have a critical density below the density of the gas, and most of the de-excitations are therefore via radiation, which is then observed as a spectral line. The forbidden lines only occur if the gas density is in the range $\sim 10 - 10^5\,\mathrm{cm^{-3}}$, and the line ratios contain important information about the physical conditions of the gas, i.e. the density, temperature, ionisation state, and abundance of the emitting gas (Osterbrock & Ferland, 2006; Peterson, 1997). These lines are some of the strongest in emission nebular spectra.

Studies of HzRGs in the early 1990s using composite emission lines showed that for

HzRG, the emission lines originating from the nucleus, were accompanied by emission lines from an additional spatially extended component. HzRGs being accompanied by giant luminous ionised gas nebulas are amongst the most remarkable features of HzRGs (Reuland et al., 2003b). These gas nebulas, or halos, can have sizes up to $\sim 200\,\mathrm{kpc}$, and studying them provides a wealth of information about the physical conditions, kinematics and origin of the gas surrounding the HzRGs.

The halos of ionised gas often have Lyα luminosities of $\sim 10^{43.5}\,\mathrm{erg\,s^{-1}}$. Emission line diagnostics by Osterbrock & Ferland (2006) showed gas temperatures of $T_e \sim 10^4 - 10^5\,\mathrm{K}$, densities of $n_e \sim 10^{0.5} - 10^{1.5}\,\mathrm{cm^{-3}}$ and masses of $10^9 - 10^{10}\,\mathrm{M_\odot}$. The filling factor of the warm ionised gas has been estimated to $\sim 10^{-5}$, which is low compared to the filling factor of the hot ionised gas (see below) which has a filling factor of about unity. Based on the properties of the emission lines and the filling factor, van Ojik et al. (1997) modelled the halo as being composed of $\sim 10^{12}$ clouds with sizes of about 40 light days (comparable to the solar system), and they speculated that these clouds might be associated with early stages of the formation of individual stars.

The morphology of Lyα halos is clumpy, irregular and with overall structures aligned with the radio axes and sometimes extend beyond the sizes of the radio sources. The halos appear to have two regimes which often blend together: the inner region close to the radio jet and the outer region. The inner region shows signs, in the form of emission line widths, of a clumpy medium with velocities widths of $> 1000\,\mathrm{km/s}$ which is being perturbed by the jet. Lines from the outer region, however, have line widths suggesting a more quiescent medium, with velocities widths of a few $100\,\mathrm{km/s}$ (e.g. Villar-Martín et al., 2003).

Using the relative intensity of the emission lines, it is possible (in principle) to disentangle the effects of ionisation, abundances, densities and temperatures:

• Ionisation: There can be multiple mechanisms for exciting the gas:
i) photoionisation from an AGN,
ii) photoionisation from stars,
iii) photoionisation by ionising X-ray photons emitted by shocked hot gas, and collisional ionisation from shocks.

Optical line ratios have been used for nearby active galaxies to study the ionisation of the gas, which have revealed evidence of both jet- and accretion powered shocks and photoionisation from central AGN (e.g. Villar-Martin & Binette, 1997; Villar-Martin et al., 1997; Bicknell et al., 2000; Groves et al., 2004a,b). These optical line ratio studies have also been developed for rest-frame UV lines (Allen et al., 1998; Groves et al., 2004b), but the interpretation of the emission line ratios is complicated, due to the effects from dust and viewing angle (Villar-Martin & Binette, 1996). A comprehensive study by Humphrey et al. (2006) used 35 emission lines throughout the rest-frame UV and optical and concluded that photoionisation is the dominant source for exciting the quiescent gas, and that harder photoionisation than from stars is required, consistent with photoionisation from an AGN. The reason that the AGN is not seen directly is believed to be due to the quasar emitting radiation anisotropically, which is heavily absorbed in the direction along the line of sight, but not in the direction of the radio axis. However, anisotropic radiation makes it

difficult to explain the symmetric shape of the Lyα line. An alternative explanation could therefore be that the radiation is isotropic but variable, with periods of short sharp intense activity and longer periods of relative passivity. Though photoionisation by an AGN is the most likely explanation, it is unlikely the *only* source of photoionisation. Evidence of collisional excitation, from shocks close to the radio jet, is seen in the form of variations in the observed emission line strengths from object to object and within individual objects (Best et al., 2000).

• Abundance and star formation: The chemical abundance of halo gas, as revealed by metal lines such as CIV, [OII] and [OIII], is similar to the solar abundance (Vernet & Cimatti, 2001; Humphrey et al., 2006). This is consistent with HzRGs having undergone prodigious star formation in early epochs. This is supported by the observed Lyα/HeII ratios, which are systematically larger for HzRGs at $z > 3$ than for those at $2 < z < 3$.

The relative intensity of the NV emission line varies from being an order of magnitude fainter than the carbon and helium lines, to being as bright as the Lyα emission line (De Breuck et al., 2000a), which has been interpreted as large variations in the metallicity from HzRG to HzRG.

• Kinematics: The kinematics of the turbulent inner regions are dominated by outflow and slow shocked gas associated with the radio lobes. The inner regions display disturbed kinematics and velocity dispersions of $> 1000\,\mathrm{km/s}$, and evidence for the presence of starburst superwinds in Lyα halos (Armus et al., 1990; Zirm et al., 2005). Along with the synchrotron jet, these starburst winds provide sufficient pressure to drive the warm gas outwards. The interaction between the radio jet and the ambient gas, has been observed to be the source of excitation and disturbances of the gas. The gas can also influence the jet, by bending, de-collimating it, and enhancing the intensity of their radio emission through shock driven particle acceleration. Small sources show more evidence of jet-gas interactions than large ones (Best et al., 2000) and at $z > 2$ the signatures of jet-gas interactions are even more vigorous (Villar-Martin et al., 1998; Villar-Martín et al., 1999a,b, 2003; Humphrey et al., 2006). The kinematics are more turbulent and the ionisation states are higher in the inner regions than in the outer more quiescent regions (Humphrey et al., 2006).

The kinematics of the outer regions show signs of systematic inward motions. The outer regions are apparently unperturbed by the jet, and the kinematics provide important information about the origin of the warm gas. These regions show systematic variations in the velocity of a few hundred km/s, which can be caused by either rotation (van Ojik et al., 1996; Villar-Martín et al., 2003, 2006) outflows (Zirm et al., 2005; Nesvadba et al., 2006) or infalling motions. Distinguishing between these effects only using velocity data is difficult, but combining it with spectroscopic and radio data gives additional information. A study of 11 HzRGs at $2.3 < z < 3.6$ by Villar-Martín et al. (2007) and Humphrey et al. (2007) revealed correlations between the kinematics of the halo and the radio structure, which showed the same asymmetry. At the bright side of the radio jet, the quiescent nebular seems systematically redshifted, compared to the fainter side of the radio jet. By

assuming that the bright jet side is moving towards the observer, and is thereby brightened by Doppler boosting (Rees, 1967; Kellermann, 2003), the quiescent gas must be moving inwards in order to be redshifted. Ro-vibrational lines from H_2 at $\sim 2000\,\mathrm{K}$ can be used as a diagnostic tool to investigate if this infalling gas is a cooling flows (Jaffe & Bremer, 1997; Jaffe et al., 2005), as these lines for high-z sources shift into the IR band observable by *Spitzer*.

The Lyα line is often used for kinematic studies due to its relatively large width and brightness. However, the Lyα line is a resonant line, and is therefore subject to strong scattering and optical depth effects. This means that the kinematics reflected by the Lyα line might not be representative for the gas as a whole, especially for the inner regions.

Though these are powerful diagnostic tools for studying the physical conditions of the gas, they are complicated and require detailed modelling.

Hot ionised gas

X-ray observations of HzRGs show widespread hot ionised gas at the centre of clusters and around radio galaxies at low redshifts. This gas has a derived temperature of $\sim 10^{7.5}\,\mathrm{K}$ and density of $\sim 0.05\,\mathrm{cm}^{-2}$, making the gas sufficient to confirm the presence of the radio emitting plasma and Lyα halo. The current X-ray telescopes have the sensitivity to only just detect similar halos out to $z \sim 2$, e.g. MRC1138-262 (aka the Spiderweb Galaxy) at $z = 2.2$ Carilli et al. (2002a). The X-ray emitting gas is extended along the axis of the radio source.

The hot ionised gas can also be studied through its effect on the polarisation of the background radio emission. As the linearly polarised radio emission propagates through a magnetoionic medium it is rotated by an angle that is proportional to the square of the wavelength. The 'amount' of rotation is known as the rotation measure, and the interpretation of the large observed rotation measure for HzRGs is that they are embedded in dense gas. At low redshift, large rotational measures are observed for radio sources in X-ray emitting clusters which are inferred as 'cooling flows' (Ge & Owen, 1994). This suggests that the high-z radio sources are likewise located in cluster environments.

Neutral gas

The cool neutral HI gas can only a be observed in absorption, either as redshifted 21 cm aborption in the radio continuum, or as deep absorption troughs in the Lyα line profiles. Both techniques can be used to constrain the physical properties of the neutral gas of HzRGs, such as the spatial extent, masses, filling factors, temperatures and spin temperatures.

Neutral hydrogen HI is very abundant in the ISM, and is detected via 21 cm emission, emitted via a hyperfine spin flip transition of the electron in the atom. This absorption line can provide a measure of the average column density of the absorbing medium. Though 21 cm absorption is a powerful tool, detections of this phenomenon are not very common, one source (B20902+34) has been detected in 21 cm absorption (Uson et al., 1991), and only tentative detections have been seen since (e.g. De Breuck & Reuland, 2005). The 21 cm absorption is caused by small ($\sim 100\,\mathrm{kpc}$) disks or torus-like structures which are

perpendicular to the radio source (Röttgering et al., 1999). The absorption line is therefore rarely seen for HzRGs, as most of them are associated with extended radio sources, the disk covering fraction is therefore small and produces insignificant absorption.

Much more commonly observed are strong absorption lines superimposed on the Lyα and CIV line profiles (e.g. MRC0934-262 and TXS0200+015, Röttgering et al. 1995; Jarvis et al. 2003). This was discovered by van Ojik et al. (1997) who detected absorption features in the majority of 18 HzRG spectra. These absorption lines (or troughs) are interpreted as being caused by HI gas surrounding the HzRGs with column densities of $10^{18} - 10^{19.5}\,\mathrm{cm}^{-2}$. They can also be used as a diagnostic tool to studying the extent, dynamics and morphology of the gas, which cannot be studied using quasar emission lines. In most cases, the Lyα line profiles show absorption over the entire spatial extent, indicating a covering factor of close to unity. The column densities and spatial scales of the absorbing gas indicate masses of the HI gas of typically $\sim 10^8\,\mathrm{M}_\odot$.

1.4.3 Dust in HzRGs and DSFGs

Dust in HzRGs and DSFGs play a significant part in the study of the molecular star-forming clouds. The dust indicates that substantial star formation has already taken place, and that the material is chemically enriched. The thermal re-production of UV photons to thermal IR emission often dominates the SED at millimetre and sub-millimetre wavelengths.

Dust in DSFGs

The DSFGs are most often selected on the Rayleigh-Jeans tail of the SED, and they therefore carry a bias against warm dust temperatures. *Herschel*/SPIRE observations of spectroscopic and photometric samples (Casey et al., 2012; Symeonidis et al., 2013; Lee et al., 2013), have shown that DSFGs at high redshifts have cooler SEDs than local ULIRGs, even after correcting for selection biases. This difference in temperature is proposed to be due to a more extended dust distribution (Swinbank, 2013) in high-z DSFGs on scales $> 2\,\mathrm{kpc}$, compared to local ULIRGs where the ISM is more compact on $\sim 1\,\mathrm{kpc}$ scales.

The lack of FIR photometric points for most galaxies has made it difficult to determine the dust temperatures and therewith the dust masses for DSFGs. But even with the lack of a well constrained dust temperature, a flux density measurement on the Rayleigh-Jeans tail of the black body curve can provide a decent estimate on the dust mass. For a sample of 850 μm selected DSFGs with a flux density of $S_{850\mu\mathrm{m}} \sim 5 - 10\,\mathrm{mJy}$ (Smail et al., 2002) at a redshift of $\langle z \rangle \sim 2$ (Chapman et al., 2005) and a dust temperature of $T_{\mathrm{dust}} = 20 - 40\,\mathrm{K}$ (Kovács et al., 2006) the implied dust mass is $\sim 5 - 20 \times 10^8\,\mathrm{M}_\odot$. However, considering a *Herschel* selected sample with a flux density of $S_{250-500\mu\mathrm{m}} \sim 20 - 60\,\mathrm{mJy}$, a redshift of $\langle z \rangle \sim 1$ and a dust temperature of $T_{\mathrm{dust}} \sim 30 - 50\,\mathrm{K}$ (Casey et al., 2012) yields a much lower dust mass of $\sim 1 - 20 \times 10^8\,\mathrm{M}_\odot$. This difference is partly due to 850 μm selected sources being older and more massive galaxies than 250-500 μm selected ones. Additionally, the *Herschel* selected sources are at lower redshifts.

Dust in HzRGs

The difference between the study of dust in HzRGs and DSFGs, is the knowledge that an AGN is for sure present in the HzRGs (Drouart et al., 2014), which is not always the case for DSFGs. The temperature of the dust in HzRGs can therefore be higher ($\sim 300\,\mathrm{K}$, Rocca-Volmerange & Remazeilles 2005) than that in DSFGs ($\sim 35\,\mathrm{K}$, Weiß et al. 2013) due to the dust absorbing emission from the AGN. However, the stars in HzRGs also heat the dust, and disentangling of the two heating sources is difficult, as the processes produce dust with overlapping temperatures. Dust heating by young O and B stars is visible in the slope of the Rayleigh-Jeans part of the thermal dust emission at millimetre and sub-millimetre wavelengths. The temperature expressed by this slope is relatively cool $\sim 50\,\mathrm{K}$ (Archibald et al., 2001; Stevens et al., 2003; Reuland et al., 2004) and similar to the temperatures observed for starburst heated dust in e.g. DSFGs. However, evidence for a warm dust component of $\sim 300\,\mathrm{K}$ is seen in HzRGs, which is consistent with dust heating by an AGN (Rocca-Volmerange & Remazeilles, 2005). The sub-millimetre emission of HzRGs is uncorrelated with the radio luminosity, implying no strong dependence on the strength of the quasar and the AGN emission.

To properly disentangle the AGN and starburst heated dust, high spatial resolution observations are required, which is now possible with facilities such as ALMA (e.g. Gullberg et al., 2015).

1.5 This thesis

This thesis explores the molecular and atomic gas and dust in a sample of lensed high-z DSFGs and two HzRGs, with the aim to investigate the physical parameters of the ISM in high-z galaxies. Facilities such as APEX, *Herschel* and ATCA made it possible to explore the physical conditions (such as optical depth of the [CII] emission line) for the diffuse gas in a sample of DSFGs from the SPT survey. Combining observations from ALMA and the Multi Unit Spectroscopic Explorer (MUSE) for a HzRG has revealed a much more complicated morphology than other wavelength observations had uncovered previously. Studying another HzRG using deep high resolution ALMA observations, reveal a surprisingly large amount of diffuse gas compared to dense gas and shock induced H_2O emission. These three different studies illustrate the crucial importance of observing objects at different wavelengths. Only multi wavelength studies will make it possible to uncover how different galaxy 'populations' evolve from the distant to the local Universe.

Chapter 2

Chapter 2 presents the observation, data reduction, analysis/discussion and conclusion of [CII] observations of 20 strongly lensed DSFGs from the SPT survey at $2.1 < z < 5.7$ using APEX and *Herschel*. The [CII] line is robustly detected in 17 sources, and combining these observations with low-J CO detections from ATCA and FIR data allows us to constrain the properties of the ISM. The [CII] to CO(1–0) luminosity ratio in this sample is 5200 ± 1800, with significantly less scatter than in other samples. This line ratio is best described by a medium of [CII] and CO emitting gas with a higher [CII] than CO excitation temperature, high CO optical depth $\tau_{\mathrm{CO(1\text{–}0)}} \gg 1$, and low to moderate [CII] optical depth $\tau_{\mathrm{[CII]}} \lesssim 1$. The geometric structure of photodissociation regions permits such conditions.

The paper

For this paper I have produced all plots and carried out the analysis and discussion. I was PI on the *Herschel*/SPIRE observations and performed data reduction of this data. Data from APEX/FLASH was reduced by a collaborator. I have written the paper, with a contribution from a collaborator i.e. § 2.2.2.

Chapter 3

Chapter 3 presents a pilot study of the $z = 2.923$ radio galaxy MRC0943-242, by for the first time combining information from ALMA and MUSE data cubes. The observations, data reduction and analysis/discussion of these data reveal that it is possible to disentangle the AGN and starburst dominated sets of components. This reveals a highly complex morphology, as the AGN, starburst, and molecular gas components show up as widely separated sources in dust continuum, optical continuum and CO line emission observations. The ALMA data show emission from CO and the MUSE data is rich in rest-frame UV

emission lines. The combination reveals a linear structure of dust, Lyα and CO emission, and redshifted absorption seen in the circum-nuclear region, which might represent an accretion flow feeding gas into this massive AGN host galaxy.

The paper

I carried out the data reduction of the ALMA data, while a collaborator performed the reduction of the MUSE science verification data. I produced all plots, and the paper was written by me and in close collaboration with the top tire, who contributed with small sections i.e. § 3.2.2 and 3.5.

Chapter 4

Chapter 4 presents a study of the diffuse and dense molecular and atomic gas in the HzRG MRC1138-262 (also known as the Spiderweb Galaxy) using high resolution deep ALMA 235 GHz continuum, H_2O, [CI]2-1 and CO(7–6) line detections. Two H_2O detections close to knots in the radio jet with no detection of underlying continuum, suggest shock induced gas heating. This is the first detection of H_2O in a high-z un-lensed galaxy. The surprisingly bright [CI]2-1 line is so wide that it blends with the CO(7–6) line and spectral de-blending reveals a line luminosity ratio of 0.2, suggesting a low excited molecular gas reservoir.

The paper

For this paper all reduction of the ALMA data and production of plot were carried out by me. I have performed the analysis and written the paper, with contributions from my collaborators to i.e. § 4.4.2.

Chapter 2

The nature of the [CII] emission in Dusty Star Forming Galaxies from the SPT survey

B. Gullberg[1], C. De Breuck[1], J. D. Vieira[2], A. Weiß[3], J. E. Aguirre[4], M. Aravena[5,6], M. Béthermin[1], C. M. Bradford[7], M. S. Bothwell[8], J. E. Carlstrom[9,10,11,12], S. C. Chapman[13], C. D. Fassnacht[14], A. H. Gonzalez[15], T. R. Greve[16], Y. Hezaveh[17], W. L. Holzapfel[23], K. Husband[18], J. Ma[15], M. Malkan[19], D. P. Marrone[20], K. Menten[3], E. J. Murphy[21], C. L. Reichardt[23], J. S. Spilker[20], A. A. Stark[24], M. Strandet[3], N. Welikala[25]

[1]European Southern Observatory, Karl Schwarzschild Straße 2, 85748 Garching, Germany [2]Department of Astronomy and Department of Physics, University of Illinois, 1002 West Green Street, Urbana, IL 61801, USA [3]Max-Planck-Institut für Radioastronomie, Auf dem Hügel 69 D-53121 Bonn, Germany [4]University of Pennsylvania, 209 South 33rd Street, Philadelphia, PA 19104, USA [5]European Southern Observatory, , Alonso de Cordova 3107, Casilla 19001 Vitacura Santiago, Chile. [6]Núcleo de Astronomía, Facultad de Ingeniería, Universidad Diego Portales, Av. Ejército 441, Santiago, Chile [7]Jet Propulsion Laboratory, 4800 Oak Grove Drive, Pasadena, CA 91109, USA [8]Cavendish Laboratory, University of Cambridge, JJ Thompson Ave, Cambridge CB3 0HA, UK [9]Kavli Institute for Cosmological Physics, University of Chicago, 5640 South Ellis Avenue, Chicago, IL 60637, USA [10]Enrico Fermi Institute, University of Chicago, 5640 South Ellis Avenue, Chicago, IL 60637, USA [11]Department of Physics, University of Chicago, 5640 South Ellis Avenue, Chicago, IL 60637, USA [12]Department of Astronomy and Astrophysics, University of Chicago, 5640 South Ellis Avenue, Chicago, IL 60637, USA [13]Dalhousie University, Halifax, Nova Scotia, Canada [14]Department of Physics, University of California, One Shields Avenue, Davis, CA 95616, USA [15]Department of Astronomy, University of Florida, Gainesville, FL 32611, USA [16]Department of Physics and Astronomy, University College London, Gower Street, London WC1E 6BT, UK [17]Kavli Institute for Particle Astrophysics and Cosmology, Stanford University, Stanford, CA 94305, USA [18]H.H. Wills Physics Laboratory, University of Bristol, Tyndall Avenue, Bristol BS8 1TL, UK [19]Department of Physics and Astronomy, University of California, Los Angeles, CA 90095-1547, USA [20]Steward Observatory, University of Arizona, 933 North Cherry Avenue, Tucson, AZ 85721, USA [21]Infrared Processing and Analysis Center, California Institute of Technology, MC 220-6, Pasadena, CA 91125, USA [24]Harvard-Smithsonian Center for Astrophysics, 60 Garden Street, Cambridge, MA 02138, USA [23]Department of Physics, University of California, Berkeley, CA 94720, USA [25]Department of Physiscs, Oxford University, Denis Wilkinson Building, Keble Road, Oxford, OX1 3RH, UK

Abstract

We present [CII] observations of 20 strongly lensed dusty star forming galaxies at $2.1 < z < 5.7$ using APEX and *Herschel*. The sources were selected on their 1.4 mm flux ($S_{1.4\,\mathrm{mm}} > 20\,\mathrm{mJy}$) from the South Pole Telescope survey, with far-infrared (FIR) luminosities determined from extensive photometric data. The [CII] line is robustly detected in 17 sources, all but one being spectrally resolved. Eleven out of 20 sources observed in [CII] also have low-J CO detections from ATCA. A comparison with mid- and high-J CO lines from ALMA reveals consistent [CII] and CO velocity profiles, suggesting that there is little differential lensing between these species. The [CII], low-J CO and FIR data allow us to constrain the properties of the interstellar medium. We find [CII] to CO(1–0) luminosity ratios in the SPT sample of 5200 ± 1800, with significantly less scatter than in other samples. This line ratio can be best described by a medium of [CII] and CO emitting gas with a higher [CII] than CO excitation temperature, high CO optical depth $\tau_{\mathrm{CO(1\text{–}0)}} \gg 1$, and low to moderate [CII] optical depth $\tau_{\mathrm{[CII]}} \lesssim 1$. The geometric structure of photodissociation regions allows for such conditions.

2.1 Introduction

The discovery of (sub)millimeter-selected dusty star forming galaxies (DSFGs) at high redshifts (e.g. Smail et al. 1997; Hughes et al. 1998; Barger et al. 1998) fundamentally changed our view of galaxy formation and evolution. DSFGs are massive ($M_* \sim 10^{11}\,\mathrm{M}_\odot$; e.g. Hainline et al. 2011; Michałowski et al. 2012) and gas-rich ($M_{\mathrm{gas}} \sim 3 - 5 \times 10^{10}\,\mathrm{M}_\odot$; e.g. Greve et al. 2005; Tacconi et al. 2010; Bothwell et al. 2013b), and have star formation rates $\gtrsim 1000\,\mathrm{M}_\odot\mathrm{yr}^{-1}$ (e.g. Chapman et al. 2005). The properties of these galaxies remain a challenge for conventional galaxy formation models (e.g. Baugh et al., 2005; Lacey et al., 2010; Benson, 2012; Hayward et al., 2013).

Thanks to the availability of new space- and ground-based sub-millimetre facilities, our knowledge of the interstellar medium (ISM) in massive gas-rich galaxies at high redshift has dramatically improved in the past decade (Solomon & Vanden Bout 2005; Carilli & Walter 2013; Casey et al. 2014). The most commonly used lines for studying the ISM in DSFGs at high redshift are the rotational transitions of carbon-monoxide (CO) and the [CII] $\lambda 158\,\mu$m fine structure line. The latter is the most important cooling line in the ISM (Dalgarno & McCray, 1972), and traces neutral gas exposed to ultraviolet photons from young stars. The [CII] line can therefore be used to probe the stellar radiation field and how it affects the physical conditions of the gas. The bulk of the [CII] emission line (70% in Stacey et al. 1991a, 2010) is believed to originate from photodissociation regions (PDRs), and the remainder from X-ray dominated regions (XDRs), cosmic ray dominated regions (CRDRs), ionised regions (HII regions) (Meijerink et al., 2007), low density warm gas and/or diffuse HI clouds (Madden et al., 1997).

The [CII] fine-structure transition ($\nu_{\mathrm{rest}}^{\mathrm{[CII]}} = 1900.54\,\mathrm{GHz}$) is nearly unobservable from the ground at $z < 1$ due to strong atmospheric absorption. The only low-z [CII] sam-

ples have been observed with airborne (Crawford et al., 1986; Stacey et al., 1991a) or space based observatories (Malhotra et al., 2001; Brauher et al., 2008; Díaz-Santos et al., 2013; Farrah et al., 2013; Sargsyan et al., 2014; De Looze et al., 2014). Submillimetre atmospheric windows provide some access to the line from the ground at $z > 1$, with atmospheric transparency continuing to improve towards higher redshifts (longer wavelengths). As a consequence, the first high-z [CII] detection was reported for the $z = 6.42$ quasar host galaxy SDSSJ1148+5251 a decade ago (Maiolino et al., 2005). The number of [CII] detections has been steadily increasing since then, thanks to facilities such as the Caltech Submillimeter Observatory (CSO), the Submillimeter Array, the IRAM[1] Plateau de Bure Interferometer, the Atacama Pathfinder EXperiment (APEX), the *Herschel Space Observatory*, the Combined Array for Research in Millimeter-wave Astronomy, and the Atacama Large Millimeter/submillimeter Array (ALMA). At $1 < z < 2$, 21 [CII] detections were made using the redshift (z) and Early Universe Spectrometer (ZEUS) on CSO (Hailey-Dunsheath et al., 2010; Stacey et al., 2010; Brisbin et al., 2015), while *Herchel* detected three [CII] lines at $1.5 < z < 3$ (Ivison et al., 2010; Valtchanov et al., 2011; George et al., 2013). Seventeen have been added to the number of $z > 4$ [CII] detections in the past decade (Maiolino et al., 2005, 2009; Iono et al., 2006; Wagg et al., 2010; Ivison et al., 2010; De Breuck et al., 2011; Cox et al., 2011; Swinbank et al., 2012; Venemans et al., 2012; Walter et al., 2012; Riechers et al., 2013; Wang et al., 2013; Rawle et al., 2014; De Breuck et al., 2014; Neri et al., 2014). Many of these objects have been selected based on the presence of a luminous active galactic nuclei (AGN; e.g. Maiolino et al., 2005; Stacey et al., 2010; Wang et al., 2013), while others have been selected as starburst galaxies (e.g. Ivison et al., 2010; Hailey-Dunsheath et al., 2010; Stacey et al., 2010; Cox et al., 2011; Swinbank et al., 2012; Walter et al., 2012; Riechers et al., 2013; Brisbin et al., 2015). This leads to a heterogeneous sample of high-z [CII] detections, containing a mixture of AGN and starburst-dominated systems. The heterogeneity of the sample complicates the interpretation of trends within it. Stacey et al. (2010) suggest, based on the [CII]/FIR and [CII] to CO(1–0) luminosity ratios, that [CII] emission originates mainly from PDRs and that the ISM and stellar radiation field in these $z \sim 1-2$ galaxies resemble that observed for local starburst systems. These studies have followed the conclusion of Crawford et al. (1985) that the [CII] emission is optically thin or reaching unity opacity ($\tau \lesssim 1$); however, this was recently challenged by Neri et al. (2014), who argued for optically thick [CII].

Here we present [CII] observations of 20 gravitationally lensed DSFGs in the redshift range $z \sim 2.1-5.7$ discovered by the South Pole Telescope (SPT; Carlstrom et al., 2011; Vieira et al., 2010). These 20 sources are a subset of those selected from the first 1300 deg^2 of the 2500 deg^2 SPT-SZ survey. Followup observations with ALMA have provided spectroscopic redshifts for all of these objects (Weiß et al., 2013; Vieira et al., 2013). We also include two new sources observed in Cycle 1 (see Appendix 2.7 for details). The bright ($S_{1.4\mathrm{mm}} > 20\,\mathrm{mJy}$) flux selection of the SPT sample ensures that virtually all sources will be gravitationally magnified, with a bias towards $z > 2$ (Hezaveh & Holder, 2011; Weiß et al., 2013). The magnified emission allows us to study the ISM in these DSFGs in greater

[1]Institute for Radio Astronomy in the Millimeter Range

detail, using fine structure and molecular lines such as [CII] and CO. By including low-J CO observations for 11 sources in our analysis, we determine the physical state of the ISM by studying the [CII] and CO(1–0) line intensity ratios.

This paper is organised as follows: in §4.2 we describe the [CII] and CO observations, and the results for these observations are given in §2.3. In §2.4 we present our analysis, and discuss the implications in §2.5. Our conclusions and summary are given in §2.6. Throughout this paper we adopt the cosmology: $H_0 = 71\,\mathrm{km\ s^{-1}\ Mpc^{-1}}$, $\Omega_\Lambda = 0.73$ and $\Omega_m = 0.27$ (Komatsu et al., 2011).

2.2 Observations

2.2.1 Supporting ALMA and ATCA observations

The 20 DSFGs presented here are a subset of 100 strongly lensed DSFGs selected over the 2500 deg^2 SPT-SZ survey. See Table 1 in Weiß et al. (2013) and Table 2.3 in Appendix 2.7 for the full names and positions. Mid- and high-J CO rotational lines (i.e. CO(3–2), CO(4–3), CO(5–4) and/or CO(6–5)) were detected for 23 [2] DSFGs with the Atacama Large Millimeter/submillimeter Array (ALMA). The redshifts of all our [CII] targets are determined by one or more CO lines plus the [CII] line itself and are therefore robust.

In addition, low-J CO emission lines (CO(1–0) or CO(2–1)) were observed with the Australia Telescope Compact Array (ATCA) for 11 of the SPT DSFGs for which [CII] observations are presented in this paper Aravena et al. 2013; Aravena *et al. in prep*). Absolute flux calibration of the ATCA data is estimated to be accurate to within 15%. Details of the observations, fluxes and associated uncertainties will be presented in a forthcoming paper by Aravena *et al.*

2.2.2 APEX/FLASH

We targeted all galaxies in the SPT DSFG sample with known redshifts that place the [CII] line at frequencies which are observable with good atmospheric transparency using the First Light APEX Submillimetre Heterodyne receiver (FLASH, Heyminck et al. 2006). Eleven sources at $4.2 < z < 5.7$ were observed in the 345 GHz channel between 2012 August and 2014 June, and six sources at $3.1 < z < 3.8$ were observed with the 460 GHz channel between 2013 March and August during Max Planck time. All observations were done in good weather conditions with an average precipitable water vapour < 1.0 mm, yielding typical system temperatures of 230 and 170 K for the 345 and 460 GHz observations, respectively. The beam sizes/antenna gains are $22.0''/40\,\mathrm{Jy\,K^{-1}}$ and $13.5''/48\,\mathrm{Jy\,K^{-1}}$ for the lowest and highest observed frequencies of the [CII] line, respectively. The beam size is much larger than the observed Einstein radii of these sources and thus they are unresolved (Vieira et al., 2013; Hezaveh et al., 2013). The 82 hours of observations were done in wobbler switching mode, with switching frequency of 1.5 Hz and a wobbler throw

[2] One source SPT0538-50 (Greve et al., 2012; Bothwell et al., 2013b), was not observed with ALMA.

of 50″ in azimuth. Pointing was checked frequently and was found to be stable to within 2.5″. Calibration was done every ~ 10 min using the standard hot/cold-load absorber measurements. The data were recorded with the MPIfR Fast Fourier Transform spectrometers (FFTS; Klein et al. 2006) providing 4×2.5 GHz of bandwidth to cover the full 4 GHz bandwidth in each of the upper and lower sidebands of the sideband-separating FLASH receiver.

The data were processed with the Continuum and Line Analysis Single-dish Software (CLASS[3]). We visually inspected the individual scans and omitted scans with unstable baselines, resulting in $< 10\%$ data loss. We subtracted linear baselines from the individual spectra in each of the two FFTS units, and regridded to a velocity resolution of $\sim 90\,\mathrm{km\,s^{-1}}$ in the averaged spectra. On-source integration times were between 1.5 and 5 hours. Table 2.1 summarises the line intensities, and Figure 2.1 shows the spectra.

We detect [CII] emission in 16 out of 17 sources observed with FLASH. The only non-detection is in the highest redshift source, SPT0243-49 at $z = 5.699$. This source has an unambiguous redshift confirmed by two high-J CO lines with ALMA (Weiß et al., 2013) and a CO(2–1) line with ATCA (Aravena *et al. in prep.*). The observed $L_{\rm [CII]}/L_{\rm FIR}$ ratio ($< 1.3 \times 10^{-3}$) is close to the median of our sample (see Table 2.1), suggesting that a [CII] detection for this source is feasible with a moderately deeper integration.

2.2.3 *Herschel*/SPIRE

For three $z \sim 2$ sources in the SPT sample (see Table 2.1), the [CII] line falls in a frequency range (500-610 GHz) where the atmosphere is opaque. We thus observed these sources with the SPIRE Fourier Transform Spectrometer (FTS; Griffin et al. 2010) onboard *Herschel*[4]. (Pilbratt et al., 2010). For more detail about the observations and results for SPT0538-50, see Bothwell et al. (2013a). The observations of SPT0551-50 and SPT0512-59 were carried out on 2013 March 2 in single-pointing mode using both the short wavelength (SSW) and long wavelength (SLW) bands covering 194-313 μm and 303-671 μm. The observations were done in high spectral resolution mode equivalent to $0.04\,\mathrm{cm^{-1}}$ (1.2 GHz) with 100 repetitions, resulting in an on-source integration time of 13752 s (3.8 h) per source.

The data were reduced and calibrated using an updated SPIRE FTS pipeline in the *Herschel* reduction tool HIPE v11, which includes all detectors in the observation and uses new calibration files. The detection of lines fainter than 1 Jy is very challenging because thermal emission from the warm optics contributes as much as 1000 Jy at 1000 GHz. We subtract the average of the off-target pixels in order to remove this excess emission from the telescope. Another possibility is to subtract a 'dark sky' observation made on the same day with the same exposure time, but in our case the noise level was lowest by subtracting the average of the off-target pixels. As the model of the telescope has an uncertainty of 0.1%, there remains a residual continuum uncertainty of ~ 1 Jy in the continuum. We therefore subtract an additional second order polynomial from the SSW and the SLW spectral part

[3] `http://www.iram.fr/IRAMFR/GILDAS/`

[4] *Herschel* is an ESA space observatory with science instruments provided by European-led Principal Investigator consortia and with important participation from NASA.

separately, and look for the [CII] line at the expected frequency (Valtchanov et al., 2011). Figure 2.2 shows the resulting spectra.

2.3 Results

Figures 2.1 and 2.2 show the [CII] emission lines and Table 2.1 lists the [CII] luminosities obtained from APEX/FLASH and *Herschel* SPIRE FTS observations, along with far-IR luminosities ($L_{\rm FIR}$). We have 17 [CII] emission line detections (16 with FLASH and one with *Herschel* SPIRE FTS) and three non-detections (one with FLASH and two with *Herschel* SPIRE FTS).

2.3.1 Velocity profiles and line fluxes

Despite an increasing number of high-z [CII] detections in the literature, only a few of these have sufficient spectral resolution and S/N and supporting data to compare line profiles with other bright lines like CO (e.g. Rawle et al. 2014). This is the first sample of sources with spectrally resolved data with S/N$\geq$ 3 in *both* [CII] and CO making it possible to compare the shapes of velocity profiles. In the following, we consider only the 17 sources observed with FLASH, as the 3 sources observed with SPIRE are not spectrally resolved.

Figure 2.1 shows the velocity profiles of the [CII] lines compared with the mid- and high-J CO lines observed with ALMA. The CO lines have been scaled to match the peak flux of the [CII] line, in order to facilitate the comparison of the velocity profiles. We first fit the CO and the [CII] lines independently with single Gaussian functions. We accept the single Gaussian fit if the reduced χ^2 does not exceed $1+5\times\sqrt{2n_{\rm dof}}$, where $n_{\rm dof}$ is the number of degrees of freedom. This quantity corresponds to 5 standard deviations of the χ^2 distribution. If the single Gaussian fit does not match the above criterion, we use a double Gaussian function, i.e. two Gaussian functions with displaced central positions. The double Gaussian function is sufficient to describe the line profiles that do not match a single Gaussian. In practice, this happens in SPT0103-45 and SPT0418-47, which have lines that display a slight asymmetry on the red side of the lines; the velocity difference between the CO and [CII] peaks is $<$150 km s^{-1}.

We then simultaneously fit the single or double Gaussian profile (depending on what is necessary to fit the profiles individually) to the CO and [CII] velocity profiles assuming the profiles are similar with just one free scaling parameter. This allows us to test if the two profiles are consistent or not. Only the [CII] and CO lines for SPT0532-50 have different velocity profiles. The remaining 16 sources have consistent line profiles with $\chi^2 < 1 + 5 \times \sqrt{2n_{\rm dof}}$.

We obtain the line widths (FWHM) listed in Table 2.1 by fitting a single Gaussian. To test the reliability of our method we also fit the spectra by taking velocity-weighted moments, and find fully consistent results. The resulting FWHMs are in the range $\sim 210 - 820$ km/s. This is comparable to the typical CO line width of ~ 460 km s^{-1} found for SPT DSFGs by stacking 22 spectra (Spilker et al., 2014). Nine out of 20 sources

have FWHM $> 500\,\mathrm{km/s}$, which is large compared to other high-z [CII] detections (e.g. $360\,\mathrm{km/s}$ on average in the sample of Wang et al. 2013).

We obtain the velocity-integrated fluxes for the FLASH/APEX detections by summing the observed line profiles over the 3σ limits obtained from the single Gaussian fits. The [CII] apparent luminosities range from 1.4 to $9.2 \times 10^{10}\,\mathrm{L_\odot}$ which is 1-2 orders of magnitude higher than their mid- and high-J CO luminosities ($\sim 3 - 30 \times 10^8\,\mathrm{L_\odot}$), where both are uncorrected for lensing.

The [CII] detection in SPT0512-59 with SPIRE FTS (see Figure 2.2 *right*) confirms the redshift at $z = 2.234$. We determine the integrated line flux in the same manner as Valtchanov et al. (2011) by fitting the emission lines with a sinc-function, and calculate the RMS using the standard deviation of each channel within $\pm 5000\,\mathrm{km\,s^{-1}}$ of the expected line centroid (see Valtchanov et al. 2011 for more details).

Our SPIRE FTS observation for SPT0551-50[5] does not detect any [CII] emission (see Figure 2.2 *left*). The redshift was reconfirmed by weak CO(1–0) emission observed with ATCA (Aravena *et al. in prep.*). We therefore take the 3σ upper limit of the expected line peak to be 3 times the RMS noise.

2.3.2 Lensing

The lensing magnification of the SPT DSFGs allows us to study the ISM in galaxies at high redshifts, but also introduces the possibility of differential lensing. The compactness and location of a region relative to the lensing caustic determines the magnification of the emission. Differential lensing amplification may thus occur between compact and extended emitting regions, or components occupying different regions (e.g. Hezaveh et al., 2012). From observations of the Milky Way and nearby galaxies, we might expect the [CII] emission to originate from more extended and diffuse media than the more optically thick low-J CO emission in giant molecular clouds (GMCs) (Fixsen et al., 1999). If the [CII] was dominated by emission from such diffuse regions, it could be subject to differential lensing compared to the more compact CO emission. However, the similar [CII] and CO velocity profiles suggest that such differential lensing is not significant.

Modelling the lensing magnification factor is of great importance, and has been performed for some of the DSFGs in this sample using ALMA data. The lens modelling is performed in the $(u, v)-$plane to properly represent the parameter uncertainties in the interferometric data (see Hezaveh et al. 2013 for more details). The four sources with lens models have lensing magnification factors μ between $\sim 5.4 - 21.0$ (Hezaveh et al., 2013) and a mean of $\langle\mu\rangle = 14.1$. In cases where the lensing magnification factor is unknown, we use the mean magnification factor to estimate the intrinsic luminosity. We then conservatively choose to span the uncertainty on the lensing magnification factor from the smallest ($\mu = 5.4$) to the largest ($\mu = 21.0$) giving the mean magnification an uncertainty of 7.8. We assume that the magnification factors derived from the dust continuum are also

[5]Note that is one of the rare cluster lenses in the SPT sample (Vieira et al., 2013). This, however, should not have any effect on the detectability of [CII] in this source.

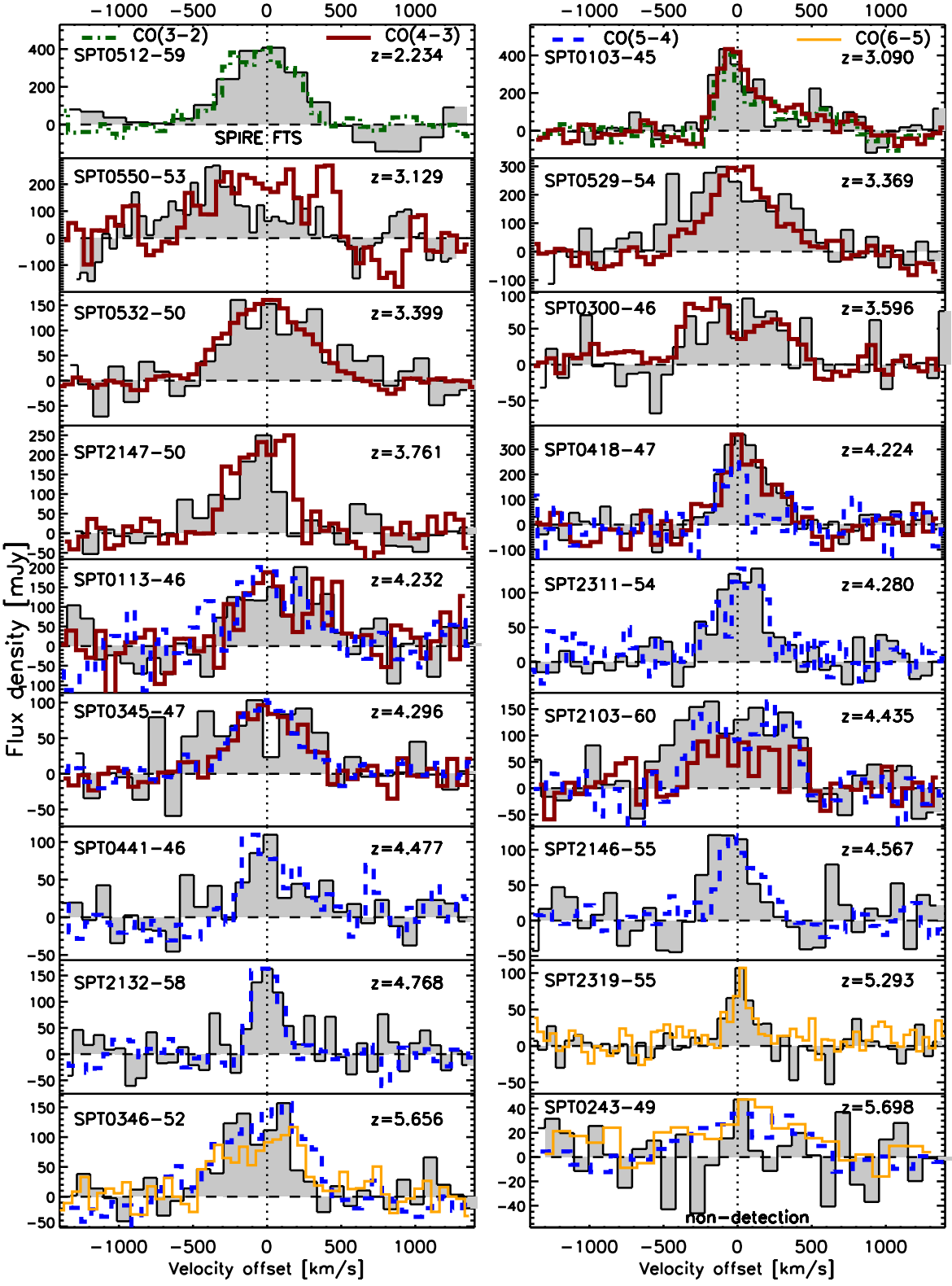

Figure 2.1: Comparison of the velocity profiles of the [CII] lines detected with APEX/FLASH and SPIRE FTS (grey filled profiles) and mid-J CO line observed with ALMA in Cycle 0 (coloured lines; Weiß et al., 2013).The CO lines have been scaled to match the [CII] peak flux. The similarities between the CO and [CII] lines for individual sources suggest that the spatial distributions are similar and differential lensing is not significant.

Source†	z	$SdV_{\rm [CII]}$ [Jy km/s]	dV (FWHM) [km/s]	$L'_{\rm [CII]}/10^{10}$ [K km/s/pc^2]	$L_{\rm [CII]}$ [10^{10} L$_\odot$]	$L_{\rm FIR}$ [10^{13} L$_\odot$]	$T_{\rm d}$ [K]	$\frac{L_{\rm [CII]}}{L_{\rm FIR}}$ [10^{-4}]	Instrument	Time [h]
SPT0551-50[1]	2.123	< 180 (3σ)	—	< 13.4	< 3.0	1.1 ± 0.1	27.2 ± 1.0	< 26.6	SPIRE FTS	3.8
SPT0512-59	2.234	227 ± 43	—	18.4 ± 3.5	4.0 ± 0.8	2.8 ± 0.2	33.2 ± 1.2	14.4 ± 2.9	SPIRE FTS	3.8
SPT0538-50[1]	2.782	< 465 (3σ)	—	< 81.9	< 18.0	5.8 ± 0.3	36.9 ± 1.4	< 31.0	SPIRE FTS★	3.8
SPT0103-45	3.090	125 ± 17	304 ± 47	17.5 ± 2.3	3.8 ± 0.5	3.4 ± 0.2	33.5 ± 1.1	11.3 ± 1.6	FLASH	2.7
SPT0550-53	3.129	129 ± 25	719 ± 124	18.5 ± 3.6	4.1 ± 0.8	1.6 ± 0.1	34.5 ± 1.8	25.4 ± 5.2	FLASH	17.3
SPT0529-54	3.369	217 ± 18	823 ± 92	35.1 ± 3.0	7.7 ± 0.7	3.0 ± 0.2	33.1 ± 1.2	25.7 ± 2.8	FLASH	3.8
SPT0532-50	3.399	113 ± 18	767 ± 124	18.6 ± 3.0	4.1 ± 0.7	6.5 ± 0.4	37.9 ± 1.4	6.3 ± 1.1	FLASH	4.6
SPT0300-46	3.596	41.5 ± 10.4	583 ± 138	7.5 ± 1.9	1.6 ± 0.4	3.3 ± 0.2	39.2 ± 1.5	5.0 ± 1.3	FLASH	12.8
SPT2147-50[2]	3.761	80.5 ± 11.7	329 ± 56	15.5 ± 2.3	3.4 ± 0.5	3.2 ± 0.2	41.4 ± 1.7	10.7 ± 1.7	FLASH	5.0
SPT0418-47[2]	4.224	127 ± 10	347 ± 29	29.5 ± 2.3	6.5 ± 0.5	5.9 ± 0.4	47.3 ± 2.5	11.0 ± 1.1	FLASH	1.5
SPT0113-46[2]	4.232	91 ± 19	619 ± 132	21.1 ± 4.4	4.6 ± 1.0	2.1 ± 0.1	32.9 ± 1.4	22.1 ± 4.8	FLASH	4.5
SPT2311-54	4.281	46.4 ± 5.3	360 ± 44	11.0 ± 1.2	2.4 ± 0.3	3.3 ± 0.3	43.3 ± 3.3	7.3 ± 1.1	FLASH	3.0
SPT0345-47[2]	4.296	63.7 ± 8.3	810 ± 200	15.2 ± 2.0	3.3 ± 0.4	9.2 ± 0.8	51.8 ± 3.2	3.6 ± 0.6	FLASH	2.3
SPT2103-60[2]	4.435	129 ± 18	780 ± 125	32.2 ± 4.4	7.1 ± 1.0	3.4 ± 0.2	39.2 ± 1.5	20.8 ± 3.1	FLASH	1.5
SPT0441-46[2]	4.477	42.5 ± 10.6	581 ± 162	10.8 ± 2.7	2.4 ± 0.6	3.7 ± 0.2	39.9 ± 1.9	6.6 ± 1.7	FLASH	3.2
SPT2146-55[2]	4.567	39.0 ± 9.0	302 ± 62	10.2 ± 2.4	2.2 ± 0.5	2.7 ± 0.3	39.2 ± 2.0	8.3 ± 2.1	FLASH	3.1
SPT2132-58	4.768	34.9 ± 6.9	212 ± 43	9.7 ± 1.9	2.1 ± 0.4	3.1 ± 0.3	39.5 ± 1.9	6.9 ± 1.5	FLASH	2.1
SPT2319-55	5.293	19.1 ± 3.2	198 ± 34	6.3 ± 1.1	1.4 ± 0.2	2.5 ± 0.2	42.0 ± 3.1	5.4 ± 1.1	FLASH	9.5
SPT0346-52[2]	5.656	63.3 ± 8.7	502 ± 72	22.8 ± 3.2	5.0 ± 0.7	12.3 ± 0.5	52.4 ± 2.2	4.1 ± 0.6	FLASH	1.4
SPT0243-49[2]	5.699	< 51 (3σ)	—	< 21.0	< 4.5	3.3 ± 0.3	35.3 ± 1.6	< 13.6	FLASH	2.2

Table 2.1: Observed [CII] and FIR properties. All luminosities are uncorrected for the lensing amplification. The upper limits for the velocity integrated fluxes given for the non-detections are obtained by assuming the FWHM observed for the CO lines. The total integration time with SPIRE FTS and FLASH is 92 hours. The integration time per sources is given in the last column.

† Full source names are listed in Table 1 of Weiß et al. (2013) or in Table 2.3.

[1] Has CO(1-0) observations (Aravena *et al., in prep.*).

[2] Has CO(2-1) observations (Aravena *et al., in prep.*).

★ See Bothwell et al. (2013a) for more details.

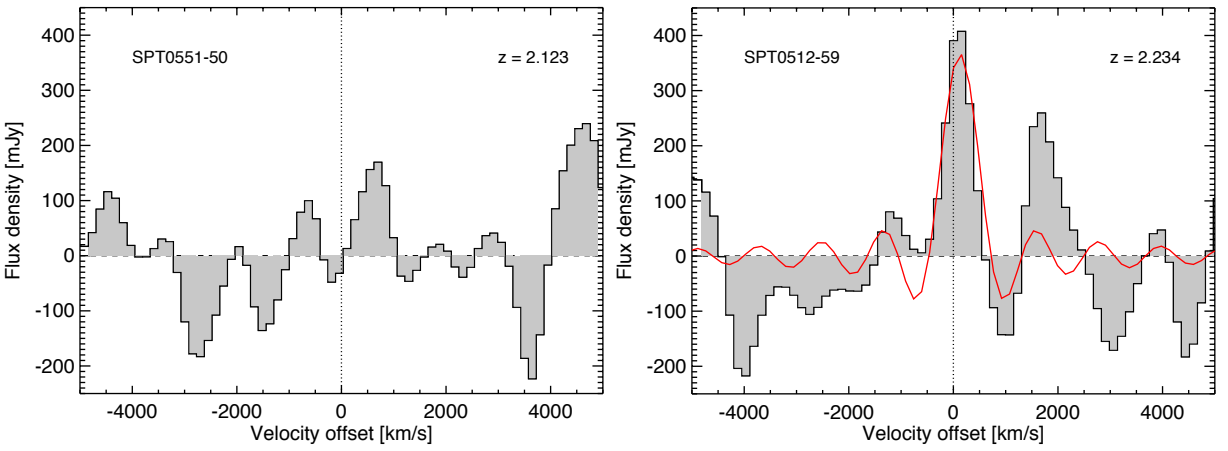

Figure 2.2: *Herschel* SPIRE FTS spectra for SPT0551-50 and SPT0512-59. *Left:* Non-detection of the [CII] emission line for SPT0551-50. *Right:* Detection of [CII] emission line for SPT0512-59. The continuous red curve is the sinc-function used to fit the [CII] line (see Valtchanov et al. 2011).

appropriate for the line emitting gas. A lens modelling analysis of the remainder of the ALMA Cycle 0 imaging data is currently under way.

2.4 Analysis

2.4.1 Comparison sample of nearby and distant galaxies

We compare the SPT sample with that of Garcia-Carpio et al. (in prep), which is comprised of 333 sources. These sources include LIRGs and ULIRGs from the Great Observatories All-sky Survey (GOALS, Díaz-Santos et al. 2013) and normal and Seyfert galaxies from Brauher et al. (2008) with spatially unresolved [CII] detections integrated over the entire individual galaxies. The sample contains 308 sources at $z < 0.4$ and 25 at $z > 1$. In addition, we have searched the literature for additional $z > 1$ DSFGs with [CII] observations, which we list in Appendix 2.8. In constructing this low and high-z comparison sample, we have paid particular attention to ensure that the photometric data are integrated over the full galaxies, as all line and continuum data for the SPT sample are also integrated values.

Conversion to CO(1–0) luminosities

Like the SPT sample (§ 2.2.1), many of the sources in the comparison sample also have published CO observations. In cases where the CO(1–0) emission lines have not been observed, Gracia-Carpio et al. (in prep) derive the $L_{\rm CO(1–0)}$ by converting the observed mid-J CO luminosities to $L_{\rm CO(1–0)}$ using scaling factors from Stacey et al. (2010). When multiple $J > 1$ CO lines were observed, we take the average of the scaled $L_{\rm CO(1–0)}$. These scaling factors are based on previous studies involving several rotational lines from both nearby galaxies, ULIRGs and high-z galaxies, which allow for the assumption of fixed CO

line ratios up to CO(4–3)/CO(1–0) (Stacey et al., 2010). The conversion factors used by Stacey et al. (2010) assume an integrated line flux ($\mathrm{W\,m^{-2}}$) ratio of CO(2–1)/CO(1–0) = 7.2, equivalent to 90% of the thermalised optically thick emission (i.e. a brightness temperature ratio of 0.9), CO(3–2)/CO(2–1) = 3.0 (90% of the thermalised optically thick emission) and CO(4–3)/CO(2–1) = 6.4 (80% of the thermalised optically thick emission).

The assumed CO(2–1) to CO(1–0) brightness temperature ratio of 0.9 for DSFGs is in agreement with observations of Bothwell et al. (2013b), who find a ratio of 0.85 for 32 luminous submm galaxies at $z \sim 1.2 - 4.1$. The [CO(2–1)/CO(1–0)] ratio has also been observed for four normal star forming galaxies by Aravena et al. (2014), resulting in a slightly lower [CO(2–1)/CO(1–0)] brightness temperature ratio of 0.7 ± 0.16 for four BzK galaxies at $z \sim 1.5 - 2.2$. Even though the ratio is consistent with Bothwell et al. (2013b) within the uncertainties, a lower [CO(2–1)/CO(1–0)] ratio is expected for normal star forming galaxies than for starburst galaxies, because the molecular gas in starburst galaxies is expected to be more highly excited. Spilker et al. (2014) find an average CO(2–1)/CO(1–0) brightness temperature ratio of 1.1 ± 0.1 for 22 of the SPT DSFGs by stacking ATCA spectra, after scaling them by their 1.4 mm continuum flux density. Given the range of values of these three methods, and for consistency with previous literature, we adopt the scaling factor of 0.9 from Stacey et al. (2010).

FIR luminosities

We obtain the FIR luminosities L_{FIR} and the dust temperature T_{d} for each source in the SPT DSFG sample by fitting the well-sampled spectral energy distributions (SEDs) with a greybody law fixing the emissivity index (β) at 2.0, $\mu_0 = 100$ and fitting $\lambda_{\mathrm{rest}} < 50\,\mu$m, following Greve et al. (2012) and Strandet et al. (in prep). We integrate the SED between $\lambda_{\mathrm{rest}} = 42 - 500\,\mu m$ in the rest frame to obtain L_{FIR}. Our SPT DSFGs all have 7 photometric data points covering observed wavelengths from 250 to 3000 μm (e.g. Weiß et al., 2013). This allows for a uniform determination of the FIR luminosity using a parametrised SED fitting[6]. The SPT sources, which have well-sampled SEDs, thus have a smaller uncertainty in L_{FIR} than sources with poor photometric coverage (see Figure 2.3).

To compare the low-z and high-z sample with the SPT sources in a consistent way, we compiled published FIR photometry (Gracia-Carpio et al. in prep; Appendix 2.8), and derived L_{FIR} and T_{d} using the same fitting code we used for the SPT sources (Greve et al., 2012). IRAS and ISO data are available for sources published by Brauher et al. (2008), and FIR data are also available for a large number of the GOALS sources at NASA/IPAC Extragalactic Database (NED[7]). The comparison sample contains 165 sources with sufficiently good photometry to derive L_{FIR} and T_{d} using the method in Greve et al. (2012); 14 of these are $z > 1$ sources (see Figure 2.3). Sources with insufficient available photometry to derive L_{FIR} using our procedure are not included in analyses requiring L_{FIR}

[6]Other studies (e.g. Stacey et al., 2010; Helou et al., 1988) use the two band definition for L_{FIR}: $F_{\mathrm{FIR}} = 1.26 \times 10^{-14} \times (2.58 f_{60\mu\mathrm{m}} + f_{100\mu\mathrm{m}})[\mathrm{W\,m^{-2}}]$ which is equivalent to the 42.5-122.5 μm luminosity (Helou et al., 1988).

[7]http://ned.ipac.caltech.edu

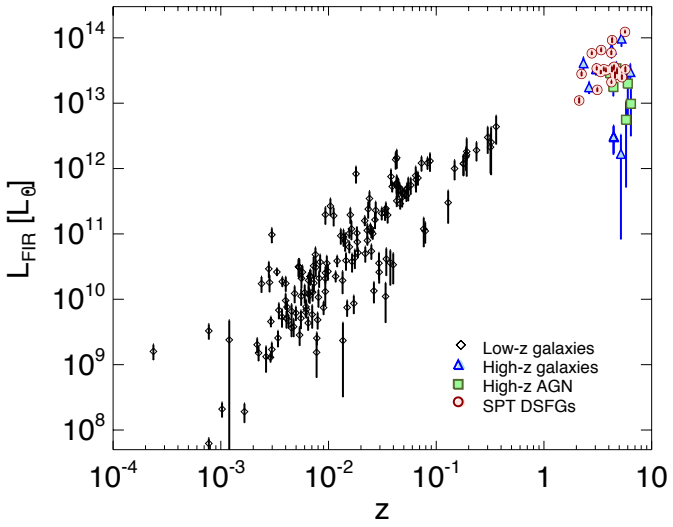

Figure 2.3: Observed $L_{\rm FIR}$ vs redshift for the 20 SPT sources and the comparison sample. No $L_{\rm FIR}$ have been corrected for lensing magnification factors. The distribution shows the Malmquist bias where high-z galaxies require either lensing magnification or very high intrinsic FIR luminosity of $L_{\rm FIR} \gtrsim 10^{12}\,{\rm L}_\odot$ to be included in the parent sample. The evolution of the luminosity function and the smaller comoving volume at low redshifts imply that objects with similar high intrinsic $L_{\rm FIR}$ are missing from the low-z sample. However, the most highly lensed DSFGs may have similar intrinsic $L_{\rm FIR}$ than the most luminous sources in the local sample.

but are still included in the $L_{\rm [CII]}/L_{\rm CO(1-0)}$ ratios.

Figure 2.3 presents the observed $L_{\rm FIR}$ distribution of our combined sample. There is a clear gap between the low and high-z samples due to the limited sensitivity of the nearby samples, and the atmospheric transparency prohibiting [CII] observations at $z < 1$ from the ground. The selection function of the high-z sample is quite complex because many sources have been pre-selected to have a good chance of detection in [CII] (e.g. by having strong dust continuum and/or CO emission). In addition, the improved atmospheric transparency at lower frequencies mostly compensates for the distance dimming in the more distant sources. The evolution of the luminosity function and the smaller co-moving volume at low redshifts imply that objects with similar high intrinsic $L_{\rm FIR}$ are missing from the low-z sample.

The SPT sources in this sample have FIR luminosities in the range $L_{\rm FIR}= (1.2-11.8)\times 10^{13}{\rm L}_\odot$. After de-magnification the range is $L_{\rm FIR}/\mu = (1.1-21.9)\times 10^{12}\,{\rm L}_\odot$, with a mean de-magnified $L_{\rm FIR}$ of $5.2\times 10^{12}\,{\rm L}_\odot$, which is similar to the most luminous sources in the low-z sample.

The uniform sensitivity of the ALMA mm spectroscopy, continuum, low-J CO and [CII] observations (all with S/N>3) lead to a high completeness of the SPT sample. This, combined with the lensing amplification factor which is about one order of magnitude (Hezaveh et al., 2013), make the SPT DSFG sample one of the most representative samples to date for massive, IR-luminous starburst galaxies at high redshifts.

AGN content

The comparison sample contains both starburst galaxies and luminous AGN. In the high-redshift sample, we distinguish the AGN-dominated sources from those without any known AGN. These high-redshift AGN are quite rare sources, mostly selected based on their bright optical emission lines (e.g. Wang et al. 2013). The SPT DSFGs are selected solely on their lensed 1.4 mm continuum flux, and direct mm imaging and spectroscopy avoids any radio/optical identification steps that may introduce biases towards AGN-dominated systems. Optical spectroscopy of the SPT DSFG sample to derive the redshifts of the foreground lensing galaxies has not shown any indications of type-1 or type-2 AGN. Strongly obscured type-2 AGN may still be present in some SPT DSFGs. Supported by the discussion in §2.4.4, we will assume in the following that the AGN contributions in the SPT DSFGs are negligible.

2.4.2 Observed [CII] to FIR ratios

Figure 2.4 presents the $L_{[\mathrm{CII}]}/L_{\mathrm{FIR}}$ ratio against L_{FIR} for the SPT sources and the comparison sample. The typical error bar for the low-z sources (in this and the following plots) is illustrated by the cross in the bottom left. This typical error bar includes the quoted uncertainties of the lines (e.g. Young et al., 1995; Negishi et al., 2001), the absolute and statistical uncertainty of the FIR photometry, and of the FIR luminosity determined by our own SED fitting. The SPT DSFGs have been corrected for lensing amplification either using the known lens model (Hezaveh et al., 2013), or assuming a mean magnification factor $\langle\mu\rangle = 14.1 \pm 7.8$ for the sources without a lens model (see section 2.3.2).

Sources with $L_{\mathrm{FIR}} \lesssim 10^{11}\,\mathrm{L}_{\odot}$ appear to have a roughly constant $L_{[\mathrm{CII}]}/L_{\mathrm{FIR}}$ ratio ($\sim 4 \times 10^{-3}$). At $L_{\mathrm{FIR}} \gtrsim 10^{11}\,\mathrm{L}_{\odot}$, the ratio drops to 6×10^{-4} for the $z < 1$ sources in the comparison sample, similar to what has been reported in previous studies (e.g. Maiolino et al., 2009; Stacey et al., 2010). Whether this is an intrinsic or observational effect due to limited sensitivity of the [CII] and/or FIR photometry in the low-z samples is not clear, and investigating this is beyond the scope of this paper. The $z > 1$ sources from the comparison sample are scattered over two orders of magnitude, which may be due to the heterogeneous mix of the parent samples. The highly complete (82% detections) and uniformly observed SPT sources have a smaller scatter and an average $L_{[\mathrm{CII}]}/L_{\mathrm{FIR}}$ ratio of $\sim 10^{-3}$. A Kolmogorov-Smirnov test results in a probability of 0.7 that the $L_{[\mathrm{CII}]}/L_{\mathrm{FIR}}$ values for $L_{\mathrm{FIR}} \gtrsim 10^{11}\,\mathrm{L}_{\odot}$ from the SPT and the low-z samples are drawn from the same distribution.

Normalising the FIR luminosity by the molecular gas mass reduces the scatter seen in Figure 2.4 for the $L_{\mathrm{FIR}} \gtrsim 10^{11}\,\mathrm{L}_{\odot}$ sources (Graciá-Carpio et al., 2011). The $L_{\mathrm{FIR}}/M_{\mathrm{H_2}}$ ratio is expected to be proportional to the star formation efficiency, specifically to the number of stars formed in a galaxy per unit molecular gas mass. This ratio has the additional advantage that the lensing magnification factor cancels out. We estimate the molecular gas masses for the 11 sources for which we also have low-J CO line detections (Aravena *et*

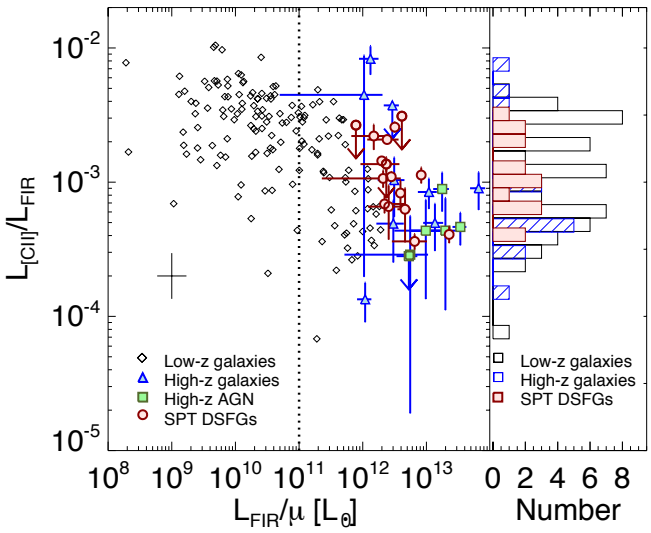

Figure 2.4: $L_{[CII]}/L_{FIR}$ vs L_{FIR} for SPT sources and the comparison sample. As reported in previous versions of this plot, the $L_{[CII]}/L_{FIR}$ is anti-correlated with L_{FIR}. In particular at $L \gtrsim 10^{11}\,L_\odot$, the $L_{[CII]}/L_{FIR}$ ratio drops and has a larger spread. For the SPT sources without known lensing models, we assume a lensing magnification factor of 14.1 (and an uncertainty which encompasses the range of 5 to 22 from the known models). The typical error bar for the literature sources is represented by the black cross in the lower left. The histogram on the right shows the distribution of galaxies with $L_{FIR} \gtrsim 10^{11}\,L_\odot$.

al, in prep.). We determine the molecular gas mass by:

$$M_{H_2} = \alpha_{CO} L'_{CO(1\text{-}0)}, \tag{2.1}$$

where α_{CO} is the CO-to-H_2 conversion factor. To be consistent with Graciá-Carpio et al. (2011), we assume $\alpha_{CO} = 0.8\,M_\odot\,(K\,km/s\,pc^2)^{-1}$ determined by Downes & Solomon (1998) for the SPT DSFGs and the low- and high-z comparison samples. Figure 2.5 plots $L_{[CII]}/L_{FIR}$ as a function of L_{FIR}/M_{H_2} and shows that the DSFGs lie among the local LIRGs. Low-z sources with $L_{FIR} \gtrsim 10^{11}\,L_\odot$ and the high-z sources have similar $L_{[CII]}/L_{FIR}$ ratios.

2.4.3 Dust temperatures

As first shown by Malhotra et al. (1997), the $L_{[CII]}/L_{FIR}$ ratio shows a strong anti-correlation with T_d. They attributed this trend to an increase in the G_0/n ratio (far-UV ionising field over density) in the hotter, more active galaxies, and hence a lower efficiency of gas heating reducing the [CII] flux while increasing the dust temperature. We here revisit this trend using the uniformly-derived set of L_{FIR} and T_d values for the SPT sources and comparison samples, derived from our SED modelling (§ 2.4.1). The top panel of Figure 2.6 compares the $L_{[CII]}/L_{FIR}$ ratio to T_d, with both quantities being independent of the lensing magnification. The strong anti-correlation of these quantities is visible in all three samples.

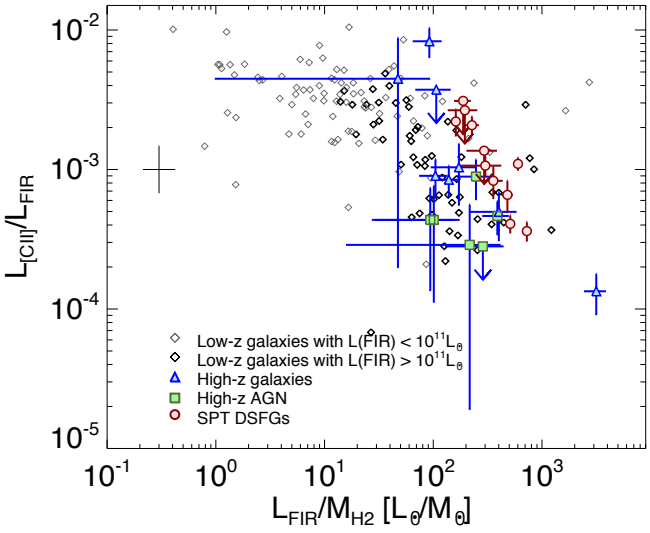

Figure 2.5: $L_{[CII]}/L_{FIR}$ vs the FIR luminosity normalised by the molecular gas mass. The molecular gas mass is derived assuming a conversion factor of $\alpha_{CO} = 0.8 M_\odot\,(\mathrm{K\,km\,s^{-1}\,pc^{-2}})^{-1}$. The L_{FIR}/M_{H_2} ratio is expected to be proportional to the number of stars formed in a galaxy per unit molecular gas mass (Graciá-Carpio et al., 2011). This M_{H_2} normalisation removes the uncertainty due to the unknown lensing magnification factors, and reduces the scatter seen in Figure 2.4, but the deficit in the $L_{[CII]}/L_{FIR}$ ratio still persists. The typical error bar is represented by the black cross.

However, if the dust and [CII] emission are coming from the same regions, and $L_{[CII]}$ is less dependent on T_d, a significant part of this anti-correlation can be explained with the Stefan-Boltzmann law which predicts $L_{FIR} \propto {T_d}^4$.

In order to look for a residual correlation, we cancel out the $L_{FIR} \propto {T_d}^4$ dependence by plotting $L_{[CII]} \times {T_d}^4/L_{FIR}$ against T_d (see bottom panel of Figure 2.6). We note that a small systematic offset in T_d would get propagated as ${T_d}^4$. To test the presence of a correlation taking into account the [CII] upper limits, we use the generalised Kendall's tau method (Lavalley et al., 1992). We find a probability that both variables are not correlated of 0.036, 0.602 and 0.151 for the low-z, high-z and SPT samples, respectively. The small displacement of the SPT sources relative to the comparison sample in Figure 2.6 is likely due to Malmquist bias and evolution effects resulting in the most luminous sources being absent in the low-z comparison sample (see § 2.4.1). While there is marginal evidence for a small positive residual correlation (especially in the low-z sample), most of the correlation seen in the top panel has canceled out. This confirms our assumptions that the dust and [CII] emission are originating from the same regions and that $L_{[CII]}$ is less dependent on T_d. We therefore conclude that the observed correlation is mostly dominated by the Stefan-Boltzmann law.

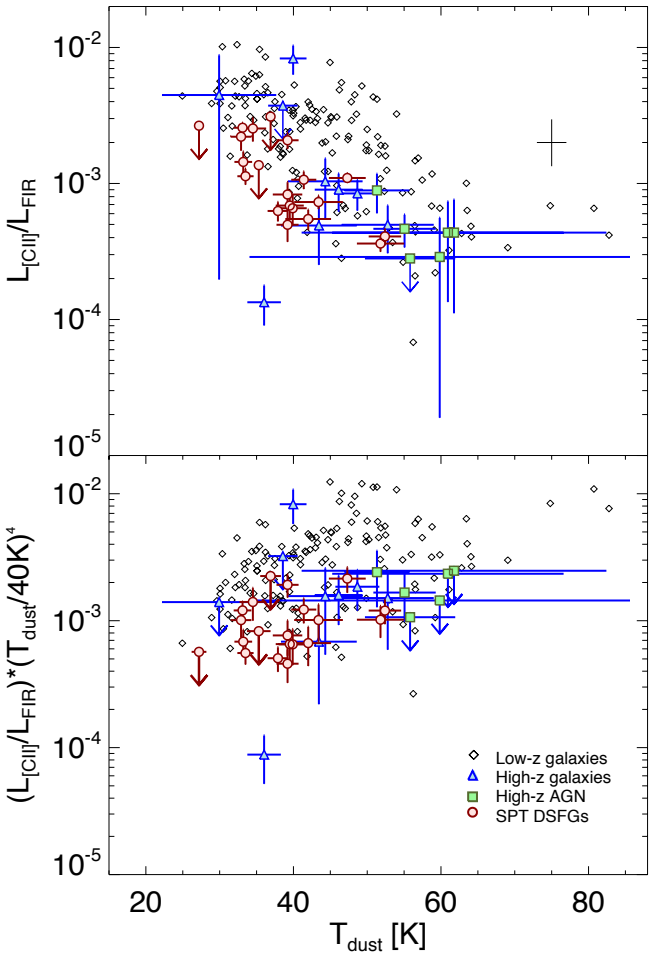

Figure 2.6: *Top panel:* $L_{[CII]}/L_{FIR}$ vs T_d for the SPT DSFGs and the low and high-z comparison sample. The anti-correlation between the $L_{[CII]}/L_{FIR}$ ratios and the dust temperatures is seen for both low- and high-z sources, and is expected because the Stefan-Boltzmann law predicts $L_{FIR} \propto {T_d}^4$. *Bottom panel:* [CII]$\times {T_d}^4/L_{FIR}$ vs T_d for the SPT DSFGs and the low and high-z comparison sample. Multiplying the $L_{[CII]}/L_{FIR}$ ratio with ${T_d}^4$ cancels out the temperature dependence of the Stefan-Boltzmann law. All lensing magnification factors and beam filling factors cancel in both panels, and the typical error bar is represented by the black cross.

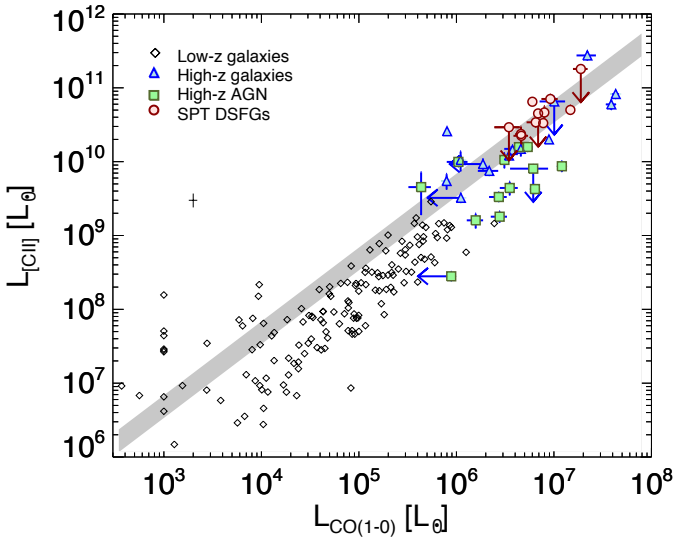

Figure 2.7: The [CII] luminosity versus the CO luminosity for the SPT DSFGs and the comparison low and high-z samples. These star forming systems show a correlation between the [CII] and CO(1-0) luminosities. Fitting a ratio to 11 SPT sources with [CII] detections and CO(1–0) data yields a slope of ~ 5200. The width of the grey shaded area represents a 1σ spread, $\sim 5200 \pm 1800$. Fitting a ratio to the low-z sample yields a slope of 1300 ± 440. The typical error bar for the low-z sources is represented by the black cross.

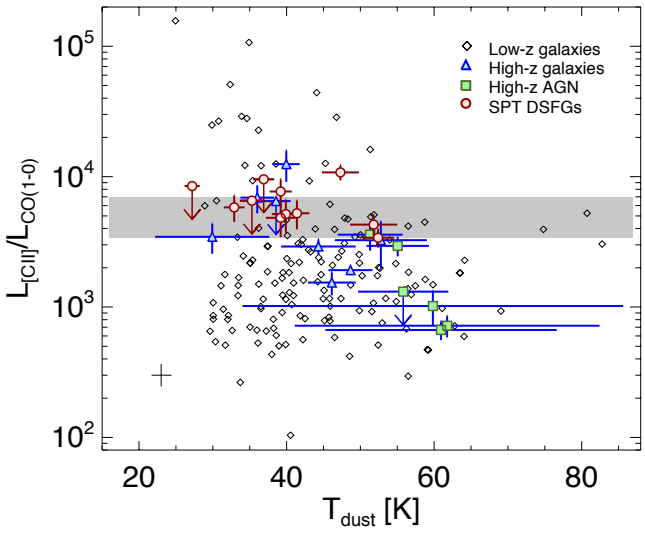

Figure 2.8: $L_{[\mathrm{CII}]}/L_{\mathrm{CO}(1-0)}$ vs T_{d} for the SPT sources and the low and high-z comparison sample. The typical error bar is represented by the black cross. The grey shaded area represents the 1σ spread of the $L_{[\mathrm{CII}]}/L_{\mathrm{CO}(1-0)}$ ratio in the SPT sample. Both the SPT sources and the low-z sample do not show any dependence on T_{d}. The high-z AGN-dominated sources are both warmer and have fainter [CII] relative to CO.

2.4.4 Observed [CII] to CO ratios

One of the strengths of the SPT DSFG sample is that more than half of the sources have both [CII] and low-J CO detections. Figure 2.7 plots the [CII] vs CO(1–0) luminosities for these 11 sources, along with high-z sources in the comparison sample[8]. All high-z sources fall close to the $L_{[CII]}/L_{CO(1-0)} \sim 4400$ relation for local galaxies reported by Crawford et al. (1985); Wolfire et al. (1989); Stacey et al. (1991a, 2010); Swinbank et al. (2012); Neri et al. (2014). This relation has been explained in terms of PDR models (Wolfire et al., 1989, 1993; Stacey et al., 1991a). Using the eight SPT DSFGs with [CII] and CO(1–0) detections, we determine the $L_{[CII]}/L_{CO(1-0)}$ ratio to be 5200 ± 1800. In section 2.5.1, we derive the physical conditions that can be derived from this ratio from first principles and eventually compare it with the PDR models.

Finally, in Figure 2.8, we test if the $L_{[CII]}/L_{CO(1-0)}$ ratio[9] depends on T_d. We find no correlation in either the low-z or the SPT DFSG sample. However, the four high-z sources with the lowest $L_{[CII]}/L_{CO(1-0)}$ ratio are all AGN dominated. This is consistent with the observations of Stacey et al. (2010) and Sargsyan et al. (2014) that AGN dominated sources have lower $L_{[CII]}/L_{FIR}$ ratios. Although our T_d determinations are rather crude, these AGN-dominated sources are also those with the warmest T_d, as expected (see, e.g., Figure 3 in Greve et al. 2012). Interestingly, only 2 out of 11 SPT DSFGs fall near the AGN-dominated sources in Fig. 2.8, supporting our conclusion (§ 2.4.1) that the SPT sample does not contain many strongly AGN-dominated sources.

2.5 Discussion

2.5.1 Possible origins of the [CII] to CO correlation

Determining the optical depth of the [CII] line

The origin of the correlation between the [CII] and CO(1–0) luminosities and the impact of their relative optical depths was first discussed by Crawford et al. (1985), and later by others in both low and high-z objects (e.g.,Wolfire et al. 1989; Stacey et al. 1991a, 2010; Swinbank et al. 2012; Neri et al. 2014). Crawford et al. (1985) assumed [CII] excitation temperatures $T_{ex,[CII]} \gg 92\,K$[10], and could therefore apply the Rayleigh-Jeans approximation. This assumption was supported by independent estimates of the gas temperature of order $\sim 300\,K$ using other fine-structure lines and assuming optically thin [CII] emission (Ellis & Werner, 1984). They remarked that their observed $L_{[CII]}/L_{CO(1-0)}$ ratio ~ 4400 is close to the [CII] to CO(1–0) frequency ratio cubed, suggesting optically thick [CII] emission.

[8]Note that Figure 2.7 presents a larger number of high-z sources than Figures 2.5, 2.6, and 2.8, as it does not involve quantities derived from continuum photometry. The calculation of L_{FIR} and T_d require photometric data that are unavailable for several of the high-z comparison objects (see section 2.4.1 and Appendix 2.8).

[9]Note that both parameters are independent of the lensing magnification.

[10]The [CII] ground state energy level is 92 K.

However, using supporting data in Orion, the Galactic centre and M82, they independetly derived [CII] optical depths $\tau_{[\rm CII]} = 0.03 - 1$. This conclusion that [CII] is mostly optically thin has been assumed several times since (e.g. Stacey et al., 1991a; Hailey-Dunsheath et al., 2010; Stacey et al., 2010; De Breuck et al., 2011; Rawle et al., 2014).

The most accurate way to determine the optical depth of the [^{12}CII] emission line is through observations of the isotopic line ratios. The two [CII] emission lines for ^{12}C and ^{13}C have been observed in local star forming regions, e.g. in M42 (Stacey et al., 1991b; Boreiko & Betz, 1996), NGC2024 (in the Orion nebula; Graf et al., 2012), the Orion Bar, Mon R2, NGC 3603, the Carina Nebula and NGC 7023 (Ossenkopf et al., 2013). These observations find optical depths ranging from $\tau \sim 1$ to $\tau \sim 3$, with on average a moderate optical dept $\tau \sim 1.4$. However, one should keep in mind that Orion and Carina are very bright [CII] emitters (to allow for a detection of the faint ^{13}C), with very strong FUV fields ($G_0 \sim 10^4 - 10^5$), implying large [CII] columns and hence rather high opacities. The galaxy-scale average may result in lower optical depths near unity. Unfortunately, this isotope ratio technique cannot be applied to galaxy-integrated [CII] observations as the [^{12}CII] fine structure line and the brightest [^{13}CII] hyperfine structure line are only separated by $\sim 110\,$km/s, which is smaller than the typical widths of these lines. The much weaker ^{13}C line is then indistinguishable from features in the profile of the ^{12}C line.

The optical depth of [CII] in very distant galaxies must therefore be estimated by other methods. The idea of optically thick [CII] emission at high redshifts was recently proposed by Neri et al. (2014) for the high-z sub-millimetre source HDF 850.1. They assume the [CII] line excitation temperature is the same as the dust and gas kinetic temperatures, and argue for high line optical depth of the [CII] line (i.e. $\tau_{[\rm CII]} \gtrsim 1$). The observed $L_{[\rm CII]}$ and predicted $L_{\rm CO(1–0)}$ by Walter et al. (2012), yield a $L_{[\rm CII]}/L_{\rm CO(1–0)}$ ratio of ~ 5200, in agreement with the ratio derived from the SPT sample of 5200 ± 1800 (§ 2.4.4). We now generalise this line ratio method by comparing the source functions. This does not require the CO and [CII] excitation temperatures to be the same, nor that the Rayleigh-Jeans approximation applies (i.e. we also consider cases where $T_{\rm ex,[CII]}$ is close to or below 91 K).

From the source functions of both lines, the luminosity ratio depends on

$$\frac{L_{[\rm CII]}}{L_{\rm CO(1–0)}} = \left(\frac{\nu_{[\rm CII]}}{\nu_{\rm CO(1–0)}}\right)^3 \times \left(\frac{\Delta\nu_{[\rm CII]}}{\Delta\nu_{\rm CO(1–0)}}\right) \times \frac{e^{h\nu_{\rm CO(1–0)}/kT_{\rm ex,CO(1–0)}} - 1}{e^{h\nu_{[\rm CII]}/kT_{\rm ex,[CII]}} - 1} \cdot \frac{1 - e^{-\tau_{[\rm CII]}}}{1 - e^{-\tau_{\rm CO(1–0)}}}, \quad (2.2)$$

where we have assumed that the [CII] and CO emitting gas have the same filling factors (see §2.4.3). This assumption is consistent with the very similar [CII] and CO velocity profiles (Figure 2.1). In this case, $\frac{\Delta\nu_{[\rm CII]}}{\Delta\nu_{\rm CO(1–0)}} = \frac{\nu_{[\rm CII]}}{\nu_{\rm CO(1–0)}}$. Also in nearby galaxies, [CII] and CO have been found to trace each other both morphologically and kinematically (e.g. Braine et al. 2012 and Mittal et al. 2011). Equation (2) has four free parameters: two excitation temperatures and two opacities. In order to obtain constraints, we therefore have to fix some of these.

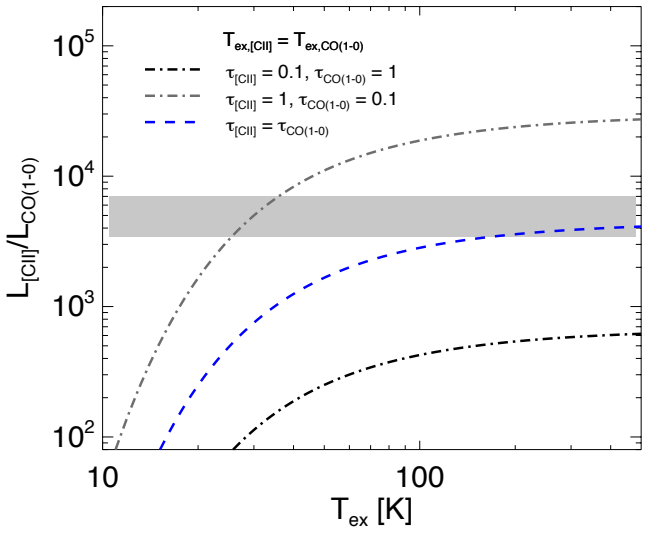

Figure 2.9: The $L_{[CII]}/L_{CO(1-0)}$ ratio predicted from the source functions versus equal [CII] and CO(1–0) excitation temperatures ($T_{ex,[CII]} = T_{ex,CO(1-0)}$), for three different cases of the optical depth: *i*) optically thin [CII] and optically thick CO(1–0) (the black dot-dashed curve), *ii*) optically thick [CII] and optically thin CO(1–0) - (the grey dot-dashed curve), *iii*) same optical depth of [CII] and CO(1–0) (blue dashed curve). The grey shaded area represents the 1σ spread of the $L_{[CII]}/L_{CO(1-0)}$ ratio in the SPT sample. Case *i* underpredicts the ratio by an order of magnitude. Cases *ii* and *iii* can both reproduce the observed ratio. However, we know from ^{12}CO to ^{13}CO ratios that CO is optically thick (e.g. Spilker et al., 2014), which rules out case *ii*. Only case *iii*, implying optically thick CO and [CII], is consistent with all observational data.

Same [CII] and CO excitation temperatures

We first consider the case suggested by Neri et al. (2014) of equal excitation temperatures (i.e. $T_{ex,[CII]} = T_{ex,CO(1-0)}$), Figure 2.9 plots $L_{[CII]}/L_{CO(1-0)}$ vs T_{ex} for the three scenarios: *i*) optically thin [CII] and (nearly) optically thick CO(1–0) emission, *ii*) (nearly) optically thick [CII] and optically thin CO(1–0) emission, *iii*) same optical depth for [CII] and CO(1–0).

Scenario *i* shown by the black dot-dashed curve underpredicts the observed ratio (grey shaded area) by an order of magnitude. In the opposite case, scenario *ii* (grey dot-dashed curve), the observed ratio is reached only for very low excitation temperatures. However, this optically thin CO scenario can be ruled out because both the ^{12}CO to ^{13}CO ratios and the low-J ^{12}CO line ratios in the SPT sample imply that CO is moderately optically thick with $\tau_{CO(1-0)} = 1 - 10$ (Spilker et al., 2014), similar to what is seen in our own galaxy (Penzias et al., 1972; Goldreich & Kwan, 1974). Scenario *iii*, where the [CII] and CO(1–0) optical depths are in the same regime is thus the only one that can fit the observed ratios, but only for excitation temperatures $\gtrsim 180$ K. While we cannot distinguish mathematically between low and high optical depth, the known $\tau_{CO(1-0)} = 1 - 10$ and the equality of both the excitation temperatures and opacities would imply that also [CII] would need to be (nearly or fully) optically thick.

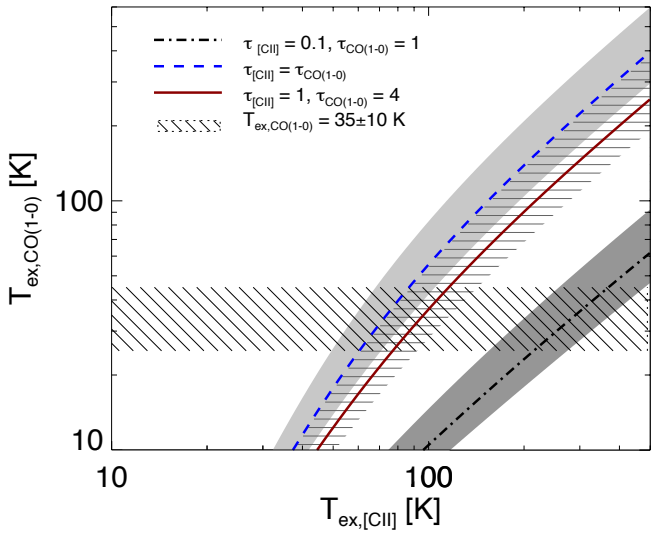

Figure 2.10: $T_{\mathrm{ex,CO(1–0)}}$ as a function of $T_{\mathrm{ex,[CII]}}$. In all cases, the excitation temperature of [CII] is higher than for CO(1–0). The *blue dashed* curve with the *light grey* shaded area shows the observed $L_{\mathrm{[CII]}}/L_{\mathrm{CO(1–0)}} = 5200 \pm 1800$ range of SPT DSFGs in the case of equal [CII] and CO optical depths. The red continuous curve and hashed area illustrates that the difference between the excitation temperatures becomes even more significant for $\tau_{\mathrm{[CII]}}$=1 and $\tau_{\mathrm{CO(1–0)}}$=4. The *dot-dashed* curve and the *dark grey* shaded area illustrate the case of $\tau_{\mathrm{[CII]}}$= 0.1 and $\tau_{\mathrm{CO(1–0)}}$= 1. The hatched horizontal area marks $T_{\mathrm{ex,CO(1–0)}} = 35 \pm 10\,\mathrm{K}$.

The only way the above scenario *iii* can fit the observed $L_{\mathrm{[CII]}}/L_{\mathrm{CO(1–0)}}$ ratio is in a thermalised region where both [CII] and CO(1–0) have excitation temperatures $\gtrsim 180\,\mathrm{K}$ (see Fig. 2.9). However, the average CO excitation temperatures in the SPT sample are $\lesssim 50\,\mathrm{K}$ (Spilker et al., 2014), well below the values required to fit the observed ratio (Fig. 2.9). The only way to reconcile the model in equation (2) with the known physical parameters of the CO ($\tau_{\mathrm{CO(1–0)}} > 1$ and $T_{\mathrm{ex,CO}} \lesssim 50\,\mathrm{K}$) is to allow for different excitation temperatures of [CII] and CO. Such different excitation temperatures also imply different [CII] and CO emitting regions within the GMCs.

Different [CII] and CO excitation temperatures

To examine the model from equation (2) with different excitation temperatures, we have to fix the observed $L_{\mathrm{[CII]}}/L_{\mathrm{CO(1–0)}}$ ratio and at least two parameters (two optical depths or an optical depths and a temperature). We first consider the case when $\tau_{\mathrm{[CII]}} = \tau_{\mathrm{CO(1–0)}}$, and plot $T_{\mathrm{ex,CO(1–0)}}$ as a function of $T_{\mathrm{ex,[CII]}}$ in Figure 2.10 (blue dashed line with grey shaded area illustrating the observed $L_{\mathrm{[CII]}}/L_{\mathrm{CO(1–0)}}$ range). We conclude that $T_{\mathrm{ex,[CII]}} > T_{\mathrm{ex,CO(1–0)}}$ throughout. In the optically thick case, we can also allow for $1 \leq \tau_{\mathrm{[CII]}} < \tau_{\mathrm{CO(1–0)}}$. The red curve in Figure 2.10 illustrates this for $\tau_{\mathrm{CO(1–0)}}$=4. Any further increase of the difference between $\tau_{\mathrm{[CII]}}$ and $\tau_{\mathrm{CO(1–0)}}$, will also increase the difference in T_{ex}. We warn that once both the [CII] and CO become strongly optically thick (i.e. $1 \ll \tau_{\mathrm{[CII]}} < \tau_{\mathrm{CO(1–0)}}$), one

can no longer determine any differences between the optical depths, and hence no longer determine $T_{\rm ex,[CII]}$.

Alternatively, we can also fix the CO opacity and excitation temperature based on existing observations of the SPT DSFG sample, and determine which $T_{\rm ex,[CII]}$ values are predicted for a given $\tau_{\rm [CII]}$. Assuming the molecular gas is traced by CO(1–0) and the dust is thermalised allows us to fix the $T_{\rm ex,CO(1–0)} = T_{\rm d} \simeq 35\,{\rm K}$ (Weiß et al., 2013). This value is consistent with the $T_{\rm kin}$ determined from the stacked ALMA spectrum of the SPT sample (Spilker et al., 2014). This $T_{\rm ex,CO(1–0)}$ =35 K case is illustrated in Figure 2.11. If $\tau_{\rm [CII]} = \tau_{\rm CO(1–0)}$, this would imply $T_{\rm ex,[CII]} \sim 60 - 90\,{\rm K}$. Raising $\tau_{\rm CO(1–0)} = 4$ while keeping $\tau_{\rm [CII]} = 1$ would imply $T_{\rm ex,[CII]} \sim 80 - 110\,{\rm K}$. The observed $L_{\rm [CII]}/L_{\rm CO(1–0)}$ ratios can also be reproduced with optically thin [CII] and (nearly) optically thick CO ($\tau_{\rm [CII]} = 0.1$ and $\tau_{\rm CO(1–0)} = 1$) when the [CII] excitation temperatures are $\sim 240 - 330\,{\rm K}$. A determination of $T_{\rm ex,[CII]}$ is therefore needed to determine $\tau_{\rm [CII]}$. If the gas densities are higher than the critical density for [CII] ($2400 - 6100\,{\rm cm^{-3}}$ for the above range of $T_{\rm ex,[CII]}$; Goldsmith et al., 2012), $T_{\rm ex,[CII]} \sim T({\rm gas})$. The gas temperatures can be obtained from observed [CII]/[OI] ratios (e.g. Stacey et al., 1983; Lord et al., 1996; Brauher et al., 2008), inferred through the peak [CII] antenna temperatures (e.g. Graf et al., 2012; Ossenkopf et al., 2013), or by theoretical modelling (e.g. Kaufman et al., 1999). These studies obtain $T({\rm gas}) = 100 - 500\,{\rm K}$, which from Fig. 2.11 would imply [CII] optical depths ranging from 0.1 to 1. However, the densities we derive from a comparison with PDR models (see §2.5.2) are in the range $100 - 10^5$ (Table 2.2), with half of our sources below the [CII] critical density, so the $T_{\rm ex,[CII]} \sim T({\rm gas})$ may not be valid for a significant part of our sample. Hence, optical depths of $0.1 < \tau < 1$ are consistent with the observed line ratios in the SPT DSFG sample.

We also compare the model predictions in Figure 2.11 with the low- and high-z comparison samples. The lower average $L_{\rm [CII]}/L_{\rm CO(1–0)}$ ratios in these samples (though with a much larger spread than for the SPT DSFGs) imply $T_{\rm ex,[CII]}$ between ~ 30 and $\sim 200\,{\rm K}$. In particular for the low-z sample, optically thick [CII] and CO emission would imply very low $T_{\rm ex,[CII]} \sim 40\,{\rm K}$, well below the ground state energy. The difference between the SPT DSFG and the low-z comparison sample could therefore be ascribed to a lower optical depths in the nearby sources. In the context of PDR models, this can also be understood as a decrease of the G_0/n ratio. Reducing this parameter implies smaller [CII] emitting columns and a smaller effective optical depth. The lower G_0/n ratio in the low-z sample could be an effect of the lower far-UV fields found in galaxies forming stars at a more modest rate (Stacey et al., 1991a, 1993; Kaufman et al., 1999).

Finally, we note that Figure 2.8 also contains some low-z sources with $L_{\rm [CII]}/L_{\rm CO(1–0)}$ ratios >15,000. Such values are difficult to explain with standard PDR models. Low metallicity has been invoked to explain these sources (e.g. Maloney & Black, 1988; Stacey et al., 1991a; Madden et al., 1997). Considering this effect is beyond the scope of this paper.

In summary, the observed $L_{\rm [CII]}/L_{\rm CO(1–0)}$ ratios in the SPT DSFGs are best described by a non-uniform medium of [CII] and CO(1–0) emitting gas with $T_{\rm ex,[CII]} > T_{\rm ex,CO(1–0)}$, $\tau_{\rm CO(1–0)} \gg 1$ and $\tau_{\rm [CII]} \lesssim 1$.

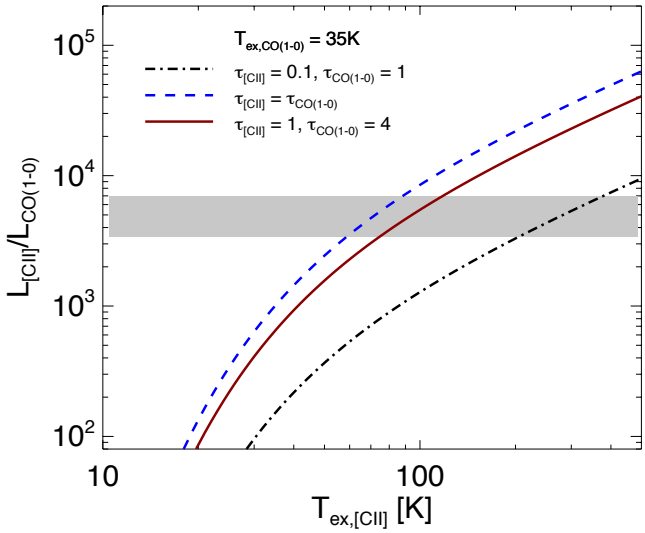

Figure 2.11: The $L_{[\mathrm{CII}]}/L_{\mathrm{CO}(1-0)}$ ratio as a function of the [CII] excitation temperature for a fixed $T_{\mathrm{ex,CO}(1-0)}$=35 K. The observed $L_{[\mathrm{CII}]}/L_{\mathrm{CO}(1-0)}$ ratio in the SPT DSFG sources (grey shaded area) is achieved within $T_{\mathrm{ex,[CII]}} \sim 60 - 90$ K for equal [CII] and CO optical depth (blue curve). In the case of $\tau_{[\mathrm{CII}]} = 1$ and $\tau_{\mathrm{CO}(1-0)} = 4$, the $L_{[\mathrm{CII}]}/L_{\mathrm{CO}(1-0)}$ ratio is achieved for $T_{\mathrm{ex,[CII]}} = 85 - 110$ K. The optically thin $\tau_{[\mathrm{CII}]} = 0.1$ and nearly optically thick $\tau_{\mathrm{CO}(1-0)} = 1$ case is reached by [CII] excitation temperatures in the range $\sim 240 - 330$ K (black dot-dashed curve).

2.5.2 Implications of different [CII] and CO(1–0) excitation temperatures

In section 2.5.1 we concluded that a homogeneous region with thermalised CO and [CII] gas is incompatible with the observed $L_{[\mathrm{CII}]}/L_{\mathrm{CO}(1-0)}$ ratios. Even in the optically thick case, the only way to reproduce the observed ratio is for higher [CII] than CO(1–0) excitation temperatures (see Figure 2.10). The cases of uniform and separated [CII] and CO gas was recently studied by Mashian et al. (2013). They explore four different models to explain the observations in the high-z submillimetre source HDF 850.1: 1) separate CO - [CII] virialised gas, 2) separate CO - [CII] unvirialised gas, 3) uniformly mixed CO - [CII] virialised gas and 4) uniformly mixed CO - [CII] unvirialised gas. Based on cosmological constraints due to the dark matter halo abundance in the standard Λ cold dark matter cosmology, they rule out three of the models and conclude that the preferred model is an unvirialised molecular cloud model with independent CO and [CII] emitting gas with a average kinetic temperature of 100 K and density of 10^3 cm^{-3} for the molecular gas. Both our conclusions and those of Mashian et al. (2013) are completely consistent with the structure described by PDR models.

PDRs are clouds of molecular gas associated with star-forming regions, as they are often found near young massive O and B stars, acting as the source of the FUV photons that determine the temperature and chemical composition of the gas (Meijerink et al., 2007). Schematically, in a PDR the increasing extinction (A_V) with depth into the cloud

creates a layer-structure, where the surface of the cloud with $A_V \sim 1$ is dominated by H^+, C^+ and OI. As the gas becomes more self-shielded against the dissociating FUV photons deeper in ($A_V \sim 2-4$), layers of HI and H_2 form and a transition region of C^+, C and CO is present. At the centre of the cloud, the molecular gas is so opaque that the chemistry and heating are dominated by cosmic rays. Hence, the [CII] fine structure line probes the surface of a PDR where $A_V \lesssim 1$ and $T \gtrsim 100\,\mathrm{K}$, while CO traces the core of the cloud. To derive detailed physical parameters from the PDR models therefore requires spatially resolved observations of different species such as C, C^+, CO, O, H_2, polycyclic aromatic hydrocarbons and dust continuum emission (e.g. Hollenbach & Tielens, 1999; Orr et al., 2014).

Implications of the photodissociation region structure

The structure of the gas in PDRs allows for different [CII] and CO(1–0) excitation temperatures. The physical parameters for the ISM in low- and high-z galaxies predicted by basic PDR models can be compared with observed data in a diagnostic diagram (Figure 2.12) first presented by Wolfire et al. (1989) and updated by e.g. Stacey et al. (1991a, 2010) and Hailey-Dunsheath et al. (2010). The diagram has the advantage of plotting ratios where the lensing magnification factors for high-z sources, beam-filling factors for low-z sources and filling factors for the PDRs (which are unknown, but assumed the same for [CII] and CO(1–0)) are divided out. It can be used to roughly estimate the strength of the FUV field and the gas density. One has to be cautious using this diagram, as the FIR luminosity can contain strong contributions from other sources not associated with PDRs (e.g. AGN tori).

The SPT sample is ideal in this respect as [CII] has been measured for 17 out of 20, and low-J CO for 11 (see Table 2.1) of these sources, so the CO luminosities for our sources (unlike the comparison samples) do not depend on uncertain scaling factors. The SPT sample is the most complete high-z sample included in this diagram. The comparison sample is also integrated over entire galaxies enabling a fair comparison to the SPT sample.

The PDR model used in this diagram (Kaufman et al., 1999) models a plane-parallel slab divided into a number of zones of different depths. The intensities are modeled for a parameter space of the FUV field strength (G_0) in units of the local Galactic interstellar radiation field (the 'Habing Field', $1.6 \times 10^{-3}\,\mathrm{ergs\ cm^{-3}s^{-1}}$; Kaufman et al. 1999) in the range $10^{-0.5} \leq G_0 \leq 10^{6.5}$ and the gas densities in the range $10\,\mathrm{cm^{-3}} \leq n \leq 10^7\,\mathrm{cm^{-3}}$. The emission from different species depends on the density, the field strength and the depth into the cloud. Hailey-Dunsheath et al. (2010) assume that 70% of the [CII] emission originates from PDRs (see also § 2.5.2), meaning that the points would move slightly down in Figure 2.12 if this was corrected for.

By comparing the SPT data points with the PDR model tracks in Figure 2.12, we obtain a rough estimate of the radiation field strength and the gas density of $100 < G_0 < 8000$ and $10^2\,\mathrm{cm^{-3}} < n < 10^5\,\mathrm{cm^{-3}}$ (see Table 2.2). These values are consistent with the ones found in previous samples of DSFGs (e.g. Stacey et al., 2010). They imply PDR surface temperatures of $300 - 500\,\mathrm{K}$ (Fig. 2 of Kaufman et al., 1999). As these surface temper-

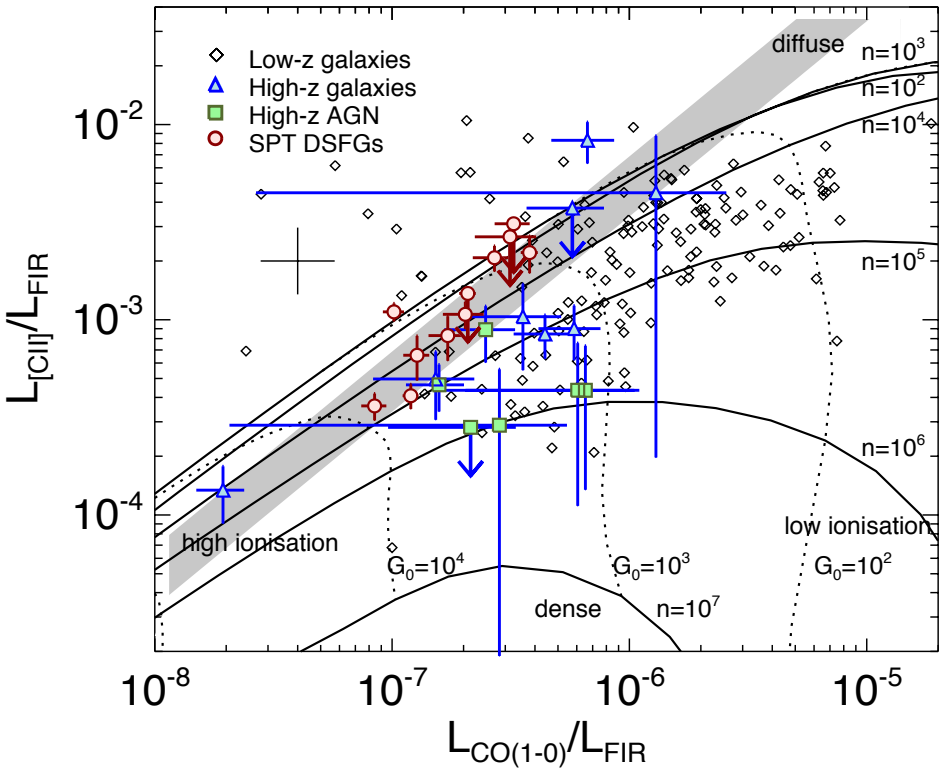

Figure 2.12: $L_{[\mathrm{CII}]}/L_{\mathrm{FIR}}$ vs $L_{\mathrm{CO}(1-0)}/L_{\mathrm{FIR}}$ for the SPT sources and the low and high-z comparison sample. The figure (e.g. Wolfire et al., 1989; Stacey et al., 2010) compares the values of the strength of the radiation field G_0 and the density n for low and high-z sources. The diagram is independent of lensing magnification factors for high-z source and beam filling factors for low-z sources as both the [CII] and CO(1–0) emission is normalised by the FIR luminosity. The typical error bar is represented by the black cross. To compare the observations with the model contours Stacey et al. (2010) assume that 70% of the [CII] emission originate from PDRs. The grey shaded area represents the 1σ spread of the $L_{[\mathrm{CII}]}/L_{\mathrm{CO}(1-0)}$ ratio in the SPT sample.

atures are representative for regions up to $A_V \sim 2$, they cover most of the [CII] emitting region. They are consistent with other derivations of the gas temperatures (see § 2.5.1). If the densitity exceeds the [CII] critical density, these temperatures also represent $T_{\rm ex,[CII]}$, which would imply optically thin [CII] (Fig. 2.11). However, in half of our sources, the densities are below the critical densities, so a range of opacities up to unity remains possible.

Sizes of PDRs

Comparing the $L_{\rm FIR}/\mu$ for the SPT sources[11], which lie in the range $(1.1 - 21.9)\mu^{-1} \times 10^{12}\,{\rm L}_\odot$, with the local starburst galaxy M82 ($L_{\rm FIR}\sim (2.3-3.2)\times 10^{10}\,{\rm L}_\odot$, Rice et al. 1988 and Colbert et al. 1999) show the significant difference in $L_{\rm FIR}$ at high and low redshifts. Using this comparison and estimates of G_0 for each SPT DSFG, we estimate approximate sizes of the PDRs populating the galaxies, following Stacey et al. (2010). For this, we assume the molecular clouds are randomly mixed with young stellar clusters, acting as the radiation sources, within the galaxy (Wolfire et al., 1990). Assuming this structure, the relationship between the average G_0, the total size of the PDRs (D, diameter) and the total luminosity ($L_{\rm FIR}$) of the source is given by $G_0 \propto \lambda L_{\rm FIR}/D^3$ (Stacey et al., 2010) for a short mean free path (λ) and $G_0 \propto L_{\rm FIR}/D^2$ for large mean free path of the FUV photons (see Wolfire et al., 1990). To estimate the approximate sizes, we read off G_0 and $L_{\rm FIR}$ for the SPT DSFGs from Figure 2.12, and scale these with the values obtained for M82 ($G_0 \sim 1000$ Lord et al. 1996, $L_{\rm FIR}\sim 2.8\times 10^{10}\,{\rm L}_\odot$, average of the values determined by Rice et al. 1988 and Colbert et al. 1999), assuming the same mean free path for the SPT sources and M82. The exact size of the PDR region in M82 is rather uncertain with reported sizes ranging from 300 pc (Joy et al., 1987) to 600 pc (Carlstrom & Kronberg, 1991). For consistency with Stacey et al. (2010), we will assume $D \sim 300\,{\rm pc}$. We warn that differential lensing (if significant, see § 2.3.2) could affect the positions of the sources in Figure 2.12 leading to different estimations of G_0 and therewith the sizes. The radii we estimate are listed in Table 2.2, along with our estimated G_0 and n. An estimate of the source radii from lens modelling is available for four sources in Table 2.2. The estimated radii of the PDRs, while fairly uncertain, are comparable to the source sizes determined by the lens models.

A rough estimate of the size ranges occupied by the molecular gas is given in Table 2.2 as well. These sizes are estimated using the molecular gas mass estimated from $L'_{\rm CO(1-0)}$. Using low and high CO-to-H_2 conversion factors often used in the literature of $\alpha_{\rm CO} = 0.8\,{\rm M}_\odot\,({\rm K\,km/s\,pc^2})^{-1}$ (see section 2.4.2, Downes & Solomon (1998)) and $\alpha_{\rm CO} = 2\,{\rm M}_\odot\,({\rm K\,km/s\,pc^{-2}})^{-1}$ (e.g. Swinbank et al. 2011), we estimate sizes of the molecular gas regions making the simplistic assumption that the gas is uniformly distributed in a sphere with radius R and density n as listed in Table 2.2. The sizes estimated using this method are quite uncertain as we do not take into account non-uniform density profiles or non-unity volume filling factors of the gas. They are roughly consistent with both the sizes obtained from the PDR model, and the more accurate sizes derived from the lens models. We note that these kpc-scales are close to the typical sizes of host galaxies, and could be

[11] See §2.3.2 for a discussion on the lensing magnification factor μ in our sample.

Source	G_0	n	R(PDR)	$R_{1/2}$(lens model)	R($L'_{CO(1-0)}$)	μ
		cm^{-3}	kpc	kpc	kpc	
SPT0113-46	10^3	10^3	$0.6-1.1$	—	$0.85-1.16$	—†
SPT0345-47	10^4	5×10^4	$0.4-0.7$	—	$0.39-0.52$	—†
SPT0346-52	8×10^3	10^5	$0.7-1.5$	0.59 ± 0.03	$0.18-0.24$	5.4±0.2
SPT0243-49	5×10^3	10^3	$0.4-0.6$	—	$0.85-1.15$	—†
SPT0418-47	10^3	100	$0.7-1.5$	1.07 ± 0.17	$2.26-3.07$	21.0±3.5
SPT0441-46	8×10^3	10^4	$0.3-0.5$	—	$0.36-0.49$	—†
SPT2103-60	10^3	100	$0.7-1.4$	—	$1.69-2.30$	—†
SPT2146-55	5×10^3	10^4	$0.5-0.8$	—	$0.42-0.56$	—†
SPT2147-50	5×10^3	10^4	$0.4-0.6$	—	$0.33-0.45$	—†
SPT0551-50	10^2	100	$1.0-2.6$	—	$1.40-1.89$	—†
SPT0538-50	10^2	100	$1.7-5.9$	1.07 ± 0.25	$2.46-3.34$	20.9 ± 4.2

Table 2.2: The first column contains the names of the sources for which both [CII] and low-J CO lines have been detected. The second and third columns list G_0 and n for the sources determined from the PDR models in Figure 2.12. Note that especially n can be very uncertain as the models are very degenerate in this part of the diagram. Column four gives the size range determined using the short and long mean free path assumed by Stacey et al. (2010). The fifth column lists the radii for the sources which have lens models (Hezaveh et al. 2013), and the sixth column gives the range in sizes of the molecular gas estimated from the molecular gas mass range given by $\alpha_{CO} = (0.8-2)\,M_\odot\,(K\,km/s\,pc^2)^{-1}$. The last column lists the lensing magnification factor from Hezaveh et al. (2013); SPT0529-54 is not included in this table as low-J CO lines have not been observed for this source. The sources marked with †, we have assumed a mean of $\langle\mu\rangle = 14.1$ (see §2.3.2).

easily spatially resolved, especially given the lensing magnification, allowing detailed future studies of their spatial distributions.

Other contributions to the [CII] emission

The [CII] emission integrated over an entire galaxy will contain contributions from regions with different physical conditions such as XDRs, CRDRs, shock dominated regions, diffuse warm gas, HII regions, and PDRs. Above, we have assumed that observed [CII] emission in the SPT DSFGs is dominated by emission from PDRs on molecular cloud surfaces (e.g. Stutzki et al., 1988; Stacey et al., 1993). We now consider the possible contributions from the alternative [CII] emitting regions in increasing order of importance.

In the vicinity of an AGN, supplying X-ray radiation, we expect XDRs. X-ray photons penetrate deeper into the volume of the interstellar clouds than the FUV photons in PDRs as the absorption cross sections are smaller for X-ray energies. As argued in § 2.4.1 and 2.4.4, the SPT sample does not show evidence for strong AGN activity, and XDR contributions are therefore expected to be negligible.

In CRDRs, the gas heating and chemistry are controlled through interactions with high-energy particles. As the energy density in cosmic rays is low compared to photons, CRDRs are thought to trace the dense, innermost regions of giant molecular clouds (GMCs), rather than the outer surfaces where [CII] emission is assumed to be more prevalent (Viti et al., 2013). We therefore assume the CRDR contribution to be negligible.

Turbulence and shocks have been suggested by Appleton et al. (2013) to be an additional source of [CII] emission. They suggest that this mechanism should be present in highly turbulent conditions such as colliding galaxies and the early stages of galaxy-disc build up. However, for low turbulent velocities, it becomes difficult to distinguish between this mechanism and low-density PDRs. The extreme $L_{[\mathrm{CII}]}/L_{\mathrm{FIR}}$ ratios Appleton et al. (2013) found for the intergalactic filament in Stephan's Quintet are $\sim 30\times$ higher than those observed in the SPT sample. Smaller shock-ionised regions may still contribute significantly to the observed [CII] emission. However, it would be difficult to explain the relatively narrow spread in the observed [CII] to CO ratio if a range of such shock-ionised regions would be a frequent occurence in our SPT sources. We therefore do not expect this mechanism to be important in our samples.

The [CII] emission could also originate from the diffuse warm low density medium in between the GMCs. Spatially resolved [CII] and CO observations are required to differentiate between the PDR and diffuse components. Observations of another lensed DSFGs, HLSJ091828.6+514223 at $z = 5.243$ (Rawle et al., 2014), do show that the [CII] and CO(1–0) have a consistent structure and velocity profile, though the resolution may not go down to the scales of the GMCs (a few hundred pc). Observations of [CII] and CO at spatial resolutions of $\sim$50 mas are required to constrain this diffuse component in our DFSGs.

HII regions surround young O and B stars which emit Lyman continuum photons with energies exceeding the ionisation energy of hydrogren (13.6 eV). Abel (2006) explore the contribution of [CII] emission from HII regions for a wide range in temperature, ionisation parameter (U) and electron density, and find that at least 10%, and sometimes up to

50-60% of the total [CII] emission comes from within the HII regions. Observations of other fine structure lines that only trace HII regions are required to determine the exact contribution from HII regions. Oberst et al. (2006, 2011) used the observed [CII]/[NII] 205 μm ratio in the Carina nebula to constrain the contribution from HII regions to 30%. This technique has since also been applied to high redshift objects (Ferkinhoff et al., 2011; Decarli et al., 2014).

2.5.3 The [CII]/FIR luminosity deficit

Several studies have reported a 'deficit' in the ratio of the [CII] line strength to the FIR luminosity ratio ($L_{[\mathrm{CII}]}/L_{\mathrm{FIR}}$) for LIRGs with $L_{\mathrm{FIR}} \gtrsim 10^{11}\,\mathrm{L}_{\odot}$ (e.g. Malhotra et al. 1997, Luhman et al. 1998, Maiolino et al. 2009; Stacey et al. 2010; Graciá-Carpio et al. 2011; Sargsyan et al. 2012). Various physical explanations for this trend have been proposed, including an increased ionisation parameter (Malhotra et al., 2001; Abel et al., 2009; Graciá-Carpio et al., 2011), collisional de-excitation of [CII] (Appleton et al., 2013) and non-PDR contributions to the FIR luminosity (Luhman et al., 2003), possibly from AGN (Sargsyan et al., 2012).

Stacey et al. (2010) argued that the lower [CII]/FIR ratio can be explained by the fact that the star-formation in local ULIRGs is confined and vigorous (leading to high G_0), while in the most distant objects, the star-formation is very large-scale, but of lower intensity (i.e. lower G_0). In PDR models, the [CII]/FIR ratio is inversely proportional with G_0. Contrary to the FIR luminosity, which scales linearly with G_0, the [CII] luminosity increases only slowly with G_0. This is because in the observed density regime, the C^+ column density scales only with dust extinction, while the emissivity is only weakly dependent on G_0 since the gas temperature is above the excitation potential of 92 K. This leads to a "saturation effect" of the [CII] emission at high luminosity in nearby ULIRGs, while the FIR remains unsaturated. This is consistent with a recent study by Díaz-Santos et al. (2014) exploring the difference in the [CII]/FIR luminosity deficit between the extended and compact (nuclei) regions in nearby LIRGs, revealing a larger deficit in the [CII]/FIR luminosity ratio for the compact regions than for the extended regions. The 'deficit' is mostly confined to the innermost compact regions, while [CII] to FIR luminosity ratio for the extended regions is similar to that found in the extended disks of normal star-forming galaxies.

A similar saturation effect would also occur when the [CII] line becomes (nearly) optically thick. The line then reaches its maximum brightness, in the sense that any additional incoming ionising photons will not increase the brightness of the line further. However the cooling of these additional ionising photons may still continue through optically thin processes, notably the dust continuum. An alternative or additional way of decreasing the [CII] to FIR luminosity ratio is therefore to have optically thick [CII] and optically thin dust continuum emission. The higher density in the more compact regions may then increase the probability of the [CII] to become optically thick.

Finally we note that the [CII] to FIR 'deficit' at high luminosities is also reported for other fine structure lines such as [OI], [OIII], [NII] and [NIII], indicating that this 'deficit'

is a general aspect of all FIR fine structure lines, regardless of their origin in the ionised or neutral phase of the interstellar medium (e.g. Graciá-Carpio et al., 2011; Farrah et al., 2013).

2.6 Conclusions

We have presented the first uniformly selected [CII] survey of lensed DSFGs covering the redshift range $z = 2.1 - 5.7$. We have detected [CII] for 17 out of 20 sources, 11 of which are also observed and detected in low-J CO lines. This sample facilitates statistical studies of the ISM at high redshift. Our main results and conclusions are:

1. We fit single or double Gaussian functions to the CO and [CII] velocity profiles, and find consistent velocity profiles in 13 out of 14 CO detections with ALMA. This suggest that differential lensing is not significant in these cases, and is consistent with the idea that the [CII] and CO(1–0) emitting gas are spatially associated.

2. The line luminosity ratio of the [CII] and CO(1–0) detections for the SPT sources is $\sim 5200 \pm 1800$, which agrees with the first reported ratio by Crawford et al. (1985). The values derived from the SPT sample are consistent with both low-z and high-z comparison samples, but with significantly smaller dispersion. This is presumably due to the homogeneity of the SPT selection and followup observations and absence of any known AGN-dominated sources, which have lower [CII] to CO(1–0) ratios.

3. The SPT sample covers the same spread in the $L_{[\mathrm{CII}]}/L_{\mathrm{FIR}}$ ratio as the $L_{\mathrm{FIR}} \gtrsim 10^{11}\,\mathrm{L}_{\odot}$ sources in both our low-z and high-z comparison samples. AGN-dominated sources increase the scatter towards lower $L_{[\mathrm{CII}]}/L_{\mathrm{FIR}}$ ratios in the comparison sample.

4. We investigate the origin of the [CII] emission using the observed $L_{[\mathrm{CII}]}/L_{\mathrm{CO(1–0)}}$ ratio, and conclude that the observed ratio is best described by a medium of [CII] and CO(1–0) emitting gas with $T_{\mathrm{ex,[CII]}} > T_{\mathrm{ex,CO(1–0)}}$, optically thick CO ($\tau_{\mathrm{CO(1–0)}} > 1$), and low to moderate [CII] optical depth ($\tau_{[\mathrm{CII}]} \lesssim 1$). The structure of PDRs allows for such different excitation temperatures of the [CII] and CO(1–0) emitting gas. Interestingly the PDR models converge to this [CII] to CO(1–0) ratio for densities below $10^5\,\mathrm{cm}^{-3}$.

5. We revisit the $L_{[\mathrm{CII}]}/L_{\mathrm{FIR}}$ 'deficit' observed for sources with $L_{\mathrm{FIR}} \gtrsim 10^{11}\,\mathrm{L}_{\odot}$, which has been explained as a "saturation effect" of the [CII] emission in compact regions with higher G_0 factors. An alternative or additional explanation for this saturation effect is (nearly) optically thick [CII] emission. In this case the [CII] line becomes saturated and reaches the maximum [CII] brightness, while cooling via the FIR continuum emission continues. The variation in the $L_{[\mathrm{CII}]}/L_{\mathrm{FIR}}$ ratio is therefore dominated by the variation in L_{FIR} rather than $L_{[\mathrm{CII}]}$.

6. We determine the FIR luminosity for both the SPT sample and the comparison low and high-z sample in a consistent way, adding 11 SPT DSFGs to the $L_{[\mathrm{CII}]}/L_{\mathrm{FIR}}$ vs $L_{\mathrm{CO(1–0)}}/L_{\mathrm{FIR}}$ plot in Figure 2.12. We compare the SPT sample with PDR models and estimate the radiation field strength and average gas density to be in the range $100 < G_0 < 8000$ and $10^2\,\mathrm{cm}^{-3} < n < 10^5\,\mathrm{cm}^{-3}$.

The reliability of [CII] as a tracer of star formation rate (SFR) has been explored by e.g. De Looze et al. (2014). They show that [CII] is a good tracer for the SFR except for low metallicity sources. Determining the metallicity using other fine structure lines such as [NII], [OII] and [OIII], and the contribution to the [CII] emission from HII regions (Croxall et al., 2012) are therefore key in finding the most reliable tracer of SFR in nearby and distant galaxies. Thus far, all high-z fine structure line measurements have been unresolved, but thanks to lens shear of gravitationally lensed sources it will become possible to resolve structures down to 100 pc scales (Swinbank et al., 2010). Hence, for PDRs of the sizes estimated here, future observations with ALMA will be able to spatially resolve [CII] emission and other fine structure lines and provide new insight into how [CII] emission traces gas.

Acknowledgments

We thank the referee for a very thorough reading of the paper and constructive comments which have significantly improved the paper. We are grateful to Javier Gracia-Carpio for providing us with a sample of low- and high-z sources with both [CII] and CO detections, ideal for comparison with the SPT sample of high-z sources. We also thank Gordon Stacey and Padelis Papadopoulos for lively, educational, and profitable discussions. We thank Göran Pilbratt, *Herschel* Project scientist for the allocated *Herschel* SPIRE Directors Discretionary Time and Richard George and Ivan Valtchanov for helpful comments on the *Herschel* SPIRE FTS data reduction.

This publication is based on data acquired with the Atacama Pathfinder Experiment (APEX). APEX is a collaboration between the Max-Planck-Institut fur Radioastronomie, the European Southern Observatory, and the Onsala Space Observatory. This paper makes use of the following ALMA data: ADS/JAO.ALMA#2011.0.00957.S, ADS/JAO.ALMA# 2011.0.00958.S and ADS/JAO.ALMA#2012.1.00844.S. ALMA is a partnership of ESO (representing its member states), NSF (USA) and NINS (Japan), together with NRC (Canada) and NSC and ASIAA (Taiwan), in cooperation with Republic of Chile. The Joint ALMA Observatory is operated by ESO, AUI/NRAO and NAOJ. The Australia Telescope Compact Array is part of the Australia Telescope National Facility which is funded by the Commonwealth of Australia for operation as a National Facility managed by CSIRO. This research has made use of the NASA/IPAC Extragalactic Database (NED) which is operated by the Jet Propulsion Laboratory, California Institute of Technology, under contract with the National Aeronautics and Space Administration. This research has made use of NASA's Astrophysics Data System Bibliographic Services

This material is based on work supported by the U.S. National Science Foundation under grant No. AST-1312950. The South Pole Telescope is supported by the National Science Foundation through grant PLR-1248097. Partial support is also provided by the NSF Physics Frontier Center grant PHY-1125897 to the Kavli Institute of Cosmological Physics at the University of Chicago, the Kavli Foundation and the Gordon and Betty Moore Foundation grant GBMF 947.

Short name	Source	R.A.	Dec.
		J2000	
SPT2311-54	SPT-S J231124-5450.5	23:11:23.94	-54:50:30.0
SPT2319-55	SPT-S J231922-5557.9	23:19:21.67	-55:57:57.8

Table 2.3: Source names are based on positions measured with the SPT (Mocanu et al. 2013). Source positions are based on the ALMA 3 mm continuum data.

Appendix

2.7 New redshifts

All but two sources observed in [CII] were published by Weiß et al. (2013), where the full source names are listed. The two new sources were selected from the list of Mocanu et al. (2013), and observed as part of our ongoing ALMA Cycle 1 project to determine redshifts of additional SPT DSFGs. Table 2.3 lists their full names and ALMA band 3 continuum positions. The redshift of SPT2319-55 is based on detections of CO(5-4) and CO(6-5), while the redshift of SPT2311-54 is based on CO(5-4) confirmed by our APEX [CII] detection (Figure 2.1).

2.8 High-z comparison galaxies

Table 2.4 lists the high-z comparison sample.

Source	z	$L_{[CII]}$ [$10^9\,L_\odot$]	$L_{CO(1-0)}$ [$10^6\,L_\odot$]	L_{FIR} [$10^{12}\,L_\odot$]	T_d [K]	lensing mag.	[CII] and CO reference
SMMJ2135-0102 (Eyelash)	2.33	5.8 ± 1.3	0.8 ± 0.04	40.9 ± 9.1	36.0 ± 2.3	32.5 ± 4.5	Swinbank et al. 2010; Ivison et al. 2010
SDP.130	2.63	< 65	10.1 ± 2.9	17.5 ± 3.6	38.6 ± 2.0	6 ± 1	Valtchanov et al. 2011; Frayer et al. 2011
SDP.81	3.04	275 ± 39	22.0 ± 5.0	33.1 ± 6.3	40.0 ± 1.8	25 ± 7	Valtchanov et al. 2011; Frayer et al. 2011
PSSJ2322+1944†	4.12	< 8.0	6.1 ± 2.6	28.6 ± 10.2	55.8 ± 6.1	5.4 ± 0.3	Benford et al. in prep., Carilli et al. 2002a
SDP.141	4.24	60 ± 9	38.7 ± 4.6	66.2 ± 17.7	46.1 ± 3.2	$10 - 30$	Cox et al. 2011
BRI1335-0417†	4.41	15.7 ± 2.5	4.4 ± 0.8	17.7 ± 4.9	51.3 ± 4.4	—	Wagg et al. 2010; Carilli et al. 2002b
ALESS65.1	4.45	3.2 ± 0.4	< 1.11	3.12 ± 1.40	44.3 ± 5.1	—	Swinbank et al. 2012; Huynh et al. 2014
BR1202-0725★†	4.69	15.8 ± 1.8	5.4 ± 0.7	34.1 ± 8.4	55.1 ± 4.3	—	Wagg et al. 2012; Carilli et al. 2002b
HDF850.1	5.19	7.5 ± 0.8	2.2 ± 0.5	1.7 ± 1.6	29.9 ± 7.7	$1.5 - 1.7$	Neri et al. 2014; Walter et al. 2012
HLSJ091828.6+514223	5.24	82.4 ± 2.3	43.0 ± 3.3	97.5 ± 24.4	48.7 ± 3.0	8.9 ± 1.9	Rawle et al. 2014
SDSSJ1044-0125†	5.78	1.6 ± 0.4	1.6 ± 0.3	5.6 ± 5.1	59.8 ± 25.8	—	Wang et al. 2013
SDSSJ2310+1855†	6.00	8.7 ± 1.4	12.1 ± 1.0	20.0 ± 14.5	61.8 ± 20.7	—	Wang et al. 2013
HerMESFLS3	6.34	14.9 ± 3.1	4.6 ± 1.5	29.9 ± 9.6	52.8 ± 6.2	2.2 ± 0.3	Riechers et al. 2013
SDSSJ1148+5251†	6.42	4.6 ± 0.5	6.4 ± 0.7	9.8 ± 6.7	60.9 ± 15.7	—	Maiolino et al. 2005
IRASF10026+4949	1.12	25.8 ± 3.2	< 0.8	—	—		Stacey et al. 2010
3C368	1.13	9.3 ± 1.5	< 1.9	—	—		Stacey et al. 2010; Evans et al. 1996
SMMJ123634.51+621241.0	1.22	14.4 ± 2.0	3.76 ± 0.12	—	—		Stacey et al. 2010; Frayer et al. 2008
MIPSJ142824.0+352619	1.32	10.5 ± 3.1	1.10 ± 0.03	—	—		Hailey-Dunsheath et al. 2010; Iono et al. 2006
SDSSJ100038.01+020822.4†	1.83	10.6 ± 2.4	3.10 ± 0.17	—	—		Stacey et al. 2010; Aravena et al. 2008
SWIREJ104704.97+592332.3	1.95	20.0 ± 2.6	8.9	—	—		Stacey et al. 2010
SWIREJ104738.32+591010.0	1.96	12.1 ± 3.2	3.5	—	—		Stacey et al. 2010
BRI0952-0115 †	4.44	4.5 ± 2.6	0.43 ± 0.11	—	—		Maiolino et al. 2009; Guilloteau et al. 1999
LESSJ033229.4-275619†	4.76	9.9 ± 1.5	1.05 ± 0.25	—	—		De Breuck et al. 2011; Coppin et al. 2010
SDSSJ0129-0035†	5.78	1.8 ± 0.3	2.8 ± 0.5	—	—		Wang et al. 2013
SDSSJ2054-0005†	6.04	3.3 ± 0.5	2.7 ± 0.6	—	—		Wang et al. 2013
ULASJ1319+0950†	6.13	4.4 ± 0.9	3.5 ± 0.7	—	—		Wang et al. 2013
CFHQSJ0210-0456†	6.43	0.30 ± 0.04	< 0.88	—	—		Willott et al. 2013
ALESS61.1	4.42	1.48 ± 0.23	—	3.0 ± 1.4	43.7 ± 5.1	—	Swinbank et al. 2012

Table 2.4: The high-z sources in the comparison sample. All but one sources (ALESS61.1) have published [CII] and CO detections. The observed CO luminosities have been scaled to CO(1–0) luminosities using the ratios from Stacey et al. 2010. The first 14 sources have a sufficient amount of photometric data published for the determination of L_{FIR} and T_d, while the remaining are unconstrained. ALESS61.1 has good photometry, but no published low-J CO observations.

★ A sum of the [CII] and CO emission from the north and south source.

† AGN dominated source.

Chapter 3

The Mysterious Morphology of MRC0943-242 as Revealed by ALMA and MUSE

Bitten Gullberg[1,6] Carlos De Breuck[1], Matthew D. Lehnert[2], Joël Vernet[1], Roland Bacon[3], Guillaume Drouart[4] Bjorn Emonts[5], Audrey Galametz[6], Rob Ivison[1,7], Nicole P. H. Nesvadba[8], Johan Richard[3], Nick Seymour[9], Daniel Stern[10], Dominika Wylezalek[11]

[1]European Southern Observatory, Karl Schwarzschild Straße 2, 85748 Garching, Germany [2]Institut d'Astrophysique de Paris, UMR 7095, CNRS, Université Pierre et Marie Curie, 98bis boulevard Arago, 75014, Paris, France[3]CRAL, Observatoire de Lyon, CNRS, Université Lyon 1, 9 avenue Ch. André, 69561, Saint Genis-Laval Cedex, France[4]Department of Earth and Space Science, Chalmers University of Technology, Onsala Space Observatory, 43992, Onsala, Sweden[5]Centro de Astrobiología (INTA-CSIC), Ctra de Torrejón a Ajalvir, km 4, 28850 Torrejń de Ardoz, Madrid, Spain[6]Max-Planck-Institut für Extraterrestrische Physik, Giessenbachstraße 1, 85748 Garching, Germany[7]Institute for Astronomy, The University of Edinburgh, Royal Observatory, Blackford Hill, Edinburgh EH9 3HJ, UK[8]Institut d'Astrophysique Spatiale, CNRS, Université Paris-Sud, Bat. 120-121, F-91405 Orsay, France[9]International Centre for Radio Astronomy Research, Curtin University, Perth WA 6845, Australia[10]Jet Propulsion Laboratory, 4800 Oak Grove Drive, Pasadena, CA 91109, USA [11]Department of Physics and Astronomy, Johns Hopkins University, 3400 N. Charles St, Baltimore, MD, 21218, USA

Abstract

We present a pilot study of the $z = 2.923$ radio galaxy MRC0943-242, where we for the first time combine information from ALMA and MUSE data cubes. Even with modest integration times, we disentangle an AGN and a starburst dominated set of components. These data reveal a highly complex morphology, as the AGN, starburst, and molecular gas components show up as widely separated sources in dust continuum, optical continuum and CO line emission observations. CO(1–0) and CO(8–7) line emission suggest that there is a molecular gas reservoir offset from both the dust and the optical continuum that is located ∼90 kpc from the AGN. The UV line emission has a complex structure in emission and absorption. The line emission is mostly due to i) a large scale ionisation cone energised

by the AGN, *ii*) a Lyα emitting bridge of gas between the radio galaxy and a heavily star-forming set of components. Strangely, the ionisation cone has no Lyα emission. We find this is due to an optically thick layer of neutral gas with unity covering fraction spread out over a region of at least ~ 100 kpc from the AGN. Other, less thick absorption components are associated with Lyα emitting gas within a few tens of kpc from the radio galaxy and are connected by a bridge of emission. We speculate that this linear structure of dust, Lyα and CO emission, and the redshifted absorption seen in the circum-nuclear region may represent an accretion flow feeding gas into this massive AGN host galaxy.

3.1 Introduction

Powerful high-z radio galaxies (HzRGs), defined as having $L_{3\,GHz} > 10^{26}\,\mathrm{W\,Hz^{-1}}$ and $z > 1$, are unique markers of the most active galaxies in the early Universe, showing signatures of both luminous AGN activity and vigorous starbursts. HzRGs are extremely luminous in both the mid-IR (Ogle et al., 2006; Seymour et al., 2007; De Breuck et al., 2010) and the sub-mm waveband (Archibald et al., 2001; Reuland et al., 2004; Drouart et al., 2014). This has been interpreted as evidence of high black hole accretion rates, combined with high star-formation rates (SFRs). HzRGs are some of the most massive galaxies known at any redshift, with $M > 10^{11}\,\mathrm{M_\odot}$ of stars (Seymour et al., 2007; De Breuck et al., 2010), confirming prior indications of their large masses from the tight correlation of the observed near-IR Hubble K-z diagram for these sources (Lilly & Longair, 1984; Eales et al., 1997; De Breuck et al., 2002). In order to be so luminous, the black holes in these galaxies must be massive. Given that stellar bulge mass correlates with black hole mass (e.g. Tremaine et al., 2002), it is therefore no surprise that the most powerful radio galaxies reside in the most massive stellar hosts.

Disentangling the AGN and starburst components requires excellent sampling of the spectral energy distribution (SED). Seymour et al. (2012) illustrate the decomposition of the starburst and AGN components using 3.5 – 850 μm photometry in the $z = 2.16$ radio galaxy, PKS 1138-262, showing that both have roughly equal contributions to the IR luminosity. Disentangling the SED of HzRG is the main goal of our HErschel Radio Galaxy Evolution (HERGÉ) project (Drouart et al., 2014). The 71 HzRG targeted in the HERGÉ project are uniformly distributed across $1.0 < z < 5.2$ with a range of radio powers. *Spitzer*, *Herschel*, SCUBA and LABOCA data suggest that the sources targeted in the HERGÉ project have very high far-IR (FIR) luminosities ($\sim 10^{13}\,\mathrm{L_\odot}$, Drouart et al. 2014), but the data do not have high enough spatial resolution to pinpoint the AGN host galaxies as the source of the FIR emission. Resolution is important, as spectral decomposition alone is probably insufficient to understand the evolutionary state of HzRGs.

Previous single sources studies of HzRGs have revealed that these systems have highly complicated morphologies, e.g. with line emission separated from the continuum emission. In several systems (e.g. 4C41.17 and 4C60.07, TXS0828+193, and B3 J2330+3927), most of the gas and dust emission originates from the companion rather than the AGN host galaxy, while others (e.g. MRC0114-211, MRC0156-252, and MRC2048-272) show no

evidence for a companion (De Breuck et al., 2003, 2005; Ivison et al., 2008, 2012; Nesvadba et al., 2009; Emonts et al., 2014). These observations confirm that spectral decomposition alone is insufficient to understand the evolutionary state of HzRGs, sufficiently high spatial resolution to separate out individual emission components is also crucial.

The sub-arcsecond spatial resolution of ALMA will undoubtedly reveal a much more complex composition of AGN and starburst dominated sources than previously thought. To illustrate this point, we conducted a pilot study of MRC0943-242 at $z = 2.9$, where we combine - for the first time - sensitive ALMA 235 GHz and VLT/MUSE observations. This combination allows us to trace the spatially-resolved distributions of the ionisation state of the warm ionised medium (T$\sim 10^4$ K) through the UV emission and absorption lines (e.g. CIV), the warm neutral gas (T$\sim$ few $\times 10^3$ K) through Lyα absorption, and the dense molecular gas as probed by the high-J CO transitions. Through this combination it is possible to get a comprehensive picture of several important phases of gas in the interstellar medium and haloes of HzRGs.

MRC0943-242 is an ultra steep spectrum radio source with a spectral index of $\alpha = -1.5$ between $1.4 - 30$ GHz and shows no evidence of a spectral curvature within this range (Carilli et al., 1997; Emonts et al., 2011). MRC0943-242 is located in a proto-cluster (with an over density of almost 5σ; Wylezalek et al., 2013) surrounded by many nearby companions detected in Lyα with known redshifts (Venemans et al., 2007) and a giant quiescent Lyα halo with a diameter of ≥ 100 kpc - extending far beyond the radio structure (Villar-Martín et al., 2003). A deep absorption trough in the Lyα emission line suggests the presence of a large amount of neutral gas (Röttgering et al., 1995). Based on a 1.5 Å-resolution spectrum Röttgering et al. (1995) conclude that the saturated absorption trough is due to a reservoir of neutral hydrogen (HI) situated within the HzRG itself. They determine a HI column density of $N_{\rm HI} = 10^{19}\,{\rm cm}^{-2}$ in the absorber. Using the same observational set-up, Binette et al. (2000) determine a HI column density similar to that of Röttgering et al. (1995) and a CIV column density of $N_{\rm CIV} = 10^{14.5\pm0.1}\,{\rm cm}^{-2}$. However based on Voigt-profile fittings to the absorption troughs in both the Lyα and CIV emission lines Binette et al. (2000) conclude that the reservoir of gas causing the absorption features is not situated within the HzRG, but rather due to a low metallicity ($Z = 0.01\,{\rm Z}_\odot$), low density gas in the outer halo at a redshift of $z = 2.29202 \pm 0.0002$. They propose that this gas is a remnant of gas expelled from the HzRG during the initial starburst. Though such a starburst is expected to enrich the expelled gas more than what is observed for MRC0943-242, Jarvis et al. (2003) still favoured this scenario. Based on numerical simulations by Bekki (1998), which predict that the outer regions of galactic halos should be less metal-rich, Jarvis et al. (2003), as Binette et al. 2000, favoured a picture where the shell lies in the halo to explain its low metallicity. Furthermore, by comparing MRC0943-242 with another HzRG (MRC0200+015), they argue that the age of the system can have an influence on the metallicity of the shells. They conclude that the metallicities of absorption shells surrounding HzRG vary from galaxy to galaxy and from shell to shell. This implies that the shells must be enriched by a variety of processes. With UVES data with a spectral resolution of 25000-40000 Jarvis et al. (2003) identified three additional weaker absorbing components of different HI column densities.

In this paper, we present a study of MRC0943-242, where we for the first time combine relatively short ALMA sub-millimetre (submm) observations with MUSE optical observations. This ALMA-MUSE-pilot study reveals an even more complex morphology of MRC0943-242 than previously seen with star-formation taking place far outside the AGN host galaxy. In § 4.2 we present our ALMA submm and MUSE optical observations. The results of these observations are given in § 4.3 and are analysed and discussed in § 3.4. In § 3.5 we speculate as to the origin and role of the substructures and in § 4.5 we summarise our conclusion.

3.2 Observations

3.2.1 ALMA observations

The Atacama Large Milimeter/submilimeter Array (ALMA) cycle 1 observations in Band 6 were carried out on 2014 April 29 for 3 min on-source time with 36 working antennas. The four 1.875 GHz spectral windows were tuned to cover the frequency ranges 233.6 − 237.1 GHz and 248.6 − 252.3 GHz. We used the Common Astronomy Software Applications (CASA) and the supplied calibration script to calibrate the data, produce the data cube and moment 0 maps. The average $T_{\rm sys}$ was $\sim$ 80 K and the average precipitable water vapour 1.3 mm. The quasar J1037-2934 was used as bandpass calibrator and results in an astrometric accuracy of 4 mas. The UV coverage was sparse, but uniform over $\sim$ 400 kλ. In order to search for CO(8–7) line emission at $\nu_{\rm rest}$ = 921.80 GHz, which is within the frequency range at $z = 2.923$, we subtracted the continuum in the UV-plane by fitting a first-order polynomial to all four spectral windows, as no strong line emission is contaminating the continuum. As our data are limited by the signal-to-noise ratio (S/N), we use a natural weighting (robust parameter of 2). This results in a $0\farcs7 \times 0\farcs6$ beam with pa = 75° and an RMS of 0.1 mJy for the continuum. We binned the line data to 10 km/s which has an RMS of 1.7 mJy. As objects are detected up to 12″ from the phase centre, we applied a primary beam correction on all our maps and spectra.

3.2.2 MUSE observations

Multi Unit Spectroscopic Explorer (MUSE) (Bacon et al., 2010) observations were obtained on 2014 February 21, during the first commissioning run of the instrument (see Bacon et al., 2014) on VLT/UT4. This one hour observation taken under $\sim$ 1″ seeing was split into three 20 min exposures taken at 45, 135 and 225 degree position angle with a small dithering offset to minimise the effect of systematics. In order to observe the Lyα line of MRC0943-242 at 476.5 nm, we used the extended wavelength range mode (i.e. without second order blocking filter), resulting in a observed wavelength range of 460–935 nm). These data were taken specifically to compare MUSE observations with previous observations with other instruments of this well-studied source. Thus it serves as a pilot study for using MUSE to study HzRGs. All data were processed with the version 1.0 of the MUSE pipeline

(Weilbacher et al., 2012) to produce a fully calibrated and sky subtracted data cube. Finally, the cube was cleaned for sky subtraction residuals with the Principal Component Analysis (PCA) based algorithm ZAP developed by Soto et al (in prep.). To analyze the line emission and to remove a few artefacts in the data, we continuum subtracted the cubes around specific emission lines such as Lyα.

3.2.3 Previous supporting *Spitzer* observations

MRC0943-242 was observed among 68 other HzRG in the redshift range $1 < z < 5.2$ in a large *Spitzer* survey (Seymour et al., 2007). MRC0943-242 was observed with the Infrared Array Camera (IRAC), the Infrared Spectrograph (IRS) and the Multiband Imaging Photometer (MIPS) on *Spitzer*, which cover the wavelengths 3.6 μm, 4.5 μm, 5.8 μm, 8.0 μm, 16 μm, 24 μm, 70 μm and 160 μm (see Seymour et al. 2007 for details on the observations and reductions). At 3.6 and 4.5 μm, we use the deeper IRAC observations (Fig. 3.1) obtained as part of the Clusters Around Radio Loud AGN project (CARLA; Wylezalek et al., 2013).The IRAC and MIPS observations reveal that the continuum emission associated with the dust features in our ALMA data is very diffuse and faint (see section § 3.3.3 for more details). In support of the *Spitzer* data, we also examined the observations of MRC0943-242 from Keck and *HST/NICMOS* (van Breugel et al., 1998; Pentericci et al., 2001). We do not see any evidence at sub-arcsecond resolution of multiple components.

3.3 Results

Combining for the first time ALMA submm observations with MUSE optical observations reveals an even more complex morphology than seen previously: with multiple components where only the AGN dominated component is visible in all wavelengths. Figure 3.1 shows the IRAC 3.6 μm and 4.5 μm image, Lyα and HeII moment-0 maps in a colour image observed with MUSE and the 235 GHz map observed with ALMA. The Lyα moment-0 map shows a bright source at the position of the HzRG (hereafter Yggdrasil) and an additional component to the South-West (SW), connected by a bridge of Lyα emission (hereafter Bifrost). Yggdrasil is visible in all four images, while Bifrost splits up into three components in the 235 GHz observations (hereafter Freja, Thor and Odin). Thor is visible in the IRAC 3.6 μm and 4.5 μm images with an extension towards both Freja and Odin. A CO(8–7) emitting component (hereafter Loke) is located even further to the SW than Freja, Thor and Odin. The complex morphology is illustrated by the schematic overview in Fig. 3.1 and additionally shows the positions of the radio lobes, and the CO(8–7) emission at the position of Yggdrasil and Loke. We now discuss each of these phases in detail.

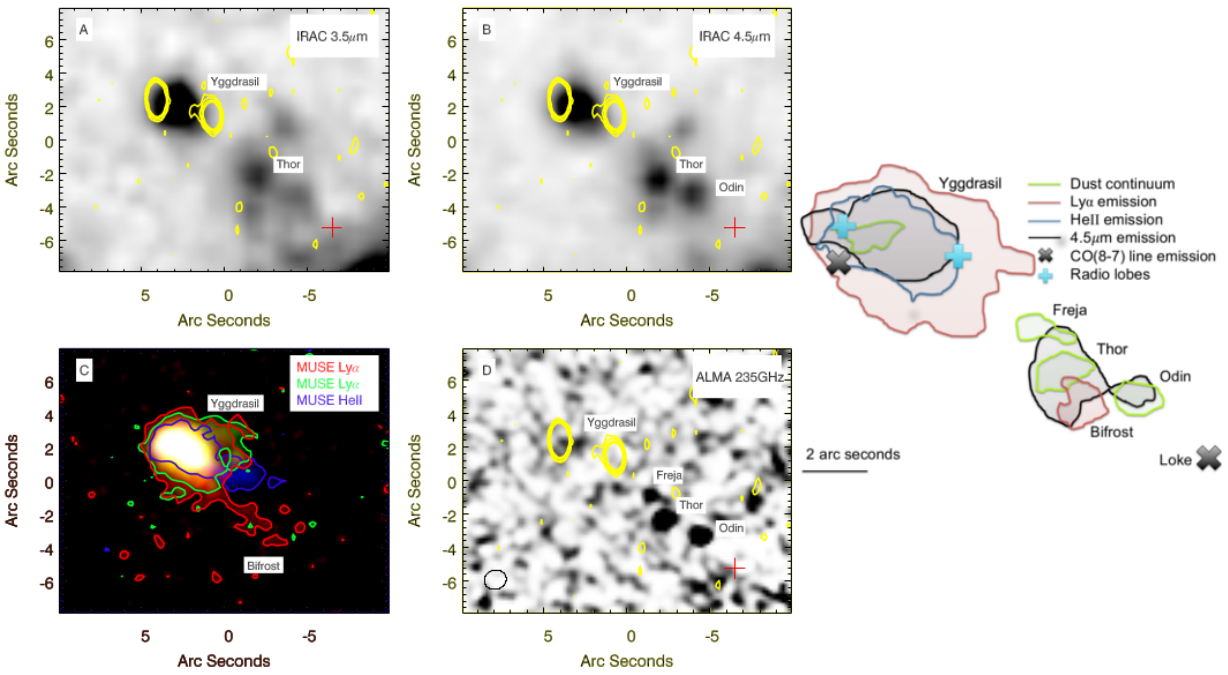

Figure 3.1: Overview of the IRAC (3.6 μm and 4.5 μm), MUSE (Lyα and HeII) and ALMA (235 GHz) maps. *Panel A and B*: The IRAC 3.6 μm and 4.5 μm images showing both Yggdrasil and Thor. Both IRAC images have a spatial sampling of 0.61″/pixel. *Panel C*: A red (Lyα), green (Lyα) and blue (HeII) image composed of moment-0 maps of the MUSE cube, which have a spatial sampling of 0.2″/pixel. The red Lyα moment-0 is summed over $\lambda_{\rm obs} = 4768.8 - 4776.2$ Å(see red bar in panel A of Fig. 3.5), the green Lyα moment-0 is summed over $\lambda_{\rm obs} = 4754.3 - 4758.8$ Å (see green bar in panel A of Fig. 3.5) and the blue HeII moment-0 map is summed over $\lambda_{\rm obs} = 6422.5 - 6430.0$ Å. The red Lyα reveals a bridge of emission connecting Yggdrasil and Bifrost (see § 4.3), while the green Lyα emission shows extended emission to the west. The Blue HeII shows an extended tail of HeII emission towards the WSW, which is not seen in Lyα emission (see § 3.3.2). *Panel D*: The ALMA dust continuum map reveals weak dust emission at the position of the AGN, but strong dust emission in three aligned components 48-65 kpc SW of the AGN. The mm continuum flux density of all four continuum sources are extracted with apertures of; Yggdrasil: 2.6″ × 1.7″, Freja: 1.8″ × 1″, Thor; 1.9″ × 1.5″ and Odin: 1.2″ × 1.4″. *Far right*: Schematic overview of the multi-wavelength components detected in MRC0943-242. VLA 4.5 GHz radio observations have been overlaid in yellow contours in Panel A, B and D. The plotted contour levels are for -3σ, $2 \times 3\sigma$, $3\sqrt{2} \times 3\sigma$, $5\sqrt{2} \times 3\sigma$, which is the same for all VLA contour levels through out the paper. The position of Loke is marked with a red cross in Panel A, B and D.

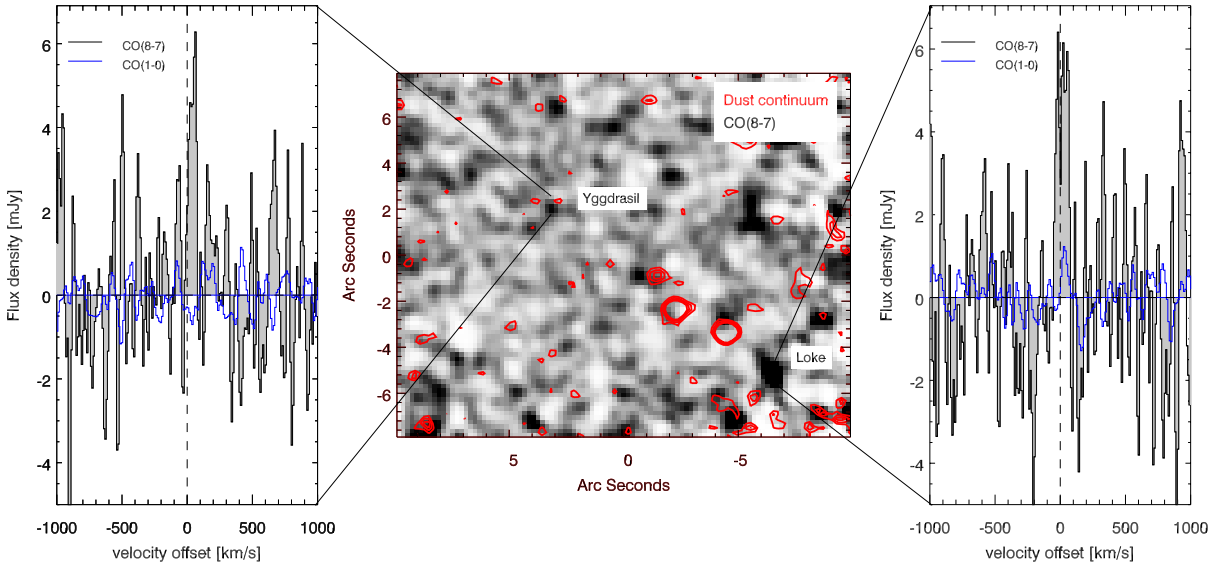

Figure 3.2: The ALMA cube shows CO(8–7) emission at two positions in the data cube: at the location of Yggdrasil and to the SW in an isolated component: Loke. *Middle panel:* The grey scale image of the CO(8–7) emission overlaid with the ALMA dust continuum contours. Note the increase in noise towards the edges due to the primary beam correction. *Left and Right:* The CO(8–7) velocity profiles for both Yggdrasil (left) and Loke (rigth). Surprisingly the CO(8–7) lines only have a small offset from the HeII systemic redshift (dashed vertical line). The spectra are extracted from a beam-sized area at the position of the emission, and have RMSs of 1.5 mJy and 1.0 mJy respectively. Both detections are unresolved at the S/N of our data.

3.3.1 Surprising dust and molecular gas distribution

Dust continuum emission

Yggdrasil shows up in the ALMA submm observations as a weak dust continuum emission source at 235 GHz, with an extracted flux density over the region of 0.8 ± 0.2 mJy (see Table 3.4). However, the vast majority of the 235 GHz dust emission originates from three components (Freja, Thor and Odin) aligned along a "string" shifted $48 - 65$ kpc towards the SW relative to the position of Yggdrasil (see Fig 3.1). Table 3.4 lists their flux densities extracted using CASA.

Considering the number counts of > 0.5 mJy sources at 235 GHz of $\sim 2 \times 10^4\,\mathrm{deg}^{-2}$ (Laurent et al., 2005), and the size of the area within the $8\farcs7$ radius from Yggdrasil to Odin, we expect to find 0.37 sources with $F_{235\,GHz} > 0.5$ mJy. We detect four sources within this area; the probability that these four sources are unrelated is therefore 0.37^4, or 2%. The probability that these four sources are associated to MRC0943-242 is thus 98%.

Molecular emission lines

Searching the ALMA cube for molecular gas tracers, we find CO(8–7) emission at two different positions. One at the position of Yggdrasil and one ~ 90 kpc SW of Yggdrasil. The 3.5σ CO(8–7) detection at the position of Yggdrasil (see Fig 3.2) is only shifted by $\sim +43$ km/s from the HeII systemic redshift. Fitting a single Gaussian to this narrow velocity profile yields a FWHM of 47 ± 13 km/s, and a velocity integrated line flux of 0.33 ± 0.06 Jy km/s. The other 3.5σ CO(8–7) detection is located ~ 90 kpc SW of Yggdrasil (Loke, see Fig. 3.1 and 3.2). Surprisingly, Loke is not detected in any dust continuum nor optical counter parts. Like the CO(8–7) line detected at the position of Yggdrasil, this CO(8–7) line is narrow with a FWHM of 53 ± 17 km/s, and only shifted by $\sim +16$ km/s from the HeII systemic redshift (see Fig.3.4). The RMS of the CO(8–7) spectrum for Yggdrasil is 1.8 mJy and 2.1 mJy for Loke. This small difference is due to a combination of the primary beam correction (affecting only Loke) and continuum subtraction residuals (affecting only Yggdrasil, as no continuum is detected in Loke).

To verify the reality of the CO(8–7) emission, ensuring that these CO(8–7) lines are not rare but insignificant noise peaks in the cube, we create 13 moment-0 maps at different frequencies in the cube by collapsing a velocity ranges in the cube of 180 km/s. This corresponds to three times the average FWHM of two CO(8–7) lines and is the same velocity width as for the CO(8–7)-moment-0 map (see Fig. 3.2). From these, we select the brightest areas in each moment-0 map and extract the spectrum from the cube for each of these areas and ensure that there is no overlap between velocity regions. From this we find 81 unique peaks for which we extract over the full $233.5 - 236.5$ GHz frequency range. We fit a Gaussian profile to the brightest peak in each spectrum and determine the S/N in each spectrum. Only two spectra show a peak of intensity with a S/N of ~ 3 and a FWHM of ~ 70 km/s which could resemble a real line. The chance of detecting a line such as Loke within 27 ± 6 km/s from Yggdrasil within our 4000 km/s bandwidth is $27/4000 = 0.67\%$. In addition, the probability of finding a ~ 50 km/s wide line like

Yggdrasil and Loke is 50/4000 = 1.25%. The combined probability of finding the observed CO(8–7) configuration in Loke and Yggdrasil is therefore only 0.84%.

Searching the archival Australian Telescope Compact Array (ATCA) data for Yggdrasil (see Emonts et al. 2011 for more details about the data reduction and data characteristics) by re-shifting the velocities to the redshift ($z = 2.92296 \pm 0.00001$ see § 3.3.2) used for this work, we find tentative CO(1–0) line emission at a 2.8σ level at the position of Loke (see Fig. 3.2), consistent with the existence of a large molecular gas reservoir. The tentative detection of CO(1–0) emission and the CO(8–7) to CO(1–0) line flux ratio of ~ 0.03 would imply the presence of a low excitation molecular gas reservoir. No CO(1–0) emission was found at the position of Yggdrasil (see Fig. 3.2). This agrees with the expectation that we should find more highly excited gas near a powerful radio-loud AGN (e.g. Weiß et al., 2007)

Unfortunately the ATCA observations are limited by the large beam and low S/N, and it is therefore not possible to determine whether or not CO(1–0) emission originates from the dust continuum sources, a free molecular gas component in the halo or both. In an attempt to explore if an extended CO(8–7) component is present, we applied a larger beam to the ALMA 235 GHz data. Unfortunately, tapering the ALMA 235 GHz data and convolving them with a beam comparable to that of ATCA did not produce useful results, as our shallow ALMA observation do not contain sufficient short baselines. We plan JVLA CO(1–0) and ALMA [CI]2-1 observations at arc-second spatial resolution to pinpoint the exact location and determine the characteristics of the molecular gas reservoir.

No CO(8–7) line emission is observed at the positions of Freja, Thor and Odin. We therefore take the 3σ upper limit of the line emission at these positions to be 3 times the RMS of the spectra extracted with the same region sizes as for the continuum emission (see Table 3.1).

3.3.2 Ionised gas

The MUSE spectrum of Yggdrasil (Fig. 3.3) detects a rich variety of ionised gas tracers. Overall, our spectrum is consistent with the Keck spectrum of Vernet et al. (2001), but now provides full spatial information over the large field ($1' \times 1'$) of view of MUSE. Table 3.1 lists the velocity and integrated fluxes for the nine emission lines detected at the position of Yggdrasil. The flux is determined by integrating the spectral line profile within 3σ of the noise. For our analysis, we adopt the redshift of HeII integrated over the peak of the continuum emission as the systemic velocity, as it is the brightest non-resonant line in our spectra. The HeII emission line is best fitted by a Lorentzian profile, with a centre corresponding to a redshift of 2.92296 ± 0.00001 and a FWHM of 862 ± 30 km/s. The flux within 3σ is given in Table 3.1. The other high ionisation lines have profiles and redshifts similar to that of HeII (Table 3.1) and Fig. 3.4.

The Lyα (λ1215.7 Å) line is by far the brightest and most extended emission line in the MUSE data cube. It peaks at the position of the AGN, but extends out to 80 kpc (see bottom panel of Fig. 3.5). Such extended Lyα haloes have been detected in several other HzRGs (e.g. van Ojik et al., 1996; Reuland et al., 2003b; Swinbank et al., 2015). The Lyα

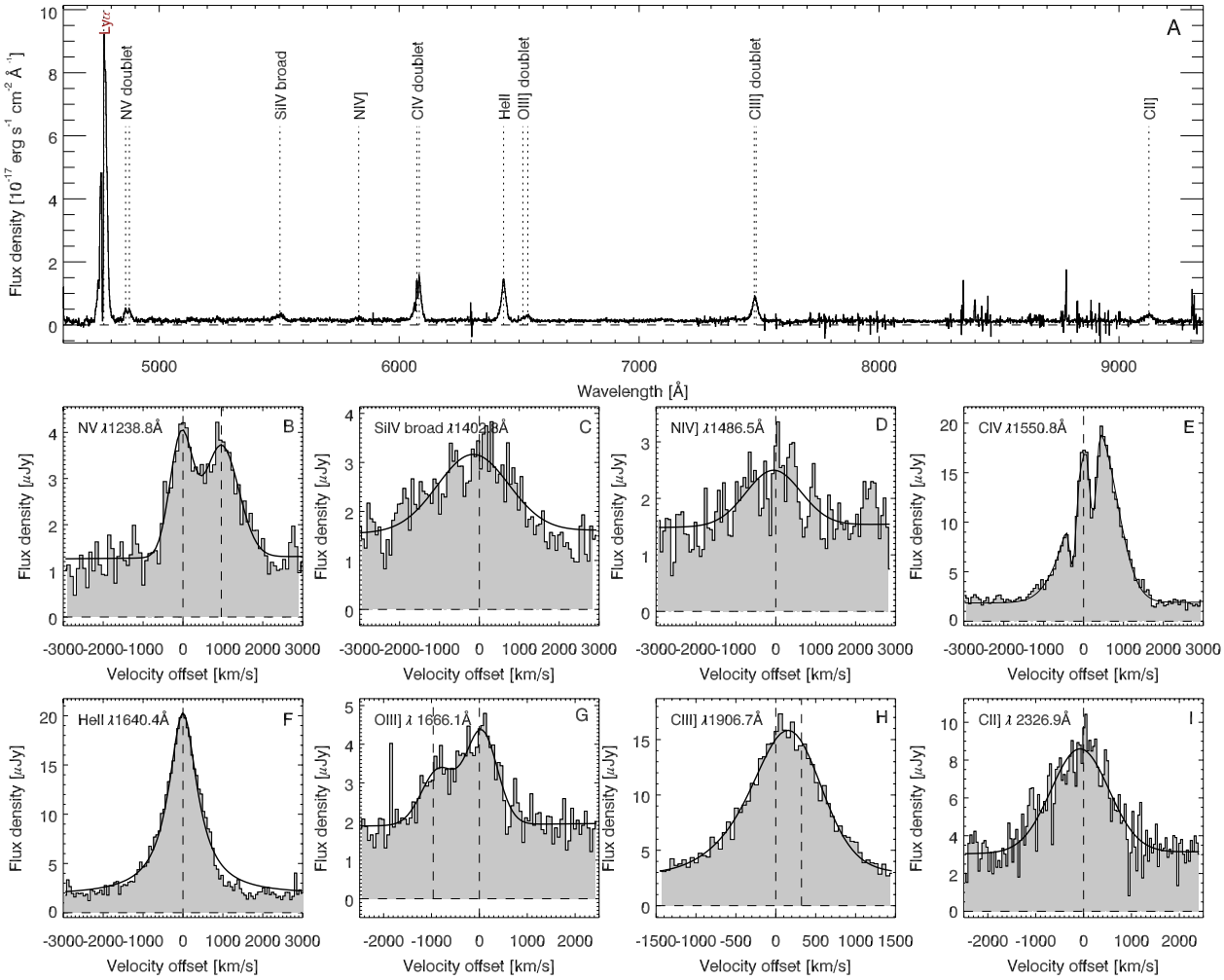

Figure 3.3: The top panel shows the full MUSE spectrum for Yggdrasil. All detected lines (other than Lyα) are indicated with a black dotted lines, and the velocity profiles are shown in Panel B-I. The velocity profiles for NV, SiIV, NIV], CIV, HeII, OIII], CIII, and CII] assume HeII as the systemic redshift. The CIV emission line shows absorption troughs like those of the Lyα emission line.

MUSE				
Line	$\lambda_{\rm rest}$ Å	$\lambda_{\rm obs}$ Å	Line flux $10^{-16}\,{\rm erg/cm^{-2}/s}$	FWHM km/s
Yggdrasil				
Lyα	1215.7	4768.9 ± 0.2	26.60 ± 0.25	1592 ± 44
NV	1238.8, 1242.8	$4859.1 \pm 0.6, 4875.5 \pm 0.9$	0.90 ± 0.04	1803 ± 174
SiIV	1402.8	5500.1 ± 1.1	0.60 ± 0.04	2493 ± 214
NIV]	1486.5	5830.3 ± 1.9	0.27 ± 0.04	1764 ± 370
CIV	1548.2, 1550.8	$6073.9 \pm 1.5, 6072.2 \pm 1.4$	4.34 ± 0.06	1410 ± 188
HeII	1640.4	6435.2 ± 0.2	3.04 ± 0.05	862 ± 30
OIII]	1660.8, 1666.1	$6516.3 \pm 1.4, 6533.8 \pm 2.5$	0.50 ± 0.03	1492 ± 292
CIII]	1906.7, 1908.7	$7479.2 \pm 0.9, 7490.9 \pm 3.1$	2.00 ± 0.06	1734 ± 124
[CII]	2326.0	9122.4 ± 1.0	0.90 ± 0.04	1606 ± 118
Bifrost				
Lyα	1215.7	4769.2 ± 1.1	0.65 ± 0.06	1018 ± 205
ALMA				
Line	$\nu_{\rm rest}$ GHz	$\nu_{\rm obs}$ GHz	SdV Jy km/s	FWHM km/s
Yggdrasil				
CO(8–7)	921.8	234.94 ± 0.1	0.33 ± 0.07	43 ± 13
Loke				
CO(1–0)	115.3	—	< 0.08	< 27
CO(8–7)	921.8	234.96 ± 0.1	0.54 ± 0.10	57 ± 17
Freja, Thor and Odin				
CO(8–7)	921.8	—	< 0.13	—
CO(8–7)	921.8	—	< 0.18	—
CO(8–7)	921.8	—	< 0.16	—

Table 3.1: Velocity integrated fluxes and FWHM of the resonance , fine-structure, and molecular lines for Yggdrasil, in-between Odin and Thor and Loke. The ATCA observations have a beam size $11.5'' \times 9.0''$ and PA 87.5°. The 3σ upper limits on the CO(8–7) line emission for Freja, Thor and Odin are given assuming a FWHM of 50 km/s, i.e. similar to the CO(8–7) lines for Yggdrasil and Loke.

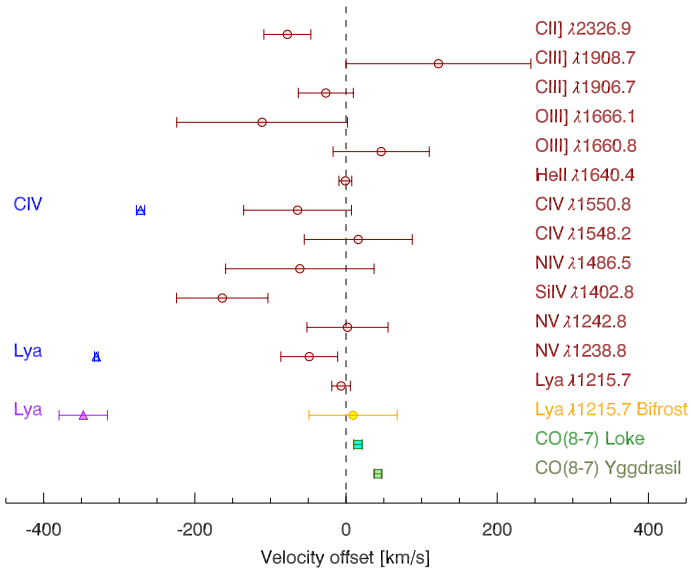

Figure 3.4: The offset of the emission line and absorption features centers from the HeII systemic redshift. Red points are emission lines observed for Yggdrasil. Yellow is the Lyα emission line for Bifrost. Green is the CO(8–7) emission line for Yggdrasil and Loke. Blue and purple are the center of the absorption feature 2. The emitting components are distributed within $\pm$200 km/s of the systemic velocity, while the absorbers are all blue shifted by $\sim$350 km/s.

halo in MRC0943-242 shows a linear filament, Bifrost, connecting Yggdrasil with the two brightest dust continuum components (Thor and Odin), strongly suggesting that they are physically connected (see Fig 3.5). The peak intensity of Bifrost is $\sim$ 18 times fainter than that for the Lyα detection of Yggdrasil (see panel A and D of Fig. 3.5).

The Lyα emission on the nucleus exhibits four absorption features in our data. We denote these absorption features as 1, 2, 3 and 4 where the bluest feature is 1, middle are 2 and 3, and the reddest absorption feature 4 (in accordance with the labelling used by Jarvis et al., 2003, see panel A of Fig. 3.5). Furthermore, component 2 is related to the strong CIV absorption observed against the nucleus (Binette et al., 2000). By centering the Lyα velocity profile at the fitted central velocity of HeII we find that the bottom of the absorption trough is at a redshift off $z_{\rm abs} = 2.91864 \pm 0.00002$. By fitting a Voigt-profile to the absorption trough, we estimate a column density of the neutral gas for component 2 of $N_{\rm HI} = 1.3 \cdot 10^{19}\,{\rm cm}^{-2}$ and a Doppler width of 64 km/s (see Table 3.2) which are comparable to the values determined by Binette et al. 2000. We note that because the line is saturated, this estimate is very uncertain and likely a lower limit to the true value. For components 1, 3 and 4, we find good agreement with the values in Jarvis et al. (2003) for the column densities and velocities.

We observe two absorption troughs in the CIV emission line; Voigt profile fitting to the two features reveals that they are caused by gas on the line of sight at redshift $z_{\rm abs} = 2.91940 \pm 0.00007$ and 2.91945 ± 0.000061 and column densities of $N_{\rm CIV} = 3.4 \cdot 10^{14}\,{\rm cm}^{-2}$ and $= 6.9 \cdot 10^{14}\,{\rm cm}^{-2}$, higher than $3.2 \cdot 10^{14}\,{\rm cm}^{-2}$ found by Binette et al. 2000.

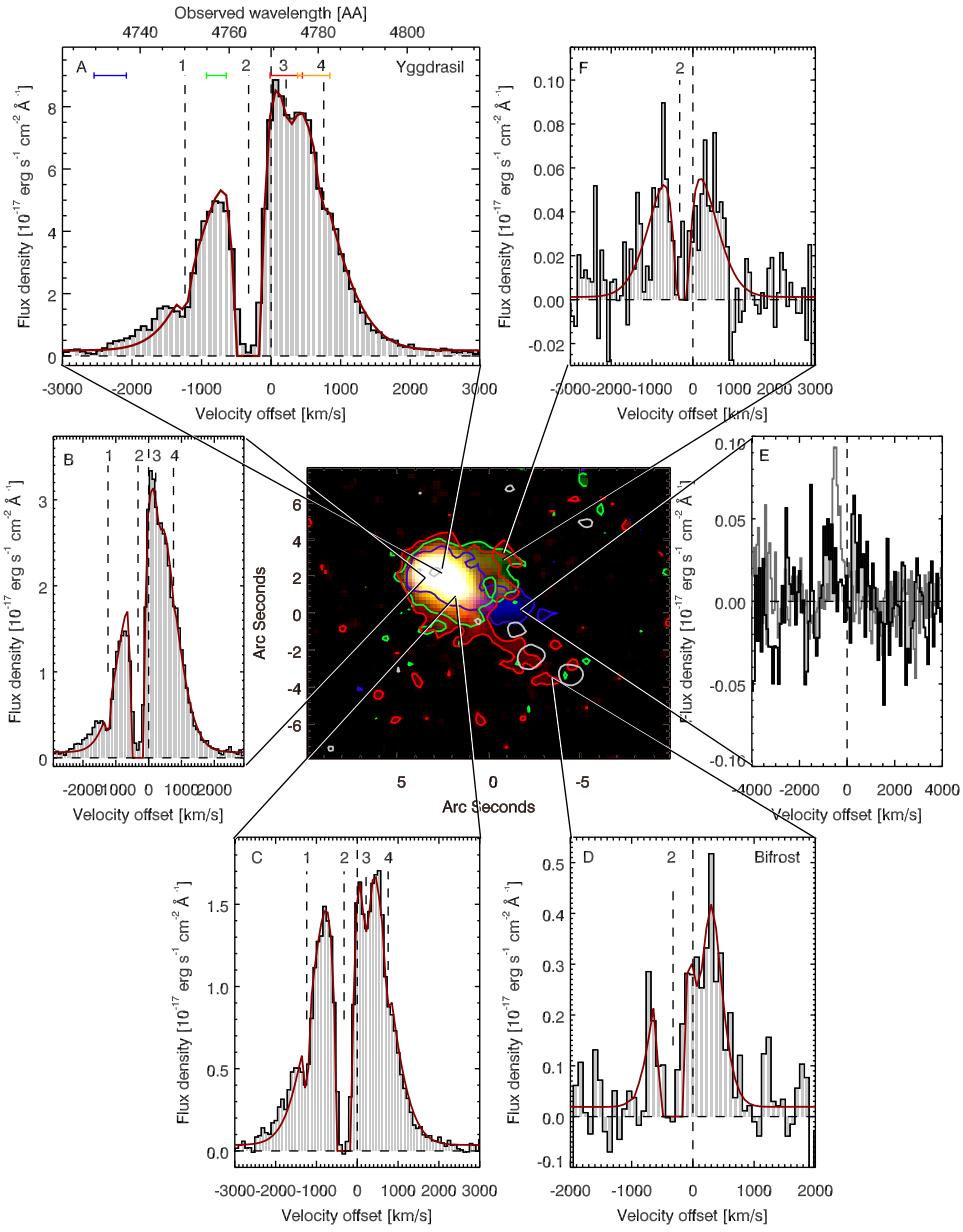

Figure 3.5: Overview of emission and absorption components at different positions around MRC0943-242. *Middle Panel:* Composite Red-Green-Blue image of Lyα and HeII emission (see caption of Fig. 3.1 for more details) with the ALMA 235 GHz contours overlaid in grey. *Panel A:* The Lyα line profile of the full area of Yggdrasil (elliptical aperture of $1.3'' \times 0.7''$), showing all four absorption components. Component 2 is the most prominent and goes to zero intensity at its center. The spectrum has an RMS of $0.3{\times}10^{-17}$ erg s^{-1} cm^{-2} Å^{-1}. The blue, green, red and orange bars above the spectrum shows the range in wavelength the channelmaps in Fig. 3.6 have been summed over. The blue corresponds to panel A, green to panel B, red to panel C and orange to panel C in Fig. 3.6. *Panel B and C:* The Lyα profiles of two areas near the nucleus (circular $0.5''$ apertures) and have RMS of $0.1{\times}10^{-17}$ erg s^{-1} cm^{-2} Å^{-1}. These profiles likewise show signs of all four absorption components. *Panel D:* The Lyα profile of Bifrost (circular $1.2''$aperture and RMS of $0.1{\times}10^{-17}$ erg s^{-1}) showing sign of absorption component 2. *Panel E:* Spectrum extracted at the HeII emitting tail ($0.7''$ aperture), showing no sign of Lyα emission and an RMS of $0.02{\times}10^{-17}$ erg s^{-1} cm^{-2} Å^{-1}. The HeII lines is over-plotted in grey. *Panel F:* The Lyα profile of the western extended Lyα emitting gas ($0.4''$ aperture). All Lyα velocity profiles have been fitted with Voigt profiles superimposed on a Gaussian profile. These fits are shown as the red curves over plotted on the spectra.

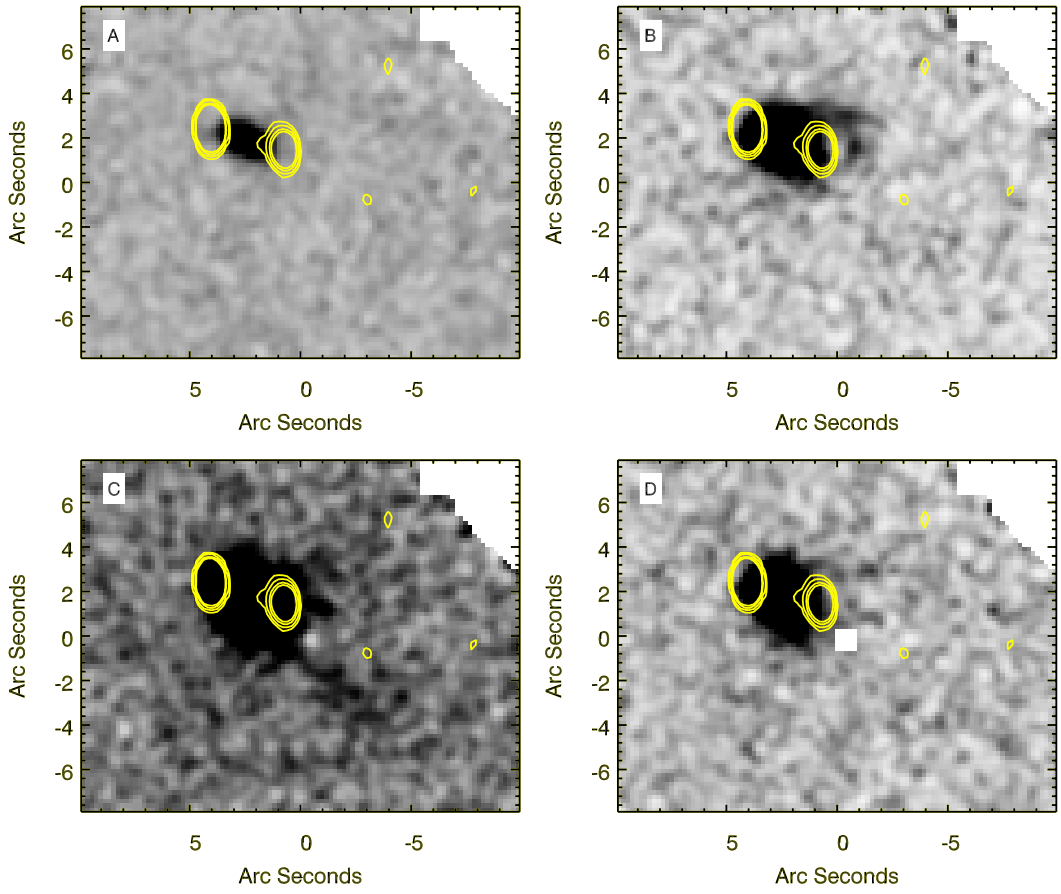

Figure 3.6: Lyα Moment-0 maps summed over the wavelength ranges illustrated with the coloured bars in panel A of Fig. 3.5: *Panel A:* sum over the blue bar ($\lambda_{\rm obs}$ = 4732.5 – 4747.5 Å). *Panel B:* sum over the green bar ($\lambda_{\rm obs}$ = 4754.3 – 4758.8 Å). *Panel C:* sum over the red bar ($\lambda_{\rm obs}$ = 4768.8 – 4776.2 Å). *Panel D:* sum over the orange bar ($\lambda_{\rm obs}$ = 4778.8 – 4793.8 Å) Over-plotted with yellow contours in all panels is the VLA radio map, as a reference.

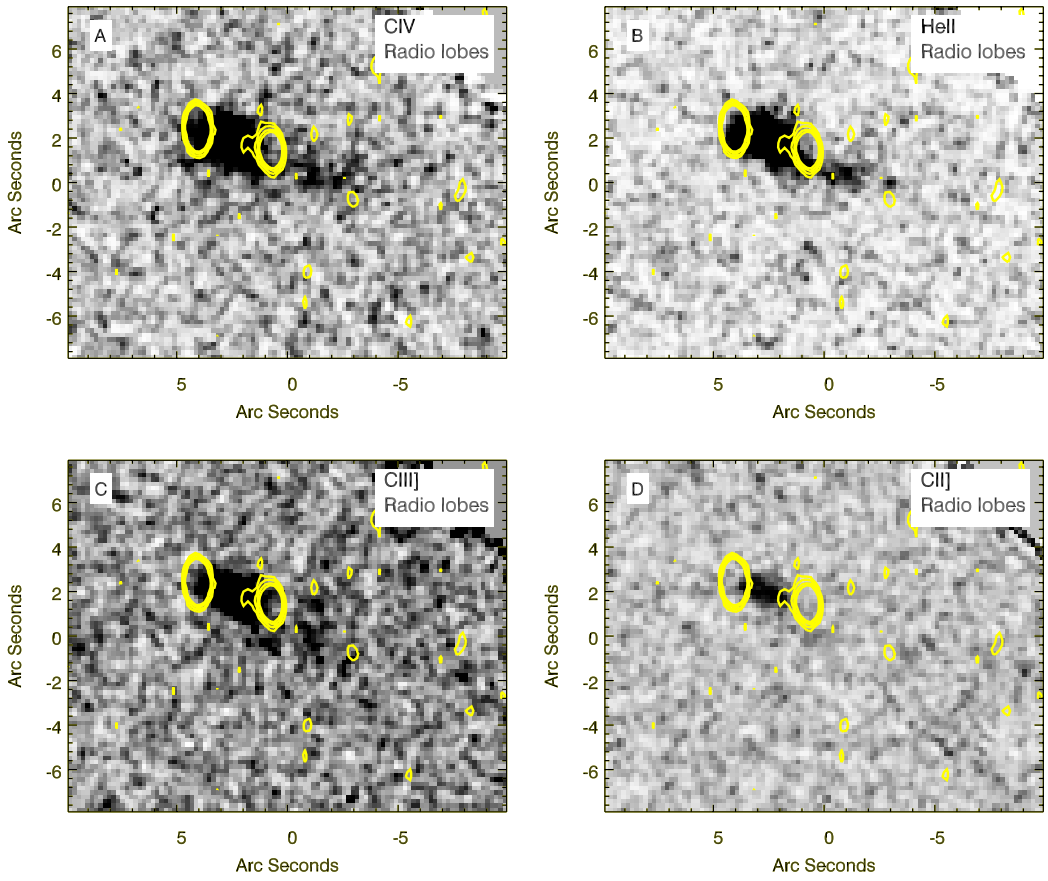

Figure 3.7: Continuum subtracted moment-0 maps of the CIV, HeII, CIII] and CII] emission lines. The continuum is determined from the nearby line free channels for each line. *Panel A:* sum over the CIV emission line for the wavelength range $\lambda_{\rm obs} = 6050 - 6090$ Å. *Panel B:* sum over the HeII emission line for the wavelength range $\lambda_{\rm obs} = 6422 - 6430$ Å and is the same image as the blue colour of the middle panel of Fig. 3.5. *Panel C:* sum over the CIII] emission line for the wavelength range $\lambda_{\rm obs} = 7455 - 7485$ Å. *Panel D:* sum over the CII] emission line for the wavelength range $\lambda_{\rm obs} = 9071 - 9171$ Å. Over-plotted with yellow contours in all panels is the VLA radio map, as a reference.

Line	$N_{\rm HI}$ $\rm cm^{-2}$	b km/s	$z_{\rm abs}$
Yggdrasil			
Lyα absorber 1	$5.0 \cdot 10^{13}$	84	2.90689 ± 0.00032
Lyα absorber 2	$1.3 \cdot 10^{19}$	64	2.91864 ± 0.00002
Lyα absorber 3	$3.7 \cdot 10^{13}$	140	2.92641 ± 0.00023
Lyα absorber 4	$1.7 \cdot 10^{13}$	33	2.93254 ± 0.00007
CIV absorber 2	$3.4 \cdot 10^{14}$	94	2.91940 ± 0.00007
	$6.9 \cdot 10^{14}$	100	2.91945 ± 0.00006
Bifrost			
Lyα absorber 2	$7 \cdot 10^{18}$	—	2.91841 ± 0.00045

Table 3.2: Parameters determined by fitting a Voigt profiles to the absorption troughs. Fits are performed on the absorption troughs in the Lyα line observed for both Yggdrasil and in-between Odin and Thor. The CIV line has been fitted with two Voigt profiles with the same fitting parameters.

Stepping through the cube towards increasing wavelengths reveals the complexity of the emission in the MRC0943-242 system (see Fig. 3.5, 3.6 and 3.7):

• $\lambda_{\rm obs} \sim 4732 - 4747$ **Å:** Considering the Lyα emission line profile at Yggdrasil (see panel A of Fig. 3.5); the emission furthest to the blue side of the line profile is spatially centred around the radio source and approximately within the region containing the radio emission (see also panel A Fig. 3.6).

• $\lambda_{\rm obs} \sim 4747 - 4754$ **Å:** As we move towards the red, over the wavelength range of absorption feature 1, we see strong nuclear emission.

• $\lambda_{\rm obs} \sim 4754 - 4759$ **Å:** Moving further to the red between absorption features 1 and 2, we observe a closed region of bubble-like emission reaching ~ 20 kpc out, surrounding the western radio lobe (see panel B of Fig. 3.6). The absorption components 1 and 2 are visible against this emission across the region of Yggdrasil (see panel A-C of Fig. 3.5).

• $\lambda_{\rm obs} \sim 4759 - 4769$ **Å:** As we step further to the red, through the wavelength range of absorption feature 2, the Lyα emission becomes fainter – down to our surface brightness detection limits. We note that this is in agreement with the Lyα profiles of all the extended emission – when we have sufficient surface brightness to have detectable line emission, we see absorption component 2 which has zero intensity in the line core. This includes the Lyα emission from Bifrost (see panel D in Fig. 3.5) and the CIV emission from Yggdrasil. The absorption component 2 in Bifrost is at a redshift of $z_{\rm abs} = 2.91841 \pm 0.00045$, consistent with that in Yggdrasil (see panel D of Fig 3.5). This suggests that the absorption feature in the spectrum of Bifrost is due to absorption component 2, meaning that absorber 2 has an extent of at least 65 kpc from Yggdrasil. The data suggest a lower column density of absorber 2 in Bifrost of $N_{\rm HI} \sim 7 \cdot 10^{18}\,\rm cm^{-2}$. We warn that this $N_{\rm HI}$ is particularly uncertain due to the low S/N of the data, and the degeneracy between $N_{\rm HI}$ and the b-parameter. Deeper and higher resolution data are required to trace column density variations across the system. We also note that in this wavelength range, we observe high ionisation emission

lines of HeII, CIV, and CIII] from gas extending over 7″ or ~ 60 kpc to the west (see panel F, the green contours of the central panel of in Fig. 3.5 and the CIV and HeII moment-0 maps in panel A and B of Fig. 3.7). Fainter, less extended emission is also observed to the east of the nucleus. Deeper data will be needed to determine the exact distribution of absorption component 2; however, since the line core is black throughout the extend of the cube, we can conclude that it is extended with a unity covering factor.

• $\lambda_{\mathbf{obs}} \sim 4769 - 4776$ **Å:** At wavelengths to the red of absorption feature 2, and containing the absorption feature 3 (see red contours of Fig. 3.5 and panel C in Fig. 3.6), we observe the emission from Bifrost. Where the Lyα emission is sufficiently bright, we see absorption component 3 superposed on the line emission (see panel A-C of Fig. 3.5).

• $\lambda_{\mathbf{obs}} \sim 4779 - 4794$ **Å:** Further to the red - at longer wavelengths than the range of absorption feature 3, component 4 shows up as a small trough (see panel A-C of Fig. 3.5 and panel D of Fig. 3.6) before we again start to see circum-nuclear emission all contained within the radius encompassing the radio lobes.

• $\lambda_{\mathbf{obs}} \sim 6025 - 6125$ and $6422 - 6430$ **Å:** Moving to wavelengths of the CIV and HeII emission, we do not have sufficient S/N to split these lines into velocity channels like for Lyα. Instead, we present line maps of the central parts of these lines in panels A and B of Fig. 3.7. Both lines display a similar morphology, which is also seen (albeit at lower S/N) in CIII] (panel C of Fig. 3.7). We detect a tail of CIV and HeII emission to the WSW (panels A and B of Fig. 3.7); however this tail is not spatially aligned with the Lyα bridge (Bifrost) connecting Yggdrasil with Freja, Thor and Odin. Interestingly, the CIV and HeII tail is not seen in Lyα (see the blue contours of the middle panel and panel E of Fig. 3.5). Fitting a Lorentz profile to this HeII emission line as well yields a redshift of $z = 2.916$ which is consistent with the emission being at the same velocity offset as absorption component 2. This suggest that this CIV and HeII emitting gas is also seen in Lyα, but that this is absorbed completely by component 2.

The large wavelength coverage of MUSE allows us to detect other fine structure lines (see panel B-I of Fig. 3.3). The three doublets NV, OIII] and CIII] are well detected at a $\geq 6\sigma$ level. The NV doublet is spatially resolved and reveals two spectral lines of similar intensity. The OIII] doublet is blended, but there is some indications of the doublet structure with the λ1660.8 Å line being a shoulder in the blue side of the OIII] λ1666.1 Å line. We also detect a broad SiIV component, a weak NIV] line at a 2.3σ level, and a CII] line at a 5.5σ level at the edge of the band. The CII] emission line is a blend of multiple lines, which explains why the line peaks on the red side of λ2326 Å. Table 3.1 lists the line parameters for these fine structure lines over the circum-nuclear region (see Fig. 3.3).

All the emission from NV, SiIV, NIV], OIII], and CII]lies within the region emcompassed by the radio lobes. The CII]emission is a particularly spectacular example as it delineates both the extension and direction of the radio jet and lobes (see panel D of Fig. 3.7).

Instrument	wavelength μm	$S_{\rm Yggdrasil}$ μJy	$S_{\rm Thor}$ μJy	$S_{\rm Loke}$ μJy
IRAC 1	3.6	21.9	9.02	¡2.10
IRAC 2	4.5	36.1	21.0	¡1.32
IRAC 3	5.8	—	—	—
IRAC 4	8.0	30.2	< 21.4	—
MIPS	24	468 ± 40	180 ± 40	—

Table 3.3: The photometric IRAC and MIPS points for Yggdrasil, Thor and Loke after de-blending. Thor is not detected in the IRAC 3 image, however the flux at the position is influenced by an image artefact from a nearby star in the field. Extracting even an upper limit at this position is therefore not possible. Loke is not detected in any of the IRAC images; we quote the 3σ upper limits (Wylezalek et al., 2013).

3.3.3 Stellar mass

The wavelengths covered by *Spitzer* probe the rest-frame near- and mid-IR part of the spectrum, which is believed to be the best tracer of the stellar-mass with almost no contributions from the thermal emission from the AGN (Seymour et al., 2007). Yggdrasil has a well sampled SED with detections at 3.6 μm, 4.5 μm, 8.0 μm 16 μm, 24 μm, and upper limits for 5.8 μm, 70 μm and 160 μm. Seymour et al. 2007 and De Breuck et al. 2010 fit a toy model to these points, composed of four components: an elliptical galaxy composite stellar population (CSP) and three blackbody (BB) components with temperatures of 60 K, 250 K and between 500-1500 K (for more details see Seymour et al. 2007 and De Breuck et al. 2010). This SED fitting results in an H-band stellar luminosity of $L_H^{\rm stellar} = 2.5 \cdot 10^{11}\,{\rm L}_\odot$, which is converted to a stellar mass of $1.7 \cdot 10^{11}\,{\rm M}_\odot$ by assuming a dust-free, passively evolving elliptical galaxy which started its formation at $z = 10$ with no recent episodes of star-formation. The SED allows for a good decomposition of the stellar and hot-dust dominated components, so the derived stellar mass is expected to be reliable (see Seymour et al., 2007, for a more detailed discussion on the uncertainties).

Examining the IRAC 3.6 μm and 4.5 μm image again, now with the knowledge of the presence of Freja, Thor and Odin, we find stellar emission at the position of Thor, with an extension towards Freja and Odin (see Fig. 3.1 top left and Table 3.3). Also for Thor are the stellar and hot-dust emission well separated in the SED. We scale the stellar mass found for Yggdrasil, to the emission seen in the IRAC 4.5 μm map (Table 3.6), yielding a stellar mass of $1.0 \times 10^{11}\,{\rm M}_\odot$. For Loke, we accordingly derive an upper limit to the stellar mass of $\lesssim 6.2 \times 10^9\,{\rm M}_\odot$.

3.3.4 Disentangling the SED

Yggdrasil has a well-sampled SED with IRAC, MIPS, SPIRE (250 μm, 350 μm and 500 μm) and PACS (24 μm, 100 μm and 160 μm) from previous studies (De Breuck et al., 2010; Drouart et al., 2014). The PACS 160 μm image (see Appendix C of Drouart et al., 2014) reveals an elongated source, spanning from the position of Yggdrasil towards Freja, Thor

Component	Position		$S_{235\,\mathrm{GHz}}$
	RA	dec	mJy
Yggdrasil	09:45:32.769	-24.28.49.29	0.8 ± 0.2
Odin	09:45:32.222	-24.28.55.06	2.0 ± 1.0
Thor	09:45:32.386	-24.28.54.05	1.9 ± 0.8
Freja	09:45:32.445	-24.28.52.55	0.6 ± 0.3
Loke	09:45:32.072	-24.28.56.94	< 0.3

Table 3.4: Positions and 235 GHz fluxes for all components of MRC0943-242. As no dust continuum is observed for the position of Loke we infer a 3σ upper limit of the 235 GHz of three times the rms. The uncertainty includes the 15% flux calibration error.

Component	L_{IR} $[10^{12}\,L_{\odot}]$	perc.
Total (Yggdrasil+Freja+Thor+Odin)	17.2	100
Freja+Thor+Odin (SB)	8.4	49
Yggdrasil (AGN)	7.5	43
Yggdrasil (SB)	1.3	8

Table 3.5: Infrared luminosities of each component, determined from our SED presented in Fig 3.8.

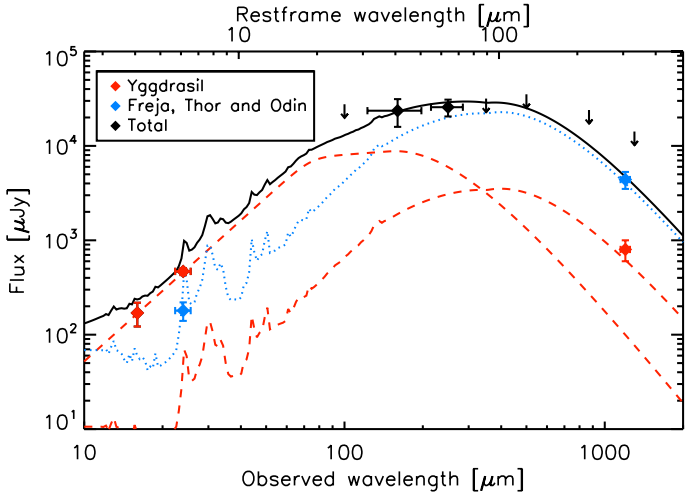

Figure 3.8: The spectral energy distribution of MRC0943-242. The spatial resolution of the ALMA data allows us to disentangle the SED in the AGN heated component (red curve) and star formation heated component (blue curve). The sum of these two components is illustrated by the black curve.

and Odin. Likewise, when returning to the IRAC 3.6 μm and 4.5 μm images (see panel A and B of Fig. 3.1), multiple components show up corresponding to Yggdrasil and Thor (see §3.3.3). While these sources can be separated in the *Spitzer* data, they are blended in the *Herschel* data. However, the high spatial resolution and sensitivity of the ALMA data allows us to disentangle the AGN and star formation heated components in the SED at 235 GHz. We conclude that the star-formation, as probed by the dust emission, is taking place at a distance of 48-65 kpc from the AGN in three smaller aligned components (Freja, Thor and Odin). Table 3.3 lists the de-blended MIPS and IRAC photometry points.

Relying on the method of Drouart et al. 2014 by fitting an SED with AGN and starburst components, we now go further, and use the sub-arcsec resolution provided by the new dust continuum image to further disentangle the relative contribution of AGN and star formation *spatially*. Figure 3.8 shows the composite SED of the system, the three components being two spatially distinct positions with *i*) Yggdrasil *ii*) and Freja, Thor and Odin photometry as red and blue points respectively. The unresolved far-IR *Herschel* detections and upper limits are shown as black points. It is important to note that each component is fitted individually, and that the black points are not used in the fit. However, the total SED and unresolved data (in black) provide a strong constraint on the total integrated flux from all components; all solutions where the sum is inconsistent with the *Herschel* photometry are excluded. In practice, the starburst component in Freja, Thor and Odin is well constrained (blue dotted line in Fig. 3.8). However, the AGN component cannot simultaneously fit both the *Spitzer* and ALMA photometry without exceeding the *Herschel* photometry. We are therefore forced to add an additional starburst component to fit the Yggdrasil ALMA point. However, with only a single point, the starburst luminosity is only loosely constrained.

We clearly see from the SED fitting that Thor is star-formation dominated, with the MIPS 24 μm and 235 GHz reproduced by the starburst model from DecompIR (Mullaney et al., 2011). Yggdrasil represents a composite of emission from an AGN and star formation as reported earlier (Drouart et al., 2014). However, the relative contribution to the IR luminosity from the AGN and the star formation is different; favoring the AGN as the main contributor. In fact, the AGN emits ∼40% of the IR luminosity of the entire system ($L^{\rm IR}_{\rm total} = 1.7 \times 10^{13}\,{\rm L}_\odot$), the remaining $\sim 60\%$ is star-formation split between *i*) Yggdrasil and *ii*) Freja, Thor and Odin at ∼10% and ∼50% levels (Table 3.3.4). According to the Kennicutt (1998a) relation, Yggdrasil and Freja, Thor and Odin have SFR of ~ 200 and $\sim 1400\,{\rm M}_\odot\,{\rm yr}^{-1}$, respectively. Which, in turn, corresponds to a sSFR of $\sim 10^{-9}$ and $10^{-8}\,{\rm yr}^{-1}$.

3.4 Discussion

The wealth of information provided by the MUSE and ALMA data, even with rather modest integration times for both sets of data, paints a complicated picture from the warm ionised gas to the cold molecular gas and dust. We now discuss how the mass is distributed in each component and what the relationship between the components is.

3.4.1 The nature of the gas and dust

The MRC0943-242 system has a complex distribution of the ionised and neutral gas. The high ionisation lines are distributed mainly around the nucleus and are confined within the radio lobes. The exception to this is the extended HeII, CIV, and CIII] emission which is most extended to the west – beyond the western radio lobe (see panel A-C of Fig. 3.7). The fact that metals are detected within this part of the halo suggests the gas is not pristine, while the high ionisation state of the gas is consistent with photoionisation by the AGN, indicating that there is a cone of ionisation along the direction of the radio jet but extending well beyond the radio lobes. The lack of very extended Lyα emission in the outer region of the ionisation cone is most likely caused by HI gas distributed over large scales absorbing the emission (absorption component 2). The inner regions of the ionisation cone, i.e. the region that lies within or just beyond the radio lobes, shows significant Lyα emission (and also absorption from component 2). Resonance scattering shifts the frequency of the Lyα photons and allow them to 'leak' out on both sides of the absorption feature and broaden the line. In fact, throughout the region of Yggdrasil, we see all absorption components either in all places (as for components 1, 2 and 3) or in particular regions (as for component 4). Since the absorption features are only rarely reaching zero intensity in their cores, the neutral gas responsible for absorption systems 1, 3, and 4 are mixed with Lyα line emitting regions (although some of it overlies the Lyα emission). Absorption component 2 must cover the full Lyα emitting region, including that out to $\sim$60 kpc, which is the projected distance to Bifrost. Since this absorption contains no flux in the line core (it is dark), the absorber must have unity covering factor and be optically thick. This being the case, our estimate of the HI column density is a lower limit.

This situation is somewhat akin to the large extended Lyα absorber on the line of sight to the HzRG TN J1338-1942 at $z = 4.1$ (Swinbank et al., 2015). In this case the neutral gas reservoir extends at least 150 kpc away from the core of the HzRG. To detect this extended emission, Swinbank et al. (2015) obtained a much deeper integration and hence significantly more extended Lyα emission and absorption. However, unlike the deepest absorption feature in TN J1338-1942, the offset velocity of the absorption component 2 in MRC0943-242, is rather more modest, only a few 100 km s^{-1} compared to 1200 km s^{-1}. Deeper data for MRC0934-242 may reveal a greater extent and more complex structure of the emitting and absorbing gas.

In addition to the ionisation cone and the general distribution of the Lyα emission around the central regions of Yggdrasil ($M_* \simeq 1.7 \times 10^{11}$ M$_\odot$), there is a bridge of material connecting the IRAC continuum emission of Thor and beyond ($M_* \simeq 1.0 \times 10^{11}$ M$_\odot$). Ivison et al. (2008) also found multiple components for the HzRG 4C60.07 at $z = 3.8$, likewise connected by a bridge of gas. They interpret this bridge as a plume of cold dust and gas in a tidal stream between two interacting galaxies. The interaction between the two galaxies is believed to be the trigger of the starburst and through this exhaust the molecular gas supply in the AGN host galaxy. One scenario which could have triggered the high star formation in Freja, Thor and Odin and perhaps the AGN activity in Yggdrasil is, like for 4C60.07, interaction between two galaxies. In this scenario, the two galaxies interact

tidally where gas flows between the galaxies trigger the AGN activity in Yggdrasil, and creates tidal tails of gas which may emit Lyα. The tidal interactions may then ignite the string of components Freja, Thor and Odin resulting in a SFR $\sim 1400\,\mathrm{M}_\odot$/yr. However, the CO(8–7) emission line from Yggdrasil is very narrow and dynamically quiescent. It shows no signs of dynamical motion, implying that this gas is not related to the tidal interaction. The CO gas appears to be quite highly excited, as may be expected for gas near the central AGN. However, we remark that the ATCA upper limit on the CO(1-0) emission is rather shallow, so we cannot put strong constraints on the CO gas excitation.

Along the same projected line as the bridge and dust emitting regions, we find CO(8–7) emission in Loke which is not detected in any optical or dust continuum counterpart. The tentative detection of CO(1–0) at the position of Loke is consistent with the presence of a large reservoir of molecular gas. However, it is not clear from the observations at hand how extended this reservoir is, if it reaches across Freja, Thor, Odin and Loke, tracing one compact region, or if the reservoir is only at the location of Loke. The tentative CO(1-0) detection suggests a lower excitation level than Yggdrasil, but more sensitive low-J observations are needed to confirm this. The only thing known is that this region contains dynamically quiet but likely highly excited gas component $\sim 90\,\mathrm{kpc}$ away from the nearest stellar emission and with a relatively low velocity compared to the systemic velocity of the AGN. A clue to its nature lies in the alignment with the AGN and starburst components along the bridge. If this represents an accretion flow of galaxies and material along this direction, the gas would experience tidal forces and accretion shocks when the galaxies get close (or enter the halo of Yggdrasil). The absorption component 2 reveals the presence of a large amount of neutral gas at a radius $> 60\,\mathrm{kpc}$ from the AGN, however the impact on this gas from merging galaxies or accreting gas is unknown. It may be that as gas enters the halo, it will encounter the large scale neutral gas, perhaps shocking it as it penetrates. Only more sensitive studies of the molecular gas in Loke may this impact be revealed.

3.4.2 Distribution of masses

To understand the nature of the MRC0943-242 system, it is important to know how the mass is distributed in the system. Following De Breuck et al. (2003), we estimate the ionised gas masses of Yggdrasil. The mass of the ionised gas is given by $M_{\mathrm{ion}} = 10^9 (f_{-5} L_{44} V_{70})^{1/2}\,\mathrm{M}_\odot$, where f_{-5} is the filling factor in units of 10^{-5}, L_{44} is the Lyα luminosity in units of $10^{44}\,\mathrm{erg/s}$ and V_{70} is the volume in units of $10^{70}\,\mathrm{cm}^3$. We assume a filling factor of 10^{-5} (McCarthy et al., 1990) and a volume of $5'' \times 2.5'' \times 2.5''$, and therewith find $\mathrm{M}_{\mathrm{ion}} = 5.2 \times 10^8\,\mathrm{M}_\odot$. This is a lower limit to the total mass since the absorption in the Lyα emission is significant. Since the distribution of the absorption components 1, 3, and 4 are only delineated by the Lyα emission, it is unknown how this gas is distributed, meaning we are most likely underestimating their column densities as the components do not fully cover the emission. This means we cannot estimate their contributions to the mass budget.

Absorption component 2 is observed in all the Lyα line profiles across the Lyα emitting regions and must therefore cover the entire Lyα emitting region out to at least

Mass	Yggdrasil $M_\odot$	Freja/Thor/Odin/Loke $M_\odot$
$M_{stellar}$	1.7×10^{11}	1×10^{11}
M_{ion}	5.2×10^{8}	—
$M_{neutral}$	3.8×10^{9}	—
M_{mol}	6×10^{10}	2.3×10^{10}

Table 3.6: The stellar mass, ionised-, neutral- and molecular gas mass for Yggdrasil and Thor.

$\sim$ 60 kpc. Assuming it is distributed as a spherical shell, we estimate the total mass of absorption component 2 again following De Breuck et al. (2003), $M_{\rm neutral} \gtrsim 3.8 \times 10^9 (R/60\,{\rm kpc})^2 (N_{\rm HI}/10^{19})\,{\rm cm^{-2}\,M_\odot}$, where R is the radius of the neutral gas and $N_{\rm HI}$ is the HI column density. We note that because the absorption is heavily damped (Jarvis et al., 2003), our column density estimate is likely a lower limit of the true column, and our mass estimate therefore a lower limit.

Using the tentative CO(1–0) detection at the position of Loke, and choosing a conservative $\alpha_{\rm CO} = 0.8\,{\rm M_\odot\,K\,km\,s^{-1}\,pc^{-2}}$ (Downes & Solomon, 1998) we estimate a molecular gas mass of $2.3 \times 10^{10}\,{\rm M_\odot}$ for Loke. Emonts et al. (2011) discovered a tentative 3σ CO(1–0) detection $\sim$ 60 kpc North-East of Yggdrasil, and estimate a molecular gas mass of $M_{\rm H_2} = 6 \times 10^{10}\,{\rm M_\odot}$, using the same value for $\alpha_{\rm CO}$.

It is clear from comparing the four mass estimates (Table 3.6) that the most of the mass is in the form of stars and molecular gas, although the contribution of the neutral shell of gas may also be significant.

3.4.3 Ionisation mechanism

The high ionisation lines such as HeII, CIV, and CIII] are extended beyond the western lobe and asymmetric on large scales (see panel A-C of Fig. 3.7). The simplest interpretation is a strong asymmetry in the gas distribution. This hypothesis is supported by the hard photons, which are most likely responsible for the ionisation of the gas, causing the asymmetry in the emission from the circum-nuclear gas. Moreover, the ALMA data show a similar asymmetry in the distribution of both the dust and CO emission. However, this emitting gas lies outside of the ionisation cone and can therefore not be affected.

The detected emission lines from Lyα, CIV, HeII, CIII] and CII]can be used as probes for the ionisation mechanisms. Both the AGN and the far-UV field of vigorous star-formation can ionise the gas. The line ratios of Lyα, CIV and HeII can be used to determine the contribution from stellar photoionisation (Fig. 4 of Villar-Martín et al. (2007)). We find that the observed (absorption corrected) line ratios of Yggdrasil (Table 3.1) are consistent with $\omega = 0$, i.e. pure AGN photo-ionisation. Similarly, we can use the CIV/HeII, CIII]/HeII, CIV/CIII], [CII]/CIII], CIV/Lyα and CIII]/Lyα flux ratios along with the diagrams of De Breuck et al. 2000a (their Fig. 13, adapted in Fig 3.9). This comparison shows that the gas within the radio lobes of Yggdrasil, is likely ionised by a combination of photo-ionisation ($\sim$70%) and shock + precursors ($\sim$30%). CII]emission is an especially sensitive tracer of

shock-ionised gas (Best et al., 2000; De Breuck et al., 2000a). Our MUSE data allow us to produce a [CII] narrow-band (moment-0) image (see panel D of Fig. 3.7). Interestingly, this image indeed reveals that the [CII] emission is confined within the radio lobes, as would be expected if this line is dominated by shock ionised gas. Deeper MUSE data would be needed to check if this is not just due to limited S/N. This also limits us to derive line ratios in the extended halo (near Bifrost), where we detect Lyα, but no other emission lines. Deeper data would allow to check if the gas at ~ 80 kpc is still ionised by the AGN, or has a more important contribution from stellar photo-ionisation or shocks.

3.4.4 AGN and starbursts

Disentangling the SED into several components suggests that the starburst activity in HzRGs is driven by the interaction of two (or more) gas-rich systems. Major mergers have been invoked to explain the high SFRs seen in submm galaxies (SMGs; e.g. Engel et al., 2010), though others argue that they may rather represent the top end of a "main sequence" of star-forming galaxies (e.g. Michałowski et al., 2012). The similar morphologies and stellar masses of HzRGs and SMGs suggest they may be related, potentially through an evolutionary sequence, a high-z extension of the local relation between QSOs and ULIRGs (Sanders et al., 1988). Both classes reside in parent halos of similar mass (Hickox et al., 2012), but direct observations of objects in transition between SMGs and QSOs remain restricted to a few examples (e.g. Simpson et al., 2012). This is where detailed observational studies of type 2 AGN like HzRGs can play an important role, as their stellar masses, unlike type 1 AGN's, can be accurately determined (Seymour et al., 2007; De Breuck et al., 2010).

In MRC0943-242, we actually observe both processes: in Yggdrasil, we observe an AGN host galaxy with a moderate SFR, while the companion galaxy Thor is surrounded by two additional star-forming companions, Odin and Freja.

3.4.5 Loke is not so atypical around radio galaxies

Our detection of CO(8–7) emission in Loke, which is not co-incident with any dust or stellar emission, and is not in the direction of the axis of the radio emission, is puzzling. It is not the first time CO line emission has been detected around a HzRG without any counterpart at other wavelengths. Table 3.7 lists ten HzRG with CO observations where the CO emission is offset from the AGN compared to the radio sources.

Nesvadba et al. (2009) found CO(3–2) emission 80 kpc from the core of the $z = 2.6$ HzRG TXS0828+193. However, the CO(3–2) emission in TXS0828+193 is aligned with the radio jet, which Nesvadba et al. (2009) suggest could be triggering the collapse and excitation of the gas. The offset of CO emission from the position of the HzRG is seen in other sources as well (see Table 3.7) such as, e.g. 4C60.07 (Ivison et al., 2008), MRC0114-211, MRC0156-252 and MRC2048-272 (Emonts et al., 2014). Ivison et al. (2008) detect CO(4–3) emission for the HzRG at $z = 3.8$ at two positions: at the location of the AGN core and 7″ SW of the AGN. The latter component is also detected in CO(1–0) emission (Greve et al., 2004). Based on the submm observations of 4C60.07, Ivison et al. (2008) point out

HzRG	z	CO detection	Separation[a]	CO/dust association	Reference
MRC0114-211	1.402	CO(1–0)	35 kpc	no	Emonts et al. (2014); Nilsson et al. in prep.
MRC0152-209	1.921	CO(1–0)/CO(6–5)	10 kpc	yes	Emonts et al. (2014, 2015a)
MRC0156-252	2.016	CO(1–0)	60 kpc	no	Emonts et al. (2014); Nilsson et al. in prep.
MRC2048-272	2.060	CO(1–0)	55 kpc	no	Emonts et al. (2014); Nilsson et al. in prep.
MRC1138-262	2.161	CO(1–0)	30-40 kpc	yes	Emonts et al. (2013); Gullberg et al. in prep.
TXS0828+193	2.572	CO(3–2)	80 kpc	no	Nesvadba et al. (2009)
MRC0943-242	2.923	CO(8–7)	80 kpc	no	*This work*
B3J2330+3927	3.086	CO(1–0)/CO(4–3)	30 kpc	yes	Ivison et al. (2012)
4C41.17	3.798	CO(4–3)	13 kpc	yes	De Breuck et al. (2005)
4C60.07	3.8	CO(1–0)/CO(4–3)	30 kpc	yes	Ivison et al. (2008); Greve et al. (2004)

Table 3.7: Overview of CO detections that are not directly associated with the radio galaxy. *a*: Separation between the AGN and the CO detection.

a complication when calculating dynamical masses using the extended CO emission, due to the misalignment of the black hole with the CO emission and dust continuum. Emonts et al. 2014 discovered CO(1–0) emission in three HzRGs that were significantly offset from the AGN and which have 4.5-9.2$\times10^{10}\,M_{\odot}$ of molecular gas, but again aligned with the radio jet. They discuss jet-induced star formation. Two molecular components traced by CO(4–3) for 4C41.17 were detected by De Breuck et al. 2005. These two components are also aligned with the radio jet, but are co-spatial with the Lyα emission.

The submm and optical observations of MRC 0943-242, adds to this complicated situation, with its many components, only two of which are traced by CO emission.

3.5 Are we seeing a multiphase accretion flow?

Numerical simulations suggest that galaxies acquire much of their gas through accretion flows generated by the growth of the cosmic web of dark matter (e.g. Agertz et al., 2011; Danovich et al., 2015). Flows of gas develop over cosmological distances and time scales, ultimately penetrating into halos and feeding baryons onto galaxies. Because the flows are associated with the growth of dark matter structures, galaxies are expected to be embedded in accretion flows. Could we be witnessing such accretion in our combined data sets?

Progressing inwards in radius towards the host galaxy of MRC 0943-242 over many 10s of kpc from Loke, through Odin, Thor, Freja, Bifrost to the redshifted absorption component 3 seen against the inner Lyα emission, we see little change in the velocity over this inward journey. In the most distant emission, i.e. Loke, the velocity offset relative to the AGN emission is small. This structure appears dynamically cold, having low dispersion in all of its spectroscopic features, implying that it is near to the plane of the sky. Aligned with this general structure is a group of (merging?) vigorous star-forming galaxies associated with the emission regions, Freja, Thor and Odin. If the coincident Lyα emission from Bifrost is representative of their projected velocity, these galaxies are embedded within this overall (in projection) linear structure. On the opposite end of the structure, we find the AGN host galaxy, Yggdrasil, which has a rather mundane rest-frame optical morphology, suggesting a heavily obscured galaxy, but not a merger (see Fig. 9 of Pentericci et al., 2001). Interestingly, the extended emission line halo does not extend on the other side of the AGN.

Admittedly, we do not have a simple explanation for the distribution of the various phases. For example, why is most of the molecular gas observed at the position of Loke? An explanation could be that the molecular gas is related to the strong, optically thick, large covering fraction of HI absorption component 2. However, the velocity offsets (Fig. 3.4) suggest that it is rather the less massive absorption component 3 that coincides with the CO(8-7) and simply part of what may be a flow into Yggdrasil.

Only a combined ALMA + MUSE survey of radio galaxies like that of MRC0943-242 (with deeper integrations than in this pilot project) can determine if it is gas accretion that is fuelling the growth of their galaxies and supermassive black-holes. These combined data cubes are our only way to obtain a complete picture of various phases which emit

strongly over a wide range of wavelengths. This will allow us to study the nature of the halo gas that results from this complex interaction. By the sensitivity of both ALMA and MUSE on the VLT are already offering tantalising clues on how the gas in this system is being acquired and modified by the interaction with the AGN and galaxies in this complex system.

3.6 Conclusions

Combining the high sensitivity of ALMA and MUSE, even with very modest integration times, has allowed us to gain insights into the environments which explain many properties of the evolutionary path of HzRGs. Surprisingly, in our pilot study of the $z = 2.9$ radio galaxy MRC0943-242, we apparently find that most of the star formation is not associated with the radio galaxy itself, but is in a companion set of galaxies which exhibits a complex pattern of dust emission which we associate with star formation. We say apparently, because the morphology of the dust emission is peculiarly distributed in three distinct sources but roughly within the diffuse stellar continuum emission of the source.

The MUSE data show that the continuum emitting source is embedded in a Lyα emitting linear filament stretching from beyond the AGN to the circum-nuclear emission of the AGN. This structure of dust and Lyα emission aligns well in projection with a region of CO(8–7) and CO(1–0) emitting gas (at lower significance) about 90 kpc in projection from the AGN.

The AGN apparently ionises a large region which is asymmetric, lying mostly on the western side of the source. This is likely due to the gas distribution as it tantalisingly lies in the direction where the dust, CO line emission, and the filamentary Lyα emission are found.

The relationship between the Lyα emission and absorption and the associate CIV absorption, paint a fascinating picture of the distribution of the warm ionised medium. There is a component of Lyα absorbing gas which reaches zero intensity throughout the Lyα emission detected across MRC0943-242 in the MUSE data. It clearly has a unity covering fraction and is highly optically thick. Since the gas is seen as an absorption feature throughout the Lyα emitting filament (Bifrost) this thick, unity covering fraction absorber is extended, and visible in absorption out to > 60 kpc. Because of its velocity and optical thickness, it literally absorbs all of the extended Lyα emission in the cube.

Appendix

3.7 Line ratio diagrams from De Breuck et al. 2000a

This appendix presents a range of emission line ratio diagrams that are directly derived from the MUSE data, compared photo-ionization and shock ionization models (Fig. 13 from De Breuck et al. 2000a).

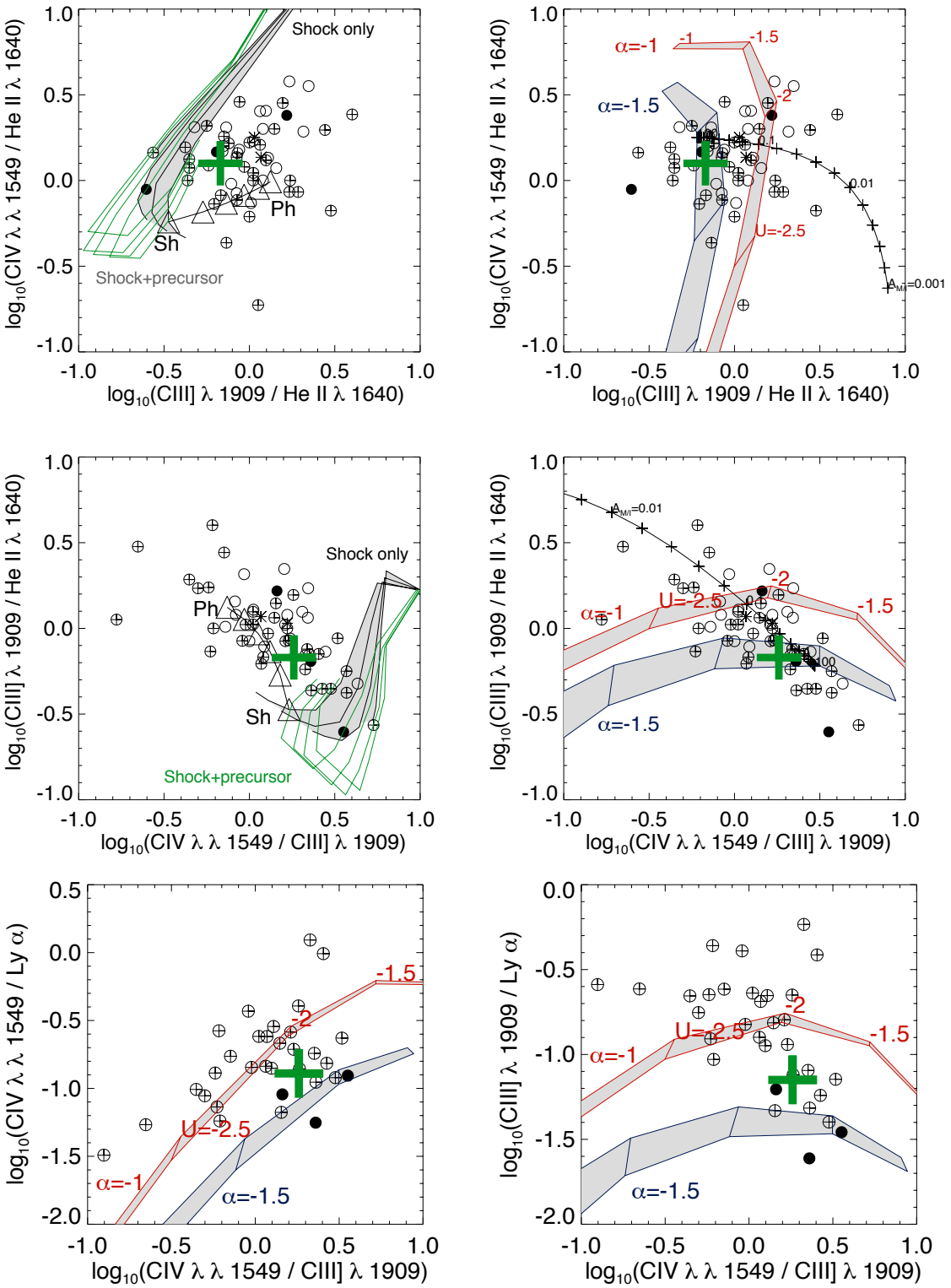

Figure 3.9: Line ratio diagnostic diagrams involving Lyα, CIV, HeII, CIII] and CII] (adapted from De Breuck et al. 2000a, their Fig. 13). The thick green cross shows the flux line ratios observed for Yggdrasil, while the circles show other HzRGs from the literature. Also shown are photo-ionization and shock models to illustrate that the observed line ratios in Yggdrasil are dominated by photo-ionization with a contribution of up to ~30% by shocks (see De Breuck et al., 2000a, for more details).

Acknowledgments

We thank the anonymous referee for her/his very thorough reading of our manuscript, and suggestions that substantially improved our paper. This publication uses data taken from the MUSE commissioning run 060.A-9100. All of the MUSE data used in this paper are available through the ESO science archive. This paper makes use of the following ALMA data: ADS/JAO.ALMA#2012.1.00039.S. ALMA is a partnership of ESO (representing its member states), NSF (USA) and NINS (Japan), together with NRC (Canada) and NSC and ASIAA (Taiwan), in cooperation with the Republic of Chile. The Joint ALMA Observatory is operated by ESO, AUI/NRAO and NAOJ. The work of DS was carried out at Jet Propulsion Laboratory, California Institute of Technology, under a contract with NASA. BE acknowledges funding through the European Union FP7 IEF grant nr. 624351. MDL acknowledges the support from the ESO visitors program and especially would like to thank Mario van den Ancker for his help and Eric Emsellem for interesting scientific discussions. Nick Seymour is the recipient of an ARC Future Fellowship.

Chapter 4

ALMA Finds Dew Drops in the Dusty Spider's Web

Bitten Gullberg[1,3] Matthew D. Lehnert[2], Carlos De Breuck[1], Steve Branchu[4,1], Helmut Dannerbauer[5], Guillaume Drouart[6], Bjorn Emonts[7], Pierre Guillard[2], Nina Hatch[8], Nicole P. H. Nesvadba[9], Alain Omont[2], Nick Seymour[10], Joël Vernet[1]

[1]European Southern Observatory, Karl Schwarzschild Straße 2, 85748 Garching, Germany [2]Institut d'Astrophysique de Paris, UMR 7095, CNRS, Université Pierre et Marie Curie, 98bis boulevard Arago, 75014, Paris, France[3]Max-Planck-Institut für Extraterrestrische Physik, Giessenbachstraße 1, 85748 Garching, Germany[4]Université de Bordeaux, LAB, UMR 5804, 33270, Floirac, France[5]Universität Wien, Institut für Astrophysik, Türkenschanzstraße 17, 1180, Wien, Austria[6]Department of Earth and Space Science, Chalmers University of Technology, Onsala Space Observatory, 43992, Onsala, Sweden[7]Centro de Astrobiología (INTA-CSIC), Ctra de Torrejón a Ajalvir, km 4, 28850 Torrejń de Ardoz, Madrid, Spain[8]School of Physics and Astronomy, University of Nottingham, University Park, Nottingham NG7 2RD, UK[9]Institut d'Astrophysique Spatiale, CNRS, Université Paris-Sud, Bat. 120-121, F-91405 Orsay, France[10]International Centre for Radio Astronomy Research, Curtin University, Perth WA 6845, Australia

Abstract

We present 0.″5 resolution ALMA detections of the observed 246 GHz continuum, [CI] $^3P_2 \rightarrow {}^3P_1$ fine structure line ([CI]2-1), CO(7–6) and H_2O lines in the $z = 2.161$ radio galaxy MRC1138-262, the "Spiderweb Galaxy". We detect strong [CI]2-1 emission both at the position of the radio core, and in a second component ∼4 kpc away from it. The 1100 km/s broad [CI]2-1 line in this latter component, combined with its H_2 mass of $1.6 \times 10^{10}\,M_\odot$ implies this emission must come from a compact region <60 pc, possibly containing a second AGN. The combined H_2 mass derived for both objects using the [CI]2-1 emission is $3.3 \times 10^{10}\,M_\odot$. The total CO(8–7)/[CI]2-1 line flux ratio of 0.2 suggests a low excitation molecular gas reservoir and/or enhanced atomic carbon in cosmic-ray dominated regions.

We detect spatially-resolved H_2O $2_{11} - 2_{02}$ emission — for the first time in a high-z un-lensed galaxy — near the outer radio lobe to the east, and near the bend of the radio jet to the west of the radio galaxy. No underlying 246 GHz continuum emission is seen at

either position. We suggest that the H_2O emission is excited in the cooling region behind slow (10-40 km s^{-1}) shocks in dense molecular gas (10^{3-5} cm^{-3}). The extended water emission is likely evidence of the radio jet's impact in cooling and forming molecules in the post-shocked gas in the halo and inter-cluster gas similar to what is seen in low-z clusters and other high-z radio galaxies. These observations imply that the passage of the radio jet in the interstellar and inter-cluster medium not only heats gas to high temperatures as is commonly assumed or found in simulations, but also induces cooling and dissipation which can lead to substantial amounts of cold dense molecular gas. The formation of molecules and strong dissipation in the halo gas of MRC1138-262 may explain both the extended diffuse molecular gas and young stars observed around MRC1138-262.

4.1 Introduction

The high-z radio galaxy (HzRG) MRC1138-262 at $z = 2.161$ is one of the best studied HzRG (e.g. Pentericci et al., 1997; Carilli et al., 1997; Pentericci et al., 1998, 2000; Carilli et al., 2002a; Stevens et al., 2003; Kurk et al., 2004b,a; Greve et al., 2006; Miley et al., 2006; Hatch et al., 2008; Humphrey et al., 2008; Hatch et al., 2009; Kuiper et al., 2011; Ogle et al., 2012; Seymour et al., 2012), with a well sampled spectral energy distribution (SED) covering from radio to X-ray. Its radio morphology is typical of distant radio galaxies with a string of radio bright knots along the radio jet extending to the west and a single lobe to the east of the central radio core (Carilli et al., 1997). The radio core has an "ultra steep" spectral index of $\alpha = -1.2$, and the spectral indices of the radio knots systematically steepen with increasing distance from the core (Pentericci et al., 1997). The radio source is embedded in an environment over-dense in galaxies over scales of hundreds of kpc (Pentericci et al., 1998; Miley et al., 2006) to Mpc scales (Pentericci et al., 2002; Kurk et al., 2004b,a; Dannerbauer et al., 2014). Many of these galaxies are clumpy and star forming (Pentericci et al., 1998; Miley et al., 2006; Dannerbauer et al., 2014). Hatch et al. (2009) predict that most of the satellite galaxies within 150 kpc will merge with the central HzRG and that the final merger galaxy will contain very little gas due to the high star-formation rate (SFR) of the satellite galaxies. X-ray observations of MRC1138-262 are inconclusive about the existent of an extended X-ray atmosphere (cf. Carilli et al., 2002a; Pentericci et al., 2000, the extended X-ray emission could be due to inverse Compton or shocks generated by the passage of the radio jets). Pentericci et al. (2000), favouring the existence of a large thermal hot X-ray emitting atmosphere, conclude that MRC1138-262 has many of the necessary ingredients of a forming galaxy cluster, i.e. an irregular velocity distribution of the Lyα emitting galaxies, an over-density of galaxies, a massive central galaxy, and a hot X-ray halo. Due to the large number of companion galaxies surrounding the HzRG being analogous to "flies caught in a spiders web", MRC1138-262 was dubbed the Spiderweb Galaxy (Miley et al., 2006).

Multi-wavelength photometry, including the infrared continuum emission (Stevens et al., 2003; Greve et al., 2006; De Breuck et al., 2010), imply an extremely high SFR in the Spiderweb Galaxy. Fitting an active galactic nucleus (AGN) and starburst component SED

to the mid- to far-IR SED, Seymour et al. (2012) find a SFR for the starburst component of $1390 \pm 150\,\mathrm{M_\odot\,yr^{-1}}$ (see also Ogle et al., 2012). This should be compared with the rest-frame UV estimates of only a couple $100\,\mathrm{M_\odot\,yr^{-1}}$ (even with an extinction correction) by Hatch et al. (2008), who emphasise how deeply embedded the majority of the intense star formation is in MRC1138-262. Although the star formation is intense, the characteristics of the vigorous outflow ($\dot{\mathrm{M}} \gtrsim 400\,\mathrm{M_\odot\ yr^{-1}}$) observed in the optical emission line gas suggest that this is predominately driven by the radio jet (Nesvadba et al., 2006).

Beyond the companion galaxies, the diffuse stellar and gaseous environment of MRC1138-262 on larger scales is also fascinatingly complex. MRC1138-262 has a significant amount of diffuse UV intergalactic light (IGL) within 60 kpc of the radio galaxy indicating ongoing star formation in the circum-galactic environment (Hatch et al., 2008). This diffuse light is embedded in a large (~ 100 kpc in diameter) Lyα emitting halo (Pentericci et al., 1997). Using semi-analytical models, Hatch et al. (2008) ruled out the possibility that the observed circum-galactic light originates from unresolved, low-mass satellite galaxies. Spectra extracted at the position of the central HzRG, of a nearby galaxy and the IGL, show Lyα emission lines with absorption troughs super imposed, suggesting the presence of warm neutral gas mixed with the ionised gas surrounding the HzRG (Pentericci et al., 1997; Hatch et al., 2008). This leads to the conclusion that the large Lyα halo emission is powered not only by the extended and diffuse star-formation (Pentericci et al., 1998; Miley et al., 2006; Hatch et al., 2008) but also by AGN photoionisation and shock heating (Nesvadba et al., 2006).

The influence of the radio jet from the AGN is seen in the VLA observations, which reveal a bend in the western string of clumps detected ~ 20 kpc from the core towards the south-west. Lyα line emitting gas has a bright spot associated with this bend and the two hotspots, implying the presence of a massive cloud of gas deflecting the radio jet and causing these features (Pentericci et al., 1997; Lonsdale & Barthel, 1986). Several different models exist for how gas might deflect radio jets, such as the jet drilling into a gas cloud where it blows a bubble in the hot plasma (Lonsdale & Barthel, 1986) or through the counter pressure generated by oblique reverse shocks in the cloud generated by a jet-cloud interaction (Bicknell et al., 1998). Given this situation, Pentericci et al. (1997) argue that the relation between the radio emitting knots in the jet and the high surface brightness Lyα halo emission, especially where the eastern jet bends, suggest an interaction between the jet and the ambient gas in the halo of MRC1138-262. However, the origin of the Lyα emitting gas reservoir is still uncertain.

This high a SFR of the HzRG means that a significant molecular gas reservoir fuelling the star formation must be present. Emonts et al. (2013) probe the diffuse extended molecular gas reservoir using the CO(1–0) line. They find that there is approximately 6×10^{10} $\mathrm{M_\odot}$ of cold $\mathrm{H_2}$ gas over a scale of 10s of kpc surrounding the HzRG (also Emonts et al. 2016, in prep.). The kinematics of the cold molecular gas is relatively quiescent (Emonts et al. 2016, in prep.). More surprisingly, Ogle et al. (2012) detect the 0-0 S(3) rotational line of $\mathrm{H_2}$ in MRC1138-262. The strength of the line, allowing for a range of plausible excitation temperatures of $\mathrm{H_2}$, imply warm ($T > 300$ K) $\mathrm{H_2}$ masses of order 10^7 to 10^9 $\mathrm{M_\odot}$. While the large *Spitzer* beam does not allow to spatially resolve the $\mathrm{H_2}$ emission,

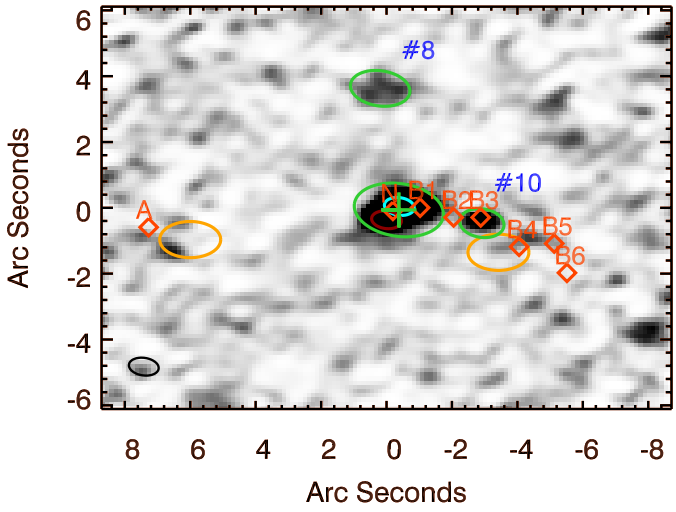

Figure 4.1: Overview of the spatial distribution of the detected components. The natural weighted 246 GHz continuum map is in grey scale and the two [CI]2–1 components 1 and 2 are marked with the blue and red ellipses, respectively. The two H_2O detections are marked with orange ellipses, and the 246 GHz continuum components marked with green ellipses. The sizes of the ellipses represent the extractions used for the photometry. The knots in the radio jet are marked with red-orange diamonds and labeled according to Pentericci et al. (1997). The numbers correspond to the numbering in Kuiper et al. 2011. The ALMA beam is shown as a black ellipse in the lower left corner.

a plausible interpretation of the relatively large mass of warm H_2 gas in MRC1138-262 is that a fraction of the jet energy is being dissipated as supersonic turbulence and shocks in the dense gas in the immediate environment of the AGN.

Though the optically thick CO(1–0) emission line is a good tracer of the diffuse molecular gas, the emission lines from neutral carbon ([CI]) are arguably even better. The [CI] lines have critical densities similar to the low-J CO lines, meaning that they probe the same phases of the molecular gas. As they are both optically thin, they therefore probe higher column densities than CO (Papadopoulos et al., 2004). While the [CI] lines are good tracers of the diffuse molecular gas, they are poor tracers of the very dense star forming gas. Molecular lines from e.g. H_2O, HCN and CS, have a much higher critical density and therefore probe the dense molecular star forming phase. Omont et al. (2013) find a relation between the far-infrared (FIR) and H_2O luminosities for a sample of high-z starburst galaxies. The H_2O detections for this sample are all associated with underlying FIR emission, implying that the H_2O emission traces star forming regions. However, the H_2O molecules can also be excited in the dissipation of supersonic turbulence in molecular gas or by slow shocks (e.g. Flower & Pineau Des Forêts, 2010). In the case of purely shock excited H_2O, it is unlikely that underlying FIR emission would be detected in regions of strong H_2O emission (e.g. Goicoechea et al., 2015).

Motivated to determine the energy source and distribution of the strong dissipation as possibly observed through H_2 emission and determining the state of the molecular gas in MRC1138-262, we proposed for ALMA observations in Cycle 1. In this paper, we present

our results for the observed 246 GHz continuum emission (rest-frame ∼740 GHz), H_2O $2_{11} - 2_{02}$ transition (at $\nu_{\rm rest} = 752.03$ GHz, which is hereafter often refereed to as H_2O), [CI] $^3P_2 \rightarrow {}^3P_1$ fine structure emission line (at $\nu_{\rm rest} = 809.34$ GHz, which is hereafter referred to as [CI]2-1) and CO(7–6) emission line observations towards the Spiderweb Galaxy. We find strong 246 GHz continuum emission at the position of the HzRG. Near both radio lobes, we detect emission from H_2O, the first spatially resolved detection of H_2O in a high-z un-lensed galaxy. We also detect strong [CI]2-1 emission blended with weak CO(7–6) emission at the position of the HzRG. In § 4.2 we present our Atacama Large Milimeter/submilimeter Array (ALMA) submm observations. The results of these observations are given in § 4.3. We analyse and discuss them in § 4.4 and summarise our conclusions in § 4.5. We assume $H_0 = 73$ km/s/Mpc, $\Omega_M = 0.27$, and $\Omega_\Lambda = 0.73$, which implies a scale of 8.172 kpc/″ at $z = 2.161$.

4.2 Observations

4.2.1 ALMA observations

The ALMA cycle 1 Band 6 observations were carried out on 2014 April 27 for 49 min on-source time with 36 working antennas. The four 1.875 GHz spectral windows were tuned to cover the frequency ranges 237.3 − 240.9 GHz and 252.6 − 256.7 GHz. We used the supplied Common Astronomy Software Applications (CASA) calibration script to produce the data cube, continuum map and moment-0 maps. The quasar J1146-2859 was used as a bandpass calibrator, and the UV range was well covered within 400 kλ.

We made a natural weighted map (Briggs robust parameter of 2), which exhibits the highest S/N, at the expense of a lower spatial resolution. The frequency range between 254.9 − 265.7 GHz (i.e. half of the upper side band) is dominated by strong [CI]2-1 and CO(7–6) line emission and is therefore not included in the continuum map. This results in a continuum map with a synthesised beam of $0\farcs69 \times 0\farcs44$ with PA 89.3° and an RMS of 50 μJy/beam. We corrected the continuum map for the primary beam of $26\farcs3$.

The H_2O emission is spatially offset from the continuum emission and a continuum subtraction is therefore not required, as it would only unnecessarily add noise. The H_2O observations are therefore not continuum subtracted. The [CI]2-1 and CO(7–6) emission lines are within the frequency range at $z = 2.1606$, and we subtract the continuum in the UV-plane by fitting a first order polynomial to the line free channels. The [CI]2-1 emission is so broad that it leaves no line free channels in spectral window 0. We therefore fit the continuum to spectral window 1 which shows no signs of line emission. We bin the [CI]2-1 line data to 20 km/s which has an RMS of 0.5 mJy and the H_2O line data to 60 km/s which has an RMS of 0.3 mJy. We primary beam correct the H_2O line data, as we find H_2O emission $\sim 6\farcs5$ from the phase centre, where the sensitivity is at 87%.

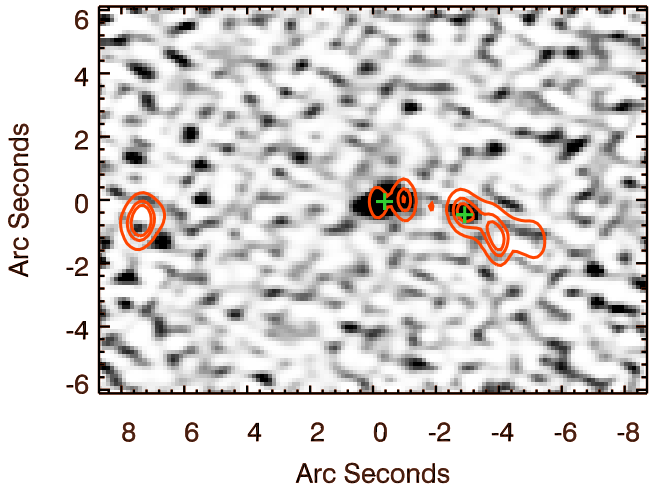

Figure 4.2: The 246 GHz continuum map with robust 0 in grey scale overlaid with the radio map in orange contours. The fitted continuum emission peaks are marked with green crosses. Companion #10 to the west is co-spatial with the knot B3 in the radio jet (Pentericci et al., 1997).

4.3 Results

The Spiderweb Galaxy is detected in both 246 GHz continuum and [CI]2-1, CO(7–6) and H_2O line emission. Figure 4.1 shows an overview of the spatial distribution of the different components. The strong [CI]2-1 line emission is seen in two components separated by 0.″5. The [CI]2-1 component 1 is centred at the position of the HzRG (marked with a light blue ellipse in Fig. 4.1) and the [CI]2-1 component 2 is located 0.″5 to the south-east (marked with a red ellipse in Fig. 4.1). The 246 GHz continuum emission peaks at the position of the HzRG (marked with green ellipses in Fig. 4.1), but shows an extension in the direction of the [CI]2-1 component 2. Emission from H_2O is also detected south-west of the HzRG (marked with the orange ellipse south of the 246 GHz continuum component in Fig. 4.1), which is co-spatial with the bend in the radio jet (Carilli et al., 1997). H_2O emission is detected east of the HzRG - west of knot A in the radio jet (marked with an orange ellipse to the left in Fig. 4.1). We now discuss each of the components separately. Table 4.2 lists the derived line parameters. Throughout, we will adopt the [CI]2-1 emission at the position of the radio core as the systemic redshift $z = 2.1606$.

4.3.1 Continuum emission

The continuum map contains bright 246 GHz continuum emission at the position of the HzRG, ~ 20 kpc to the west and tentative emission to the north (see Fig. 4.1).

Component	Position		$S_{246\,\mathrm{GHz}}$	z
	RA	dec	mJy	
HzRG	11:40:48.34	-26:29:08.656	1.78 ± 0.29	2.1606 ± 0.0041
companion #8	11:40:48.38	-26:29:04.940	< 0.25	2.1437
companion #10	11:40:48.15	-26:29:09.490	0.19 ± 0.01	2.1446
Water (West)	11:40:48.82	-26:29:09.58	< 0.2	
Water (East)	11:40:48.12	-26:29:09.97	< 0.2	

Table 4.1: The peak positions and 246 GHz continuum flux of the HzRG and companion #8 and #10. The continuum fluxes are calculated by integrating under the fitted double 2D Gaussian profile. Companion #8 is a tentative detection and therefore an upper limit. We take the 3σ upper limit of the 246 GHz continuum emission at the positions of the H_2O emission to the west and east to be three times the RMS.

The HzRG

The 246 GHz continuum emission at the position of the HzRG shows an east-west elongation, in the same orientation as the radio source (see Fig. 4.1). A similar orientation was seen in the SCUBA and LABOCA maps (Stevens et al., 2003; Dannerbauer et al., 2014), but those extensions were on a much larger scale than the separation seen in Fig. 4.1. Though the continuum only has one peak, the elongation suggests a two component system, similar to what is seen in the [CI]2-1 line emission (see § 4.3.2) . Using the peak positions from component 1 and 2 in the [CI]2-1 moment-0 maps, we fit a double 2D Gaussian profile to the continuum by fixing the centres of the Gaussians at the peak positions of the [CI]2-1 emission line. This results in a continuum ratio for the two components of $\sim$5. Integrating the fitted double 2D Gaussian yields the flux density of 1.78 ± 0.29 mJy (see Table 4.1). This emission is probably dominated by thermal dust emission, though we warn that a linear extrapolation of the $S(8.2\,\mathrm{GHz}) = 1.88$ mJy Pentericci et al. (1997) and the $S(36.5\,\mathrm{GHz}) = 1.02$ mJy (Emonts et al, in prep.) for the core predicts a synchrotron contribution of 0.47 mJy at 235 GHz. Any star-formation parameters derived directly from the 246 GHz should therefore be considered as an upper limit.

The companion sources

We detect 246 GHz continuum emission from a bright companion ~ 20 kpc to the west of the HzRG (see Fig. 4.1). This companion is associated with knot B3 in the radio jet (Carilli et al., 1997; Pentericci et al., 1997, see Fig. 4.1) and a small group of galaxies (denoted D by Pentericci et al. (1997) and #10 by Kuiper et al. (2011), see Fig. 4.4). This is also the position of a high surface brightness region of Lyα emission (Pentericci et al., 1997). This companion is also seen in e.g. *HST* F814W imaging (Miley et al., 2006) and at other optical wavelength e.g. R-band (Pentericci et al., 1997). Companion #10 is co-spatial with companion D in Pentericci et al. (1997) at RA = 11:40:48.14, dec = -26.29.09.2, and is offset by only 0.″8 to the Lyα emitter #491 from Kurk et al. (2004b). This Lyα emitter at RA = 11:40:48.2, dec = -26.29.09.5 (marked with the purple circle in Fig. 4.3 and 4.4) is

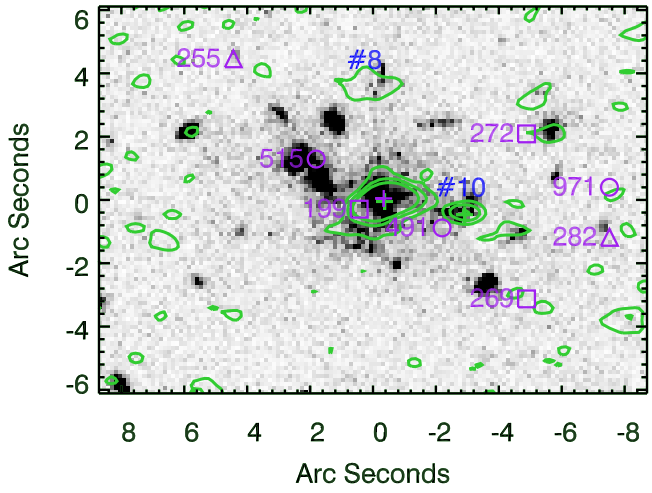

Figure 4.3: *HST* F814W image (Hatch et al., 2008) in grey scale overlaid with the natural weighted 246 GHz continuum map in green contours with levels of 1.5σ, 3σ and 5σ. In the natural weighted continuum map we detect emission from companion #10 (and tentatively from #8) of Kuiper et al. 2011. The purple cross marks the position of the nearby Lyα emitter at the position of the HzRG. The purple circles mark the positions of Lyα emitters, the squares mark the position of Hα and the triangles extremely red objects within the Lyα halo or MRC1138-262. The Lyα emitter #491 is offset by $0\farcs8$ from the companion source seen in 246 GHz continuum emission west of the HzRG (see also Fig. 4.4).

inside the Lyα halo of the Spiderweb Galaxy (Kurk et al., 2004b), and so are three other Lyα emitters, three Hα emitters and two Extremely Red Objects (ERO) (also marked in Fig. 4.3). Fitting a 2D Gaussian profile to companion #10 we find a flux density of 0.19 ± 0.01 mJy (see Table 4.1).

To examine the nature of the 246 GHz emission of companion #10, we compared the flux density in the spectral windows not contaminated by line emission. The expected ratio between 238.28 and 253.48 GHz (i.e. the lower and upper side bands: LSB and USB) from thermal blackbody radiation at 40 K is 0.80, while the observed ratio is 1.19 ± 0.22. The decreasing spectral slope with increasing frequency of #10 is more consistent with a synchrotron rather than a thermal dust origin. Indeed, a straight extrapolation of the $S_{8.2\mathrm{GHz}} = 5.9$ mJy (Pentericci et al., 1997) and the $S_{36.5\mathrm{GHz}} = 1.8$ mJy (Emonts et al., in prep) implies $S_{239\mathrm{GHz}} = 0.4$ mJy. Our observed 0.2 mJy is therefore fully consistent with synchrotron emission, and even allows for the expected spectral steepening at high frequencies. Thus synchrotron dominated submm emission is consistent with companion #10 having very blue UV colours with no signs of a Balmer break or significant extinction (Hatch et al., 2009). On the other hand, it could also be that the most obscured regions are not visible in the optical images, but only the bluest, least obscured regions are. Higher resolution dust continuum and a broad sub-millimetre wavelength coverage can test these hypotheses.

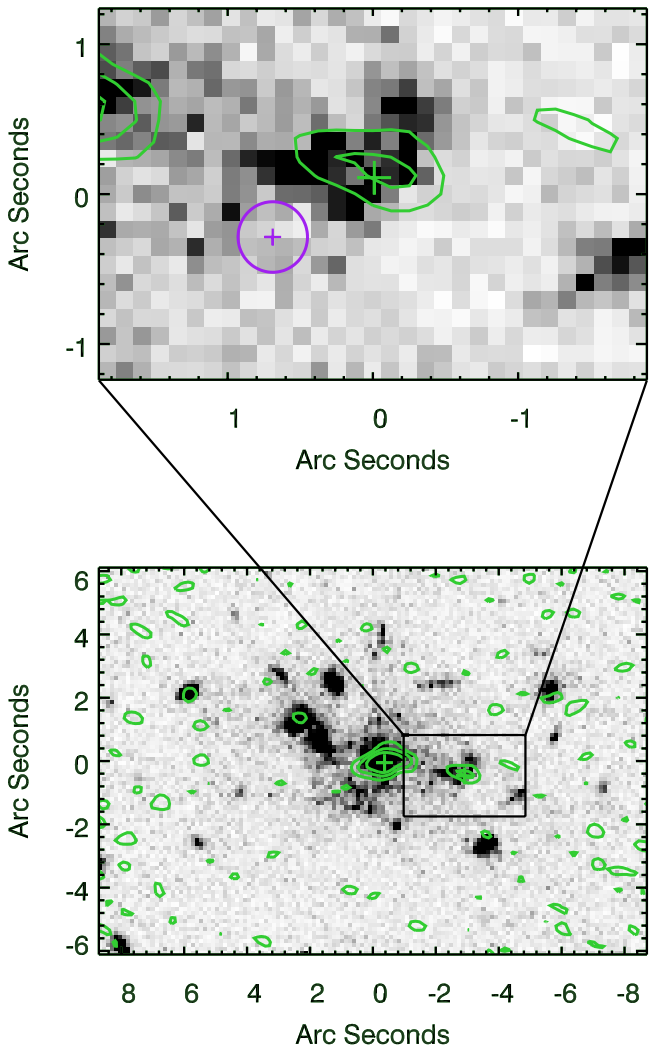

Figure 4.4: The *HST* F814W image in grey scale overlaid with the 246 GHz continuum in green contours. *Bottom panel*: The full region of the Spiderweb Galaxy, where the companion #10 is co-aligned with a group of galaxies. *Top panel:* Zoom in of the region around the companion sources. The purple circle mark the position of the Hα emitter #491 (Kurk et al., 2004b), which is the close to the dust continuum emission companion source.

4.3.2 [CI]2-1 and CO(7–6) line emission

The HzRG

Strong emission from the [CI] $^3P_2 \rightarrow {}^3P_1$ fine structure emission line is detected at the position of the HzRG. The [CI]2-1 emission line has a double peaked velocity profile with peaks at 0 km/s and $\sim$ 350 km/s (see top right in Fig. 4.5). Moment-0 maps of the channels containing the emission of the first (see bottom left in Fig. 4.5) and second (see bottom middle in Fig. 4.5) peaks reveal a spatial mis-alignment of the two [CI]2-1 peaks, which suggests two components. The emission corresponding to the 0 km/s peak is at the location of the HzRG (component 1, marked with a blue cross in Fig. 4.5), while the $\sim$ 350 km/s gas is shifted 0.″5 to the south-east (component 2, marked with the red cross in Fig. 4.5). A broad underlying components is visible in the spectrum for component 2. Unfortunately, the spatial resolution of the data and the broad underlying component do not allow for a clearer separation of the two components.

The spectral velocity profile of component 1, with no overlap with component 2 (see Fig. 4.5 left), has a Lorentzian-shaped profile, with a full-width at half-maxima (FWHM) of 270 ± 15 km/s and a redshift of $z = 2.1606 \pm 0.0041$, which agrees with the redshift determined from the CO(1–0) line (Emonts et al., 2013). We adopt this as the systemic redshift as the [CI]2-1 line has higher spectral resolution and S/N compared to the HeII λ1640 Å (Hatch et al., 2008). At the expected frequency of the CO(7–6) line, we detect a 3.5σ Gaussian shaped CO(7–6) emission line with FWHM of 435 ± 85 km/s. The broadness of the [CI]2-1 line makes the spectroscopic separation of the [CI]2-1 and CO(7–6) lines difficult, as very few line-free channels separate them. To avoid the lines contaminating each other, the velocity integrated line flux for the [CI]2-1 line is calculated by integrating the fitted profile from -610 km/s to 530 km/s, while the integrated CO(7–6) line flux is integrated from 690 km/s to 1390 km/s. The CO(7–6) to [CI]2-1 line luminosity ratio is 0.2. The peak ratio of the two [CI]2-1 components is $\sim$ 3 times lower than the ratio of the 246 GHz continuum at these positions, implying that component 2 is relatively brighter in [CI]2-1 than in 246 GHz emission.

The velocity profile of component 2 shows evidence for two components, one broad and one much narrower component (see Fig. 4.5). The best two-component Gaussian fit has a FWHM of 1100 ± 65 km/s for the broad, and 230 ± 35 km/s for the narrow components. The centre of the narrow component is shifted $\sim$ 360 km/s redward of the systemic velocity of the [CI]2-1 line for component 1. The CO(7–6) emission line is also detected for component 2, at a level of 4.8σ, which is more significant than the CO(7–6) detection for component 1. The CO(7–6) line peaks at $\sim$ 1275 km/s relative to the centre of the [CI]2-1 line, corresponding to a rest velocity for the CO(7–6) line of $\sim$ 280 km/s. The narrow component of the [CI]2-1 line and the CO(7–6) line both have an offset of 80 km/s relative to the systemic redshift of component 1. Just as for component 1, separating the two lines spectroscopically is difficult and we therefore calculate the integrated flux of the [CI]2-1 line from -825 km/s to 990 km/s and the integrated flux of the CO(7–6) line from 1000 km/s to 1490 km/s. We additionally derive the flux of the narrow and broad

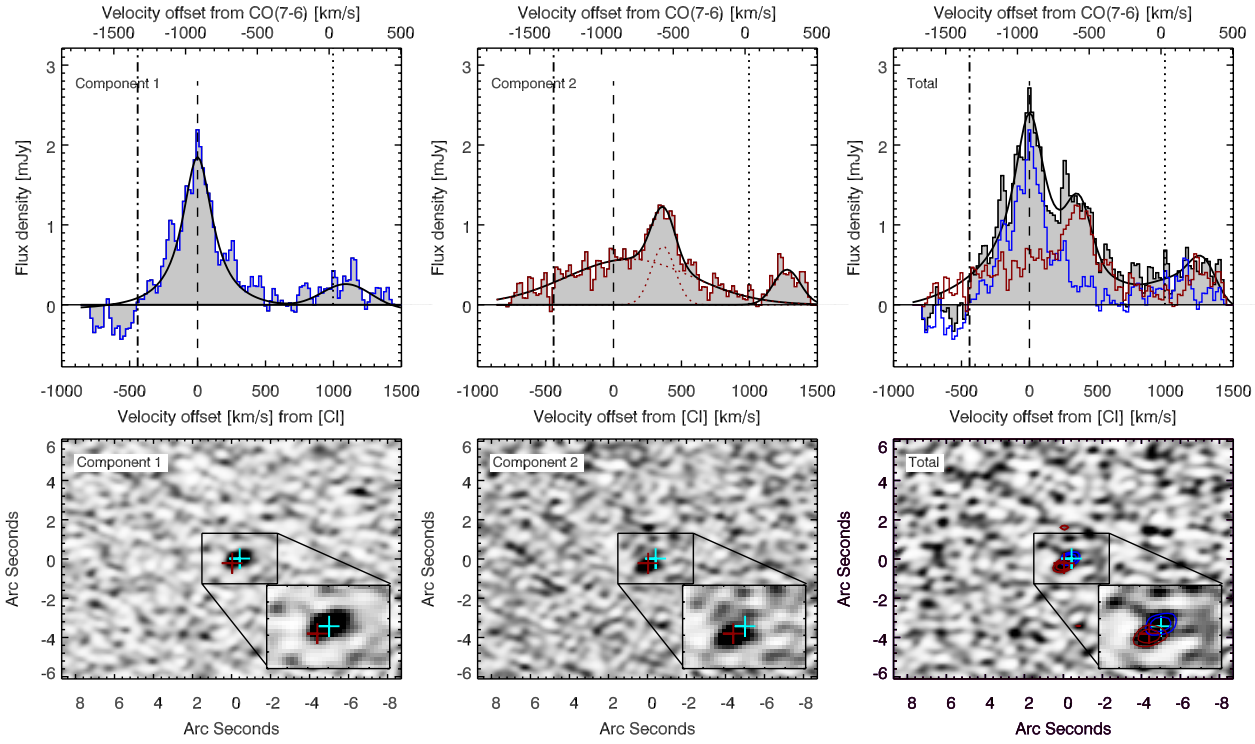

Figure 4.5: [CI]2–1 spectra and moment-0 maps for component 1, component 2 and the total [CI]2–1 and CO(7–6) emission. *Top row:* The spectra extracted from beam sized areas for component 1, component 2 and the total. The areas from which the spectra of component 1 and component 2 are extracted do not overlap. The Lorentzian profile for the component 1 [CI]2–1 line (top left), the double Gaussian profile for the component 2 [CI]2–1 line (top middle) and the single Gaussian fits for the two CO(7–6) lines are over-plotted as black curves. The sum of the Lorentzian and Gaussian profiles is over-plotted in black in the total spectrum (top right). The dashed lines mark the 0-velocity of the [CI]2–1 frequency at $z = 2.1606$, and the dotted lines mark the 0-velocity for the CO(7–6) frequency at the same redshift. This redshift is in agreement with the redshift determined from the CO(1–0) line (Emonts et al., 2013). The dotted-dashed line marks the 0-velocity of the [CI]2–1 frequency at $z = 2.156$ determined from the HeII λ1640Å line (which as a non-resonant line, should represent the systemic velocity of the AGN, Humphrey et al., 2008). *Bottom row:* The moment-0 maps of the [CI]2–1 emission from component 1 (bottom left), component 2 (bottom middle) and the total (bottom right) [CI]2–1 emission and zoom-ins of the centres of the images. The total [CI]2–1 moment-0 maps is overlaid with [CI]2–1 line contours of component 1and 2. The blue and red crosses indicate the peaks of the [CI]2–1 emission of component 1 (blue) and component 2 (red).

components separately, by integrating the fitted Gaussian profiles. The CO(7–6) to [CI]2-1 line luminosity ratio is 0.14, lower than for component 1. The two components have a [CI]2-1 line peak ratio of 1.7, and a CO(7–6) line peak ratio of 0.4.

The total spectrum of the two components (see Fig. 4.5 right) clearly shows a double peaked [CI]2-1 line and a broad CO(7–6) line. We sum the Lorentzian fit of component 1 and the two Gaussian fits of component 2, which results in a profile that fits well the observed integrated [CI]2-1 line of both components. We likewise sum the two single Gaussians fitted to the CO(7–6) lines in component 1 and component 2. The full [CI]2-1 plus CO(7–6) profile is over-plotted on the full spectrum in the top right panel of Fig. 4.5. The CO(7–6) line in the total spectrum is even broader than for component 1 and 2, making the separation even more difficult. We therefore calculate the [CI]2-1 integrated line flux from -590 km/s to 700 km/s and the CO(7–6) integrated line flux is integrated from 700 km/s to 1390 km/s. The CO(7–6) to [CI]2-1 line luminosity ratio for the total spectrum is 0.2, the same as for component 1.

The companion source

We detect line emission in companion #10 ~ 20 kpc to the west of the HzRG (see Fig. 4.6). SINFONI spectroscopy of this companion shows line emission from Hα, [OII] and OIII], and that companion #10 has a velocity offset of ~ -1360 km/s, corresponding to a redshift of $z = 2.1446$ (Kuiper et al., 2011). Unfortunately, the [CI]2-1 is shifted out of the observed band at this redshift and the H_2O line falls in a gap in the response of the band. However, the CO(7–6) line is offset by 997 km/s from the [CI]2-1 line and therefore still lies within the band at this redshift. We identify the detected emission line as CO(7–6) line emission from companion #10 (see Fig. 4.6). It is therefore highly likely that the 246 GHz continuum emission that we detect at this position is related to companion #10. This CO(7–6) line can be fitted with a Gaussian profile with a FWHM of 130 ± 20 km/s and the integrated line flux from -170 km/s to 150 km/s of 0.08±0.01 Jy km/s (Table 4.2). We do not detect any line emission at the position of the tentative 246 GHz continuum companion #8.

4.3.3 H_2O line emission

We detect emission from the H_2O $2_{11} - 2_{02}$ transition ~ 25 kpc to the west and ~ 50 kpc to the east of the radio core at the expected observed frequency for H_2O at $z = 2.1606$. The western 4σ detection is located just south of the strongest 246 GHz continuum companion, at the bend of the radio jet i.e. at radio knot B4 (see Fig. 4.7). The eastern 3.7σ detection is located west of the radio knot A (see Fig. 4.7). To establish that this emission is real we perform a 'Jackknife' test, cutting the observed time in half. The two H_2O lines show up in both halves of the data with a $\gtrsim 2\sigma$ significance, which suggests that the emission lines are real and not simply noise peaks. Fitting Gaussian profiles to the emission lines result in FWHMs and relative velocities of 230 ± 50 and 160±20 km/s for the western detection and 350 ± 70 and 125±30 km/s for the eastern detection respectively. No 246 GHz continuum emission is detected at the positions of the two H_2O detections down to an RMS of 40 μJy,

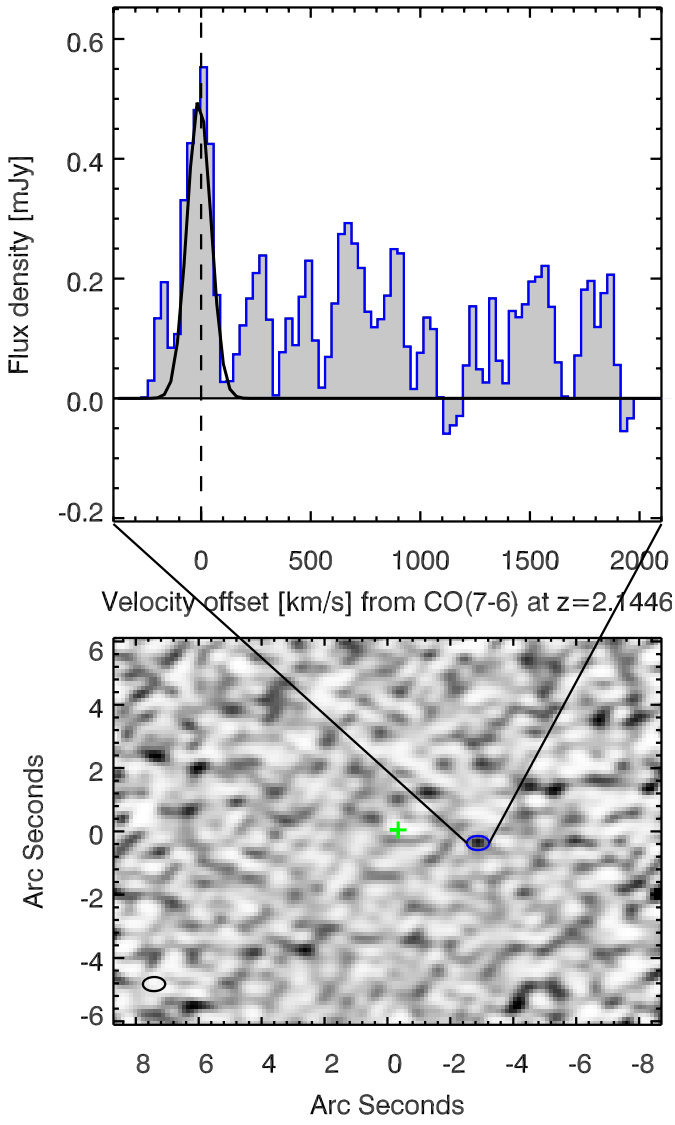

Figure 4.6: *Bottom panel:* Moment-0 map of the CO(7–6) emission at the position of the brightest companion. *Top panel:* The spectrum extracted from the beam size area shown by the light blue ellipse at the position of the companion sources in the bottom panel and is binned to 30 km/s channels. The spectrum shows both the continuum and CO(7–6) line emission. The redshift of the line is consistent with the optical $z = 2.1446$ (Kuiper et al., 2011) which was taken as zero velocity in the spectrum.

Transition	Frequency	Position		SdV	FWHM	
	GHz	RA	dec	Jy km/s	km/s	km/s
West						
H_2O	752.03	11:40:48.82	-26:29:9.580	0.05 ± 0.01	230 ± 50	—
East						
H_2O	752.03	11:40:48.11	-26:29:9.970	0.1 ± 0.02	350 ± 70	—
component 1						
CO(7–6)	806.65	11:40:48.33	-26:29:8.582	0.13 ± 0.02	435 ± 85	—
[CI]2-1	809.34	11:40:48.33	-26:29:8.582	0.66 ± 0.02	270 ± 15	—
component 2						
CO(7–6)	806.65	11:40:48.36	-26:29:8.822	0.11 ± 0.01	230 ± 35	—
[CI]2-1	809.34	11:40:48.36	-26:29:8.822	0.79 ± 0.03^a	1100 ± 65	205 ± 20
component 1+ component 2						
H_2O	752.03	11:40:48.33	-26:29:8.582	$< 0.9^b$	—-	—
CO(7–6)	806.65	11:40:48.33	-26:29:8.582	0.28 ± 0.02	720 ± 110	—
[CI]2-1	809.34	11:40:48.33	-26:29:8.582	1.30 ± 0.03	420 ± 30	280 ± 40
Companion #10						
CO(7–6)	806.65	11:40:48.15	-26:29:09.075	0.08 ± 0.01	130 ± 20	—

Table 4.2: The H_2O, [CI]2–1 and CO(7–6) emission line positions, velocity integrated fluxes and FWHMs. Fluxes and fitted FWHMs are given for [CI]2–1 component 1, 2, total and the H_2O components. The spectra are extracted within a synthesised beam size which for the [CI]2–1 observations is $0\farcs72 \times 0\farcs45$ with pa 87.4° and for the H_2O observations is $0\farcs94 \times 0\farcs56$ with pa −84.1°. [a]The [CI]2–1 flux is composed of 0.63 ± 0.03 Jy km/s for the broad velocity gas, and 0.16 ± 0.03 Jy km/s for the narrow velocity gas. [b]The 3σ upper limit of the H_2O emission taking to be $3\times$ the RMS in 60 km/s wide channels and assuming a width of the line to be that of the CO(7–6) line.

and no H_2O emission line is detected at the position of the HzRG (see Fig. 4.7) down to an RMS of 40 μJy in 60 km/s wide channels; assuming the 720 km/s width of the CO(7–6) line from the total spectrum, yields a 3σ upper limit of 0.9 Jy km/s.

4.4 Analysis and discussion

The lines we have detected in the Spiderweb Galaxy are useful for a wide range of gas diagnostics. The atomic forbidden line of carbon, [CI]2-1, is a good tracer of relatively diffuse, low extinction molecular gas (e.g. Papadopoulos et al., 2004), as its line strength is linearly proportional to the column density of molecular gas (Glover et al., 2015). CO(7–6) emission is strong in dense, highly excited optically thick molecular gas. The thermal dust continuum over the range of a few 100 GHz represents the cooling of dust heated by the intense stellar and AGN radiation fields within the Spiderweb Galaxy. The H_2O $2_{11} - 2_{02}$ line is excited both in slow shocks ($10 - 40$ km/s) in dense molecular gas (10^{3-5} cm^{-3}; Flower & Pineau Des Forêts, 2010) or by IR pumping (e.g. van der Werf et al., 2011). Thus our data, in principle, probe a wide range of conditions and heating/excitation mechanisms in (relatively dense) molecular and atomic gas.

4.4.1 Diffuse and dense molecular gas

Line velocity profiles

Fitting of Lorentzian and Gaussian profiles for the emission line shows that the [CI]2-1 and CO(7–6) lines component 1 and 2 have very different velocity profiles. Figure 4.8 compares the velocity profiles of the [CI]2-1 and CO(7–6) emission lines for component 1 (left), component 2 (middle) and the total (right). Both the [CI]2-1 and CO(7–6) emission lines of component 1 are broad, but though [CI]2-1 and CO(7–6) do not trace exactly the same phases of the molecular gas, the broadness of the two lines does suggest that the two phases are related. The velocity profiles of the [CI]2-1 and CO(7–6) lines for component 2 show similarities between the narrow [CI]2-1 component and the CO(7–6) line. The broad [CI]2-1 component is not seen in the CO(7–6) line because of both limited spectral coverage of our observations on the high velocity end of our bandpass, and limited S/N of this faint line. The fact that the narrow velocity gas in component 2 is detected in both [CI]2-1 and CO(7–6) emission and with similar FWHM indicate that this is a well-defined object. High spatial resolution observations would be required to determine if this is a separate self-gravitating object, or a kinematic feature within the same physical object. The broadness of the CO(7–6) emission in the total spectrum indicates that this emission is dominated by the CO(7–6) emission from component 1.

The CO(7–6) lines for both component 1 and 2, show an offset from the systemic redshift of $\sim 90 - 100$ km/s. A similar offset between the [CI] and CO lines is seen in a study of H1413+117 (the Cloverleaf Galaxy) by Weiß et al. (2003). They conclude that the reason for the shift is unclear, but that gravitational amplification should not alter the frequency of the lines, unless the distribution of the [CI] and CO emitting gas is different.

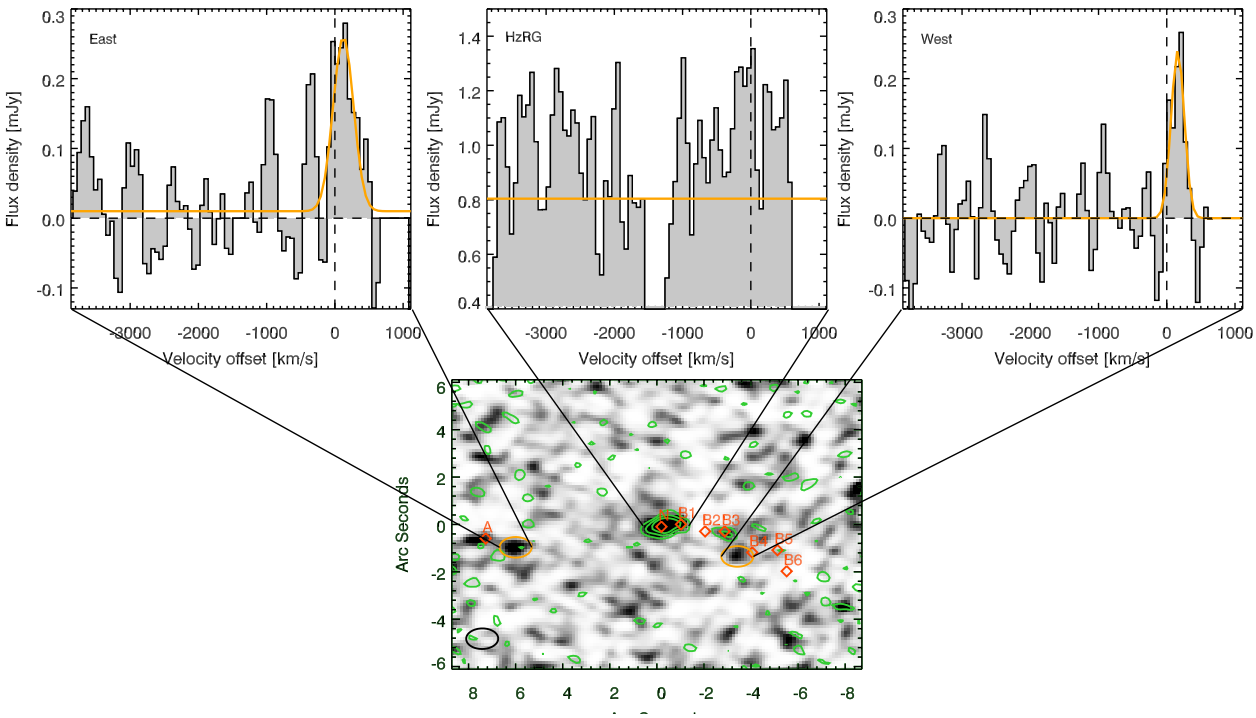

Figure 4.7: The non-continuum subtracted H_2O spectra for the detection of the west and east and the non detection at the position at the HzRG and H_2O moment-0 map. *Top left panel:* The H_2O line detected ~ 50 kpc to the east of the radio core, has a 3.7σ significance. The emission is located due west of the knot A in the radio jet. The fitted Gaussian is over-plotted in orange. *Top middle panel:* Spectrum at the position of the radio core, shows no detection of H_2O emission – only continuum emission. A small separation between the two spectral windows results in the gap in the continuum between -1300 and -1500 km/s. *Top right panel:* The H_2O line detected ~ 25 kpc to the west of the radio core, showing a 4σ H_2O detection at the expected frequency for $z = 2.161$. The emission is located at the bend of the radio jet, B4 (Pentericci et al., 1997). The best fit Gaussian is over-plotted in orange. *Bottom panel:* Moment-0 map of the H_2O emission (*without* continuum subtraction), overlaid with the 246 GHz continuum emission in green contours. The orange ellipses mark the H_2O emission and the orange-red diamonds the positions of the knots in the radio jet given by Pentericci et al. (1997).

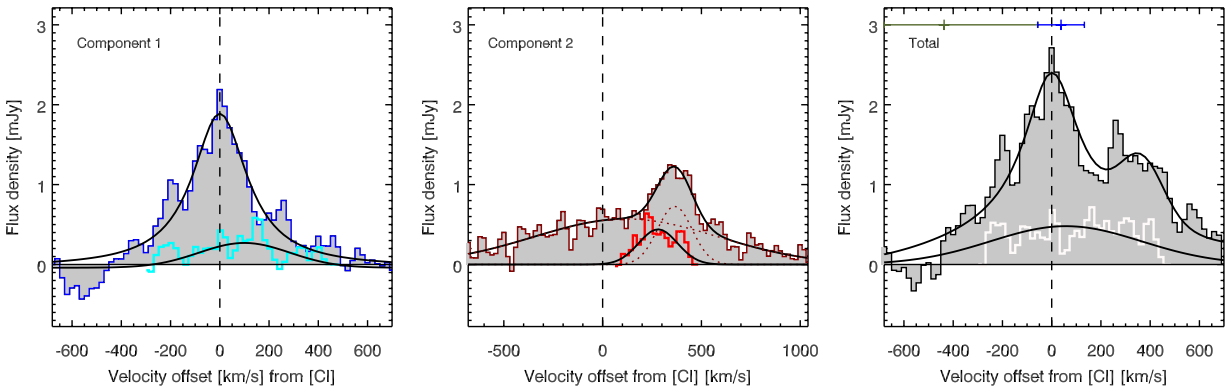

Figure 4.8: The [CI]2–1 spectra (dark blue, dark red and black histograms) for component 1, component 2 and the total over-plotted with the respective CO(7–6) lines (light blue, orange and white histograms) to compare the velocity profiles. The fitted profiles from § 4.3 are over-plotted as black curves, with the individual velocity components as dotted lines. The narrow [CI]2–1 component of component 2 is offset by 365 km/s from the systemic redshift. The bar above the velocity profiles in the right plot, marked the HeII redshift and errors (olive bar) from Roettgering et al. (1997) and the CO(1–0) redshift and error (blue bar) from Emonts et al. (2013).

The [CI] and CO lines for the Cloverleaf Galaxy have low S/N, Weiß et al. (2003) therefore conclude that high S/N observations are necessary to confirm the offset and its origin, but that, if it is genuine, it is most likely due to opacity effects. Since we here see a similar offset for the Spiderweb Galaxy, which is an un-lensed source, differential lensing cannot be the cause of this offset, however, differences in the opacity of the two lines can. The CO(7–6) line has a higher optical depth ($\tau_{\mathrm{CO(7–6)}} = 1 - 10$, Spilker et al. 2014) than the [CI]2-1 line ($\tau_{\mathrm{[CI]}} = 0.1$, Weiß et al. 2003), meaning that the CO(7–6) emitted photons go through internal absorption and emission. The line photons whose frequencies have been shifted away from the systemic frequency of the CO(7–6) emission line, have a higher probability of escaping, thus shifting the overall observed frequency.

The Hα line for the Spiderweb Galaxy was detected with SINFONI (Nesvadba et al., 2006) and ISAAC (Humphrey et al., 2008). The Hα (λ 6550), [NII] (λ 6585) lines and [SII] ($\lambda\lambda$ 6718, 6733) doublet are spectrally very close and the lines are therefore blended together. Both studies fit the blended lines with multiple Gaussians. Nesvadba et al. (2006) finds FWHM = 14900 km/s for the AGN component and FWHM $<$ 2400 km/s for the emission originating from a region surrounding the AGN. This is the same order of magnitude as what Humphrey et al. (2008) find by fitting a six Gaussian profiles, including two Hα components. These two Hα components consist of a transmitted broad line region from the AGN (FWHM = 13900 $\pm$ 500 km/s), and a component with FWHM = 1200$\pm$80 km/s. The relatively low spectral resolution of the ISAAC spectrum does not allow for a further de-blending of the lines. However, the Hα line profile does show the presence of a broad and narrow component, similar to what we observe in the [CI]2-1 emission of component 2. This strengthens the idea that the [CI]2-1 emission traces the bulk of the gas in the galaxy,

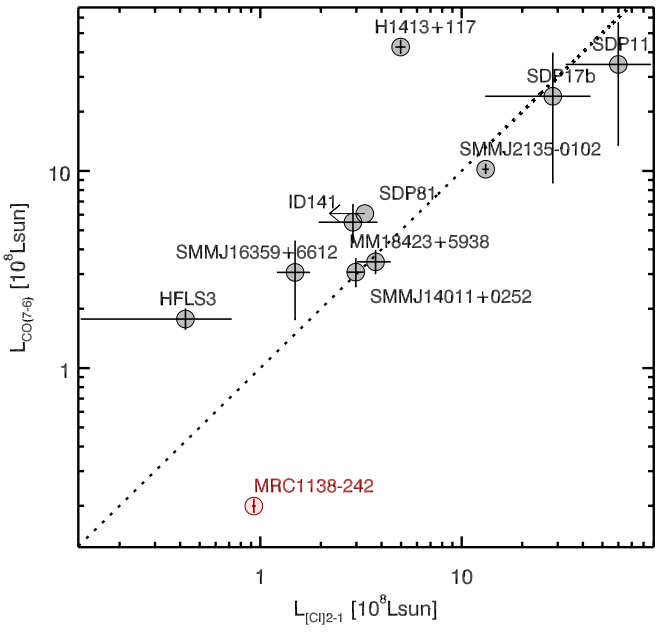

Figure 4.9: The CO(7–6) vs the [CI]2-1 luminosity for a sample of high-z SMGs and QSO (grey circles) and the Spiderweb Galaxy (red circles). The dotted curve is the 1-1 relation.

which is consistent with the [CI] emitting gas being distributed throughout and generally tracing gas of moderate extinctions and relatively low density molecular gas (Papadopoulos et al., 2004).

The large widths of the lines can be explained as a gas-rich merger. The SINFONI spectral study of the Spiderweb Galaxy by Kuiper et al. (2011) shows dynamics of the galaxies surrounding the radio galaxy itself. They detected rest-frame optical emission lines with line centres covering a velocity range of ∼1500 km/s ($2.158 < z < 2.173$), which suggests two groups (or regions) of galaxies likely flowing into the circum-galactic environment. The velocity distribution they find in the satellite galaxies is bi-modal in redshift, with the redshifted and blue shifted galaxies on approximately opposite sides in projection of the radio galaxy. Comparing this distribution of velocities and galaxies with a massive halo at $z \sim 2$ in the Millennium Simulation, shows similar velocity differences and dispersions of satellite galaxies. Kuiper et al. (2011) conclude that the Spiderweb Galaxy is best described by a merger of two galaxy groups or flows. This merger scenario can likewise explain the broad [CI]2-1 and Hα emission lines seen in the immediate region of the radio galaxy although the velocities of the [CI]2-1 or CO is in general much smaller (see also Emonts et al., 2015a, in prep.).

Line ratios

The utility of using the [CI] emission lines as tracers of the H_2 column density has been examined by Papadopoulos et al. (2004) by considering the [CI]2-1 to CO line ratio. The

Source	z	μ	$SdV_{\mathrm{CO(7–6)}}$ [Jy km/s]	$SdV_{\mathrm{[CI]}}$ [Jy km/s]	reference
SDP.11	1.7860	18	18 ± 14	31 ± 14	Lupu et al. (2012); Ferkinhoff et al. (2014)
SDP17.b	2.3080	4.3	11 ± 7	13 ± 7	Lupu et al. (2012)
SMMJ2135-0102	2.3259	32.5	12.6 ± 0.6	16.2 ± 0.6	Danielson et al. (2011)
SMMJ16359+6612	2.5160	22	3.3 ± 1.4	1.6 ± 0.3	Kneib et al. (2005); Walter et al. (2011)
H1413+117	2.5585	11	44.6 ± 3.1	5.2 ± 0.3	Alloin et al. (1997); Weiß et al. (2003)
SMMJ14011+0252	2.5650	23	3.2 ± 0.5	3.1 ± 0.3	Downes & Solomon (2003); Walter et al. (2011)
SDP.81	3.0370	9.5	12 ± 4	< 6.5	Lupu et al. (2012)
MM18423+5938	3.9296	12	3.9 ± 0.5	4.2 ± 0.8	Lestrade et al. (2010)
ID141	4.2430	10-30	6.5 ± 1.4	3.4 ± 1.1	Cox et al. (2011)
HFLS3	6.3369	2.2	2.2 ± 0.3	0.5 ± 0.4	Riechers et al. (2013)
			$SdV_{\mathrm{H_2O}}$ [Jy km/s]	L_{IR} [$10^{13}\,L_\odot$]	reference
SDP9	1.574	8.5	14.4 ± 1.1	4.4	Lupu et al. (2012)
NAv1144	2.202	5.3	7.5 ± 0.9	5.7	Omont et al. (2013)
G15v2779	4.244	4.1	4.1 ± 0.6	8.5	Omont et al. (2013)
APM08279+5255	3.912	4.0	< 1.1	20	van der Werf et al. (2011); Walter et al. (2011)
HFLS3	6.3369	2.2	2.6 ± 0.8	4.2	Riechers et al. (2013)

Table 4.3: SMGs and QSOs from the literature with published [CI]2–1, CO(7–6) and H_2Odetections along with published IR luminosities used for comparison to the Spiderweb Galaxy.

[CI] lines, [CI]$^3P_1 \rightarrow^3 P_0$ ([CI]1–0) and [CI] $^3P_2 \rightarrow^3 P_1$ ([CI]2-1), have critical densities of $n_{\rm cr,[CI]1\text{-}0} \sim 500\,{\rm cm}^{-3}$ and $n_{\rm cr,[CI]2\text{-}1} \sim 10^3\,{\rm cm}^{-3}$, similar to that of CO(1–0) and CO(2–1), which are often used as H_2 tracers. The [CI] lines have low to moderate optical depths ($\tau \approx 0.1-1$, Weiß et al. 2003), which means that these lines have the advantage, compared to CO, of tracing higher column-density cold diffuse molecular gas. The [CI] lines are also more easily excited. These properties make the [CI] lines more direct tracers of the molecular gas mass than the optically thick ^{12}CO lines. Though the H_2-tracing capability of [CI] decreases for low metallicities, Papadopoulos et al. (2004) conclude it is still a better H_2 tracer than ^{12}CO (see also Glover et al., 2015).

The ground-state transition, [CI]1-0, is the most direct H_2 gas mass tracer of the two [CI] lines because it is (relatively) less sensitive to the excitation conditions of the gas. However, the [CI]2-1 is still a much better tracer of the H_2 gas than the CO(7–6) line at similar frequency. The much higher critical density of the CO(7–6) line of $n_{\rm cr,CO(7\text{-}6)} \sim 3\times10^6\,{\rm cm}^{-3}$ and higher excitation energy of $E_{76}/k \sim 155\,{\rm K}$, compared to $E_{21}/k \sim 62\,{\rm K}$ for the [CI]2-1 line, means that the [CI]2-1 and CO(7–6) lines are unlikely to trace exactly the same molecular gas phases. The CO(7–6) line is likely tracing the higher density, more highly excited molecular gas.

We searched the literature for high-z sources with observations of both the [CI]2-1 and CO(7–6) emission lines and determined IR luminosities, and find nine lensed sub-millimetre galaxies (SMG) and QSOs (see Table 4.3). To compare the lensed sources and the un-lensed Spiderweb Galaxy, which have different luminosities, we normalise the [CI]2-1 and CO(7–6) line luminosities by the IR luminosity, which cancels out the lensing magnification for the lensed sources (assuming there is no differential lensing between the IR and line emission). Figure 4.9 shows a positive correlation between these normalised line luminosities. The only outlier in the comparison sample is the highly lensed Cloverleaf galaxy (Alloin et al., 1997; Weiß et al., 2003; van der Werf et al., 2011). The Spiderweb Galaxy is an outlier, but on the low side of the correlation.

Possible causes of observed line ratio

The Spiderweb Galaxy is, like the Cloverleaf galaxy, an outlier compared to lensed galaxies. This unusually low CO(7–6)/[CI]2-1 line ratio can be due to the Spiderweb Galaxy being an extraordinary HzRG, with a highly unusual ratio between the diffuse and dense molecular gas, or due to impact of cosmic-ray heating and ionisation, or differential lensing.

Comparing $L'_{\rm CO(7-6)} = 1.2\times10^{10}\,{\rm K\,km/s\,pc^2}$ with $L'_{\rm CO(1-0)} = 6.5\times10^{10}\,{\rm K\,km/s\,pc^2}$ (Emonts et al., 2013), we find that the CO(7–6) emission is only 18% of the value for thermalised gas. This indicates that the molecular gas phase is not thermalised and dominated by the cold and diffuse gas, traced by the [CI]2-1 emission line [1]. Alternatively, a fraction of the CO in the Spiderweb Galaxy may be dissociated by cosmic-rays, increasing the fraction of atomic carbon in the molecular gas without strongly affecting the excitation of

[1]Note, however, that the high spatial resolution of the ALMA observation means that up to 2/3 of the CO(7–6) emission may not be detected due to lack of sensitivity to very extended, low surface-brightness line emission (Emonts et al. 2016, in prep).

[CI]2-1 or the ionisation state of carbon (Bisbas et al., 2015). In the circum-nuclear region of a powerful radio galaxy, it is likely that cosmic-rays may have a significant impact on the nature of the molecular gas. More observations of other atomic and molecular species in the Spiderweb Galaxy are necessary to investigate this quantitatively.

However, since the comparison sample are all lensed galaxies, the difference could also be caused by differential lensing in the comparison sample. Dense (traced by CO(8–7)) and diffuse (traced by [CI]2-1) gas in galaxies is may be subject to differential lensing, where the emission from the densest gas have a higher overall magnification than the diffuse gas. Serjeant (2012) showed that for lensing magnifications $\mu > 2$, the CO ladder can be strongly distorted by differential lensing. Since all the SMGs and QSOs listed in Table 4.3 have a magnification $\mu > 2$ it may be that their line ratios are all influenced by the affect of differential lensing. If so, this implies that the CO(7–6) emission likely has a higher magnification than the [CI]2-1 emission, which would mean that the intrinsic CO(8–7)/[CI]2-1 ratio would be lower. We note however, that although some of the data are limited by S/N and/or low resolution, the line profiles of CO(7–6) and [CI]2-1 are consistent with each other (see references listed in Table 4.3). While not conclusive, the similarity of their dynamics suggests that the gas probed by CO(7–6) and [CI]2-1 follow the same over all dynamics and are perhaps not strongly affected by differential lensing.

We are planning to extend our ALMA [CI] observations to eight HzRGs to verify if this low CO/[CI] ratio is a common feature and also more detailed studies of the Spiderweb Galaxy to investigate this puzzle.

4.4.2 Cooling of the post-shock gas due to slow molecular shocks in halos

Interestingly, the two regions of H_2O emission that we detect do not appear to be associated with significant dust continuum emission. This is a puzzle as a close association between a dense gas tracer such as the H_2O and dust is expected, as the excitation of the H_2O emission in other high-z (lensed) sources has been attributed to IR pumping (van der Werf et al., 2011; Omont et al., 2013). Moreover, no H_2O emission is detected at the position of the HzRG (Fig. 4.7), which is surprising given its strong IR emission and high rate of mechanical energy injection via the radio jets (Fig. 4.7). Specifically, Omont et al. (2013) detected H_2O seven high-z lensed sources from the H-ATLAS survey. Five were detected in H_2O $2_{11} - 2_{02}$ emission, and three in H_2O $2_{02} - 1_{11}$ emission. Comparing these H_2O detections to the 8-1000 μm IR luminosity Omont et al. (2013) find a correlation between the IR and H_2O line luminosity of $L_{H_2O} = L_{IR}^{1.1-1.3}$, with the exact exponent depending on which of the two H_2O lines is used in the analysis. From this relation, they conclude that IR pumping is the most likely mechanism for exciting the water molecules and their line emission. This is consistent with H_2O tracing dense gas surrounding regions of intense star formation. Furthermore, a similar conclusion was reached in a somewhat more detailed study of the H_2O emission from the lensed QSO, APM 08279+5255 at $z = 3.9$ (van der Werf et al., 2011). In order to constrain the excitation of H_2O, van der Werf et al. (2011)

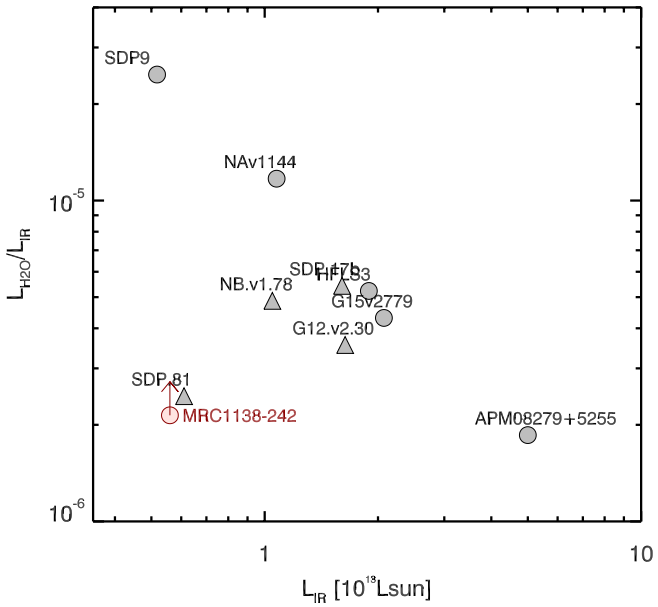

Figure 4.10: The $L_{\mathrm{H_2O}}/L_{\mathrm{IR}}$-ratio versus *intrinsic* L_{IR} for the H_2O detections from Omont et al. 2013 along with the H_2O detection for the Spiderweb Galaxy. The grey circles are sources from Omont et al. 2013 with directed detections of the $2_{02}-1_{11}$ line and the grey triangles are sources with $2_{11}-2_{02}$ detection scaled using Mrk231 as a template to get an estimate on the $2_{02}-1_{11}$ luminosity. The Spiderweb Galaxy is marked with the red point. We here plot the summed H_2O emission of the Western and Eastern detection, as the IR luminosity is integrated over the full source.

observed four H_2O lines with a range of excitation energies ($3_{2,1}-3_{1,2}$, $4_{22}-4_{13}$, $2_{02}-1_{11}$, and $2_{11}-2_{02}$). Crucially, they were able to tightly constrain the brightness of a very low lying level of H_2O (the $1_{10}-1_{01}$ line), which is predicted to be strong in collisionally excited gas (Flower & Pineau Des Forêts, 2010). Thus while the strength and ratios of the more highly excited lines, such as $2_{02}-1_{11}$ and $2_{11}-2_{02}$ were consistent with collisionally excited gas, the relative weakness of the H_2O $1_{10}-1_{01}$ line ruled out this excitation mechanism. IR pumping is able to produce such strong high transition lines (i.e. the $3_{21}-3_{12}$ and $4_{22}-4_{13}$) compared to the lower transitions (i.e. the $2_{02}-1_{11}$ and $2_{11}-2_{02}$) and very weak $1_{10}-1_{01}$ line. The same conclusions have been obtained at low redshift by Yang et al. (2013), who use 45 H_2O emission lines at different rotational levels.

Figure 4.10 plots $L_{\mathrm{H_2O}}/L_{\mathrm{IR}}$ versus L_{IR} and shows an anti-correlation for IR luminous high-z lensed sources (Omont et al., 2013; van der Werf et al., 2011). SDP.81 is an outlier in this relation, most likely due to an underestimating of the H_2O luminosity because of low S/N in the spectrum, and the large extent of the source (Omont et al., 2013). We plot the Spiderweb Galaxy as the sum of the H_2O luminosities of the western and eastern detections and the total infrared luminosity. The H_2O emission originates from two small regions, and any more widespread emission would not be detected due to the lack sensitivity of our ALMA data on larger spatial scales. The IRAM Plateau de Bure observations of the comparison sample of Omont et al. (2013) have 2 to 7× larger synthesised beam sizes, and may be more sensitive to emission at larger scales. The $L_{\mathrm{H_2O}}/L_{\mathrm{FIR}}$ ratio for the Spiderweb

Galaxy is therefore a lower limit and shows that it is an outlier in this trend. The lack of 246 GHz continuum emission at the H_2O positions, which would imply a much larger deviation from the trend, implies that the emission is not pumped by the IR emission. The H_2O detection is spatially located at the bend in the radio continuum emission (knot B3) and upstream to the radio jet. Similarly, the eastern H_2O detection upstream from knot A in the radio emission, is likely associated with the jet which is projected onto the plane of the sky. The most straight-forward explanation for the H_2O emission at these positions, the lack of associated significant 246 GHz continuum emission, and the offset from the anti-correlation in Fig. 4.10, is that the H_2O emitting gas is shock-heated and represents strong cooling in post-shock heated gas by the passage of the radio jet. After the shock impact, the molecular gas cools via H_2O emission lines and various other species (Flower & Pineau Des Forêts, 2010). The small offset of the line peaks from the systemic [CI]2-1 redshift and the narrow average line width of 290 km/s of the two H_2O lines, suggest slow shocks within a very turbulent medium. In other words, the width of the lines represents the dispersion of the clouds within which the mechanical energy is being dissipated. Please note that H_2O is one of the main carriers of oxygen along with CO, but has many more radiative degrees of freedom, meaning that it can lose energy efficiently under a wide range of (low energy) excitation conditions and thus contribute significantly to the overall cooling of dense molecular gas (see discussion in Flower & Pineau Des Forêts, 2010). Moreover, we emphasise that due to the position of the H_2O emission in our bandpass, higher negative offset velocity emission, such as that from companion # 10 would not lie within our bandpass (Kuiper et al., 2011).

Furthermore, it is unlikely that the dense molecular gas has been entrained during the passage of the radio jet and lifted out of the radio galaxy or any of its companions. There are several reasons why this is unlikely. First, both regions of H_2O emission are almost at the systemic velocity of the radio galaxy (as determined from CO(1-0), [CI]2-1 or CO(8–7)). The H_2O lines have systemic velocities that are significantly lower than any of the companion galaxies with determined redshifts near the sites of H_2O emission. Second, the cooling time of the dense shock gas is of-order $10^3 - 10^4$ yr for a 20 km/s shock driven into a gas with a density of $10^5\,\mathrm{cm}^{-3}$ (Flower & Pineau Des Forêts, 2010), much shorter than any plausible dynamical time. These facts suggest that the dense molecular gas is forming in situ in the post-shocked gas after the passage of the radio jet. It is not surprising, within this context, to see the emission near the bend in the jet and near the terminal hot spot of the western radio lobe as these are sites where the interaction between the jet and ambient medium are likely to be strong. In such strong interaction zones, dissipation of energy in a turbulent cascade is important (e.g. Guillard et al., 2010). The eastern terminal lobe of the jet is, for example, the working surface of the jet as it propagates outwards, just the region where you would expect strong dissipation of the bulk kinetic energy of the jet.

The molecular gas likely formed *in situ* in the post-shock gas, which has important implications for the state of the circum-galactic halo and cluster gas. Recent observations of the Spiderweb Galaxy using ATCA discovered a large region of CO(1–0) surrounding the HzRG with strong emission near some of the radio knots and lobes suggesting that the passage of the radio jet enhances the molecular column densities (Emonts et al. in prep.).

Finding strong H_2O line emission near the radio jet provides evidence of the formation of molecular gas in the post-shocked gas of the expanding radio source (see Guillard et al., 2010, 2012; Appleton et al., 2013, for a discussion of this mechanism in the violent collision in the Stephan's Quintet group). This is also substantiated by the low relative velocities of the H_2O emission which are consistent with the low velocities observed in the extended diffuse CO emission. Such a mechanism might also explain the distribution of the CO emission observed in local clusters (Salomé et al., 2011) and around other HzRGs (Emonts et al., 2014, and references therein). Finding H_2O emission indicating strong dissipation of the bulk kinetic energy of expanding radio jets provides a direct link between the jets and the formation of molecular gas and stars in the halo of the radio galaxy.

4.4.3 Mass Estimates

As argued above, the [CI]2-1 line is a better tracer of the cold molecular gas than the high-J CO lines, due to their lower critical density. We therefore use the [CI]2-1 to estimate the total molecular gas mass, following the approach of Papadopoulos et al. (2004) and Alaghband-Zadeh et al. (2013):

$$M_{\rm H_2} = 1375.8\, D_L^2\, (1+z)^{-1} \left[\frac{X_{\rm [CI]}}{10^{-5}}\right]^{-1} \times \left[\frac{A_{21}}{10^{-7}{\rm s}^{-1}}\right]^{-1} Q_{21}^{-1} \left[\frac{S_{\rm [CI]2\text{-}1} dV}{\rm Jy\,km\,s^{-1}}\right], \qquad (4.1)$$

where $X_{\rm [CI]}$ is the [CI]-to-H_2 abundance for which we adopt the literature-standard of 3×10^{-5}, Q_{21} is the density dependent excitation factor for which we assume the median value of 0.57 (see Papadopoulos et al., 2004), and A_{21} is the Einstein A coefficient of $2.68 \times 10^{-7}\,{\rm s}^{-1}$. We find a total H_2 molecular gas mass for both components of $3.3 \times 10^{10}\,{\rm M}_\odot$. We note that this value depends on the adopted Q_{21}: for the highest $Q_{21} = 1.0$, the $M(H_2)$ drops to $2.2 \times 10^{10}\,{\rm M}_\odot$, while for the lowest $Q_{21} = 0.15$, the $M(H_2)$ is $1.5 \times 10^{11}\,{\rm M}_\odot$ The median value is close to $M(H_2) = 6 \times 10^{10}\,{\rm M}_\odot$ derived from CO(1-0) (Emonts et al., 2013). This total mass of diffuse molecular gas as probed by the [CI]2-1 emission is clearly higher than the warm ($T > 300\,{\rm K}$) molecular gas mass of order 10^7 to $10^9\,{\rm M}_\odot$ (Ogle et al., 2012) which suggest an order of magnitude ratio of warm-to-cold molecular gas between $0.1 - 10\%$. Ogle et al. (2012) suggest that the gas is heated by the radio jet from the AGN interacting with the ambient ISM of the HzRG. Furthermore, Nesvadba et al. (2006) find a mass of ionised gas of $\sim 3 \times 10^9\,{\rm M}_\odot$. The gas masses of various components of the ISM of the HzRG are up to one order of magnitude lower than the stellar mass of $< 1.8 \times 10^{12}\,{\rm M}_\odot$ (De Breuck et al., 2010), suggesting that this is already a quite evolved galaxy.

For component 2, the H_2 gas mass of the broad component is $1.6 \times 10^{10}\,{\rm M}_\odot$. We use this to constrain the size of this region by knowing that $M(H_2) < M_{\rm dyn} = R \cdot v^2/G$, and the velocity from the FWHM (see Table 4.2) we find that $R < 60\,{\rm pc}$. Though uncertain, this region has a size comparable to those of the obscuring torus and the inner narrow line regions of QSOs, thus suggesting the presence of an additional radio quiet AGN, merging with the radio loud AGN in component 1 (Emonts et al., 2015a). Applying the same

Component	M_d [$M_\odot$]	L_{FIR} [$L_\odot$]	SFR [$M_\odot\,yr^{-1}$]
HzRG	$< 6.1 \times 10^8$	$< 4.4 \times 10^{12}$	< 440
companion #8	$< 8.5 \times 10^7$	$< 6.2 \times 10^{11}$	< 62
companion #10	$< 6.5 \times 10^7$	$< 4.7 \times 10^{11}$	< 47
Sum	—	$< 5.4 \times 10^{12}$	< 549
Water (West)	$< 7.0 \times 10^7$	$< 5.7 \times 10^{11}$	< 57
Water (East)	$< 7.0 \times 10^7$	$< 5.7 \times 10^{11}$	< 57

Table 4.4: The estimated dust masses, FIR luminosities and SFRs for the HzRG and companions using the measured and listed in Table 4.1 and equation 1-5. The dust masses, FIR luminosities and SFRs are all upper limits, as the HzRG and companion #10 have contribution from synchrotron emission and companion #8 is a tentative detection.

methods on component 1, which has a H_2 gas mass of $1.7 \times 10^{10}\,M_\odot$, puts an upper limit of 1 kpc on the size of the emitting region.

To determine the dust mass, we need to integrate over the full SED of the dust emission. As we only have a single observation at 235 GHz, we fix the shape of the SED by assuming a greybody characterised by $\beta = 1.5$ and $T_d = 40\,K$. Following the approach of De Breuck et al. (2003), using,

$$M_d = \frac{S_{\rm obs} D_L^2}{(1+z)\kappa_d(\nu_{\rm rest}) B(\nu_{\rm rest}, T_{\rm d})}, \tag{4.2}$$

where $S_{\rm obs}$ is the flux density at the observed frequency, D_L is the luminosity distance, $\kappa_d(\nu_{\rm rest})$ is the rest-frequency mass absorption coefficient, which we here calculate by scaling the 850 μm absorption coefficient of $0.076\,m^2\,kg^{-1}$ from Stevens et al. (2003) to 246 GHz and $B(\nu_{\rm rest}, T_{\rm d})$ is the the Planck function for isothermal dust grain emission at a dust temperature $T_{\rm d}$ (De Breuck et al., 2003), we derive a dust mass of $M_d = 6.1 \times 10^8\,M_\odot$ for the HzRG. This is marginally higher than what was estimated by Stevens et al. 2003 of $4.6 \times 10^8\,M_\odot$ using the 850 μm flux peak flux.

Using the same approach and assumed dust temperature, we find the dust masses of the two companions #8 and #10 (see Table 4.4).

4.4.4 Star-formation rate

Using *Spitzer* and *Herschel* PACS+SPIRE photometry, Seymour et al. (2012) showed that the strong AGN and vigorous star-formation contribute with roughly equal shares to the IR luminosity in the Spiderweb Galaxy. While the AGN component dominates at the high frequency end of the thermal dust emission, the star-formation is expected to contribute $> 90\%$ of the flux at the observed (comparatively low) frequencies of our ALMA data. However, the flux spectral index of the HzRG and companion #10, implies that the flux at these wavelength are likely to be contaminated by synchrotron emission. We can therefore use our continuum flux to determine upper limits on the SFR in the host galaxy and the companions.

We estimate the SFR of the HzRG and companions by fixing the dust temperature and emissivity index (as for the dust masses), and calculating $L_{\rm FIR}$ using:

$$L_{\rm FIR} = 4\pi M_d \int_0^\infty \kappa_d(\nu_{\rm rest}) B(\nu_{\rm rest}, T_{\rm d}) d\nu, \tag{4.3}$$

which yields

$$L_{\rm FIR} = 4\pi\Gamma[\beta+4]\zeta[\beta+4] D_L^2 x^{-(\beta+4)}(e^x-1) S_{\rm obs}\nu_{\rm obs}, \tag{4.4}$$

where Γ and ζ are the Gamma and Riemann ζ functions and $x = h\nu_{\rm rest}/kT_{\rm d}$ (De Breuck et al., 2003). Again assuming $\beta = 1.5$ and $T_{\rm d} = 40\,{\rm K}$, we find the $L_{\rm FIR} < 5.1\times10^{12}\,{\rm L}_\odot$ for the HzRG, and $< 7.2\times10^{11}\,{\rm L}_\odot$ for companion #8 and $< 5.4\times10^{11}\,{\rm L}_\odot$ for companion #10 (see Table 4.4). Using,

$${\rm SFR} = \delta_{\rm MF}\delta_{\rm SB}(L_{\rm FIR}/10^{10}\,L_\odot)\,M_\odot\,{\rm yr}^{-1}, \tag{4.5}$$

where $\delta_{\rm MF}$ is the stellar mass function and $\delta_{\rm SB}$ is the fraction of FIR emission heated by the starburst, which we assume to be unity at these long wavelengths, the $L_{\rm FIR}$ can be converted to the SFR. We assume $\delta_{\rm MF} = 1$ and derive the SFRs of $< 440\,{\rm M}_\odot$ yr^{-1} for the HzRG, $< 62\,{\rm M}_\odot$ yr^{-1} for companion #8 and $< 47\,{\rm M}_\odot$ yr^{-1} for companion #10 (see Table 4.4). The sum of the estimated FIR luminosity of the HzRG and the two companion sources is higher than the total starburst-heated IR luminosity of $5.6\times10^{12}{\rm L}_\odot$ of Drouart et al. 2014, less than the $7.9\times10^{12}{\rm L}_\odot$ of Seymour et al. (2012). We warn that our approximation of the SED with a single grey body function with an assumed emissivity index is rather crude; moreover the 246 GHz emission from the HzRG and companion #10 may also contain a contribution from synchrotron emission, which would over-estimate the SFR.

The SFRs we determine here for the HzRG and companion #10 and #8 are $\sim 10-50$ times higher than determined by Hatch et al. (2009) using optical *HST* imaging. However, the continuum emission in both the HzRG and companion #10 are contaminated by synchrotron emission.

4.5 Conclusions

We have observed the HzRG MRC1138-262 (the Spiderweb Galaxy) with ALMA Band 6 in Cycle 1 for 49 min on-source.

- We detect strong 246 GHz continuum emission at the position of the HzRG, weaker 246 GHz continuum emission for a companion to the west and tentative emission to the north. Companion #10 of Kuiper et al. (2011) at $z = 2.1446$ is the brightest of the two companions and is detected in CO(8–7), while [CI]2-1 is shifted out of the observed band. The other companion is too weak to be detected in line emission.

- The flat spectral indexes of the HzRG and companion #10 suggest a contribution to the 246 GHz continuum emission from synchrotron emission. This means the FIR luminosities and SFRs of these two components are upper limits.

- We detect strong [CI]2-1 emission in two components: one at the position of the HzRG, and one with a small offset of 0.″5 to the south-east from the central position. The [CI]2-1 emitting components show significantly different velocity profiles: component 1 shows a Lorentzian profile, and component 2 is a double Gaussian with velocity widths of 250 and 1100 km/s.

- Using the molecular gas mass estimate of the broad [CI]2-1 of component 2, we put an upper limit on the size of the emitting region of 60 pc. This size suggests the possible existence of an additional radio quiet AGN, merging with the radio loud AGN in component 1.

- The CO(7–6)/[CI]2-1 line ratio for the Spiderweb Galaxy is lower than in a comparison sample. This ratio can be due to a relatively low excitation molecular gas reservoir and/or a strong cosmic ray field which preferentially destroys CO. As the comparison sample is composed of only lensed sources from the literature, differential lensing may also have an influence, where the dense CO(7–6) gas in the comparison sample is amplified more than the more diffuse [CI]2-1 gas.

- We detect $\sim 4\sigma$ H_2O emission lines at two positions: to the west at knot B4 (at the bend) in the radio jet and to the east, upstream of knot A. No 246 GHz continuum emission is detected at the position of the H_2O emission lines, meaning that heating from IR emission cannot be the source of the H_2O emission. The positions (upstream of the two knots in the radio jet), the lack of 246 GHz continuum emission at these positions and the small offset of the line centres, are consistent with heating by slow shocks in dense molecular gas. The relatively bright H_2O emission indicates strong dissipation of the energy of the expanding jets in the halo of MRC1138-262.

Multiple studies have established that the Spiderweb Galaxy is a system of merging galaxies, and the likely progenitor of a cD galaxy. Our water detections upstream of the main radio hotspots show that the radio jets can cause the gas in the ISM and inter-cluster gas to cool, increasing the fraction of extended molecular gas (Emonts et al. 2016, in prep.). The formation of this molecular reservoir likely supports the formation of the young stars observed in the halo of MRC1138-262. The much brighter than expected [CI]2-1 emission indicates the power of this line to study the detailed distribution of the molecular gas reservoir in this intriguing source, and possibly other HzRGs.

Acknowledgements

This paper makes use of the following ALMA data: ADS/JAO.ALMA#2012.1.01087.S. ALMA is a partnership of ESO (representing its member states), NSF (USA) and NINS (Japan), together with NRC (Canada), NSC and ASIAA (Taiwan), and KASI (Republic of Korea), in cooperation with the Republic of Chile. The Joint ALMA Observatory is operated by ESO, AUI/NRAO and NAOJ.

Chapter 5

Outlook

With the commissioning of new millimetre/sub-millimetre facilities (such as ALMA) and extension and upgrade of exciting millimetre/sub-millimetre facilities (such as the PdBI to NOEMA), this is a particular interesting time to study the ISM in high-z galaxies. These facilities allow us to study the molecular and atomic star-forming and quiescent gas at high redshift in more detail and in shorter observing time than has been possible before. At the same time numerical simulations are reaching a point where they can resolve giant molecular clouds on galaxy-scales.

An important task for future studies of molecular gas is to find a reliable CO-to-H_2 conversion factor or turn to other tools for determining the H_2 mass in galaxies, such as [CI] observations. The [CI] lines have been suggested to be a better tracer of the diffuse molecular gas than low-J CO lines. But only with facilities available now has it become possible to test this theory on large samples of high-z galaxies and compare with masses estimated using low-J CO lines.

However the [CI] lines will not replace CO observations completely as the denser molecular gas is poorly traced by the [CI] lines. Though molecular lines such as HCN, CS and H_2O are gaining more and more attention to trace the dense molecular gas at high redshift, it will still be a while until these lines will provide statistical samples. CO will therefore still have a prominent role in future studies of molecular gas in high-z galaxies.

Though this is the era of millimetre and sub-millimetre studies, the power of multi-wavelength studies should not be forgotten. Combining new and cutting edge facilities and combining millimetre/sub-millimetre observations with optical or UV observations can reveal components, structures and dynamics which would have been un-detected otherwise. The combination of 3D data from ALMA and MUSE has proven to be highly efficient in unraveling emission and absorbing components which are not visible in only one data cube.

We are privileged to be in an era with facilities allowing for detailed high-z studies, and the future will bring even more facilities such as JWST, LOFAR, CCAT and many more, which will all open windows in the study of the high-z Universe and hopefully a better understanding of the evolutions of the Universe to what we see in our neighbourhood.

Bibliography

Abel, N. P. 2006, MNRAS, 368, 1949

Abel, N. P., Dudley, C., Fischer, J., Satyapal, S., & van Hoof, P. A. M. 2009, ApJ, 701, 1147

Agertz, O., Teyssier, R., & Moore, B. 2011, MNRAS, 410, 1391

Alaghband-Zadeh, S., Chapman, S. C., Swinbank, A. M., et al. 2013, MNRAS, 435, 1493

Allen, M. G., Dopita, M. A., & Tsvetanov, Z. I. 1998, ApJ, 493, 571

Alloin, D., Barvainis, R., & Guilloteau, S. 2000, ApJL, 528, L81

Alloin, D., Guilloteau, S., Barvainis, R., Antonucci, R., & Tacconi, L. 1997, A&A, 321, 24

Andrews, B. H. & Thompson, T. A. 2011, ApJ, 727, 97

Antonucci, R. R. J. & Miller, J. S. 1985, ApJ, 297, 621

Appleton, P. N., Guillard, P., Boulanger, F., et al. 2013, ApJ, 777, 66

Aravena, M., Bertoldi, F., Schinnerer, E., et al. 2008, A&A, 491, 173

Aravena, M., Hodge, J. A., Wagg, J., et al. 2014, MNRAS, 442, 558

Aravena, M., Murphy, E. J., Aguirre, J. E., et al. 2013, MNRAS, 433, 498

Archibald, E. N., Dunlop, J. S., Hughes, D. H., et al. 2001, MNRAS, 323, 417

Armus, L., Heckman, T. M., & Miley, G. K. 1990, ApJ, 364, 471

Athreya, R. M. & Kapahi, V. K. 1998, Journal of Astrophysics and Astronomy, 19, 63

Bacon, R., Accardo, M., Adjali, L., et al. 2010, in Society of Photo-Optical Instrumentation Engineers (SPIE) Conference Series, Vol. 7735, Society of Photo-Optical Instrumentation Engineers (SPIE) Conference Series, 8

Bacon, R., Vernet, J., Borisova, E., et al. 2014, The Messenger, 157, 13

Barger, A. J., Cowie, L. L., Sanders, D. B., et al. 1998, Nature, 394, 248

Barthel, P. D. 1989, ApJ, 336, 606

Baugh, C. M., Lacey, C. G., Frenk, C. S., et al. 2005, MNRAS, 356, 1191

Begelman, M. C. & Cioffi, D. F. 1989, ApJL, 345, L21

Bekki, K. 1998, ApJ, 504, 50

Benson, A. J. 2012, New A, 17, 175

Best, P. N., Kauffmann, G., Heckman, T. M., et al. 2005, MNRAS, 362, 25

Best, P. N., Longair, M. S., & Roettgering, H. J. A. 1998, MNRAS, 295, 549

Best, P. N., Röttgering, H. J. A., & Longair, M. S. 2000, MNRAS, 311, 23

Béthermin, M., De Breuck, C., Sargent, M., & Daddi, E. 2015, A&A, 576, L9

Bicknell, G. V., Dopita, M. A., Tsvetanov, Z. I., & Sutherland, R. S. 1998, ApJ, 495, 680

Bicknell, G. V., Sutherland, R. S., van Breugel, W. J. M., et al. 2000, ApJ, 540, 678

Bigiel, F., Leroy, A., Walter, F., et al. 2008, AJ, 136, 2846

Binette, L., Kurk, J. D., Villar-Martín, M., & Röttgering, H. J. A. 2000, A&A, 356, 23

Bisbas, T. G., Papadopoulos, P. P., & Viti, S. 2015, ApJ, 803, 37

Blain, A. W. & Longair, M. S. 1993, MNRAS, 264, 509

Blain, A. W., Smail, I., Ivison, R. J., Kneib, J.-P., & Frayer, D. T. 2002, Phys. Rep., 369, 111

Blumenthal, G. & Miley, G. 1979, A&A, 80, 13

Blundell, K. M. & Rawlings, S. 1999, Nature, 399, 330

Blundell, K. M., Rawlings, S., Eales, S. A., Taylor, G. B., & Bradley, A. D. 1998, MNRAS, 295, 265

Boreiko, R. T. & Betz, A. L. 1996, ApJL, 467, L113

Bornancini, C. G., De Breuck, C., de Vries, W., et al. 2007, MNRAS, 378, 551

Bothwell, M. S., Aguirre, J. E., Chapman, S. C., et al. 2013a, ApJ, 779, 67

Bothwell, M. S., Chapman, S. C., Tacconi, L., et al. 2010, MNRAS, 405, 219

Bothwell, M. S., Smail, I., Chapman, S. C., et al. 2013b, MNRAS, 429, 3047

Bradford, C. M., Aguirre, J. E., Aikin, R., et al. 2009, ApJ, 705, 112

Braine, J., Gratier, P., Kramer, C., et al. 2012, A&A, 544, A55

Brauher, J. R., Dale, D. A., & Helou, G. 2008, ApJS, 178, 280

Brisbin, D., Ferkinhoff, C., Nikola, T., et al. 2015, ApJ, 799, 13

Bruzual, A. G. 2007, in IAU Symposium, Vol. 241, IAU Symposium, ed. A. Vazdekis & R. Peletier, 125–132

Bussmann, R. S., Pérez-Fournon, I., Amber, S., et al. 2013, ApJ, 779, 25

Carilli, C. L., Daddi, E., Riechers, D., et al. 2010, ApJ, 714, 1407

Carilli, C. L., Harris, D. E., Pentericci, L., et al. 2002a, ApJ, 567, 781

Carilli, C. L., Kohno, K., Kawabe, R., et al. 2002b, AJ, 123, 1838

Carilli, C. L., Röttgering, H. J. A., van Ojik, R., et al. 1997, ApJS, 109, 1

Carilli, C. L. & Walter, F. 2013, ARA&A, 51, 105

Carlstrom, J. E., Ade, P. A. R., Aird, K. A., et al. 2011, PASP, 123, 568

Carlstrom, J. E. & Kronberg, P. P. 1991, ApJ, 366, 422

Casey, C. M., Berta, S., Béthermin, M., et al. 2012, ApJ, 761, 140

Casey, C. M., Narayanan, D., & Cooray, A. 2014, Phys. Rep., 541, 45

Chabrier, G. 2003, ApJL, 586, L133

Chambers, K. C., Miley, G. K., & van Breugel, W. 1987, Nature, 329, 604

Chambers, K. C., Miley, G. K., & van Breugel, W. J. M. 1990, ApJ, 363, 21

Chapin, E. L., Pope, A., Scott, D., et al. 2009, MNRAS, 398, 1793

Chapman, S. C., Blain, A. W., Smail, I., & Ivison, R. J. 2005, ApJ, 622, 772

Code, A. D., Meade, M. R., Anderson, C. M., et al. 1993, ApJL, 403, L63

Colbert, J. W., Malkan, M. A., Clegg, P. E., et al. 1999, ApJ, 511, 721

Coppin, K. E. K., Chapman, S. C., Smail, I., et al. 2010, MNRAS, 407, L103

Cox, P., Krips, M., Neri, R., et al. 2011, ApJ, 740, 63

Crawford, M. K., Genzel, R., Townes, C. H., & Watson, D. M. 1985, ApJ, 291, 755

Crawford, M. K., Lugten, J. B., Fitelson, W., Genzel, R., & Melnick, G. 1986, ApJL, 303, L57

Croft, S., van Breugel, W., de Vries, W., et al. 2006, ApJ, 647, 1040

Croxall, K. V., Smith, J. D., Wolfire, M. G., et al. 2012, ApJ, 747, 81

Cruz, M. J., Jarvis, M. J., Blundell, K. M., et al. 2006, MNRAS, 373, 1531

Daddi, E., Elbaz, D., Walter, F., et al. 2010, ApJL, 714, L118

Dalgarno, A. & McCray, R. A. 1972, ARA&A, 10, 375

Danielson, A. L. R., Swinbank, A. M., Smail, I., et al. 2011, MNRAS, 410, 1687

Dannerbauer, H., Kurk, J. D., De Breuck, C., et al. 2014, A&A, 570, A55

Danovich, M., Dekel, A., Hahn, O., Ceverino, D., & Primack, J. 2015, MNRAS, 449, 2087

De Breuck, C., Downes, D., Neri, R., et al. 2005, A&A, 430, L1

De Breuck, C., Hunstead, R. W., Sadler, E. M., Rocca-Volmerange, B., & Klamer, I. 2004, MNRAS, 347, 837

De Breuck, C., Maiolino, R., Caselli, P., et al. 2011, A&A, 530, L8

De Breuck, C., Neri, R., Morganti, R., et al. 2003, A&A, 401, 911

De Breuck, C. & Reuland, M. 2005, in Multiwavelength Mapping of Galaxy Formation and Evolution, ed. A. Renzini & R. Bender, 374

De Breuck, C., Röttgering, H., Miley, G., van Breugel, W., & Best, P. 2000a, A&A, 362, 519

De Breuck, C., Seymour, N., Stern, D., et al. 2010, ApJ, 725, 36

De Breuck, C., van Breugel, W., Röttgering, H., et al. 2001, AJ, 121, 1241

De Breuck, C., van Breugel, W., Röttgering, H. J. A., & Miley, G. 2000b, AAPS, 143, 303

De Breuck, C., van Breugel, W., Stanford, S. A., et al. 2002, AJ, 123, 637

De Breuck, C., Williams, R. J., Swinbank, M., et al. 2014, A&A, 565, A59

De Looze, I., Baes, M., Bendo, G. J., Cortese, L., & Fritz, J. 2011, MNRAS, 416, 2712

De Looze, I., Cormier, D., Lebouteiller, V., et al. 2014, A&A, 568, A62

De Young, D. S. 1989, ApJL, 342, L59

Deane, R. P., Heywood, I., Rawlings, S., & Marshall, P. J. 2013, MNRAS, 434, 23

Decarli, R., Walter, F., Carilli, C., et al. 2014, ApJL, 782, L17

Dey, A., van Breugel, W., Vacca, W. D., & Antonucci, R. 1997, ApJ, 490, 698

Díaz-Santos, T., Armus, L., Charmandaris, V., et al. 2014, ApJL, 788, L17

Díaz-Santos, T., Armus, L., Charmandaris, V., et al. 2013, ApJ, 774, 68

Downes, D. & Solomon, P. M. 1998, ApJ, 507, 615

Downes, D. & Solomon, P. M. 2003, ApJ, 582, 37

Drouart, G., De Breuck, C., Vernet, J., et al. 2012, A&A, 548, A45

Drouart, G., De Breuck, C., Vernet, J., et al. 2014, A&A, 566, A53

Dunlop, J. S. 2011, in Astronomical Society of the Pacific Conference Series, Vol. 446, Galaxy Evolution: Infrared to Millimeter Wavelength Perspective, ed. W. Wang, J. Lu, Z. Luo, Z. Yang, H. Hua, & Z. Chen, 209

Dunlop, J. S. & Peacock, J. A. 1990, MNRAS, 247, 19

Eales, S., Dunne, L., Clements, D., et al. 2010, PASP, 122, 499

Eales, S., Rawlings, S., Law-Green, D., Cotter, G., & Lacy, M. 1997, MNRAS, 291, 593

Eales, S. A. & Rawlings, S. 1996, ApJ, 460, 68

Ellis, Jr., H. B. & Werner, M. W. 1984, in Bulletin of the American Astronomical Society, Vol. 16, Bulletin of the American Astronomical Society, 463

Emonts, B. H. C., De Breuck, C., Lehnert, M. D., et al. 2015a, ArXiv e-prints

Emonts, B. H. C., Feain, I., Röttgering, H. J. A., et al. 2013, MNRAS, 430, 3465

Emonts, B. H. C., Mao, M. Y., Stroe, A., et al. 2015b, MNRAS, 451, 1025

Emonts, B. H. C., Norris, R. P., Feain, I., et al. 2014, MNRAS, 438, 2898

Emonts, B. H. C., Norris, R. P., Feain, I., et al. 2011, MNRAS, 415, 655

Engel, H., Tacconi, L. J., Davies, R. I., et al. 2010, ApJ, 724, 233

Evans, A. S., Sanders, D. B., Mazzarella, J. M., et al. 1996, ApJ, 457, 658

Fan, X., Narayanan, V. K., Lupton, R. H., et al. 2001, AJ, 122, 2833

Farrah, D., Lebouteiller, V., Spoon, H. W. W., et al. 2013, ApJ, 776, 38

Ferkinhoff, C., Brisbin, D., Nikola, T., et al. 2011, ApJL, 740, L29

Ferkinhoff, C., Brisbin, D., Parshley, S., et al. 2014, ApJ, 780, 142

Fixsen, D. J., Bennett, C. L., & Mather, J. C. 1999, ApJ, 526, 207

Flower, D. R. & Pineau Des Forêts, G. 2010, MNRAS, 406, 1745

Frayer, D. T., Harris, A. I., Baker, A. J., et al. 2011, ApJL, 726, L22

Frayer, D. T., Koda, J., Pope, A., et al. 2008, ApJL, 680, L21

Fu, H., Cooray, A., Feruglio, C., et al. 2013, Nature, 498, 338

Gao, Y., Carilli, C. L., Solomon, P. M., & Vanden Bout, P. A. 2007, ApJL, 660, L93

Gao, Y. & Solomon, P. M. 2004a, ApJS, 152, 63

Gao, Y. & Solomon, P. M. 2004b, ApJ, 606, 271

Ge, J. & Owen, F. N. 1994, AJ, 108, 1523

Genzel, R., Tacconi, L. J., Gracia-Carpio, J., et al. 2010, MNRAS, 407, 2091

George, R. D., Ivison, R. J., Hopwood, R., et al. 2013, MNRAS, 436, L99

Glover, S. C. O., Clark, P. C., Micic, M., & Molina, F. 2015, MNRAS, 448, 1607

Goicoechea, J. R., Chavarría, L., Cernicharo, J., et al. 2015, ApJ, 799, 102

Goldreich, P. & Kwan, J. 1974, ApJ, 189, 441

Goldsmith, P. F., Langer, W. D., Pineda, J. L., & Velusamy, T. 2012, ApJS, 203, 13

Graciá-Carpio, J., Sturm, E., Hailey-Dunsheath, S., et al. 2011, ApJL, 728, L7

Graf, U. U., Simon, R., Stutzki, J., et al. 2012, A&A, 542, L16

Graham, J. A. 1998, ApJ, 502, 245

Greve, T. R., Bertoldi, F., Smail, I., et al. 2005, MNRAS, 359, 1165

Greve, T. R., Ivison, R. J., & Papadopoulos, P. P. 2004, A&A, 419, 99

Greve, T. R., Ivison, R. J., & Stevens, J. A. 2006, Astronomische Nachrichten, 327, 208

Greve, T. R., Vieira, J. D., Weiß, A., et al. 2012, ApJ, 756, 101

Griffin, M. J., Abergel, A., Abreu, A., et al. 2010, A&A, 518, L3

Groves, B., Dopita, M., & Sutherland, R. 2004a, in IAU Symposium, Vol. 222, The Interplay Among Black Holes, Stars and ISM in Galactic Nuclei, ed. T. Storchi-Bergmann, L. C. Ho, & H. R. Schmitt, 263–266

Groves, B. A., Dopita, M. A., & Sutherland, R. S. 2004b, ApJS, 153, 75

Guillard, P., Boulanger, F., Cluver, M. E., et al. 2010, A&A, 518, A59

Guillard, P., Boulanger, F., Pineau des Forêts, G., et al. 2012, ApJ, 749, 158

Guilloteau, S., Omont, A., Cox, P., McMahon, R. G., & Petitjean, P. 1999, A&A, 349, 363

Gullberg, B., De Breuck, C., Lehnert, M. D., et al. 2015, ArXiv e-prints

Hailey-Dunsheath, S., Nikola, T., Stacey, G. J., et al. 2010, ApJL, 714, L162

Hainline, L. J., Blain, A. W., Smail, I., et al. 2011, ApJ, 740, 96

Hatch, N. A., Crawford, C. S., & Fabian, A. C. 2007, MNRAS, 380, 33

Hatch, N. A., Overzier, R. A., Kurk, J. D., et al. 2009, MNRAS, 395, 114

Hatch, N. A., Overzier, R. A., Röttgering, H. J. A., Kurk, J. D., & Miley, G. K. 2008, MNRAS, 383, 931

Hayward, C. C., Narayanan, D., Kereš, D., et al. 2013, MNRAS, 428, 2529

Helfer, T. T., Thornley, M. D., Regan, M. W., et al. 2003, ApJS, 145, 259

Helou, G., Khan, I. R., Malek, L., & Boehmer, L. 1988, ApJS, 68, 151

Heyminck, S., Kasemann, C., Güsten, R., de Lange, G., & Graf, U. U. 2006, A&A, 454, L21

Hezaveh, Y. D. & Holder, G. P. 2011, ApJ, 734, 52

Hezaveh, Y. D., Marrone, D. P., Fassnacht, C. D., et al. 2013, ApJ, 767, 132

Hezaveh, Y. D., Marrone, D. P., & Holder, G. P. 2012, ApJ, 761, 20

Hickox, R. C., Wardlow, J. L., Smail, I., et al. 2012, MNRAS, 421, 284

Hodge, J. A., Carilli, C. L., Walter, F., et al. 2012, ApJ, 760, 11

Hodge, J. A., Karim, A., Smail, I., et al. 2013, ApJ, 768, 91

Hollenbach, D. J. & Tielens, A. G. G. M. 1999, Reviews of Modern Physics, 71, 173

Hopkins, P. F., Cox, T. J., Younger, J. D., & Hernquist, L. 2009, ApJ, 691, 1168

Hopkins, P. F., Narayanan, D., Murray, N., & Quataert, E. 2013, MNRAS, 433, 69

Hughes, D. H., Serjeant, S., Dunlop, J., et al. 1998, Nature, 394, 241

Humphrey, A., Villar-Martín, M., Fosbury, R., et al. 2007, MNRAS, 375, 705

Humphrey, A., Villar-Martín, M., Fosbury, R., Vernet, J., & di Serego Alighieri, S. 2006, MNRAS, 369, 1103

Humphrey, A., Villar-Martín, M., Vernet, J., et al. 2008, MNRAS, 383, 11

Huynh, M. T., Kimball, A. E., Norris, R. P., et al. 2014, MNRAS, 443, L54

Illingworth, G. 1999, ApSS, 269, 165

Iono, D., Yun, M. S., Elvis, M., et al. 2006, ApJL, 645, L97

Ivison, R. J., Morrison, G. E., Biggs, A. D., et al. 2008, MNRAS, 390, 1117

Ivison, R. J., Papadopoulos, P. P., Smail, I., et al. 2011, MNRAS, 412, 1913

Ivison, R. J., Smail, I., Amblard, A., et al. 2012, MNRAS, 425, 1320

Ivison, R. J., Smail, I., Le Borgne, J.-F., et al. 1998, MNRAS, 298, 583

Ivison, R. J., Swinbank, A. M., Smail, I., et al. 2013, ApJ, 772, 137

Ivison, R. J., Swinbank, A. M., Swinyard, B., et al. 2010, A&A, 518, L35+

Jackson, N. & Browne, I. W. A. 1991, MNRAS, 250, 422

Jaffe, W. & Bremer, M. N. 1997, MNRAS, 284, L1

Jaffe, W., Bremer, M. N., & Baker, K. 2005, MNRAS, 360, 748

Jarvis, M. J., Rawlings, S., Willott, C. J., et al. 2001, MNRAS, 327, 907

Jarvis, M. J., Wilman, R. J., Röttgering, H. J. A., & Binette, L. 2003, MNRAS, 338, 263

Joy, M., Lester, D. F., & Harvey, P. M. 1987, ApJ, 319, 314

Karim, A., Swinbank, A. M., Hodge, J. A., et al. 2013, MNRAS, 432, 2

Kaufman, M. J., Wolfire, M. G., Hollenbach, D. J., & , M. L. 1999, ApJ, 527, 795

Kellermann, K. I. 2003, in Astronomical Society of the Pacific Conference Series, Vol. 300, Radio Astronomy at the Fringe, ed. J. A. Zensus, M. H. Cohen, & E. Ros, 185

Kennicutt, Jr., R. C. 1989, ApJ, 344, 685

Kennicutt, Jr., R. C. 1998a, ARA&A, 36, 189

Kennicutt, Jr., R. C. 1998b, ApJ, 498, 541

Klamer, I. J., Ekers, R. D., Bryant, J. J., et al. 2006, MNRAS, 371, 852

Klamer, I. J., Ekers, R. D., Sadler, E. M., & Hunstead, R. W. 2004, ApJL, 612, L97

Klein, B., Philipp, S. D., Krämer, I., et al. 2006, A&A, 454, L29

Kneib, J.-P., Neri, R., Smail, I., et al. 2005, A&A, 434, 819

Komatsu, E., Smith, K. M., Dunkley, J., et al. 2011, ApJS, 192, 18

Kovács, A., Chapman, S. C., Dowell, C. D., et al. 2006, ApJ, 650, 592

Krumholz, M. R. & McKee, C. F. 2005, ApJ, 630, 250

Krumholz, M. R. & Thompson, T. A. 2007, ApJ, 669, 289

Kuiper, E., Hatch, N. A., Miley, G. K., et al. 2011, MNRAS, 415, 2245

Kurk, J. D., Pentericci, L., Overzier, R. A., Röttgering, H. J. A., & Miley, G. K. 2004a, A&A, 428, 817

Kurk, J. D., Pentericci, L., Röttgering, H. J. A., & Miley, G. K. 2004b, A&A, 428, 793

Lacey, C. G., Baugh, C. M., Frenk, C. S., et al. 2015, ArXiv e-prints

Lacey, C. G., Baugh, C. M., Frenk, C. S., et al. 2010, MNRAS, 405, 2

Laurent, G. T., Aguirre, J. E., Glenn, J., et al. 2005, ApJ, 623, 742

Lavalley, M. P., Isobe, T., & Feigelson, E. D. 1992, in Bulletin of the American Astronomical Society, Vol. 24, Bulletin of the American Astronomical Society, 839–840

Lee, N., Sanders, D. B., Casey, C. M., et al. 2013, ApJ, 778, 131

Leech, K. J., Völk, H. J., Heinrichsen, I., et al. 1999, MNRAS, 310, 317

Leroy, A. K., Walter, F., Bigiel, F., et al. 2009, AJ, 137, 4670

Lestrade, J.-F., Combes, F., Salomé, P., et al. 2010, A&A, 522, L4+

Lilly, S. J. & Longair, M. S. 1984, MNRAS, 211, 833

Lilly, S. J., Tresse, L., Hammer, F., Crampton, D., & Le Fevre, O. 1995, ApJ, 455, 108

Lonsdale, C. J. & Barthel, P. D. 1986, AJ, 92, 12

Lord, S. D., Hollenbach, D. J., Haas, M. R., et al. 1996, ApJ, 465, 703

Luhman, M. L., Satyapal, S., Fischer, J., et al. 1998, ApJL, 504, L11

Luhman, M. L., Satyapal, S., Fischer, J., et al. 2003, ApJ, 594, 758

Lupu, R. E., Scott, K. S., Aguirre, J. E., et al. 2012, ApJ, 757, 135

Ma, J., Gonzalez, A. H., Spilker, J. S., et al. 2015, ApJ, 812, 88

Madau, P., Ferguson, H. C., Dickinson, M. E., et al. 1996, MNRAS, 283, 1388

Madden, S., Geis, N., Genzel, R., et al. 1997, in ESA Special Publication, Vol. 401, The Far Infrared and Submillimetre Universe., ed. A. Wilson, 111

Magorrian, J., Tremaine, S., Richstone, D., et al. 1998, AJ, 115, 2285

Maiolino, R., Caselli, P., Nagao, T., et al. 2009, A&A, 500, L1

Maiolino, R., Cox, P., Caselli, P., et al. 2005, A&A, 440, L51

Malhotra, S., Helou, G., Stacey, G., et al. 1997, ApJL, 491, L27

Malhotra, S., Kaufman, M. J., Hollenbach, D., et al. 2001, ApJ, 561, 766

Malmquist, K. G. 1924, Meddelanden fran Lunds Astronomiska Observatorium Serie II, 32, 3

Maloney, P. & Black, J. H. 1988, ApJ, 325, 389

Mashian, N., Sternberg, A., & Loeb, A. 2013, MNRAS, 435, 2407

McCarthy, P. J., Kapahi, V. K., van Breugel, W., et al. 1996, ApJS, 107, 19

McCarthy, P. J., Spinrad, H., Dickinson, M., et al. 1990, ApJ, 365, 487

McCarthy, P. J., van Breugel, W., Spinrad, H., & Djorgovski, S. 1987, ApJL, 321, L29

Meijerink, R., Spaans, M., & Israel, F. P. 2007, A&A, 461, 793

Merloni, A. & Heinz, S. 2013, Evolution of Active Galactic Nuclei, ed. T. D. Oswalt & W. C. Keel, 503

Michałowski, M., Hjorth, J., & Watson, D. 2010, A&A, 514, A67

Michałowski, M. J., Dunlop, J. S., Cirasuolo, M., et al. 2012, A&A, 541, A85

Miley, G. K., Overzier, R. A., Zirm, A. W., et al. 2006, ApJL, 650, L29

Mittal, R., O'Dea, C. P., Ferland, G., et al. 2011, MNRAS, 418, 2386

Mocanu, L. M., Crawford, T. M., Vieira, J. D., et al. 2013, ApJ, 779, 61

Mullaney, J. R., Alexander, D. M., Goulding, A. D., & Hickox, R. C. 2011, MNRAS, 414, 1082

Narayanan, D., Cox, T. J., Shirley, Y., et al. 2008, ApJ, 684, 996

Narayanan, D., Krumholz, M. R., Ostriker, E. C., & Hernquist, L. 2012, MNRAS, 421, 3127

Narayanan, D., Turk, M., Feldmann, R., et al. 2015, Nature, 525, 496

Negishi, T., Onaka, T., Chan, K.-W., & Roellig, T. L. 2001, A&A, 375, 566

Neri, R., Downes, D., Cox, P., & Walter, F. 2014, A&A, 562, A35

Nesvadba, N. P. H., Lehnert, M. D., Eisenhauer, F., et al. 2006, ApJ, 650, 693

Nesvadba, N. P. H., Neri, R., De Breuck, C., et al. 2009, MNRAS, 395, L16

Nikola, T., Genzel, R., Herrmann, F., et al. 1998, ApJ, 504, 749

Nikola, T., Hailey-Dunsheath, S., Stacey, G. J., et al. 2003, in Society of Photo-Optical Instrumentation Engineers (SPIE) Conference Series, Vol. 4855, Millimeter and Submillimeter Detectors for Astronomy, ed. T. G. Phillips & J. Zmuidzinas, 88–99

Oberst, T. E., Parshley, S. C., Nikola, T., et al. 2011, ApJ, 739, 100

Oberst, T. E., Parshley, S. C., Stacey, G. J., et al. 2006, ApJL, 652, L125

Ogle, P., Davies, J. E., Appleton, P. N., et al. 2012, ApJ, 751, 13

Ogle, P., Whysong, D., & Antonucci, R. 2006, ApJ, 647, 161

Oke, J. B., Cohen, J. G., Carr, M., et al. 1995, PASP, 107, 375

Oliver, S. J., Bock, J., Altieri, B., et al. 2012, MNRAS, 424, 1614

Omont, A., Yang, C., Cox, P., et al. 2013, A&A, 551, A115

Orr, M. E., Pineda, J. L., & Goldsmith, P. F. 2014, ApJ, 795, 26

Orr, M. J. L. & Browne, I. W. A. 1982, MNRAS, 200, 1067

Ossenkopf, V., Röllig, M., Neufeld, D. A., et al. 2013, A&A, 550, A57

Osterbrock, D. E. 1978, Proceedings of the National Academy of Science, 75, 540

Osterbrock, D. E. & Ferland, G. J. 2006, Astrophysics of gaseous nebulae and active galactic nuclei

Ostriker, E. C. & Shetty, R. 2011, ApJ, 731, 41

Ouchi, M., Ellis, R., Ono, Y., et al. 2013, ApJ, 778, 102

Papadopoulos, P. P., Röttgering, H. J. A., van der Werf, P. P., et al. 2000, ApJ, 528, 626

Papadopoulos, P. P., Thi, W.-F., & Viti, S. 2004, MNRAS, 351, 147

Pei, Y. C. 1995, ApJ, 438, 623

Pentericci, L., Kurk, J. D., Carilli, C. L., et al. 2002, A&A, 396, 109

Pentericci, L., Kurk, J. D., Röttgering, H. J. A., et al. 2000, A&A, 361, L25

Pentericci, L., McCarthy, P. J., Röttgering, H. J. A., et al. 2001, ApJS, 135, 63

Pentericci, L., Roettgering, H. J. A., Miley, G. K., Carilli, C. L., & McCarthy, P. 1997, A&A, 326, 580

Pentericci, L., Röttgering, H. J. A., Miley, G. K., et al. 1999, A&A, 341, 329

Pentericci, L., Röttgering, H. J. A., Miley, G. K., et al. 1998, ApJ, 504, 139

Penzias, A. A., Solomon, P. M., Jefferts, K. B., & Wilson, R. W. 1972, ApJL, 174, L43

Peterson, B. M. 1997, An Introduction to Active Galactic Nuclei

Phinney, E. S. 1985, in Astrophysics of Active Galaxies and Quasi-Stellar Objects, ed. J. S. Miller, 453–496

Pilbratt, G. L., Riedinger, J. R., Passvogel, T., et al. 2010, A&A, 518, L1

Rawle, T. D., Egami, E., Bussmann, R. S., et al. 2014, ApJ, 783, 59

Rawlings, S. & Saunders, R. 1991, Nature, 349, 138

Rees, M. J. 1967, MNRAS, 135, 345

Rees, M. J. 1989, MNRAS, 239, 1P

Reuland, M., Röttgering, H., van Breugel, W., & De Breuck, C. 2004, MNRAS, 353, 377

Reuland, M., van Breugel, W., Röttgering, H., et al. 2003a, ApJL, 582, L71

Reuland, M., van Breugel, W., Röttgering, H., et al. 2003b, ApJ, 592, 755

Rice, W., Lonsdale, C. J., Soifer, B. T., et al. 1988, ApJS, 68, 91

Rickard, L. J., Palmer, P., Morris, M., Zuckerman, B., & Turner, B. E. 1975, in Bulletin of the American Astronomical Society, Vol. 7, Bulletin of the American Astronomical Society, 529

Riechers, D. A., Bradford, C. M., Clements, D. L., et al. 2013, Nature, 496, 329

Riechers, D. A., Carilli, L. C., Walter, F., et al. 2011a, ApJL, 733, L11

Riechers, D. A., Cooray, A., Omont, A., et al. 2011b, ApJL, 733, L12

Riechers, D. A., Hodge, J., Walter, F., Carilli, C. L., & Bertoldi, F. 2011c, ApJL, 739, L31

Riechers, D. A., Walter, F., Carilli, C. L., & Bertoldi, F. 2007, ApJL, 671, L13

Rocca-Volmerange, B., Le Borgne, D., De Breuck, C., Fioc, M., & Moy, E. 2004, A&A, 415, 931

Rocca-Volmerange, B. & Remazeilles, M. 2005, A&A, 433, 73

Roettgering, H. J. A., van Ojik, R., Miley, G. K., et al. 1997, A&A, 326, 505

Röttgering, H., de Bruyn, G., & Pentericci, L. 1999, in The Most Distant Radio Galaxies, ed. H. J. A. Röttgering, P. N. Best, & M. D. Lehnert, 113

Röttgering, H. J. A., Hunstead, R. W., Miley, G. K., van Ojik, R., & Wieringa, M. H. 1995, MNRAS, 277, 389

Röttgering, H. J. A., Lacy, M., Miley, G. K., Chambers, K. C., & Saunders, R. 1994, AAPS, 108, 79

Salomé, P., Combes, F., Revaz, Y., et al. 2011, A&A, 531, A85

Salpeter, E. E. 1955, ApJ, 121, 161

Sanders, D. B., Soifer, B. T., Elias, J. H., et al. 1988, ApJ, 325, 74

Sandstrom, K. M., Leroy, A. K., Walter, F., et al. 2013, ApJ, 777, 5

Sargsyan, L., Lebouteiller, V., Weedman, D., et al. 2012, ApJ, 755, 171

Sargsyan, L., Samsonyan, A., Lebouteiller, V., et al. 2014, ApJ, 790, 15

Schmidt, M. 1959, ApJ, 129, 243

Scoville, N. Z., Yun, M. S., Windhorst, R. A., Keel, W. C., & Armus, L. 1997, ApJL, 485, L21

Serjeant, S. 2012, MNRAS, 3078

Seymour, N., Altieri, B., De Breuck, C., et al. 2012, ApJ, 755, 146

Seymour, N., Stern, D., De Breuck, C., et al. 2007, ApJS, 171, 353

Simpson, C. & Eisenhardt, P. 1999, PASP, 111, 691

Simpson, C., Rawlings, S., Ivison, R., et al. 2012, MNRAS, 421, 3060

Smail, I., Ivison, R. J., & Blain, A. W. 1997, ApJL, 490, L5+

Smail, I., Ivison, R. J., Blain, A. W., & Kneib, J.-P. 2002, MNRAS, 331, 495

Smith, H. E. & Spinrad, H. 1980, PASP, 92, 553

Smolcic, V., Aravena, M., Navarrete, F., et al. 2012, ArXiv e-prints

Solomon, P. M., Downes, D., & Radford, S. J. E. 1992, ApJL, 387, L55

Solomon, P. M. & Sage, L. J. 1988, ApJ, 334, 613

Solomon, P. M. & Vanden Bout, P. A. 2005, ARA&A, 43, 677

Spilker, J. S., Marrone, D. P., Aguirre, J. E., et al. 2014, ApJ, 785, 149

Spinrad, H. 1976, PASP, 88, 565

Spinrad, H., Westphal, J., Kristian, J., & Sandage, A. 1977, ApJL, 216, L87

Springel, V. & Hernquist, L. 2005, ApJL, 622, L9

Stacey, G. J., Geis, N., Genzel, R., et al. 1991a, ApJ, 373, 423

Stacey, G. J., Hailey-Dunsheath, S., Ferkinhoff, C. an d Nikola, T., et al. 2010, ApJ, 724, 957

Stacey, G. J., Jaffe, D. T., Geis, N., et al. 1993, ApJ, 404, 219

Stacey, G. J., Smyers, S. D., Kurtz, N. T., & Harwit, M. 1983, ApJL, 265, L7

Stacey, G. J., Townes, C. H., Geis, N., et al. 1991b, ApJL, 382, L37

Stahler, S. W. & Palla, F. 2005, The Formation of Stars, 865

Staniszewski, Z., Ade, P. A. R., Aird, K. A., et al. 2009, ApJ, 701, 32

Stevens, J. A., Ivison, R. J., Dunlop, J. S., et al. 2003, Nature, 425, 264

Strong, A. W., Moskalenko, I. V., Reimer, O., Digel, S., & Diehl, R. 2004, A&A, 422, L47

Stutzki, J., Stacey, G. J., Genzel, R., et al. 1988, ApJ, 332, 379

Swinbank, A. M. 2013, Astrophysics and Space Science Proceedings, 37, 299

Swinbank, A. M., Papadopoulos, P. P., Cox, P., et al. 2011, ApJ, 742, 11

Swinbank, A. M., Simpson, J. M., Smail, I., et al. 2014, MNRAS, 438, 1267

Swinbank, A. M., Smail, I., Longmore, S., et al. 2010, Nature, 464, 733

Swinbank, A. M., Smail, I., Sobral, D., et al. 2012, ApJ, 760, 130

Swinbank, A. M., Vernet, J. D. R., Smail, I., et al. 2015, MNRAS, 449, 1298

Symeonidis, M., Vaccari, M., Berta, S., et al. 2013, MNRAS, 431, 2317

Tacconi, L. J., Genzel, R., Neri, R., et al. 2010, Nature, 463, 781

Tacconi, L. J., Genzel, R., Smail, I., et al. 2008, ApJ, 680, 246

Tacconi, L. J. & Young, J. S. 1987, ApJ, 322, 681

Tadhunter, C. N., Morganti, R., Robinson, A., et al. 1998, MNRAS, 298, 1035

Teyssier, R., Chapon, D., & Bournaud, F. 2010, ApJL, 720, L149

Tielens, A. G. G. M., Miley, G. K., & Willis, A. G. 1979, AAPS, 35, 153

Torres, D. F. 2003, ArXiv Astrophysics e-prints

Tremaine, S., Gebhardt, K., Bender, R., et al. 2002, ApJ, 574, 740

Uson, J. M., Bagri, D. S., & Cornwell, T. J. 1991, Physical Review Letters, 67, 3328

Valtchanov, I., Virdee, J., Ivison, R. J., et al. 2011, MNRAS, 415, 3473

van Breugel, W., Filippenko, A. V., Heckman, T., & Miley, G. 1985, ApJ, 293, 83

van Breugel, W. J. M. & Dey, A. 1993, ApJ, 414, 563

van Breugel, W. J. M., Stanford, S. A., Spinrad, H., Stern, D., & Graham, J. R. 1998, ApJ, 502, 614

van der Werf, P. P., Berciano Alba, A., Spaans, M., et al. 2011, ApJL, 741, L38

van Ojik, R., Roettgering, H. J. A., Carilli, C. L., et al. 1996, A&A, 313, 25

van Ojik, R., Roettgering, H. J. A., Miley, G. K., & Hunstead, R. W. 1997, A&A, 317, 358

Venemans, B. P., McMahon, R. G., Walter, F., et al. 2012, ApJL, 751, L25

Venemans, B. P., Röttgering, H. J. A., Miley, G. K., et al. 2007, A&A, 461, 823

Vernet, J. & Cimatti, A. 2001, A&A, 380, 409

Vernet, J., Fosbury, R. A. E., Villar-Martín, M., et al. 2001, A&A, 366, 7

Vieira, J. D., Crawford, T. M., Switzer, E. R., et al. 2010, ApJ, 719, 763

Vieira, J. D., Marrone, D. P., Chapman, S. C., et al. 2013, Nature, 495, 344

Villar-Martin, M. & Binette, L. 1996, A&A, 309, 97

Villar-Martin, M. & Binette, L. 1997, A&A, 317, 350

Villar-Martín, M., Binette, L., & Fosbury, R. A. E. 1999a, A&A, 346, 7

Villar-Martín, M., Humphrey, A., De Breuck, C., et al. 2007, MNRAS, 375, 1299

Villar-Martín, M., Sánchez, S. F., Peletier, R., et al. 2006, Astronomische Nachrichten, 327, 187

Villar-Martin, M., Tadhunter, C., & Clark, N. 1997, A&A, 323, 21

Villar-Martín, M., Tadhunter, C., Morganti, R., Axon, D., & Koekemoer, A. 1999b, MNRAS, 307, 24

Villar-Martin, M., Tadhunter, C., Morganti, R., et al. 1998, A&A, 332, 479

Villar-Martín, M., Vernet, J., di Serego Alighieri, S., et al. 2003, NewAR, 47, 291

Viti, S., Bayet, E., Hartquist, T. W., et al. 2013, in Advances in Solid State Physics, Vol. 34, Cosmic Rays in Star-Forming Environments, ed. D. F. Torres & O. Reimer, 7

Wagg, J., Carilli, C. L., Wilner, D. J., et al. 2010, A&A, 519, L1

Wagg, J., Wiklind, T., Carilli, C. L., et al. 2012, ApJL, 752, L30

Walter, F., Brinks, E., de Blok, W. J. G., Thornley, M. D., & Kennicutt, R. C. 2005, in Astronomical Society of the Pacific Conference Series, Vol. 331, Extra-Planar Gas, ed. R. Braun, 269

Walter, F., Decarli, R., Carilli, C., et al. 2012, Nature, 486, 233

Walter, F., Weiß, A., Downes, D., Decarli, R., & Henkel, C. 2011, ApJ, 730, 18

Wang, R., Wagg, J., Carilli, C. L., et al. 2013, ApJ, 773, 44

Wardlow, J. L., Cooray, A., De Bernardis, F., et al. 2013, ApJ, 762, 59

Wardlow, J. L., Smail, I., Coppin, K. E. K., et al. 2011, MNRAS, 415, 1479

Weilbacher, P. M., Streicher, O., Urrutia, T., et al. 2012, in Society of Photo-Optical Instrumentation Engineers (SPIE) Conference Series, Vol. 8451, Society of Photo-Optical Instrumentation Engineers (SPIE) Conference Series, 0

Weiß, A., De Breuck, C., Marrone, D. P., et al. 2013, ApJ, 767, 88

Weiß, A., Downes, D., Neri, R., et al. 2007, A&A, 467, 955

Weiß, A., Henkel, C., Downes, D., & Walter, F. 2003, A&A, 409, L41

Weiß, A., Kovács, A., Coppin, K., et al. 2009, ApJ, 707, 1201

Willott, C. J., Omont, A., & Bergeron, J. 2013, ApJ, 770, 13

Willott, C. J., Rawlings, S., Blundell, K. M., Lacy, M., & Eales, S. A. 2001, MNRAS, 322, 536

Wilson, R. W., Jefferts, K. B., & Penzias, A. A. 1970, ApJL, 161, L43

Wolfire, M. G., Hollenbach, D., & Tielens, A. G. G. M. 1989, ApJ, 344, 770

Wolfire, M. G., Hollenbach, D., & Tielens, A. G. G. M. 1993, ApJ, 402, 195

Wolfire, M. G., Tielens, A. G. G. M., & Hollenbach, D. 1990, ApJ, 358, 116

Wong, T. & Blitz, L. 2002, ApJ, 569, 157

Wylezalek, D., Galametz, A., Stern, D., et al. 2013, ApJ, 769, 79

Yan, L., Tacconi, L. J., Fiolet, N., et al. 2010, ApJ, 714, 100

Yang, C., Gao, Y., Omont, A., et al. 2013, ApJL, 771, L24

Young, J. S., Xie, S., Tacconi, L., et al. 1995, ApJS, 98, 219

Zavala, J. A., Yun, M. S., Aretxaga, I., et al. 2015, MNRAS, 452, 1140

Zirm, A. W., Overzier, R. A., Miley, G. K., et al. 2005, ApJ, 630, 68

Curriculum Vitae

European Southern Observatory
Karl-Schwarzschild-Str. 2
D-85748 Garching, Germany
+49 (0)89 3200 6858

E-mail: bgullber@eso.org
Citizenship: Danish
Languages: Danish (native), English (fluent), German

Education

Postdoc, November 2015 - present

- University of Durham
- Working under Prof Ian Smail

Ph.D. student, September 2012 - October 2015

- IMPRS[1] student at the European Southern Observatory (ESO) in Garching bei München
- Title of Ph.D. *Exploring Star Formation in high-z Galaxies using Atomic and Molecular Emission Lines*
- Supervisors: Prof. Ralf Bender (LMU) and Dr. Carlos De Breuck (ESO)

M.Sc. in Physics, 2010 - 13. August 2012

- Master in physics at the Niels Bohr Institute/Dark Cosmology Centre, University of Copenhagen
- Title of master thesis: *Exploring the Star Forming Gas in Distant Massive Galaxies*
- Supervisor: Dr. Thomas R. Greve

B.Sc. in Astronomy, 2007 - 2010:

- Bachelor in astronomy at the Niels Bohr Institute/Dark Cosmology Centre University of Copenhagen
- Title of bachelor project: *Emission from high metallicity Damped Lyα Absorbers*
- Supervisor: Prof. Johan P. U. Fynbo

[1] International Max Planck Research School

Refereed publications

First author

ALMA finds Dew Drops in the Dusty Spider's Web
Gullberg, B., *Lehnert, M. D., De Breuck, C., Branchu, S., Dannerbauer, H., Drouart, G., Emonts, E., Guillard, P. Hatch, N., Nesvadba, N. P. H., Omont, A., Seymour, N., and Vernet, J.* submitted to A&A

The Mysterious Morphology of MRC0943-242 as Revealed by ALMA and MUSE,
Gullberg, B., *De Breuck, C., Lehnert, M. D., Vernet, J., Bacon, R., Drouart, G., Emonts, B., Galametz, A., Ivison, R., Nesvadba, N. P. H., Richard, J., Seymour, N., Stern, D., Wylezalek, D.* A&A 2015 ADS

Optically thick [CII] emission in lensed dusty star-forming galaxies from the SPT-survey,
Gullberg B. , *De Breuck C., Vieira J. D., WeißA., Aguirre J. E., Aravena M., Bethermin M., Bradford C. M., Bothwell M. S., Carlstrom J. E., Chapman S. C., Fassnacht C. D., Gonzalez A. H., Greve T. R., Hezaveh Y., Holzapfel W. L., Husband K., Ma J., Malkan M., Marrone D. P., Menten K., Murphy E. J., Reichardt C. L., Spilker J. S., Stark A. A., Strandet M., Welikala N.* MNRAS 2015 ADS

Co-author

ALMA unveils a triple merger and gas exchange in a hyper-luminous radio galaxy at z=2: the Dragonfly Galaxy (II) *Emonts, B. H. C., De Breuck, C., Lehnert, M. D., Vernet, J.,* **Gullberg, B.**, *Villar-Martn, M., Nesvadba, N., Drouart, G., Ivison, R., Seymour, N., Wylezalek, D., Barthel, P.* A&A 2015 ADS

Stellar Masses and Star Formation Rates of Lensed, Dusty, Star-forming Galaxies from the SPT Survey *Ma, J., Gonzalez, A. H., Spilker, J. S., Strandet, M., Ashby, M. L. N., Aravena, M., Bthermin, M., Bothwell, M. S., de Breuck, C., Brodwin, M., Chapman, S. C., Fassnacht, C. D., Greve, T. R.,* **Gullberg, B.**, *Hezaveh, Y., Malkan, M., Marrone, D. P., Saliwanchik, B. R., Vieira, J. D., Weiss, A., Welikala, N.* ApJ 2015 ADS

The Rest-frame Submillimeter Spectrum of High-redshift, Dusty, Star-forming Galaxies,
Spilker J. S., Marrone D. P., Aguirre J. E., Aravena M., Ashby M. L. N., Bethermin M., Bradford C. M., Bothwell M. S., Brodwin M., Carlstrom J. E., Chapman S. C., Crawford T. M., De Breuck C., Fassnacht C. D., Gonzalez A. H., Greve T. R., **Gullberg B.**, *Hezaveh Y., Holzapfel W. L., Husband K., Ma J., Malkan M., Murphy E. J., Reichardt C. L., Rotermund K. M., Stalder B., Stark A. A., Strandet M., Vieira J. D., WeißA., Welikala*

N. ApJ 2014 ADS.

SPT 0538-50: Physical Conditions in the Interstellar Medium of a Strongly Lensed Dusty Star-forming Galaxy at z = 2.8,
Bothwell M. S., Aguirre J. E., Chapman S. C., Marrone D. P., Vieira J. D., Ashby M. L. N., Aravena M., Benson B. A., Bock J. J., Bradford C. M., Brodwin M., Carlstrom J. E., Crawford T. M., De Breuck C., Downes T. P., Fassnacht C. D., Gonzalez A. H., Greve T. R., **Gullberg B.**, *Hezaveh Y., Holder G. P., Holzapfel W. L., Ibar E., Ivison R., Kamenetzky J., Keisler R., Lupu R. E., Ma J., Malkan M., McIntyre V., Murphy E. J., Nguyen H. T., Reichardt C. L., Rosenman M., Spilker J. S., Stalder B., Stark A. A., Strandet M., Vernet J., WeißA., Welikala N.* ApJ 2013 ADS.

Large gas reservoirs and free-free emission in two lensed star-forming galaxies at $z = 2.7$,
Aravena M., Murphy E. J., Aguirre J. E., Ashby M. L. N., Benson B. A., Bothwell M., Brodwin M., Carlstrom J. E., Chapman S. C., Crawford T. M., De Breuck C., Fassnacht C. D., Gonzalez A. H., Greve T. R., **Gullberg B.**, *Hezaveh Y., Holder G. P., Holzapfel W. L., Keisler R., Malkan M., Marrone D. P., McIntyre V., Reichardt C. L., Sharon K., Spilker J. S., Stalder B., Stark A. A., Vieira J. D., WeißA.* MNRAS 2013 ADS.

Dusty starburst galaxies in the early Universe as revealed by gravitational lensing,
Vieira J. D., Marrone D. P., Chapman S. C., De Breuck C., Hezaveh Y. D., WeißA., Aguirre J. E., Aird K. A., Aravena M., Ashby M. L. N., Bayliss M., Benson B. A., Biggs A. D., Bleem L. E., Bock J. J., Bothwell M., Bradford C. M., Brodwin M., Carlstrom J. E., Chang C. L., Crawford T. M., Crites A. T., de Haan T., Dobbs M. A., Fomalont E. B., Fassnacht C. D., George E. M., Gladders M. D., Gonzalez A. H., Greve T. R., **Gullberg B.**, *Halverson N. W., High F. W., Holder G. P., Holzapfel W. L., Hoover S., Hrubes J. D., Hunter T. R., Keisler R., Lee A. T., Leitch E. M., Lueker M., Luong-van D., Malkan M., McIntyre V., McMahon J. J., Mehl J., Menten K. M., Meyer S. S., Mocanu L. M., Murphy E. J., Natoli T., Padin S., Plagge T., Reichardt C. L., Rest A., Ruel J., Ruhl J. E., Sharon K., Schaffer K. K., Shaw L., Shirokoff E., Spilker J. S., Stalder B., Staniszewski Z., Stark A. A., Story K., Vanderlinde K., Welikala N., Williamson R.* NATURE 2013 ADS.

Galaxy Counterparts of metal-rich Damped Lyman-α Absorbers - I: The case of the $z = 2.35$ DLA towards Q 2222-0946,
Fynbo J. P. U., Laursen P., Ledoux C., Møller P., Durgapal A. K., Goldoni P., **Gullberg B.**, *Kaper L., Maund J., Noterdaeme, P., Östlin G., Strandet M. L., Toft S., Vreeswijk P. M., Zafar T.* MNRAS 2010 ADS.

Acknowledgements

I have been wanting to achieve a PhD and to carry out research in extragalactic astronomy since my first year at the Niels Bohr Institute. That was how the 'Purpose and Goals' section of my IMPRS[2] application started. This application got me to an invitation to the IMPRS workshop in Garching three cold days in February 2011, and let to an offer from ESO. As you know, I accepted the offer, and though it has been three (slightly) turbulent years I have not regretted accepting that offer! I feel I have grown so much, experienced so much and gotten to know so many wonderful people! I would like to thank all these people and my family for their help, friendship and support these three years. However, I do wish to add a few words to some of these people:

If you have come this far into this thesis you might have noticed the dedication page. I have dedicated this thesis to **my parents, Ida** and **Ib**. You have always been there for me, always supported me and always believed in me. You have always supported me in my choice of career, though you had probably hoped for something a bit closer to home. I have enjoyed all your visits here in Munich and all our adventures in Bavaria, trips to cities, lakes, castles, etc. I hope you will come and explore the north of England as well.

I want to thank my lovely **brother, Bjarke**, for challenging me by talking me to highest I never thought I would go. You have always been a proper big-brother, and taken care of me, supported me and protected me. I can always count on you to take my mind of troubling things, and make me forget for a bit. You are the best brother ever! At the same time I would like to thank my **sister-in-law, Helene**, for your support and for telling me the gossip my brother does not ;) Thank you both for being there for me and (no to forget) helping me move to Munich three years ago.

With my family far away, people in Garching became my 'local' family. I wish to thank **Carlos** for being an amazing and supportive supervisor. Thank you for all your help and support in difficult times, when it was hard to see the light at the end of the tunnel. Thank you for all the brilliant scientific and (not to forget) gossip chats. I likewise wish to thank **Joël** for his help and support this last part of my thesis. We have only work together, for a short time, but it made all the difference. Thanks both of you, for being the best supervisors I could have asked for.

I would like to thank ESO for making it possible for me to go to conferences, meetings and on an observing trip and making way for my career. I have met so many wonderful people at ESO, who mean the world to me! The students, fellows and staff at ESO have

[2]International Max Planck Research School

made meetings, coffees, Friday beers, summer/winter parties, social days, etc unforgettable! Thank you for that! The environment at ESO is unique and precious, take good care of it. There are a few people a wish to add a few more words to (in a random order):

Clau and **Rodrigo**, you guys are way *waaay* too far away now, and you left ESO way *waaay* too early! Thank you for all the fun times. You guys have given me so much and helped me grow so much. **Izas**, thank you for giving me the hug I needed, when I needed it! Your calmness can tame the most angry and panicked lion. Thank you for your advice, motivation and support. **Kate**, thank you for all the support, laughs and chats during bouldering, skiing, beer festivals, dinners and many many other occasion. **Maud**, thank you for all the laughs, swimming trips, hikes, beer festivals, listening, giving advice and much more. You have been an immense support and motivation! You four girls (Clau, Izas, Kate and Maud) have been huge role models and I have learned so much from you!

Officemate and hiking buddy, **Anna**, you sent me a message in May 2014 saying: *'what do you say, would you like to have me in your office?'* and my reply was *YEAH YEAH!!! would be great! YEAH! new officemate* :). I was alone in the office at the time and getting you as an officemate made all the difference in the world. We have had some wonderful (and a bit steep) hikes in the Alps, which I will never forget! Thank you for all your love, support, chats, coffees and dinners. **Gergö** and **Anke**, no moment is boring with you two around! Thank you for your support and all the hilarious moments! Gergö thank you for all your CASA help and all the elevator rides ;) Take care of all the minions and get them all safe to shore, Caption Gergö! **Katha**, it is a shame we did not get to overlap more at ESO, you should have come to ESO earlier (or I should have stayed longer ;)). Thank you for all your help! In a stressful time it is so wonderful to have friends you can count on! Maud, Anna, Anka, Katha and Gergö the video and the 'cub song' are priceless and I will miss you guys too!

Tullia, thank you for all your encouraging words (*'You can do it'*), support and wonderful skiing trips to the Alps! **Madhura**, thank you for the long chats, the bouldering tricks and your friendship. You are awfully far away now, but I know we are going to see each other again, I am going to make sure of that. *'Ehi!* ***Marco'***! Thank you for all the fun times and all the brilliant jokes! Be careful with the small stones and the canon, and I hope you got yourself that 'pretty' par of (pink?) shoes to so wanted ;) **Neale**, thank you for your (as always) brilliant advice, I will try to follow it and go 'up'! **Laura**, thanks for all the fun times, the laughs and the sushi dinners! Lets keep that Whatsapp chat alive. **Tim, Grant** and **Roberto**, the last time we met was in Tokyo, and it was (as always) an unforgettable time with you guys! Thank you for all the laughs and support!

Nora for being there for me, helping me find my feet in Munich and listening to me when I needed to chatted. Though you are now on the other side of the 'pond' I am so happy that we keep in contact and I enjoy seeing all your Snapchats. **Anna**, I know I can always count on you being there if/when I need it. You will let go of what you have in your hands and come to 'the rescue' if you can, thank you! **Leticia** for being the happy, lively and exotic contribution to the girls group. Your happiness and laugh is so contagious and you can always make me smile.

There are also friends and family back home I would like to thank:

The physics girls (fysik pigerne), **Maria, Mette, Mathilde, Eva, Simone, Turi, AK** and **Pernille**, we have stuck together since the first year at the NBI. We have laughed, cried and 'kvantet i måneskin' together so many times. We have been through so much together and we stuck together through it all, and I believe we are going to keep sticking for many years to come. Skype is our weapon!

My two high school girls (gymnasie pigerne), **Cecil** and **Nille**, I wish to thank you girls for alway having been there and always believed in me. We have know each other for more than 10 years, and though our jobs and interests are very different now, it is still like old times when we meet. I cherish our friendship and hope that it will last many years to come.

I also wish to thank my family back home, for your support and interest in my work!

I better stop here before the acknowledgements turns into a chapter on its own. I wish to finish by saying 'thank you' to everybody I have gotten to know or helped me through these past three years!

Tak!